



Body movement is the result of cascades of complex chemical, electrical, and mechanical processes taking place at different length and time scales. This thesis deals with the biophysical modelling of these processes. In detail, the generation of electrical signals in spinal motor neurons is investigated based on the Hodgkin-Huxley formalism. Next, the complex signalling pathway leading from electrical excitation to contraction and force generation of the muscle fibres is modelled. Based on a structural model of the muscle and the bidomain equations, a method is proposed to predict electromyographic (EMG) signals, which are frequently recorded in the clinic and result from electrical signals propagating along muscle fibres to induce the contraction. Extending this model by a continuum-mechanical approach, a multiscale model of the neuromuscular system is obtained that considers chemical, electrical, and mechanical properties and allows to predict force generation, muscle deformation, and the EMG signal during fixed-length and non-isometric contractions. The proposed framework can potentially be used as an in-silico laboratory to investigate changes in the chemo-electro-mechanical behaviour resulting from pathological conditions or drug treatment.



Thomas Heidlauf

ISBN 978-3-946412-00-7

T. Heidlauf

Modelling of the Neuromuscular System

CBM-01 (2015)

Chemo-Electro-Mechanical Modelling of the Neuromuscular System

Thomas Heidlauf



Universität Stuttgart

Chemo-Electro-Mechanical Modelling of the Neuromuscular System

Von der Fakultät Bau- und Umweltingenieurwissenschaften und
dem Stuttgart Research Centre for Simulation Technology
der Universität Stuttgart zur Erlangung der Würde
eines Doktor-Ingenieurs (Dr.-Ing.)
genehmigte Abhandlung

vorgelegt von

Dipl.-Ing. Thomas Heidlauf

aus

Saulgau (jetzt Bad Saulgau)

Hauptberichter: Prof. Oliver Röhrle, Ph. D.

1. Mitberichter: Prof. Dario Farina, Ph. D.

2. Mitberichter: Prof. Dr. Tobias Siebert

Tag der mündlichen Prüfung: 28. September 2015

Institut für Mechanik (Bauwesen) der Universität Stuttgart
Research Group on Continuum Biomechanics and Mechanobiology
Prof. Oliver Röhrle, Ph. D.

2015

Report No.: CBM-01
Institut für Mechanik
Lehrstuhl für Kontinuumsmechanik
Research Group on Continuum Biomechanics and Mechanobiology
Universität Stuttgart, Germany, 2015

Editor:

Prof. O. Röhrle, Ph. D.

© Thomas Heidlauf
Institut für Mechanik
Lehrstuhl für Kontinuumsmechanik
Research Group on Continuum Biomechanics and Mechanobiology
Universität Stuttgart
Pfaffenwaldring 7
70569 Stuttgart, Germany

All rights reserved. No part of this publication may be reproduced, stored in a retrieval system, or transmitted, in any form or by any means, electronic, mechanical, photocopying, recording, scanning or otherwise, without the permission in writing of the author.

ISBN 978-3-946412-00-7
(D93 – Dissertation, Universität Stuttgart)

Acknowledgements

The work presented in this thesis was carried out between 2009 and 2015, while I was working as assistant researcher at the University of Stuttgart, Institute of Applied Mechanics (Civil Engineering), Chair of Continuum Mechanics, Research Group on Continuum Biomechanics and Mechanobiology. Many people contributed to the realisation of this work. Their support is gratefully acknowledged.

First of all, I would like to express my deepest gratitude to my advisor Professor Oliver Röhrle for giving me the opportunity to prepare this thesis in his research group. His constant support, ideas, and willingness to discuss provided the framework for this work. The experienced lack of pressure and freedom to develop and work out new ideas made this research group the perfect workplace for me.

I am grateful to Professors Dario Farina and Tobias Siebert for taking the co-chairs of my promotion procedure. From both of them I learned a lot about (modelling of) the neuromuscular system. Working with Professor Dario Farina and his postdoc Francesco Negro was always very inspiring. The exciting discussions with Professor Tobias Siebert were highly appreciated and led to a fruitful collaboration.

Further, I want to thank all colleagues at the Institute of Applied Mechanics. In particular, I thank Arndt Wagner, Sami Bidier, and David Koch. I am also grateful to Professor Bernd Markert, with whom I worked initially at the institute, and without whom I would probably not have entered the field of mechanics.

Moreover, I would like to thank Chris Bradley at the Auckland Bioengineering Institute for providing comprehensive support for `OpenCMISS`.

I have always loved working with my colleagues of the Research Group on Continuum Biomechanics and Mechanobiology and want to thank them for the great time. I learned a lot from each of them. Especially my office mates Michael Sprenger and Christian Bleiler I owe a debt of gratitude. Discussing all aspects of mechanics, they certainly contributed to the success of this work. Furthermore, I thank my colleagues and former master students Mylena Mordhorst and Ekin Altan. The excellent work of Mylena became part of this thesis, and Ekin's great work set the initial stage for an extension of the presented model. I would also like to thank all my other students. Working with such talented people was always a great pleasure for me.

Last not least, I thank my family and especially my parents. Their generous support enabled my studies, which eventually led to this thesis. Without them, this would not have been possible.

Stuttgart, September 2015

Thomas Heidlauf

If I have seen further, it is by standing on the shoulders of giants.

Sir Isaac Newton (1642 – 1726/7)

Contents

Deutschsprachige Zusammenfassung	ix
Motivation	ix
Stand der Forschung, Zielsetzung und Vorgehensweise	x
Gliederung der Arbeit	xvi
Abbreviations	xix
Nomenclature	xxi
Conventions	xxi
Symbols	xxii
1 Introduction	1
1.1 Motivation	1
1.2 Scope, Aims, and State of the Art	2
1.3 Overview	7
1.4 List of Publications	9
2 Anatomical and Physiological Fundamentals	11
2.1 Summary	11
2.2 Basic Anatomy of the Motor Unit	12
2.3 The Cell Membrane of Excitable Cells	12
2.3.1 Resting Membrane Potential	13
2.3.2 Action Potentials	14
2.3.3 Synapses, Excitatory and Inhibitory Postsynaptic Potentials	15
2.4 Neurons	17
2.4.1 The Structure of a Neuron	17
2.4.2 Types of Neurons	18
2.4.3 The Physiology of the Neural System	18
2.5 Skeletal Muscle	19
2.5.1 Skeletal Muscle Architecture	19
2.5.2 Muscle Fibre Contractions	21
2.6 The Motor Unit	23
2.6.1 Properties of Motor Units	24
2.6.2 Types of Contractions	24
3 Mathematical and Mechanical Prerequisites	25
3.1 Finite Element Method for the Spatial Discretisation of Partial Differential Equations	25
3.1.1 The Weak Form	26

3.1.2	The Finite Element Method	26
3.2	Numerical Methods for Ordinary Differential Equations	27
3.2.1	Introduction	28
3.2.2	Linear Multistep Methods	29
3.2.3	Convergence, Stability, and Stiffness	31
3.3	Newton's Method	32
3.4	Continuum-Mechanical Fundamentals	33
3.4.1	Kinematic Relations	33
3.4.2	Stress Measures	37
3.4.3	Balance Relations	38
4	Biophysical Cell Modelling of the Neuromuscular System	41
4.1	The Hodgkin-Huxley Model of the Membrane Electrophysiology	41
4.2	Modelling Motor Neurons and the Motor Neuron Pool	44
4.2.1	Mathematical Description of the Motor Neuron Model	44
4.2.2	Motor Neuron Pool Modelling	45
4.2.3	Input to Motor Neurons	46
4.2.4	Behaviour of the Motor Neuron Model	47
4.3	Modelling the Subcellular Behaviour of Skeletal Muscles	51
4.3.1	Mathematical Description of the Skeletal Muscle Model	51
4.3.2	Parametrisation	57
4.3.3	Behaviour of the Isometric Skeletal Muscle Model	60
4.3.4	Extension to Non-Isometric Contractions	65
4.4	Modelling of the Neuromuscular System	69
4.4.1	Coupling the Motor Neuron Model and the Muscle Unit Force Model	69
4.4.2	Linear Ramp Increase and Decrease	70
4.4.3	Force Variability	74
4.4.4	Tremor	77
4.5	Discussion	77
5	Propagation of Electrical Signals Through Biological Tissues	81
5.1	The Bidomain Model	82
5.1.1	Derivation of the Bidomain Equations	83
5.2	The Monodomain Model	86
5.2.1	Numerical Methods for Solving the Monodomain Equation	88
5.3	Simulating the Action Potential Propagation	90
5.3.1	Comparing the Monodomain and Bidomain Models	90
5.3.2	Propagation of the Action Potential Along Muscle Fibres	95
5.3.3	Influence of the Time Step Size	95
5.3.4	Influence of the Element Size	96
5.3.5	Influence of Material Parameters	97
5.3.6	Influence of the Activation History	98
5.4	Simulating Electromyographic Signals	100
5.4.1	Propagation of Electrical Signals Through a Volume Conductor	100
5.4.2	Surface and Intramuscular EMG in a Rectangular Cuboid	103
5.4.3	Effect of Membrane Fatigue on the EMG	105
5.5	Discussion	108

6	A Multiscale Skeletal Muscle Model	111
6.1	Constitutive Modelling	111
6.1.1	Preliminary Assumptions and Resulting Equations	111
6.1.2	Resulting Strain Energy Functions	114
6.2	Numerical Treatment of the Multiscale Model	119
6.2.1	Overview of the Multiscale Muscle Model	120
6.2.2	Monodomain Model on a Deforming Domain	121
6.2.3	High-Performance Computing	122
6.3	Applications of the Multiscale Model	126
6.3.1	Parameter Identification	127
6.3.2	The Multiscale Computational Model	131
6.3.3	Investigating Different Muscle Fibre Arrangements	135
7	A Multiscale Model of the Neuromuscular System	143
7.1	Overview of the Multiscale Model of the Neuromuscular System	143
7.2	Modelling Electromyographic Signals Under Non-Isometric Conditions . . .	144
7.3	Applications of the Multiscale Model of the Neuromuscular System	145
7.3.1	Isometric and Non-Isometric Contractions of a Rectangular Cuboid	145
7.3.2	Modelling the Tibialis Anterior Muscle	148
8	Summary, Discussion, and Outlook	153
8.1	Summary	153
8.2	Discussion and Outlook	155
A	Additional Continuum-Mechanical Details	159
A.1	Natural Basis Representation	159
A.1.1	Covariant and Contravariant Basis	159
A.1.2	Covariant and Contravariant Transport Operations	159
A.2	Thermodynamic Considerations	160
A.2.1	Determinism, Equipresence, and Local Action	160
A.2.2	Material Frame Indifference	161
A.2.3	Universal Dissipation	161
A.2.4	Material Symmetry	162
A.2.5	Theory of Invariants	163
A.2.6	Further Physical and Mathematical Requirements	163
B	The Motor Neuron Model	165
C	Comparing the Monodomain Model and the Bidomain Model	167
D	Weak Forms	169
D.1	Weak Form of the Monodomain Equation	169
D.2	Weak Form of the Extracellular Bidomain Equation	169
D.3	Weak Form of the Continuum-Mechanical Model	170

Curriculum Vitae

List of Figures

2.1	The cell membrane	13
2.2	The action potential	15
2.3	Structure of a neuron	17
2.4	Schematic representation of the structure of a skeletal muscle	19
2.5	Structure of a sarcomere	20
2.6	Schematic representation of excitation-contraction coupling in a muscle fibre	22
2.7	Force-length relationship	23
2.8	Force-velocity relationship	23
3.1	Motion of a mechanical body	33
4.1	Hodgkin-Huxley model	43
4.2	Equivalent electrical circuit of the motor neuron model	45
4.3	Action potentials in the motor neuron model	47
4.4	Input-output behaviour of the motor neuron model	48
4.5	Motor neuron discharge rates for varying synaptic inputs	49
4.6	Schematic representation of the model of Shorten et al. [240]	52
4.7	The muscle cell membrane model and the calcium dynamics model	53
4.8	The cross-bridge dynamics model and the fatigue model	55
4.9	Average cross-bridge distortion during isometric contractions	56
4.10	Twitch forces in the proposed model and the reference model	59
4.11	Basic twitch properties in the proposed model and the reference model	61
4.12	Modelled muscle forces in response to constant frequency stimulation	62
4.13	Doublet stimulations in a slow-twitch motor unit	63
4.14	Doublet stimulations in a fast-twitch motor unit	64
4.15	Force-length and force-velocity relations	66
4.16	Average cross-bridge distortions induced through filament sliding	66
4.17	Active contractions for different shortening velocities	68
4.18	Structure of the biophysical model of the neuromuscular system	69
4.19	Comparison of the proposed model and the reference model	72
4.20	Comparison of the mean discharge rates of different motor neuron models	73
4.21	Behaviour of the model for slow and fast synaptic inputs	73
4.22	Coefficient of variation of the force versus mean force	74
4.23	Total force and power spectrum of the force variability example	76
4.24	Power spectrum, coherence, and total forces in the tremor example	78
5.1	Overview of the model of a muscle fibre	81
5.2	Schematic representation of the bidomain model	82
5.3	Schematic representation of operator splitting methods	89

5.4	Bidomain and monodomain models for anisotropic conductivity tensors without equal anisotropy ratios	92
5.5	Bidomain and monodomain models for muscle tissue-like conductivities	93
5.6	Extracellular potential distributions in monodomain and bidomain models	94
5.7	Evolution of the membrane potential during high-frequency stimulation	99
5.8	Evolution of the potassium and sodium concentrations in the T-tubules	100
5.9	Overview of the model of the EMG	101
5.10	Schematic representation of different finite element meshes	102
5.11	Motor unit fibre distribution and motor neuron discharge times	103
5.12	Muscle fibre action potentials and the resulting EMG signals	104
5.13	High-density surface EMG signals	105
5.14	Intramuscular and surface EMG signals at different positions	106
5.15	Model setup for studying the influence of membrane fatigue on the EMG	107
5.16	The influence of membrane fatigue on the surface EMG signal	108
6.1	Rheological model corresponding to the superposition of passive and active stresses	113
6.2	Overview of the multiscale muscle model	120
6.3	Schematic representation of finite element meshes in the multiscale model	123
6.4	Schematic representation of the time-stepping scheme	123
6.5	Schematic drawing of regions and meshes	125
6.6	Schematic drawing of the domain decomposition	127
6.7	Comparison of the model and passive experimental data	129
6.8	Comparison of the model and passive anisotropic experimental data	130
6.9	Force-length and force-velocity relations of the multiscale model	133
6.10	Influence of the time step size of the continuum-mechanical model	133
6.11	Influence of fibre length on force during sustained contractions	137
6.12	Membrane potential and deformation in single twitch experiments	138
6.13	Influence of fibre length on force during single twitch contractions	139
7.1	Overview of the multiscale model of the neuromuscular system	143
7.2	Schematic representation of the different finite element meshes	144
7.3	Discharge times, nominal stresses, and deformation in the cuboid example	146
7.4	Deformation, muscle fibre action potentials, and the resulting EMG signals	147
7.5	The geometry of the TA and the surrounding fat/skin tissue	148
7.6	Membrane potential distribution and deformation of the TA	150
7.7	Membrane potential distribution and EMG signal in the superficial TA	151
C.1	Bidomain and monodomain models for isotropic conductivities	167
C.2	Bidomain and monodomain models for anisotropic conductivity tensors with equal anisotropy ratios	168
D.1	Taylor-Hood elements	171

List of Tables

4.1	Parameters for the Hodgkin-Huxley model	43
4.2	Initial conditions for the Hodgkin-Huxley model	43
4.3	Reaction rates for the cross-bridge dynamics model of the human FDI muscle	58
4.4	Coefficients of variation of the force variability example	75
4.5	Mean discharge rate and mean coefficients of variation for the tremor example	77
5.1	Material parameters for the monodomain equation	95
5.2	Influence of the time step size on the propagation velocity	96
5.3	Influence of the element size on the propagation velocity	97
5.4	Influence of material parameters on the propagation velocity	98
5.5	Electrical conductivities	102
6.1	Passive material parameters of the mechanical model (<i>A</i>)	128
6.2	Passive material parameters of the mechanical model (<i>B</i>)	129
6.3	Material parameters of the active mechanical model	131
6.4	Speed-up factors achieved through parallelisation	134
6.5	Minimum and maximum sarcomere lengths in single twitch contractions . .	139
B.1	Material parameters of the motor neuron model	166

Deutschsprachige Zusammenfassung

Motivation

Das neuromuskuläre System wird im Allgemeinen definiert als „die Muskeln des Körpers zusammen mit den Nerven, die diese innervieren“ [146]. Die Aufgabe des neuromuskulären Systems ist die Bewegung des Körpers, die nur durch das Zusammenspiel von speziellen Nervenzellen (Motoneuronen) und den Muskeln des Körpers (Skelettmuskeln) ermöglicht wird. Funktionsstörungen des neuromuskulären Systems beeinträchtigen folglich die Motoneurone, die peripheren Nerven, die Muskelfasern und die neuromuskulären Endplatten (die Stelle, an der die Nerven und Muskelfasern aufeinander treffen). Zu den häufigeren Funktionsstörungen des neuromuskulären Systems zählen periphere Neuropathien, verschiedene Muskeldystrophien, entzündliche und andere Myopathien sowie Störungen der neuromuskulären Signalübertragung [44, 62, 63]. Viele dieser Funktionsstörungen sind schwerwiegend oder sogar tödlich. Bei der spinalen Muskelatrophie vom Typ I zum Beispiel tritt der Tod bereits im Kindesalter ein, aber auch andere Funktionsstörungen des neuromuskulären Systems verlaufen tödlich [62]. Erkrankungen des neuromuskulären Systems sind oft erblich bedingt, sie können aber auch durch eine abnormale Immunreaktion oder eine genetische Mutation hervorgerufen werden.

Emery folgerte aus seiner umfassenden Literaturübersicht [62], dass mindestens einer von 3500 der Weltbevölkerung von einer beeinträchtigenden, vererblichen Erkrankung des neuromuskulären Systems betroffen ist. Laut MacIntosh et al. [161] ist allein etwa jeder dreitausendste Mann von der Muskeldystrophie des Typs Duchenne, einer X-chromosomal-rezessiv vererblichen Funktionsstörung, betroffen. Diese Muskeldystrophie wird durch einen Mangel an dem Membranprotein Dystrophin hervorgerufen und resultiert in einer fortschreitenden Muskelschwächung, die zum Tod führt. Andere, weniger häufige Formen von Muskeldystrophien werden durch andere Proteine Defekte verursacht (eine Übersicht findet sich in Emery [63]). Um eine Dystrophie zu diagnostizieren und neurogene Ursachen einer Muskelschwäche auszuschließen, stellt die Elektromyographie eine wichtige Methode dar [63].

Bis heute können Dystrophien nicht geheilt werden, und auch für andere neuromuskuläre Funktionsstörungen gibt es oft kein wirksames Heilmittel. Da Erkrankungen des neuromuskulären Systems häufig genetisch bedingt sind, könnten in Zukunft gentechnische Veränderungen und eine Stammzellentherapie zu einer effektiven Behandlung führen, aber auch ein wirksames Medikament könnte entdeckt werden [63]. Bisher jedoch können nur Symptome behandelt werden, um die Lebensqualität der Betroffenen zu verbessern. Zur effektiven Behandlung von Symptomen und für die Entwicklung eines wirksamen Medikaments ist ein umfassendes Verständnis der Physiologie des neuromuskulären Systems Voraussetzung. Um dies zu Erlangen, ist es zweckmäßig zunächst das gesunde System zu studieren, bevor pathologische Bedingungen, wie sie bei neuromuskulären Funktionsstörungen auftreten, untersucht werden.

Da biophysikalische Größen experimentell oft nur schwer oder überhaupt nicht bestimmt werden können (vor allem in Menschen und *in vivo*), können mathematische Modelle verwendet werden, um fehlende Daten zu generieren. Der Vorteil der mathematischen Modellierung liegt vor allem auch darin, dass Daten in einer kontrollierten Umgebung bestimmt werden können, was in Experimenten häufig unmöglich ist. Existierende Modelle des neuromuskulären Systems haben zu einem verbesserten Verständnis der Physiologie beigetragen [76, 104]. Diese Modelle basieren jedoch zumindest zum Teil auf einer phänomenologischen Beschreibung, die den biophysikalischen Prozessen des betrachteten Systems nicht nachempfunden ist. Da die phänomenologische Beschreibung die Anwendung und die Vorhersagefähigkeit dieser Modelle maßgeblich einschränkt, werden detaillierte, biophysikalische Modelle von Skelettmuskeln und der zugehörigen Motoneurone benötigt, um das neuromuskuläre System besser zu verstehen. Die vorliegende Arbeit befasst sich folglich mit der Entwicklung von Methoden und Modellen für die biophysikalische Simulation des chemoelektromechanischen Verhaltens des neuromuskulären Systems.

Stand der Forschung, Zielsetzung und Vorgehensweise

Bei der Modellierung biologischer Systeme kann ganz allgemein zwischen phänomenologischen und biophysikalischen Modellen unterschieden werden. Phänomenologische Modelle basieren auf experimentell ermittelten Eingangs-/Ausgangsbeziehungen und sind oft einfacher, weniger rechenaufwändig und auf weniger Parameter angewiesen als entsprechende biophysikalische Modelle. Beschränkt auf den Bereich, in dem die Modellparameter an experimentelle Daten angepasst wurden, können phänomenologische Modelle das Verhalten des Systems akkurat wiedergeben. Ein vollständiges Verständnis der zugrundeliegenden Physiologie kann mit phänomenologischen Modellen jedoch nicht erreicht werden. Im Gegensatz dazu bauen biophysikalische Modelle auf den vorhandenen Kenntnissen der Physiologie des entsprechenden Systems auf und können daher als *in-silico* Labor verwendet werden, um das Verhalten des betrachteten Systems unter normalen und pathologischen Bedingungen zu untersuchen.

Dem Aufbau des neuromuskulären Systems entsprechend konzentrieren sich die existierenden mathematischen Modelle entweder auf die Krafterzeugung in den Muskelfasern oder auf die Kontrolle der Muskeln durch das koordinierte Verhalten der Motoneurone als Ensemble. Betrachtet man zunächst die Motoneurone, lassen sich phänomenologische und biophysikalische Modelle in der Literatur finden. Zum Beispiel wurden von Fuglevand et al. [76] und Heckman & Binder [104], basierend auf der Beziehung zwischen synaptischer Erregung eines Motoneurons und der Frequenz mit der das Motoneuron Aktionspotentiale (kurzzeitige Depolarisierungen des Membranpotentials einer Zelle, die verwendet werden, um Informationen zwischen verschiedenen Teilen des Körpers auszutauschen) abfeuert [29], phänomenologische Modelle entwickelt. Diese werden häufig zum Testen von neurophysiologischen Hypothesen oder zur Interpretation von experimentellen Daten verwendet, siehe z. B. [10, 142, 143, 180]. Eine wichtige Einschränkung von phänomenologischen Motoneuronenmodellen ist jedoch, dass sie es nicht erlauben synaptische und gemeinsame Eingangssignale an die Motoneurone zu berücksichtigen. Biophysikalische Motoneuronenmodelle sind von dieser Einschränkung nicht betroffen, da sie Eingangssignale auf der Ebene der Zellmembran einbinden. In „integrate-and-fire“-Modellen [1, 73]

zum Beispiel bindet ein Motoneuron synaptische Ströme von verschiedenen Quellen ein, was zu einem Anstieg seines Membranpotentials führt. Wenn das Membranpotential einen bestimmten Schwellenwert erreicht, wird angenommen, dass das Motoneuron ein Aktionspotential abfeuert, und sein Membranpotential wird zurück auf den Ruhewert gesetzt.

Die komplexen, biophysikalischen Prozesse, die zum Öffnen und Schließen von verschiedenen spannungsgesteuerten Ionenkanälen während eines Aktionspotentials führen, wurden zuerst von Alan L. Hodgkin und Andrew F. Huxley [120] beschrieben. Basierend auf dieser Darstellung wurden zunehmend komplexere, biophysikalische Modelle der Motoneurone entwickelt (siehe z. B. Cisi & Kohn [39], Cushing et al. [41], Powers et al. [208]), die zusätzliche Ionenströme und/oder eine höhere Anzahl an Kompartimenten berücksichtigen.

Um Motoneurone zu simulieren, übernimmt die vorliegende Arbeit das Zweikompartimentmodell von Negro & Farina [186], das auf der Beschreibung von Cisi & Kohn [39] basiert. Interessanterweise berücksichtigt dieses biophysikalische Motoneuronenmodell bereits von sich aus das Hennemansche Größenprinzip der sequentiellen Rekrutierung [112, 113] (kleine Motoneurone mit niedrigem Erregungsschwellenwert werden vor größeren Motoneuronen mit höherem Erregungsschwellenwert rekrutiert) und die „onion-skin“-Eigenschaft [46, 47] (für ein bestimmtes Level an synaptischer Erregung feuern Motoneurone mit niedrigerem Erregungsschwellenwert mit einer höheren Frequenz als Motoneurone mit hohem Erregungsschwellenwert).

Die von den Motoneuronen abgefeuerten Aktionspotentiale lösen in den Muskelfasern die Krafterzeugung aus. Zur Simulation der Krafterzeugung wurden verschiedene Ansätze verfolgt. Heckman & Binder [104] zum Beispiel schlugen, basierend auf dem Eingangs-/Ausgangsverhalten von Muskelfasern (der Kraft-Frequenz-Beziehung), ein phänomenologisches Modell vor. Besonders populär ist die analytische Formulierung von Fuglevand et al. [76], die die Impulsantwort eines kritisch gedämpften Systems zweiter Ordnung verwendet, um die Muskelzuckung zu beschreiben. Dieses vereinfachte Kraftmodell wurde von mehreren Wissenschaftlern übernommen und erweitert, siehe z. B. Cisi & Kohn [39], Dideriksen et al. [50, 51, 52].

Während diese Modelle auf einer stationären Eingangs-/Ausgangsbeziehung basieren und auf isometrische Bedingungen beschränkt sind, sind die sogenannten Hill-Modelle nicht von diesen Einschränkungen betroffen. Hill-Modelle basieren auf der Beschreibung von Archibald V. Hill von 1938 [117] und sind wahrscheinlich die häufigste Darstellung des mechanischen und kinematischen Muskelverhaltens, siehe z. B. Günther et al. [92–94], van Ingen Schenau et al. [133], Pandy [198], Siebert et al. [242, 243], Till et al. [261], Zajac [282]. Hillsche Muskelmodelle sind phänomenologische Formulierungen der makroskopischen Muskelphysiologie, bei der eine längenabhängige, passive Kraft (Spannungs-Dehnungs-Beziehung in Abwesenheit von neuronaler Stimulation) mit einer Kraft superponiert wird, die von der neuronalen Aktivierung des Muskels herrührt und von der Muskellänge und Kontraktionsgeschwindigkeit abhängt. Aufgrund ihrer Einfachheit, dem relativ geringen Rechenaufwand und der geringen Anzahl an Parametern, werden Hill-Modelle häufig zur Interpretation von experimentellen Daten oder zur Beschreibung von Bewegungen und Kräften im Rahmen von Mehrkörpersimulationen verwendet, siehe z. B. Rupp et al. [227], Siebert et al. [241].

Sowohl die Hillschen als auch die analytischen Muskelmodelle, die die Impulsantwort verwenden, um die Muskelzuckung darzustellen, weisen signifikante Nachteile auf, da

sie alle strukturellen und funktionellen Eigenschaften eines Muskels auf nur wenige Parameter reduzieren. Zum Beispiel beschreiben die Hillschen Modelle das Muskelverhalten an einem einzigen Punkt durch Feder- und Dämpfungskonstanten und ein einzelnes Aktivierungsniveau. Die berechnete Muskelkraft wird dann entlang einer vorgegebenen Wirkungslinie aufgebracht. Darüber hinaus vernachlässigen diese vereinfachten, auf rein phänomenologischen Ansätzen basierenden Modelle Nichtlinearitäten in der Kraftantwort, die aus der zurückliegenden Aktivierung resultieren, vgl. z. B. [76, 204, 230].

Die Erkenntnis, dass Hill-Modelle für Muskeln mit komplexer Geometrie nur ungenaue Ergebnisse liefern (vgl. z. B. Röhrle & Pullan [222]), führte zur Entwicklung von kontinuumsmechanischen Modellen, die auf der Theorie der finiten Deformationen beruhen, siehe z. B. [16, 167, 222, 229, 288]. Um das kontraktile Verhalten von Herz- und Skelettmuskeln in einem kontinuumsmechanischen Modell zu beschreiben, wurden häufig Hill-Modelle verwendet, siehe z. B. Göktepe et al. [88], Johansson et al. [135], Kojic et al. [147], Pelteret & Reddy [203]. Während kontinuumsmechanische Modelle komplexe Muskelfaserverteilungen [15], eine lokal variierende Aktivierung und eine dynamisch bestimmte Wirkungslinie [222] berücksichtigen können, sind die gewonnenen Erkenntnisse doch beschränkt auf rein mechanische, makroskopische Aspekte der Krafterzeugung. Eine detailliertere Beschreibung des kontraktilen Verhaltens in einem volumetrischen Muskelmodell kann durch den Einsatz von Mehrskalmodellen erreicht werden, die die Kontinuumsmechanik mit kinetischen Zellmodellen koppelt.

Das erste biophysikalische, kinetische Zellmodell wurde von Andrew F. Huxley [128, 129] entwickelt. Dieses Modell basiert auf der Filamentgleittheorie, die 1953/1954 gleichzeitig, jedoch unabhängig voneinander, von Andrew F. Huxley und Ralph Niedergerke [130] sowie Hugh E. Huxley und Jean Hanson [99, 132] vorgeschlagen wurde. Das kinetische Modell von Huxley [128] unterscheidet zwischen Querbrücken im gebundenen und gelösten Zustand und wurde später auf Verteilungsfunktionen generalisiert, die Populationen von verschiedenen biochemischen Zuständen als Funktion von Bindungslänge und Zeit darstellen, siehe z. B. [280, 281]. Der Vorteil dieser biophysikalischen Modelle liegt darin, dass sie direkt auf der mikroskopischen Struktur und den molekularen Mechanismen der Kontraktion basieren. Ihre mathematische Beschreibung führt jedoch zu einem Satz von gekoppelten partiellen Differentialgleichungen. Um die komplizierte Lösung von partiellen Differentialgleichungen zu vermeiden, wurden Approximationen entwickelt, die als gewöhnliche Differentialgleichungen in der Zeit formuliert werden können, siehe z. B. der Ansatz von Zahalak [280]. Dieser Ansatz wurde von Gielen et al. [83] verwendet, um das kontraktile Verhalten in einem kontinuumsmechanischen Mehrskalmodell zu beschreiben.

Ferner wurde im Kontext von kinetischen Zellmodellen von Razumova, Campell und Kollegen ein Modell der Querbrückendynamik entwickelt, das drei verschiedene Zustände der Querbrücken (ein gelöster und zwei gebundene Zustände) berücksichtigt, und annimmt, dass die Kraft in einem Sarkomer proportional zum Produkt aus der Anzahl der Querbrücken im jeweiligen gebundenen Zustand und ihrer durchschnittlichen Verzerrung ist [36, 37, 214, 215]. Obwohl dieses Modell durch relativ simple gewöhnliche Differentialgleichungen beschrieben werden kann, reicht es aus, um die wesentlichen Charakteristiken von Muskelkontraktionen zu beschreiben [214].

Neben den biophysikalischen Beschreibungen der Querbrückendynamik wurden auch biophysikalische Modelle von anderen Teilen des komplexen Signalwegs von der elektrischen Stimulation zur Krafterzeugung in Muskelfasern entwickelt. Zum Beispiel schlu-

gen Adrian & Peachey [2], basierend auf dem Hodgkin-Huxley-Formalismus [120], ein elektrophysiologisches Modell der Muskelfasermembran vor. Dieses Modell wurde später von Wallinga et al. [272] auf ein Multikompartimentmodell erweitert, das Ionenströme über das Sarkolemm und die T-Tubulemembran einer Muskelfaser berücksichtigt. Um den gesamten Signalweg von der Erregung zur Kontraktion einer Muskelfaser zu beschreiben, koppelte Shorten et al. [240] eine vereinfachte Version des elektrophysiologischen Membranmodells von Wallinga [272] an ein Modell des Kalziumausstoßes aus dem sarkoplasmatischen Retikulum [217], ein Modell der intrazellulären Kalziumdynamik [12] und eine Erweiterung des Modells der Querbrückendynamik von Razumova et al. [214]. Darüber hinaus beinhaltet das Modell von Shorten et al. [240] eine Beschreibung der metabolischen Ermüdung.

Ein großer Vorteil des Modells von Shorten et al. [240] ist, dass es die zugrunde liegende Physiologie sehr gut abbildet. Im Gegensatz zu phänomenologischen Modellen berücksichtigt diese biophysikalische Beschreibung nichtlineare Effekte in der Kraftentwicklung, die zum Beispiel aus der zurückliegenden Aktivierung resultieren, und erlaubt darüber hinaus eine detaillierte Analyse von pathologischen Bedingungen. Obwohl das Modell von Shorten et al. [240] viele Details des Signalwegs von der Erregung zu Kontraktion beinhaltet, unterliegt es mehreren Limitationen. Zum Beispiel betrachten Shorten et al. [240] nur idealisierte Stimulationen des gesamten Muskels bei konstanter Frequenz. Außerdem kann das Modell nur isometrische Kontraktionen beschreiben.

Aus diesem Grund erweitert die vorliegende Arbeit das Modell von Shorten et al. [240] auf nichtisometrische Kontraktionen. Außerdem wird das Modell von Shorten et al. [240] auf eine Beschreibung der Muskelfasern der verschiedenen motorischen Einheiten eines Muskels erweitert. Eine motorische Einheit bezeichnet hierbei ein Motoneuron zusammen mit allen Muskelfasern, die von diesem Motoneuron innerviert werden. Um willkürliche Kontraktionen zu simulieren, wird das resultierende Muskelmodell mit dem Motoneuronenmodell von Negro & Farina [186] gekoppelt. Dies führt zu einem neuen, integrierten Modell des neuromuskulären Systems, das in all seinen Hauptteilen biophysikalisch ist.

Röhrle und Kollegen koppelten das Modell des Signalwegs von der Erregung zur Kontraktion von Shorten et al. [240] mit bioelektrischen Feldgleichungen und einem kontinuumsmechanischen Konstitutivgesetz, um die Ausbreitung von Aktionspotentialen entlang von Muskelfasern bzw. die Krafterzeugung und Deformation des Muskels zu simulieren [219–221, 223]. Um willkürliche Muskelkontraktionen zu simulieren, verwendeten Röhrle et al. [221] das phänomenologische Motoneuronenmodell von Fuglevand et al. [76], um ihr mehrskaliges, chemoelektromechanisches Muskelmodell anzuregen. Das Modell von Röhrle und Kollegen berücksichtigt die Rekrutierung und Frequenzmodulation von motorischen Einheiten, die biophysikalischen Prozesse, die von der elektrischen Stimulation zur Kontraktion führen, sowie die Ausbreitung von Aktionspotentialen im Muskelgewebe und überwindet somit viele der Einschränkungen von anderen kontinuumsmechanischen Modellen. Zum Beispiel beinhaltet das Modell von Hernández-Gascón et al. [114] nur eine phänomenologische Beschreibung der zellulären Prozesse und ignoriert biophysikalische Prinzipien der Ausbreitung des Aktionspotentials und der Querbrückendynamik. Ferner verwenden Fernandez et al. [74] ein Motoneuronenmodell um ein Aktionspotential gleichzeitig in allen Muskelfasern zu erzeugen, wobei die Tatsache, dass motorische Einheiten in Skelettmuskeln unabhängig voneinander aktiviert werden, vernachlässigt wird. Sowohl in Fernandez et al. [74] als auch in Böhl et al. [22] breitet sich

das Aktionspotential im dreidimensionalen Muskelgewebe aus, anstatt entlang einzelner Muskelfasern, wie in Skelettmuskeln. Ferner verwenden beide Modelle eine rein phänomenologische Beschreibung des Zusammenhangs zwischen dem Aktionspotential und der Krafterzeugung.

Obwohl das chemoelektromechanische Modell von Röhrle und Kollegen viele physiologische Eigenschaften des neuromuskulären Systems berücksichtigt, unterliegt es strukturellen Einschränkungen, die die Erweiterung zu einem voll gekoppelten Modell, das neuronale Aktivierung, Krafterzeugung und Rückkopplungsmechanismen beinhaltet, nicht erlauben. Der limitierende Faktor ist hierbei, dass die zellulären Gleichungen nur einseitig an das mechanische Modell gekoppelt sind. Genauer gesagt wird das elektrochemische Verhalten einzelner Muskelfasern vorberechnet und in einer Nachschlagetabelle gespeichert. Im mechanischen Modell werden die zellulären Variablen, die mit der Krafterzeugung zusammenhängen, in ein detailliertes dreidimensionales Modell kopiert und homogenisiert, um den Spannungstensor zu berechnen. Das Vorberechnen des zellulären Verhaltens war notwendig, um den Rechenaufwand zu reduzieren, da das ursprüngliche Simulationsprogramm (CMISS) auf einer veralteten seriellen Implementierung basiert, die Datenstrukturen verwendet, die nicht unbedingt für eine Parallelisierung geeignet sind. Diese Formulierung erlaubt es nicht Änderungen in der Muskelfasergeometrie, wie z. B. eine Längenänderung, zu berücksichtigen, die aus der Kontraktion resultiert. Ferner betrachteten Röhrle und Kollegen nur isometrische Kontraktionen, was das Vernachlässigen der Kraft-Geschwindigkeits-Beziehung rechtfertigte.

Die vorliegende Arbeit präsentiert ein voll gekoppeltes, mehrskaliges, chemoelektromechanisches Modell für die Simulation von Muskelkontraktionen unter isometrischen und nichtisometrischen Bedingungen. Dieses Modell basiert auf der Open-Source-Software-Bibliothek `OpenCMISS` [26], die konzipiert wurde, um maximale Flexibilität und Effizienz zu erreichen. Ermöglicht wird dies durch den Einsatz neuartiger Datenstrukturen wie `FieldML` [38], den Zugang zu Modellbibliotheken durch die Verwendung von `CellML` [82, 107, 158, 188] und einer `Distributed-Memory-Implementierung`, die Recheneffizienz gewährleistet und es somit ermöglicht große Rechenbeispiele auszuführen. Die neuen Bibliotheken und Datenstrukturen bilden die Basis, um Finite Elemente Netze mit verschiedener Dimension innerhalb eines Modells zu kombinieren. Dies erlaubt es zum Beispiel innerhalb eines Modells nulldimensionale Ansätze für das zelluläre Verhalten, eindimensionale Ansätze für die Ausbreitung des Aktionspotentials und dreidimensionale Ansätze für strukturmechanische Untersuchungen miteinander zu koppeln. Die präsentierte Implementierung ermöglicht eine starke und wechselseitige Kopplung zwischen dem elektrochemischen und dem mechanischen Verhalten (elektromechanische und mechanoelektrische Rückkopplung, siehe Nash & Panfilov [185]). Zusätzlich ermöglicht es eine spätere Erweiterung des Modells um Propriozeptoren, die den mechanischen Zustand des Muskels in neuronale Signale übersetzen, um die Frequenzmodulation der Motoneurone an die vorliegenden Bedürfnisse anzupassen (sensorische Rückkopplung), siehe Heidlauf et al. [108].

Wenn in existierenden kontinuumsmechanischen Muskelmodellen die neuronale Kontrolle berücksichtigt wurde, wurden dafür phänomenologische Modelle eingesetzt, siehe z. B. Röhrle et al. [221]. Im Gegensatz dazu koppelt die vorliegende Arbeit das präsentierte Mehrskaligenmodell mit dem biophysikalischen Motoneuronenmodell von Negro & Farina [186], um willkürliche Muskelkontraktionen zu simulieren. Dies führt zu einem in-

tegrierten, mehrskaligen und multiphysikalischen Modell des neuromuskulären Systems. Andere Erweiterungen oder der Austausch von Modellkomponenten, wie z.B. das zelluläre Modell, sind aufgrund der modularen Organisation des Programms relativ einfach durchführbar.

Da das entwickelte mehrskalige Muskelmodell die elektrophysiologischen Vorgänge in der Zellmembran und die Ausbreitung des Aktionspotentials entlang der Muskelfasern beschreibt [240, 272], kann es zur Simulation von elektromyographischen (EMG) Signalen verwendet werden. EMG Signale spiegeln die elektrische Aktivität eines Muskels wider. Ihre hohe klinische Relevanz kann darauf zurückgeführt werden, dass EMG Signale relativ einfach in vivo gemessen werden können. Ein großer Nachteil von EMG Signalen ist jedoch, dass sie schwer zu interpretieren und analysieren sind [70]. Mathematische Modelle haben daher großes Potential die Signalinterpretation zu verbessern. Im Gegensatz zu vorherigen EMG Modellen, die die Form des Aktionspotentials und seine Ausbreitungsgeschwindigkeit vorgeben (siehe z.B. Farina & Merletti [71], Farina et al. [72], Lowery et al. [160], Merletti & Parker [168], Mesin [169]), berücksichtigt der vorgestellte, auf dem Hodgkin-Huxley-Formalismus basierende Ansatz Änderungen in der Form und Ausbreitungsgeschwindigkeit des Aktionspotentials, die zum Beispiel durch Membranermüdung hervorgerufen werden. Darüber hinaus berücksichtigt keins der ein-skaligen EMG Modelle die Deformation des Gewebes, was bedeutet, dass diese Modelle auf isometrische Bedingungen beschränkt sind, vgl. Mesin et al. [171]. Das präsentierte mehrskalige und multiphysikalische Modell ist von diesen Einschränkungen nicht betroffen und kann Muskelkontraktionen und EMG Signale unter isometrischen und nicht-isometrischen Bedingungen simulieren. Darüber hinaus erlaubt es der vorgestellte Ansatz beliebige Muskelgeometrien, komplexe Muskelfaserarchitekturen und beliebige Heterogenitäten zu berücksichtigen.

Die mathematische Formulierung des mehrskaligen Muskelmodells führt zu partiellen Differentialgleichungen, die mit der Finiten Elemente Methode approximiert werden [123, 286]. Da der integrierte Ansatz offensichtlich zu rechenintensiven Modellen führt, müssen Optimierungsstrategien betrachtet werden. Zum Beispiel werden verschiedene Finite Elemente Netze für das bioelektrische und das kontinuumsmechanische Modell verwendet, aber auch „Operator-Splitting“-Techniken und gestaffelte Lösungsansätze werden vorgestellt, die es erlauben verschiedene Zeitschritte für die Lösung der verschiedenen Teilsysteme zu verwenden.

Im Rahmen der kontinuumsmechanischen Muskelmodellierung wurde unlängst von mehreren Forschern eine multiplikative Zerlegung des Deformationsgradiententensors vorgeschlagen, um das passive und aktiv kontraktile Verhalten von Muskeln zu beschreiben, siehe z.B. Murtada et al. [182], Rossi et al. [224, 225], Sharifimajd & Stålhand [239], Stålhand et al. [246, 247]. (Ursprünglich wurde diese Zerlegung für die Beschreibung von elastoplastischem Materialverhalten entwickelt [154].) Während dieser Ansatz zunächst in Bezug auf eine thermodynamisch konsistente Formulierung vorteilhaft erschien, haben Rossi et al. [224] gezeigt, dass thermodynamische Konsistenz auch möglich ist, wenn der klassische Ansatz verwendet wird, bei dem konstitutiv eine Superposition des passiven und aktiven Spannungstensors (oder der Verzerrungsenergie) angenommen wird, siehe auch Gizzi et al. [86]. Die kontinuumsmechanische Formulierung in der vorliegenden Arbeit folgt deshalb dem klassischen Ansatz.

Die vorliegende Arbeit widmet sich der mathematischen Beschreibung und Simu-

lation von Prozessen des neuromuskulären Systems, die zur Muskelkontraktion und Krafterzeugung führen. Während diese Prozesse detailliert behandelt werden, ist die Beschreibung des passiven Muskelgewebes relativ einfach gehalten und basiert auf einer makroskopischen, kontinuumsmechanischen Formulierung. Genauer gesagt wird angenommen, dass das passive Muskelgewebe sich transversal isotrop, hyperelastisch und inkompressibel verhält. Ansätze, die in der Beschreibung des passiven Materialverhaltens zwischen Muskelfasern und extrazellulärem Bindegewebe unterscheiden, sind eingeschränkt durch Unsicherheiten in den Materialparametern und einem zusätzlichen Rechenaufwand [237, 238, 271]. Darüber hinaus vernachlässigt die vorliegende Arbeit viskoelastische Effekte in der Beschreibung des passiven Materialverhaltens [24, 267, 269]. Eine teilweise Rechtfertigung für dieses Vorgehen ist gegeben durch die Arbeit von Tian et al. [260], die zeigt, dass die viskosen Effekte in passivem Muskelgewebe relativ gering sind.

Gliederung der Arbeit

Zunächst gibt *Kapitel 2* einen Überblick über die Anatomie und Physiologie des neuromuskulären Systems, d. h. eines Muskels und der zugehörigen Motoneurone. Beleuchtet wird vor allem die hierarchische Struktur des Muskels, da die Kraft aus Kontraktion auf der mikroskopischen Ebene des Halbsarkomers erzeugt wird, aber eine Deformation des gesamten Muskels bedingt. Da sich die vorliegende Arbeit mit der biophysikalischen Modellierung des neuromuskulären Systems befasst, erfolgt außerdem eine detaillierte Beschreibung der Physiologie. Während klassischerweise zuerst die Anatomie gefolgt von der Physiologie eingeführt wird, übernimmt die vorliegende Arbeit ein modernes Mantra der Biologie, das besagt, dass die Struktur die Funktion bedingt, und behandelt beide Themen gleichzeitig.

Das Ziel von *Kapitel 3* ist es die mathematischen und kontinuumsmechanischen Grundlagen einzuführen, die im Verlauf der weiteren Arbeit benötigt werden. Das Kapitel präsentiert zunächst eine Einführung in die numerische Lösung von Differentialgleichungen. Darüber hinaus gibt das Kapitel eine allgemeine Einführung in die Kontinuumsmechanik, welche in Kapitel 6 auf den speziellen Fall der Muskelmodellierung angepasst wird.

Kapitel 4 präsentiert biophysikalische Zellmodelle von Motoneuronen und Muskelfasern. Zunächst werden das klassische Hodgkin-Huxley-Modell und das Modell von Negro & Farina [186] vorgestellt. Letzteres wird in der vorliegenden Arbeit zur Beschreibung des Verhaltens der Motoneurone verwendet. Im Anschluss daran wird das biophysikalische Modell des Signalwegs von der Erregung zur Kontraktion in den Muskelfasern von Shorten et al. [240] präsentiert. Dieses Modell wird erweitert, um nichtisometrische Kontraktionen zu simulieren und um das Verhalten der verschiedenen motorischen Einheiten eines Muskels zu beschreiben. Ein Modell des neuromuskulären Systems, das in allen wesentlichen Teilen biophysikalisch ist, entsteht durch die Kopplung des Muskelmodells mit dem Motoneuronenmodell von Negro & Farina [186]. Um das Potential des kombinierten Ansatzes zu demonstrieren, wird exemplarisch der erste dorsale Interosseusmuskel des Menschen simuliert.

Eine Erweiterung der Formulierung von Kapitel 4 um räumliche Dimensionen erlaubt es in *Kapitel 5* die Ausbreitung von Aktionspotentialen durch das Muskelgewebe zu beschreiben. Die Ausbreitung von Aktionspotentialen entlang von Muskelfasern wird hier-

bei mit Hilfe des Monodomain-Modells dargestellt. Das Monodomain-Modell wird vom allgemeineren, jedoch komplexen Bidomain-Modell abgeleitet, welches ein Kontinuumsansatz für die Beschreibung von elektrisch erregbaren Geweben darstellt. Numerische Experimente belegen, dass die Monodomain-Vereinfachung für die präsentierten Anwendungen gültig ist. Darüber hinaus wird die Formulierung der Ausbreitung von Aktionspotentialen auf eine biophysikalische Beschreibung des EMG Signals erweitert. Mehrere numerische Beispiele demonstrieren die Vorteile dieses Modells gegenüber anderen EMG Modellen. Einige dieser Beispiele wurden bereits in Mordhorst et al. [178] gezeigt.

Kapitel 6 führt ein mehrskaliges, chemoelektromechanisches Muskelmodell ein, das auf der Theorie der finiten Deformationen der Kontinuumsmechanik basiert. Unter Verwendung geeigneter Konstitutivannahmen wird ein kontinuumsmechanischer Spannungstensor hergeleitet, der geeignet ist das passive und aktive Verhalten von Muskeln zu repräsentieren. Die Beschreibung des passiven Verhaltens des Muskelgewebes erfolgt hierbei makroskopisch als transversal isotropes, hyperelastisches und inkompressibles Material. Die Formulierung des aktiv kontraktile Teils basiert auf der biophysikalischen, zellulären Beschreibung des Signalwegs von der Erregung zur Kontraktion (eingeführt in Kapitel 4), welches, wie in Kapitel 5 beschrieben, wiederum an das Monodomain-Modell gekoppelt ist.

Die numerische Behandlung des chemoelektromechanischen Muskelmodells führt zu einem mehrskaligen Berechnungsmodell, dessen numerische Lösung rechentechnisch anspruchsvoll ist. Deshalb präsentiert *Kapitel 6* neben dem mehrskaligen Berechnungsmodell auch geeignete Optimierungsstrategien, die zuvor bereits in Bradley et al. [26] und Heidlauf & Röhrle [109] dargestellt wurden. Darüber hinaus wird das mehrskalige Berechnungsmodell verwendet, um Unterschiede in der Muskelkontraktion und Krafterzeugung aufzuzeigen, die aus einer unterschiedlichen Anordnung der Muskelfasern resultiert. Hierfür werden Muskelmodelle mit parallel zueinander angeordneten Muskelfasern miteinander verglichen, wobei sich die Muskelfasern entweder über die gesamte Länge des Muskels erstrecken oder intrafaszikulär enden. Die Ergebnisse dieser Studie wurden bereits in Heidlauf & Röhrle [111] veröffentlicht.

Um das Verhalten des gesamten neuromuskulären Systems zu simulieren, wird das mehrskalige Muskelmodell in *Kapitel 7* mit dem Motoneuronenmodell von Negro & Farina [186] gekoppelt. Basierend auf dem resultierenden Modell und dem Ansatz zur Simulation von EMG Signalen (Kapitel 5) werden Simulationen durchgeführt, die gleichzeitig die Muskelkrafterzeugung, die Deformation des Muskelgewebes und das EMG Signal während isometrischen und nichtisometrischen Kontraktionen vorhersagen.

Schließlich liefert *Kapitel 8* eine abschließende Diskussion und Vorschläge für potentielle Anwendungen der vorgestellten Methoden sowie Weiterentwicklungen des präsentierten Modells. Zusätzliche mathematische und mechanische Details werden im *Appendix* dargestellt.

Abbreviations

Symbol	Description
0D	zero-dimensional (ODE model, no spatial dependency)
1D/2D/3D	one-/two-/three-dimensional
Ca^{2+}	calcium cation
Cl^-	chloride anion
K^+	potassium cation
Mg^{2+}	magnesium cation
Na^+	sodium cation
P_i	inorganic phosphate
$F\text{-}\ell$	force-length
$F\text{-}v$	force-velocity
ACh	acetylcholine
ADP	adenosine diphosphate
AHP	afterhyperpolarisation potential
AP	action potential
ATP	adenosine triphosphate
BDF	backward differentiation formula
CoV	coefficient of variation
DHPR	dihydropyridine receptor
EDL	extensor digitorum longus
EMG	electromyographic
EPSP	excitatory postsynaptic potential
FDI	first dorsal interosseous
FEM	finite element method
IPSP	inhibitory postsynaptic potential
ISI	interspike interval
MN	motor neuron
MU	motor unit
MUAP	motor unit action potential
NDF	numerical differentiation formula
ODE	ordinary differential equation
PDE	partial differential equation
RyR	ryanodine receptor
sEMG	surface electromyographic
SR	sarcoplasmic reticulum
TA	tibialis anterior
XB	cross-bridge
XF	cross-fibre

Nomenclature

Conventions

General Conventions

(\cdot)		placeholder for arbitrary quantities
a, b, \dots	or ϕ, ψ, \dots	scalars (zero-order tensors)
$\mathbf{a}, \mathbf{b}, \dots$	or $\boldsymbol{\phi}, \boldsymbol{\psi}, \dots$	vectors (first-order tensors)
$\mathbf{A}, \mathbf{B}, \dots$	or $\boldsymbol{\Phi}, \boldsymbol{\Psi}, \dots$	second-order tensors

Operators

$\text{grad}(\cdot) = \frac{\partial}{\partial \mathbf{x}}(\cdot)$	spatial gradient w. r. t. the actual position vectors
$\text{Grad}(\cdot) = \frac{\partial}{\partial \mathbf{X}}(\cdot)$	spatial gradient w. r. t. the referential position vectors
$\text{div}(\cdot) = \frac{\partial}{\partial \mathbf{x}} \cdot (\cdot)$	divergence operator w. r. t. the actual position vectors
$\text{Div}(\cdot) = \frac{\partial}{\partial \mathbf{X}} \cdot (\cdot)$	divergence operator w. r. t. the referential position vectors
$\text{rot}(\cdot) = \overset{3}{\mathbf{E}}[\text{grad}(\cdot)]^T$	rotation operator w. r. t. the actual position vectors
$\text{Rot}(\cdot) = \overset{3}{\mathbf{E}}[\text{Grad}(\cdot)]^T$	rotation operator w. r. t. the referential position vectors
$\text{cof}(\cdot) = \det(\cdot) (\cdot)^{T-1}$	cofactor operator
$\text{tr}(\cdot) = (\cdot) \cdot \mathbf{I}$	trace operator
$\det(\cdot)$	determinant operator
$(\cdot)^{-1}$	inverse tensor
$(\cdot)^T$	transposed tensor

Indices

$(\cdot)^B$	body domain
$(\cdot)^I$	muscle-body interface
$(\cdot)^M$	muscle domain
$(\cdot)^d$	dendrite compartment
$(\cdot)^s$	soma compartment, sarcolemma
$(\cdot)^t$	T-tubule membrane
$(\cdot)_i$	intracellular domain
$(\cdot)_e$	extracellular domain

Symbols

Symbol	Unit	Description
dv	[cm ³]	actual volume element
dV	[cm ³]	referential volume element
ℓ_S	[μ m]	sarcomere length
ℓ_S^0, ℓ_S^{opt}	[μ m]	resting and optimal sarcomere lengths
f_s	[Hz]	stimulation frequency
$f_\ell(\ell_S)$	[-]	normalised isometric active force-sarcomere length relation
f_0, f'	[1/ms]	XB-attachment rate, XB-detachment rate (from the A_1 state)
\bar{f}	[1/ms]	XB-attachment rate of an isometric contraction
g_i, \bar{g}_i	[mS/cm ²]	conductance per unit area to ion species i , maximum value
g_0	[1/ms]	XB-detachment rate (from the A_2 state)
\bar{g}	[1/ms]	XB-detachment rate if no neighbour is in the A_2 state
h_0, h'	[1/ms]	power stroke forward rate and backward rate
h	[ms]	time step size
h^{ODE}	[ms]	time step size of the cellular model
h^{DEQ}	[ms]	time step size of the diffusion equation
h^{CMM}	[ms]	time step size of the continuum-mechanical model
p	[N/cm ²]	hydrostatic pressure
t	[ms]	time
v, v_{max}	[cm/ms]	velocity and maximum shortening velocity
x_0	[μ m]	average distortion induced through the power stroke
x_1, x_2	[μ m]	average distortions in the pre-/post-power stroke states
A_1, A_2	[μ M]	XB concentrations in pre-/post-power stroke states
A_m	[1/cm]	membrane specific capacitance
B	[N]	half-sarcomere-based active force of Razumova et al. [214]
B_{iso}	[N]	isometric half-sarcomere-based active force of [214]
C_m	[μ F/cm ²]	membrane specific capacitance
$CaRF$	[-]	calcium recovery function
E_i	[mV]	Nernst or equilibrium potential of ion species i
F, F_{iso}	[N]	(isometric) half-sarcomere-based active force
F_{MU_i}	[N]	active force of motor unit i
I_m	[μ A/cm ²]	total current flow across the cell membrane
I_{ion}	[μ A/cm ²]	sum of the ionic currents crossing the cell membrane
I_i	[μ A/cm ²]	current density of ion species i
I, II, III	[-]	first, second, and third principal invariants
IV, V	[-]	fourth and fifth (mixed) invariants
J	[-]	Jacobian determinant
N	[-]	number of motor units in a pool
N_e	[-]	number of elements in a finite element mesh
P^{max}	[N/cm ²]	maximum isometric nominal stress
T_{tot}	[-]	total number of XBs in a sarcomere
$TPRF$	[-]	twitch peak recovery function
V_m	[mV]	membrane potential

Vectors

Symbol	Unit	Description
\mathbf{a}	[-]	vector of length λ_f pointing in the actual fibre direction
\mathbf{a}_0	[-]	referential unit vector pointing in fibre direction
\mathbf{b}	[cm/ms ²]	mass-specific acceleration (e. g. gravitation)
$\mathbf{b}_0, \mathbf{c}_0$	[-]	referential unit vectors normal to the fibre direction
$d\mathbf{a}$	[cm ²]	oriented actual area element
$d\mathbf{A}$	[cm ²]	oriented referential area element
$d\mathbf{k}_s$	[N]	incremental force element
$d\mathbf{x}$	[cm]	actual line element
$d\mathbf{X}$	[cm]	referential line element
$\mathbf{e}_1, \mathbf{e}_2, \mathbf{e}_3$	[-]	(Cartesian) orthonormal basis vectors
\mathbf{n}	[-]	actual surface normal vector
\mathbf{n}_0	[-]	referential surface normal vector
\mathbf{t}	[N/cm ²]	traction vector
\mathbf{u}	[cm]	displacement vector
\mathbf{x}	[cm]	position vector in the actual configuration
\mathbf{X}	[cm]	position vector in the reference configuration

Second and Higher-Order Tensors

Symbol	Unit	Description
\mathbf{A}	[-]	Almansiian strain tensor
\mathbf{B}	[-]	left Cauchy-Green deformation tensor
\mathbf{C}	[-]	right Cauchy-Green deformation tensor
\mathbf{E}	[-]	Green-Lagrangean strain tensor
\mathbf{F}	[-]	(material) deformation gradient tensor
\mathbf{I}	[-]	second-order identity tensor
\mathcal{M}_a	[-]	Referential structural tensor associated w/ the fibre direction
$\mathcal{M}_b, \mathcal{M}_c$	[-]	Referential structural tensors associated w/ the XF directions
\mathbf{P}	[N/cm ²]	first Piola-Kirchhoff stress tensor
\mathbf{R}	[-]	proper orthogonal rotation tensor
\mathbf{S}	[N/cm ²]	second Piola-Kirchhoff stress tensor
\mathbf{S}_E	[N/cm ²]	second Piola-Kirchhoff extra stress tensor
\mathbf{T}	[N/cm ²]	Cauchy or true stress tensor
\mathbf{T}_E	[N/cm ²]	Cauchy extra stress tensor
\mathbf{U}, \mathbf{V}	[-]	right and left stretch tensors
$\overset{3}{\mathbf{E}}$	[-]	Ricci permutation tensor (third-order fundamental tensor)

Calligraphic Letters

Symbol	Unit	Description
\mathcal{B}	[–]	material body
\mathcal{P}	[–]	material point
\mathcal{W}	[J/cm ³]	volume-specific strain energy function

Greek Letters

Symbol	Unit	Description
γ	[–]	normalised, sarcomere-based active stress
$\bar{\gamma}$	[–]	homogenised, normalised, sarcomere-based active stress
η	[kg/s ²]	stiffness of one cross bridge
ϑ	[–]	level of distortion dependence
λ_f	[–]	fibre stretch (length)
$\lambda_f^{opt}, \lambda_f^0$	[–]	optimal and initial fibre stretches
ν	[–]	influence of cooperative effects
ρ	[g/cm ³]	actual mass density
ρ_0	[g/cm ³]	referential mass density
ϕ_i	[mV]	intracellular potential
ϕ_e	[mV]	extracellular potential
ϕ_o	[mV]	potential of the body region
Γ	[–]	domain boundary of the material body
Ω	[–]	domain of the material body
ν_i	[–]	orthonormal fibre coordinate system
σ_i	[mS/cm]	intracellular conductivity tensor
σ_e	[mS/cm]	extracellular conductivity tensor
σ_o	[mS/cm]	conductivity tensor of the body region
σ_{eff}	[mS/cm]	effective conductivity tensor
\mathcal{T}	[N/cm ²]	Kirchhoff stress tensor
χ	[–]	motion or placement function

1 Introduction

1.1 Motivation

The American Heritage Medical Dictionary [146] defines the neuromuscular system as “the muscles of the body together with the nerves supplying them”. Only the interplay of specialised nerve cells called motor neurons and the skeletal muscles (i.e., muscles of the body) enables movement of the body, which is the task of the neuromuscular system. Following this, neuromuscular disorders are diseases that impact the motor neurons, the peripheral nerves, the muscle fibres, and the neuromuscular junctions (the location where nerves and muscles come together). Among the more common disorders of the neuromuscular system are peripheral neuropathies, various muscular dystrophies, inflammatory and other myopathies, and neuromuscular transmission disorders [44, 62, 63]. Many of these disorders are serious or even fatal. For example, children affected by type-I spinal muscular atrophy do not survive beyond the first few years of life, and some other disorders also lead to premature death [62]. Neuromuscular diseases are often genetic, but they can also result from an abnormal immune response or a genetic mutation.

Emery concluded from his comprehensive literature survey [62] that at least one in 3500 of the population is affected by a disabling inherited neuromuscular disease. Moreover, according to MacIntosh et al. [161], Duchenne muscular dystrophy, a X-linked recessive inherited disorder, affects one in 3000 males. This muscular dystrophy is caused by the absence of the muscle membrane protein dystrophin and results in a progressive weakening of the skeletal muscles that leads to death. Other, less common forms of muscular dystrophies are caused by other protein defects, see Emery [63] for an overview. For the diagnosis of a dystrophy and to exclude neurogenic causes of a muscle weakness, electromyography is an important method [63].

As yet, there is no cure for any of the dystrophies, and there exists frequently no efficacious remedy for other neuromuscular disorders either. Since neuromuscular diseases are often genetic, advances in gene manipulation and stem-cell therapy might lead to an effective treatment in the future, although the discovery of an effective drug treatment is also possible [63]. However, for now, the focus is on providing improvements in the patients’ quality of life by reducing symptoms [63]. Obviously, both the development of techniques required for this purpose and the design of an effective drug are conditional to having a comprehensive understanding of the physiology of the neuromuscular system. To this end, it is pertinent to first investigate the physiology of the healthy system, before studying pathological conditions occurring in neuromuscular disorders.

Due to the fact that many biophysical quantities are difficult or even impossible to determine experimentally, in particular, in human subjects and in vivo, mathematical models can be used to generate missing data. In this respect, mathematical modelling has the advantage of generating data in a controlled environment, which is usually impossible in experiments. Existing models of the neuromuscular system contributed to further

the knowledge of the physiology of the neuromuscular system [76, 104]. However, these models are based on phenomenological descriptions that do not mimic the biophysical processes of the underlying system. The phenomenological description significantly limits their application and their predictive capabilities, for example, with respect to pathological conditions. To gain a better understanding of the physiology of the neuromuscular system, detailed biophysical models of the skeletal muscles and the motor neurons innervating them need to be developed. So, the thesis at hand is concerned with the development of methods and tools for the biophysical simulation of the chemo-electro-mechanical behaviour of the healthy neuromuscular system.

1.2 Scope, Aims, and State of the Art

In general, one can distinguish between phenomenological and biophysical approaches when modelling biological systems. Being based on experimentally determined input-output relations, phenomenological models are often simpler, computationally more efficient, and rely on fewer parameters than their biophysical counterparts. Within the range in which the model's parameters have been fitted to experiments, phenomenological models can accurately reproduce the system's behaviour. However, phenomenological models cannot provide a full understanding of the underlying physiology. In contrast, biophysical models are built on the existing knowledge of the physiology of the respective system, and hence, they can be used as an *in-silico* laboratory to investigate the behaviour of the modelled system under normal and pathological conditions.

Based on the constitution of the neuromuscular system, existing mathematical models either focus on the generation of force in the muscle fibres or the muscle's control through the coordinated operation of the motor neurons as an ensemble. Drawing attention first to the motor neuron pool, phenomenological and biophysical models have been proposed in the literature. For example, based on the relation between the synaptic input to a motor neuron and its output discharge rate [29], Fuglevand et al. [76] and Heckman & Binder [104] developed phenomenological models that are frequently used for the testing of neurophysiologic hypotheses or for interpreting experimental data, see e.g. [10, 142, 143, 180]. An important limitation of phenomenological descriptions of the motor neuron behaviour, however, is that they do not allow the integration of synaptic or common inputs to motor neurons. Conversely, biophysical models of motor neurons do not suffer from this limitation, since they perform the integration at the motor neuron membrane level. For example, in integrate-and-fire models [1, 73], the motor neurons integrate synaptic currents from different sources, which yields an increase in their membrane potential. When the membrane potential reaches a certain threshold, the motor neuron is assumed to discharge an action potential (AP, a short depolarisation of a cell's membrane potential used to transmit information between different parts of the body) and the neuron's membrane potential is reset to its resting value.

The complex biophysical processes leading to the opening and closing of different voltage-gated ion channels in the neuron's membrane during an AP were first described by Alan L. Hodgkin and Andrew F. Huxley [120] based on their experiments on the giant axon of the squid. Expanding this description with respect to the number of considered ionic currents and/or compartments, progressively more complex models of motor neurons have been developed, see e.g. Cisi & Kohn [39], Cushing et al. [41], Powers et al. [208].

To simulate the motor neuron pool, this work adopts the biophysical model of Negro & Farina [186], which builds on the description of the motor neurons by Cisi & Kohn [39]. This two-compartment, Hodgkin-Huxley-type model balances biophysical details and computational performance. Interestingly, the biophysical description of the motor neuron behaviour inherently accounts for the size principle of motor neuron recruitment of Henneman et al. [112, 113] (small, low-threshold motor neurons are recruited before larger motor neurons with higher excitation threshold) and the “onion-skin” property [46, 47] (for a certain level of synaptic input to the motor neuron pool, low-threshold motor neurons have higher discharge rates than high-threshold motor neurons).

The APs generated by the motor neurons trigger the force generation in the skeletal muscle fibres. For the simulation of the force generation, different approaches have been followed. For example, Heckman & Binder [104] proposed a phenomenological model based on the input-output behaviour of muscle units (the muscle fibres innervated by a single motor neuron) during an isometric contraction (the force-frequency relation). One of the most popular models is the analytical formulation of Fuglevand et al. [76], which uses the impulse response of a critically damped, second-order system to represent the twitch force. This simplified muscle unit force model has been adopted and enhanced by several researchers, see e.g. Cisi & Kohn [39], Dideriksen et al. [50, 51, 52].

While these models are based on steady-state input-output relations and are limited to isometric conditions, the so-called Hill-type models do not suffer from these limitations. Hill-type models are based on the description of Archibald V. Hill in 1938 [117], and they are probably the most common representation of a muscle’s mechanical and kinematic behaviour, see e.g. Günther et al. [92–94], van Ingen Schenau et al. [133], Pandy [198], Siebert et al. [242, 243], Till et al. [261], Zajac [282]. Hill-type models are phenomenological formulations of the macroscopic muscle physiology that superpose a length-dependent passive force (stress-strain relation in the absence of neural stimulation) with a force that results from the neural activation of the muscle (in the following termed active force) and depends on the muscle’s length and contraction velocity. Due to their simplicity, computational effectiveness, and the low number of involved parameters, Hill-type muscle models are commonly used to interpret experimental data or describe movement and forces of (parts of) the muscular system within the framework of multibody dynamics, see e.g. Siebert et al. [241] and Rupp et al. [227].

Both Hill-type models and analytical models that use the impulse response to represent the twitch force exhibit significant drawbacks, since they lump together all functional and structural properties of a muscle to a few parameters. For example, Hill-type models are described at a point in space through spring constants, damper properties, and one activation level, and the calculated muscle force acts along a predefined line of action. Moreover, these simplified approaches neglect nonlinearities in the force response of muscle units, which are due to their activation history, for example, fatigue, post-tetanic potentiation, doublet potentiation, and serial dependence of twitch responses, cf. [76, 204, 230]. Furthermore, these models are based on purely phenomenological approaches.

Based on the finding that Hill-type models inaccurately predict muscle forces in complex geometries (cf. e.g. Röhrle & Pullan [222]), continuum-mechanical models based on the finite-elasticity theory have been proposed, see e.g. [16, 167, 222, 229, 288]. To describe the contractile behaviour of skeletal and cardiac muscles within a continuum-mechanical framework, Hill-type models were employed by Göktepe et al. [88], Johansson

et al. [135], Kojic et al. [147], Pelteret & Reddy [203], and others. While continuum-mechanical models can take into account complex muscle fibre distributions [15], regional activation properties, and a dynamically generated line of action [222], they restrict their findings purely to macroscopic mechanical aspects of muscle force generation. To achieve a more detailed description of the contractile behaviour within a volumetric muscle model, multiscale models linking continuum mechanics to cellular kinetics can be used.

The first biophysical cellular kinetics model was developed by Andrew F. Huxley [128, 129] based on the sliding filament theory, which was proposed simultaneously but independently in 1953/1954 by Andrew F. Huxley and Ralph Niedergerke [130] and Hugh E. Huxley and Jean Hanson [99, 132]. The kinetic model of Huxley [128] distinguishes between cross-bridges in the attached and detached states, and it was subsequently generalised to distribution functions representing populations of various biochemical states as functions of bond length and time, see e. g. [280, 281]. These biophysical models have the advantage of being directly based on the muscle's microscopic structure and the molecular mechanisms of contraction. However, their mathematical formulation leads to a set of coupled partial differential equations (PDEs). To avoid the complexity of solving PDEs, approximations can be formulated in terms of ordinary differential equations (ODEs) in time, see, for example, the distributed moments approach of Zahalak [280]. The approach of Zahalak [280] was used by Gielen et al. [83] to describe the contractile behaviour within a continuum-mechanical muscle model.

Further, in the context of cellular kinetics models, Razumova, Campell, and co-workers proposed a cross-bridge dynamics model [36, 37, 214, 215] that considers three distinct cross-bridge states (two attached and one detached) and assumes that the force in a sarcomere is proportional to the product of the number of cross-bridges in each attached state and their average distortion. Although the ODEs describing this model are relatively simple, the model is sufficient to reproduce key characteristics of muscle contraction [214].

Besides biophysical descriptions of cross-bridge dynamics, biophysical models of other parts of the complex signaling pathway from electrical stimulation to force generation in skeletal muscle fibres have been developed. For example, based on the Hodgkin-Huxley formalism, Adrian & Peachey [2] proposed a model of the membrane electrophysiology of muscle fibres. This model was extended by Wallinga et al. [272] to a multicompartment model of the ionic currents crossing the T-tubule membrane and the sarcolemma of a muscle fibre. To simulate the entire excitation-contraction pathway in muscle fibres, Shorten et al. [240] coupled a simplified version of Wallinga's model of the membrane electrophysiology [272] to a model of calcium release from the sarcoplasmic reticulum [217], a model of intracellular calcium dynamics [12], and an extended version of the cross-bridge dynamics model of Razumova et al. [214]. Furthermore, the model of Shorten et al. [240] includes a description of metabolic fatigue based on the accumulation of inorganic phosphate in the sarcoplasm.

A major advantage of the model of Shorten et al. [240] is that it closely represents the underlying physiology. In contrast to phenomenological models, this biophysical description can represent history-dependent and other nonlinear effects, provide insights into the complex signaling pathway from electrical activation to force generation, and allows a detailed analysis of pathological conditions. Although including many details of the excitation-contraction pathway, the model of Shorten et al. [240] is limited in several respects. For example, Shorten et al. [240] considered only idealised, constant-frequency

stimulations of entire muscles under isometric conditions.

Following this, the work at hand extends the model of Shorten et al. [240] to non-isometric conditions. Moreover, the present work enhances the model of Shorten et al. [240] to a description of the muscle units within a muscle taking into account their different mechanical behaviours. To simulate voluntary contractions, the resulting muscle model is coupled to the model of the motor neuron pool of Negro & Farina [186]. This yields a novel, integrated model of the neuromuscular system that is biophysical in all main parts.

Previously, the model of the excitation-contraction pathway of Shorten et al. [240] has been coupled to bioelectrical field equations and a continuum-mechanical constitutive equation by Röhrle and co-workers [219–221, 223] to simulate the propagation of APs along muscle fibres and the force generation and deformation of muscle, respectively. The resulting multiscale chemo-electro-mechanical muscle model has been linked to the phenomenological motor neuron model of Fuglevand et al. [76] to control the simulated muscle contractions, see [221]. Accounting for motor unit recruitment and rate coding, the biophysical processes leading from electrical excitation to contraction, and the propagation of APs within the muscle tissue, the model of Röhrle and co-workers overcomes many of the limitations of other continuum-mechanical muscle models. For example, Hernández-Gascón et al. [114] include a phenomenological description of the cellular processes and ignore biophysical principles of AP propagation and cross-bridge dynamics. Further, Fernandez et al. [74] use a neuron model to simultaneously generate an AP in all muscle fibres neglecting the fact that motor units (the muscle unit together with their corresponding motor neuron) in skeletal muscle are activated independently of each other. In both Fernandez et al. [74] and Böl et al. [22] the AP propagates anisotropically through the three-dimensional (3D) muscle tissue instead of along single muscle fibres as in skeletal muscle. Moreover, both models use purely phenomenological descriptions to relate the AP to force generation.

Although the chemo-electro-mechanical model of Röhrle and co-workers includes many physiological properties of the neuromuscular system, it has framework-inherent limitations that do not allow an extension to a fully coupled framework embracing neural inputs, force generation, and feedback mechanisms. The major limitation is that the cellular equations are only coupled unidirectionally to the mechanical model. In detail, the electro-chemical behaviour of single muscle fibres is precomputed and stored in a look-up table. Within the mechanical model, the cellular variables associated with force generation are copied into a detailed 3D structural model and homogenised to compute the resulting stress tensor. The choice of precomputing the cellular behaviour has been chosen to reduce the overall computational cost. This was necessary as the original framework (CMISS) is based on serial legacy code, appealing to data structures not necessarily suitable for parallelisation. This formulation does not allow to consider geometrical variations of the muscle fibres, such as, for example, a length change, resulting from the contraction. Therefore, Röhrle and co-workers considered only isometric contractions, which provided justification for neglecting the force-velocity relationship.

The thesis at hand presents a fully coupled, multiscale, chemo-electro-mechanical simulation framework for skeletal muscle modelling under isometric and non-isometric conditions. This framework is based on the open-source software library `OpenCMISS`¹ [26], which

¹An Open-source software library for Continuum Mechanics, Image analysis, Signal processing and System identification.

was designed to achieve maximal flexibility and efficiency through the use of new data structures such as FieldML [38], access to well-established model repositories via CellML [82, 107, 158, 188], and a distributed-memory foundation for computational efficiency and executing large problems. The new libraries and the data structure provide the basis for combining different mesh regions with different dimensionality within one framework, for example, zero-dimensional (0D) models for the cellular behaviour, one-dimensional (1D) models for the AP propagation, and 3D models for the mechanical analysis. This allows for a strong and bidirectional coupling of the electro-chemical model on the one hand and the mechanical model on the other hand (electro-mechanic and mechano-electric feedbacks, cf. Nash & Panfilov [185]). Additionally, this will allow the integration of proprioceptors, which translate the mechanical state of the muscle into neural signals that influence the rate modulation of the motor neurons (sensory feedback), in the framework at a later point in time, see Heidlauf et al. [108].

If neural control has been considered in previous continuum-mechanical muscle models, a phenomenological description of the motor neurons was employed, see e. g. Röhrle et al. [221]. In contrast, to simulate voluntary muscle contractions, this work couples the multiscale muscle model to the biophysical motor neuron model of Negro & Farina [186]. This yields an integrated multiscale and multiphysics model of the neuromuscular system. Further extensions of the model and substitution of model components, e. g. the cellular model, are straightforward due to the modular organisation of the framework.

Since the developed multiscale skeletal muscle model contains a description of the membrane electrophysiology and the AP propagation along muscle fibres [240, 272], it can be used to simulate electromyographic (EMG) signals. EMG signals reflect the electrical activity of a skeletal muscle. Their strong clinical relevance can be explained by the fact that EMG signals can be measured *in vivo* in a relatively easy way. One of the major drawbacks of EMG signals is that they are hard to interpret and analyse [70]. Thus, mathematical models have a great potential to improve signal interpretation. In contrast to previous, phenomenological EMG models, which prescribe the AP shape and propagation velocity (see e. g. Farina & Merletti [71], Farina et al. [72], Lowery et al. [160], Merletti & Parker [168], Mesin [169]), the presented biophysical Hodgkin-Huxley-type approach can account for changes in the amplitude and propagation velocity of the AP that result, for example, from membrane fatigue. Moreover, none of the existing single-scale and single-physics EMG models takes into account tissue deformation, and hence, these models are restricted to isometric conditions, cf. Mesin et al. [171]. The proposed multiscale and multiphysics model is not subject to such restrictions and can simulate muscle contractions and the EMG under isometric and non-isometric conditions. Moreover, the presented approach allows to consider arbitrary geometries, complex muscle fibre architectures, and different heterogeneities.

The mathematical formulation of the multiscale muscle model leads to PDEs that are approximated using the finite element method (FEM), see [123, 286]. Furthermore, it is obvious that the integrated approach leads to a computationally expensive model. Hence, optimisation strategies have to be considered. For example, different finite element meshes for the bioelectrical and the continuum-mechanical models, as well as operator-splitting techniques and staggered solution schemes allowing to use different time step sizes for the solution of the different subsystems are employed.

Within the framework of continuum mechanics, recently, some researchers proposed a

multiplicative split of the deformation gradient tensor (initially developed in the field of elasto-plasticity, see Lee [154]) to describe the active (contractile) and passive behaviours of muscle, cf. e. g. Murtada et al. [182], Rossi et al. [224, 225], Sharifimajd & Stålhand [239], Stålhand et al. [246, 247]. At first, this approach was believed to have certain advantages with respect to a thermodynamically consistent formulation, but Rossi et al. [224] showed that thermodynamic consistency is also possible when using the more classical approach of constitutively assuming a superposition of passive and active stress tensors (or strain energies), cf. also Gizzi et al. [86]. Following this, the continuum-mechanical model in this work is based on the more classical formulation.

The work at hand is devoted to the mathematical description and simulation of the processes of the neuromuscular system leading to muscle contraction and force generation. While these processes are considered in detail, the description of the passive muscle tissue is relatively simple and is based on a macroscopic continuum-mechanical formulation. In detail, the passive muscle tissue is assumed to behave transversely isotropic, hyperelastic, and incompressible. Approaches distinguishing muscle fibres and the extracellular connective tissue in the passive material description are limited by material-parameter uncertainties and an additional computational complexity [237, 238, 271]. Besides lumping together muscle fibres and extracellular connective tissue, the presented passive material description neglects viscoelastic effects [24, 267, 269]. Partial justification for doing so is given by Tian et al. [260], who demonstrated that the viscous effects in passive muscle tissue are rather small.

1.3 Overview

First, *Chapter 2* reviews the basic anatomy and physiology of the neuromuscular system, i. e., a motor neuron pool and its associated skeletal muscle. In particular, the hierarchical structure of the muscle is of interest, as the contractile force is generated at the microscopic half-sarcomere level, but it causes a deformation of the entire muscle. Further, since this work is concerned with the biophysical modelling of the neuromuscular system, a detailed description of the physiology is provided. While classical works often first introduce the anatomy followed by the physiology of a system, this work adopts a modern mantra of biology stating that structure dictates function and covers both topics simultaneously.

The objective of *Chapter 3* is to introduce the mathematical and continuum-mechanical concepts required in the remainder of the thesis. The chapter presents a brief introduction to numerical methods for the solution of differential equations. This is followed by a general introduction to continuum mechanics, which will be further specified in Chapter 6 to the special case of skeletal muscle modelling.

Chapter 4 presents biophysical cellular models for motor neurons and skeletal muscle fibres. First, the classical Hodgkin-Huxley model and the model of Negro & Farina [186] are reviewed. The latter is used in this work to describe the behaviour of a motor neuron pool. Next, the biophysical model of the excitation-contraction coupling in skeletal muscle fibres of Shorten et al. [240] is presented, extended to non-isometric contractions, and augmented to a description of the muscle units within a muscle. Coupling the resulting muscle unit model and the motor neuron model of Negro & Farina [186] yields a model of the neuromuscular system that is biophysical in all main parts. The human first dorsal interosseous muscle is exemplarily simulated to demonstrate the capabilities of the

combined approach.

Expanding the formulation of Chapter 4 by spatial dimensions, the propagation of electrical signals through the muscle tissue is covered in *Chapter 5*. To simulate the propagation of APs along muscle fibres, the monodomain model is employed. The monodomain model is derived from the more general but complex bidomain model, which is a continuum approach for the description of electrically excitable tissues. Numerical experiments reveal that the monodomain approximation is valid for the presented applications. Furthermore, the formulation of the AP propagation is extended to a biophysical description of EMG signals. The advantages of this model over previous models of the EMG are demonstrated in several numerical examples, some of which have already been presented in Mordhorst et al. [178].

Chapter 6 introduces a multiscale, chemo-electro-mechanical skeletal muscle model that is based on the finite-elasticity theory of continuum mechanics. Based on appropriate constitutive assumptions, a continuum-mechanical stress tensor is derived that is capable of representing passive and active skeletal muscle behaviour. The passive behaviour of the muscle tissue is modelled macroscopically as a transversely isotropic, hyperelastic, and incompressible material. The formulation of the active contractile part relies on the biophysical cellular description of the excitation-contraction coupling (introduced in Chapter 4), which in turn links to the monodomain model as described in Chapter 5.

The numerical treatment of the chemo-electro-mechanical muscle model yields a multiscale computational model, whose numerical solution is computationally challenging. Thus, *Chapter 6* presents the multiscale computational framework as well as appropriate optimisation strategies, which have previously been described in Bradley et al. [26] and Heidlauf & Röhrle [109]. Moreover, the multiphysics model is used to investigate differences in the muscle contraction and force generation arising from the muscle fibre arrangement. To this end, parallel-fibred muscle models, in which the muscle fibres either span the entire length of the muscle or terminate intrafascicularly, are compared to each other. The results of this study have previously appeared in Heidlauf & Röhrle [111].

To simulate the behaviour of the entire neuromuscular system, *Chapter 7* couples the multiscale skeletal muscle model to the model of the motor neurons of Negro & Farina [186]. Based on the resulting model of the neuromuscular system and the approach to simulate EMG signals (Chapter 5), simulations are carried out predicting simultaneously muscle force generation, muscle tissue deformation, and the EMG signal during isometric and non-isometric contractions.

A final discussion is provided in *Chapter 8* including suggestions for potential applications of the presented methods as well as further developments of the presented modelling framework. Further, for the sake of convenience, the *Appendix* provides additional mathematical and mechanical details.

1.4 List of Publications

Research leading to the results presented in this thesis has previously been published in the following articles, some of which are still under review.

Peer-Reviewed Journal Articles

C. P. BRADLEY, A. BOWERY, R. BRITTEN, V. BUDELMANN, O. CAMARA, R. CHRISTIE, A. COOKSON, A. F. FRANGI, T. GAMAGE, T. HEIDLAF, S. KRITTIAN, D. LADD, C. LITTLE, K. MITHRARATNE, M. NASH, D. NICKERSON, P. NIELSEN, Ø. NORDBØ, S. OMHOLT, A. PASHAEI, D. PATERSON, V. RAJAGOPAL, A. REEVE, O. RÖHRLE, S. SAFAEI, R. SEBASTIÁN, M. STEGHÖFER, T. WU, T. YU, H. ZHANG & P. J. HUNTER. OpenCMISS: a multi-physics & multi-scale computational infrastructure for the VPH/Physiome project. *Progress in Biophysics and Molecular Biology* **107**, p. 32–47, 2011

T. HEIDLAF & O. RÖHRLE. Modeling the chemoelectromechanical behavior of skeletal muscle using the parallel open-source software library OpenCMISS. *Computational and Mathematical Methods in Medicine* **2013**, p. 1–14, 2013

T. HEIDLAF & O. RÖHRLE. A multiscale chemo-electro-mechanical skeletal muscle model to analyze muscle contraction and force generation for different muscle fiber arrangements. *Frontiers in Physiology* **5**, p. 1–14, 2014

M. MORDHORST, T. HEIDLAF & O. RÖHRLE. Predicting electromyographic signals under realistic conditions using a multiscale chemo-electro-mechanical finite element model. *Interface Focus* **5**, p. 1–11, 2015

K. KUPCZIK, H. STARK, R. MUNDY, F. T. NEININGER, T. HEIDLAF & O. RÖHRLE. Reconstruction of muscle fascicle architecture from iodine-enhanced microCT images: a combined texture mapping and streamline approach. *Journal of Theoretical Biology* **382**, p. 34–43, 2015

O. RÖHRLE, V. NEUMANN & T. HEIDLAF. The Role of Parvalbumin, Sarcoplasmic Reticulum Calcium Pump Rate, Rates of Cross-Bridge Dynamics, and Ryanodine Receptor Calcium Current on Peripheral Muscle Fatigue: a Simulation Study. *Journal of Muscle Research and Cell Motility*, under review

T. HEIDLAF, T. KLOTZ, C. RODE, E. ALTAN, C. BLEILER, T. SIEBERT & O. RÖHRLE. A multi-scale continuum model of skeletal muscle mechanics predicting force enhancement based on actin-titin interaction. *Biomechanics and Modeling in Mechanobiology*, under review

J. FERNANDEZ, J. ZHANG, T. HEIDLAF, M. SARTORI, T. BESIER, O. RÖHRLE & D. LLOYD. Multiscale Modelling, Data-Model Fusion and Integration of Organ Physiology in the Clinic: Musculoskeletal. *Interface Focus*, under review

M. MORDHORST, T. STRECKER, D. WIRTZ, T. HEIDLAF & O. RÖHRLE. POD-DEIM reduction of dynamic skeletal muscle models *Journal of Computational Science*, under review

Book Chapters

O. RÖHRLE, M. SPRENGER, E. RAMASAMY & T. HEIDLAF. Multiscale skeletal muscle modeling: From cellular level to a multi-segment skeletal muscle model of the upper limb. *Computer Models in Biomechanics*, p. 103–116, 2013

Peer-Reviewed Conference Proceedings

T. HEIDLAF, F. NEGRO, D. FARINA & O. RÖHRLE. An integrated model of the neuromuscular system. *6th International IEEE/EMBS Conference on Neural Engineering (NER) 2013*, p. 227–230, 2013

Non-Reviewed Conference Proceedings

T. HEIDLAF & O. RÖHRLE. A geometrical model of skeletal muscle. *Proceedings in Applied Mathematics and Mechanics* **12**, p. 119–120, 2012

T. HEIDLAF & O. RÖHRLE. On the treatment of active behaviour in continuum muscle mechanics. *Proceedings in Applied Mathematics and Mechanics* **13**, p. 71–72, 2013

M. MORDHORST, T. HEIDLAF & O. RÖHRLE. Mathematically modelling surface EMG signals. *Proceedings in Applied Mathematics and Mechanics* **14**, p. 123–124, 2014

2 Anatomical and Physiological Fundamentals

This chapter introduces the anatomy and physiology of the neuromuscular system, i. e., the structure and function of the skeletal muscles and the nerves supplying them. Due to their complexity, only a brief overview of the anatomy and physiology of the neuromuscular system is given here. The reader is referred to the literature for more details. An elaborate description of the nervous system and its components, the neurons, can be found, for example, in Kandel et al. [139]. MacIntosh et al. [161] give full account on the anatomy and physiology of skeletal muscles and provides some details on the motor neurons (MNs). The motor unit as the functional unit of the neuromuscular system has recently been reviewed by Heckman & Enoka [105, 106]. The mechanisms involved in human movement, from neural control to muscle mechanics, are comprehensively described in Enoka [65]. With regard to theoretical and mathematical descriptions, the reader is referred to Keener & Sneyd [144, 145], Tuckwell [264], and Herzog [116].

2.1 Summary

This section summarises briefly the processes of the neuromuscular system leading to force generation. The following sections then explain the anatomy and physiology of MNs and muscles in more detail.

Nerves are cord-like bundles of nervous tissue. They are made up of nerve fibres that connect the central nervous system with other parts of the body [146]. In the context of this work, especially those nerve cells (neurons) are of interest that are known as motor neurons. This is due to the fact that motor neurons innervate skeletal muscles. Skeletal muscles consist of parallel-aligned muscle fibres that are embedded in a matrix of extracellular connective tissue. Each muscle fibre is a long, cylindrical, biological cell.

The cell body (or soma) of a MN is located in the spinal cord, which is part of the central nervous system. There, the MN receives signals from other neurons, such as those of the motor cortex of the brain. Depending on the received signals, the MN itself might generate action potentials (electrical signals of short duration), which are transmitted along the MN's axon (nerve fibre) to the muscle. At its end, the axon branches profusely, with each end linking to a muscle fibre. The AP of the neuron is transmitted to the muscle fibre at a site called neuromuscular junction. Starting from the neuromuscular junction, the AP propagates along the length of the muscle fibre. The propagating signal triggers the release of calcium ions from an intracellular calcium storage called sarcoplasmic reticulum (SR). The released calcium binds, amongst others, to the troponin-tropomyosin regulatory unit. When two calcium ions are bound to the regulatory unit, it undergoes a conformational change that allows myosin heads to attach to actin binding sites. Myosin and actin are proteins within so-called thick and thin filaments, respectively. The thick and thin

filaments are structural components within a sarcomere, which is the basic contractile unit in a muscle fibre. The process of binding, bending, and unbinding of the myosin head is called cross-bridge cycling. As a result, the thick filament moves relative to the thin filament, which induces the contraction and force generation in the muscle fibres.

2.2 Basic Anatomy of the Motor Unit

The entity of a MN and all the muscle fibres innervated by that MN is called motor unit (MU). The MU is considered the functional unit of a skeletal muscle, since its MN stimulates all muscle fibres belonging to the MU conjointly, and these fibres contract simultaneously in response to the stimulation. Depending on the size of a muscle and the task assigned to it, the number of its MUs ranges from about one hundred to several thousand. In the human tibialis anterior (TA) muscle, about 300 000 muscle fibres are innervated by approximately 450 MNs.

The group of muscle fibres innervated by a single MN is referred to as a muscle unit. The muscle unit is not locally concentrated in one part of the muscle, but distributes over a part of the muscle's cross-sectional area and interdigitates with other muscle units. The number of fibres in a muscle unit, i. e., the number of fibres innervated by a single MN, is commonly referred to as the innervation number and can vary from tens to thousands, often within a single muscle. For example, in the human TA muscle the innervation number ranges from 50 to 12000 [105]. The human TA muscle, as all other muscles, consists of many small and few large MUs, such that the average innervation number (the ratio of the total number of muscle fibres and the number of MUs in a muscle) is about 600. The combination of many parallel-arranged MUs and the wide range in innervation number allows a single muscle to exert a huge spectrum of outputs, ranging from precise movements to large forces. This spectrum of outputs is controlled through the coordinated action of the MUs.

The MNs innervating a muscle are usually clustered into an elongated motor nucleus within the ventral horn of the spinal cord that may extend over one to four spinal cord segments [139]. The MNs receive synaptic input from various sources, such as from the motor cortex via the corticospinal pathway, the brain stem and other descending pathways, as well as from neighbouring motor nuclei, spinal cord interneurons, and afferent neurons. These signals affect the neuron's membrane potential, which is described in detail in the next section.

2.3 The Cell Membrane of Excitable Cells

The cell membrane, known as sarcolemma, is formed by phospholipids. Phospholipids have a globular head that is hydrophilic (attracted to water) and two fatty acid tails that are hydrophobic (repelled by water) [211]. Given an aqueous environment such as that in the human body, phospholipids have the property of forming a bilayered structure, where the lipid's hydrophilic heads form the inner and outer boundary of the membrane, while the lipid's hydrophobic tails are pointing towards the interior of the membrane, cf. Figure 2.1.

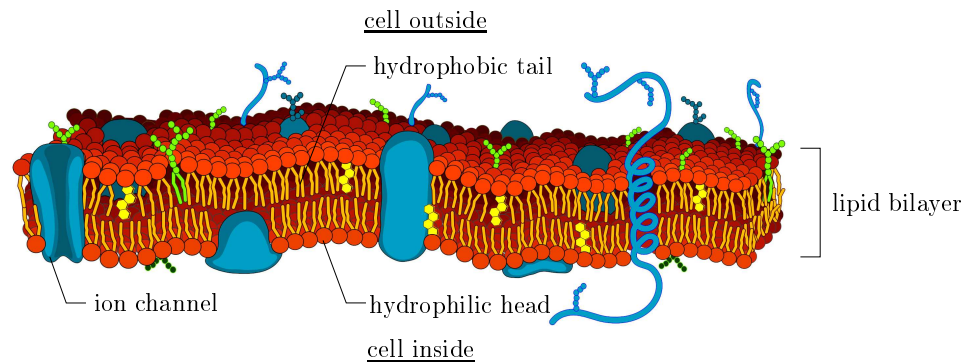


Figure 2.1: *The cell membrane.*

Embedded in the sarcolemma are many types of large protein structures, for example, several different types of receptors and transport proteins. Some of these proteins are capable either of actively transporting specific ions from one side of the membrane to the other (transport proteins, ion pumps) or providing channels through which certain ions can move (ion channels). Passage through ion channels is governed by their opening and closing in response to chemical or electrical signals. The actions of transport proteins and ion channels enable the cell to establish a resting membrane potential and shape APs, both of which are discussed in the following sections.

2.3.1 Resting Membrane Potential

The sarcolemma's low permeability to ions enables the cell to have a chemical composition in the cytosol (the solution in a biological cell) different to the fluid surrounding the cell. In excitable cells, there is a surplus in the concentration of potassium (K^+) cations in the cytosol, and a surplus of sodium (Na^+) and calcium (Ca^{2+}) cations as well as chloride (Cl^-) anions in the extracellular matrix. These differences in the ionic concentrations are sustained by the cell membrane and its embedded ion pumps and channels. Most relevant in establishing the resting potential is the Na^+K^+ pump, which transports three Na^+ ions out of the cell and two K^+ ions in, at the cost of one adenosine triphosphate (ATP). Further, Na^+Ca^{2+} -exchangers, exchanging three Na^+ ions from the extracellular space for one Ca^{2+} ion from the intracellular space, ensure a very low Ca^{2+} ion concentration in the cytosol in the resting state. Cl^- is not actively transported but can move through so-called leakage channels that remain open all the time. Leakage channels are selectively permeable to either Cl^- or K^+ ions.

K^+ cations leak out of the cell along their concentration gradient leaving behind relatively immobile anions. This leads to a net negative charge inside the cell with respect to the cell outside, i. e., a potential difference across the membrane arises. At the so-called equilibrium potential the outward flux of K^+ ions due to their concentration gradient is balanced by an inward flux of K^+ ions due to the negative electrical charge of the cell inside. The equilibrium potential E_i of ion species i , with $i = \{K, Na, Cl, Ca\}$, can be determined using the Nernst equation:

$$E_i = \frac{RT}{z_i F} \ln \frac{[i]_o}{[i]_i}. \quad (2.1)$$

Therein, R is the universal gas constant, T is the absolute temperature, and F denotes the Faraday constant. Furthermore, z_i is the charge of the ion, and $[i]_i$ and $[i]_o$ denote the ion's intracellular and extracellular concentrations, respectively.

As the equilibrium potential is different for different ion species, the resting membrane potential of a cell consists of the contributions of all involved ions. The resting potential can be determined using the Goldman-Hodgkin-Katz equation and is defined as the weighted average of the equilibrium potentials of the involved ions, where the relative permeability of the membrane to the specific ion species is used as weight, cf. e.g. MacIntosh et al. [161]. Commonly, only K^+ , Na^+ , and Cl^- ions are considered. Since the cell membrane is much more permeable to K^+ and Cl^- than to Na^+ , the resting membrane potential is close to the equilibrium potentials of K^+ (-90 mV, all values given at physiological temperature) and Cl^- (-85 mV) but slightly shifted towards the equilibrium potential of Na^+ ($+75$ mV). This results in a cell's resting potential of about -70 to -80 mV, with a negative voltage inside the cell as compared to the cell outside.

2.3.2 Action Potentials

In the resting state, the cell membrane is relatively impermeable to Na^+ ions. If, due to a stimulus, the membrane becomes more permeable to Na^+ ions, a strong Na^+ ion influx occurs. This current is driven by the difference between the membrane potential and the equilibrium potential of Na^+ and is particularly strong as Na^+ is far away from its equilibrium potential. The resulting change in the membrane potential towards the equilibrium potential of Na^+ is called depolarisation, since the membrane potential becomes less negative. If the depolarisation is strong enough, i. e., the membrane potential exceeds a certain threshold value (approximately -55 mV), voltage-gated ion channels open, which allows for a large inward flux of Na^+ ions and an outward flux of K^+ ions. Due to the dominating Na^+ flux, the membrane potential changes towards the equilibrium potential of Na^+ resulting in an inversion of the membrane voltage. The raised membrane voltage causes the voltage-gated Na^+ channels to close, and the still ongoing K^+ outward flux repolarises the membrane potential, which changes again towards the equilibrium potential of K^+ (repolarisation). When the membrane potential is repolarised, the voltage-gated K^+ channels close, and the resting membrane potential is restored. This short (2–5 ms) event, in which the electrical potential of the cell is inverted and restored again, is known as action potential. Figure 2.2 shows the typical course of an AP. In neurons, a short-lasting drop in the membrane potential below the resting membrane potential occurs at the end of the repolarisation process. This drop is called afterhyperpolarisation. The afterhyperpolarisation potential (AHP) inhibits the development of subsequent APs by increasing the amount of stimulus required to reach the threshold value for AP generation.

It is noteworthy that the actual concentrations of Na^+ and K^+ hardly change throughout the AP, and a cell can fire many thousands of APs without actively pumping Na^+ out of the cell or K^+ into it. This is important, since neurons transmit information only through the AP discharge frequency, and not through the magnitude of the AP, which is similar for each discharge.

In excitable cells, APs are used to transmit signals between different parts of the cell. The mechanism is as follows. The currents flowing locally into the cell during an AP spread out along the length of the cell. This yields a depolarisation of the potential of ad-

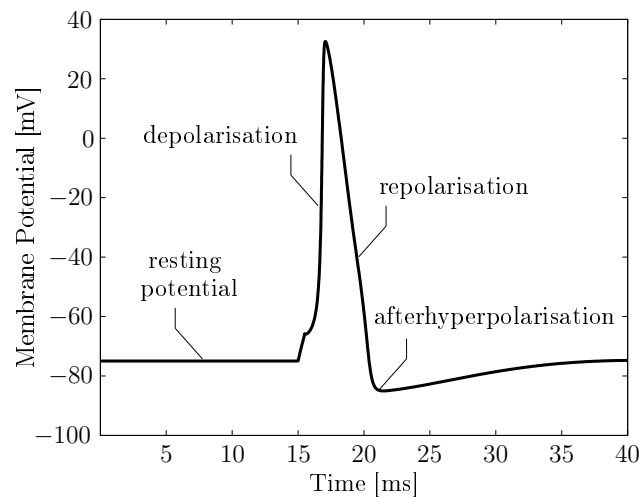


Figure 2.2: *The action potential.*

jacent patches of the cell membrane. If the depolarisation is strong enough, voltage-gated Na^+ channels open, and the AP is reproduced in this neighbouring patch. Subsequent reproductions of the AP on successive patches result in a wave-like propagation of the AP along the membrane of an excitable cell. Note that voltage-gated Na^+ channels fall into an inactive state after closing for a short period of time, which ensures that the AP moves only in one direction.

APs propagate along muscle fibres at a speed of 2–10 m/s [157, 159]. This is relatively slow compared to AP propagation speeds of up to 100 m/s found in neurons [127]. The fast AP propagation speeds in neurons result from an insulating myelin sheath that is wrapped around the nerve fibres, cf. Section 2.4.1.

APs are assigned different tasks in neurons and muscle fibres. Neurons transmit signals between different parts of the body, while in muscle fibres, the AP triggers internal processes that eventually lead to force generation.

2.3.3 Synapses, Excitatory and Inhibitory Postsynaptic Potentials

Synapses are connections between cells, at which signals are transmitted from a neuron to another cell, which does not necessarily have to be a neuron. The following description of synapses is restricted to chemical synapses, which are present in the neuromuscular system, and occur either between neurons or between MNs and muscle fibres. Besides chemical synapses, electrical and immunological synapses exist in the human body.

Chemical synapses pass information unidirectionally, i. e., at a certain synapse, signals are exclusively transmitted from a signal-passing, presynaptic neuron to a signal-receiving, postsynaptic cell. At the synapse, both the presynaptic and postsynaptic cells contain specialised structures that enable signal transmission. In the presynaptic cell, the synaptic bouton (axon terminal) contains neurotransmitters enclosed in synaptic vesicles. When an AP, which propagates along the membrane of the presynaptic cell, reaches the synapse, the membrane depolarisation causes Ca^{2+} channels to open. The resulting inward flux of Ca^{2+} ions increases the Ca^{2+} concentration in the cell immediately, since the intracellular Ca^{2+} concentration is kept at a very low level during the resting state. The rise in intracellular

Ca^{2+} concentration causes a release of neurotransmitter into the narrow space between the presynaptic and postsynaptic cells called synaptic cleft. The neurotransmitter binds to receptors embedded in the membrane of the postsynaptic cell, which either open ligand-gated ion channels (in both neurons and muscle fibres) or activate intracellular signaling pathways (only in neurons).

Assuming, first, that the presynaptic cell is a MN, and the postsynaptic cell is a muscle fibre, the neurotransmitter is acetylcholine (ACh), and the synapse is called neuromuscular junction. The neuromuscular junction is a huge synapse, and an AP discharged by the presynaptic MN always causes an AP in the postsynaptic muscle fibre. (Excluded are pathological cases, which are not within the scope of this thesis.) Due to this one-to-one relation between motor neuron APs and muscle APs, the term motor unit action potential (MUAP) is commonly used. Following the release of ACh from the MN at the neuromuscular junction, the ACh molecules bind to ACh receptor channels in the cell membrane of the muscle fibre, which, in response, become permeable to Na^+ ions. An inward current carried by positive-charged Na^+ ions develops, which causes a depolarisation of the membrane potential, and an AP is generated at the muscle fibre membrane. The muscle AP propagates along the length of the muscle fibre, from the neuromuscular junction towards the ends of the fibre.

If the presynaptic and postsynaptic cells are neurons, the situation is more complex. First, it is assumed that the input is an ionotropic signal. In this case, the neurotransmitter-binding receptors open ligand-gated channels. Depending on the released neurotransmitter and the type of ion channel activated, the resulting change in the postsynaptic potential is excitatory or inhibitory. If the opened channel is, for example, a Na^+ channel, the resulting inward flux of Na^+ ions will depolarise the membrane of the postsynaptic neuron, i.e., an excitatory postsynaptic potential (EPSP) is generated. In general, the amplitude of the EPSP resulting from a single presynaptic AP is not sufficient to exceed the threshold potential, however, postsynaptic potentials can overlap and summate, both in space (from different nearby synapses) and time (subsequent signals at the same synapse). The most common excitatory neurotransmitter in MNs is glutamate. In contrast, if the activated channel is a K^+ channel, an outward flux of K^+ ions will hyperpolarise the postsynaptic neuron's membrane, and an inhibitory postsynaptic potential (IPSP) is generated. The most common inhibitory neurotransmitters in MNs are GABA and glycine.

If the input, however, is neuromodulatory, the neurotransmitter-binding receptors will activate intracellular signaling pathways to control the state of excitability of the postsynaptic neuron. This is often realised through persistent inward currents that raise or lower the membrane potential relative to the previous resting membrane potential, and can last for hours. The resting membrane potential in MNs should therefore not be considered as a static quantity, but rather as one that is constantly adjusted through neuromodulatory input to MNs [106].

2.4 Neurons

The key characteristic of neurons, i. e., their ability to transmit signals between different parts of the body, has been described in previous sections. This section provides detailed information on the neural structure and the physiology of the MN pool.

2.4.1 The Structure of a Neuron

A neuron consists of three parts: the cell body or soma, the dendrites, and the axon (nerve fibre). Some details of the neuron's structure are shown in Figure 2.3. Dendrites are thin structures arising from the cell body that extend and branch extensively. Dendrites largely enhance the surface area of neurons and often account for 95% of a neuron's surface. Since the dendrites account for most of the neuron's surface area, the majority of synapses from other neurons connect there, and hence, the dendrites receive the most neural input. While a neuron has typically many dendrites, it only has a single axon. The axon, a long, slender, cylindrical-shaped extension, arises from the cell body at a site called axon hillock. At the axon hillock, where the density of ion channels is very high, APs are generated, which then propagate along the length of the axon towards its end. At its end, the axon branches profusely and each branch ends in a synapse. Depending on the kind of neuron, the synapse connects to, for example, another neuron or a muscle fibre. The axon of neurons is covered with myelin sheaths, which are, in the peripheral nervous system, produced by Schwann cells. The purpose of the myelin sheaths is to increase the propagation speed of APs in the axon by insulating it from ions in the surrounding fluid. The exchange of ions across the sarcolemma during an AP, as described in Section 2.3.2, can only take place at the sites between the myelin sheaths called nodes of Ranvier. This phenomenon is known as saltatory conduction and largely accelerates the AP propagation, cf. e. g. Huxley & Stämpeli [131]. Note that multiple sclerosis, an inflammatory disease, in which parts of the nervous system lose their ability to communicate, is caused by a pathological loss of the myelin sheaths that insulate axons in the brain and spinal cord.

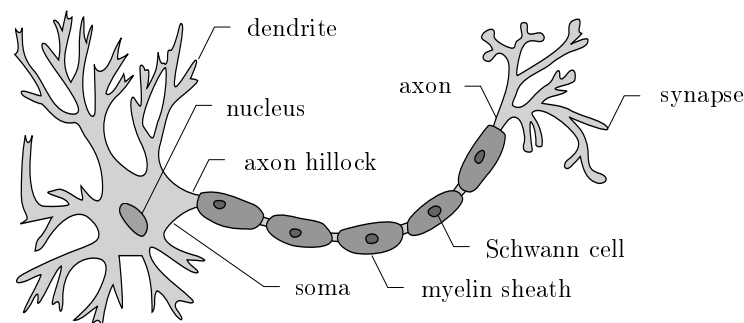


Figure 2.3: Schematic representation of the structure of a neuron. [Figure modified from Quasar Jarosz at <http://en.wikipedia.org/> with permission]

2.4.2 Types of Neurons

Different types of neurons are distinguished. Neurons that conduct signals from the periphery towards the central nervous system, e.g. sensory neurons, are referred to as afferent neurons. Neurons that carry impulses away from the central nervous system, e.g. motor neurons, are referred to as efferent neurons. Further, spinal cord interneurons, e.g., Renshaw cells, Ia and Ib inhibitory neurons (IaIN, IbIN), form a connection between other nearby neurons. These spinal cord neurons and other neurons, such as those of the brain are not considered in this thesis.

2.4.3 The Physiology of the Neural System

The term motor unit pool refers to all MUs in a muscle. Analogously, the term motor neuron pool denotes the entity of the neurons that subserves a single muscle. The electrical properties of MNs and their size vary across a MN pool. Typically, a MN pool consists of many small, low-threshold MNs and few large, high-threshold MNs, cf. e.g. Powers & Binder [207]. Note that the size of the MN is proportional to the size of its corresponding muscle unit, i.e., small MNs innervate few muscle fibres, while large MNs innervate large muscle units consisting of many fibres.

The MN pool is subject to signals of different sources, viz. cortical input, afferent signals, e.g. from muscle spindles, and signals from interneurons and Renshaw cells. Motor neurons integrate all the excitatory and inhibitory signals that they receive from presynaptic neurons. This causes changes in their membrane potential. Once the input is large enough such that the MN exceeds its threshold potential, an AP is discharged. The fact that a neuron either discharges an AP or not, but nothing in between, is known as all-or-none principle and results from the existence of a threshold potential, i.e., if and only if the threshold potential is exceeded, then the neuron will discharge an AP.

Mechanisms of Recruitment and Rate Coding

It is not completely understood how the MN pool in the central nervous system operates as an ensemble to control the force that is exerted by a skeletal muscle. In general, to vary this force, the central nervous system has two options: (i) recruitment, i.e., altering the number of active MUs, and (ii) rate coding, i.e., changing the frequency of electrical impulses driving the MUs. It is generally accepted that MUs follow an orderly recruitment according to Henneman's size principle [112, 113], that is, from the smallest MU (the smallest MN innervating the fewest muscle fibres) to the largest MU (the largest MN innervating the largest muscle unit). However, there is some evidence that the size principle might not be the only principle applied. Butler & Gandevia [34], for example, postulate the idea that also the biomechanical efficiency needs to be taken into account. An increased synaptic input to the MN pool will not only result in an increase of the number of recruited MUs, but it will also increase the discharge rate of all MUs that have already been recruited. Following this, the small, low-threshold MUs always discharge APs at a higher frequency than larger, higher-threshold MUs independent of the synaptic input to the MN pool. This property is known as onion skin property, cf. De Luca and co-workers [46, 47].

2.5 Skeletal Muscle

Skeletal muscles are composed of muscle fibres that are mechanically coupled to each other by a network of extracellular connective tissue. The extracellular connective tissue is composed of mainly collagen and elastin, and it is hierarchically organised in different structures called endomysium, perimysium, and epimysium. The endomysium is a dense sheath of collagen fibres that envelops each muscle fibre and is connected to the basement membrane, which is part of the muscle fibre's cell membrane. The perimysium divides the muscle into bundles of fibres, called fascicles. Its tough and relative thick structure keeps the individual fibres together, and provides the pathway for the major blood vessels and nerves running through the muscle. The muscle as a whole is coated by the epimysium, which is a particularly tough woven network of thick collagen fibres. The epimysium separates muscles from each other and is connected to the perimysium, cf. Figure 2.4.

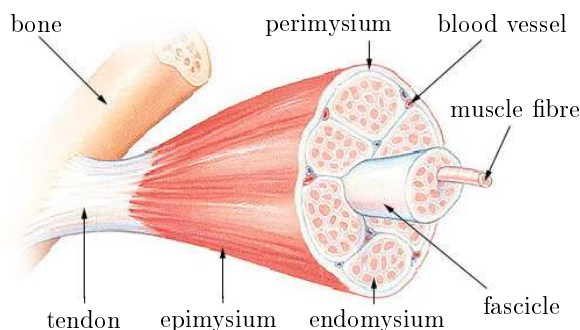


Figure 2.4: *Schematic representation of the structure of a skeletal muscle.*

The connective tissue serves several functions. Besides holding the fibres together and giving the muscle its shape, it contains the blood vessels and nerves, which are necessary for the supply of the muscle fibres. Further, the connective tissue resists excessive stretching of the muscle and distributes forces to minimise damage to the muscle fibres. The elasticity of the elastin and the wavy collagen bundles enable the muscle belly to regain its shape when external forces are removed. Furthermore, the extracellular connective tissue plays a key role in the force transmission from the muscle fibres to the tendons, see e.g. Huijing [124, 125], Monti et al. [177], Street [252], Street & Ramsey [253], Yucesoy et al. [278, 279].

2.5.1 Skeletal Muscle Architecture

Although all skeletal muscles are made up of the same components, viz. muscle fibres and extracellular connective tissue, they come in different forms and sizes depending on their specific task. The muscles in the human body range from very small, consisting of only a few hundred muscle fibres, to very large, consisting of more than a million fibres. Depending on the arrangement of their fascicles, muscles are classified in distinct forms. In parallel-fibred muscles, for example, the fascicles run from tendon to tendon and are aligned with the muscle's force-generating axis. If the directions of the fascicles form an angle to the muscle's line of action, the muscle is called pennate, and the fascicles attach to aponeuroses, which run along each side of the muscle. Pennate muscles can exhibit

larger forces than parallel-fibred muscles of the same volume due to their higher effective or physiological cross-sectional area (PCSA), i. e., the cross-sectional area perpendicular to the fascicle direction. However, the pennation angle decreases the amount a muscle can shorten as well as its contraction velocity. While the direction of the muscle fibres is determined by the fascicle direction, in large mammalian skeletal muscles, muscle fibres might not span the entire length of the fascicle, but they can also be arranged in series and terminate intrafascicularly, see e. g. Heron & Richmond [115], Loeb et al. [159], Richmond et al. [216], Young et al. [277], and Section 6.3.3.

The Structure of a Skeletal Muscle Fibre

Muscle fibres are long, cylindrical-shaped cells with a diameter of approximately 50–80 μm . The most prominent structures within the muscle fibres are the myofibrils, which are parallel-aligned, rod-shaped units that are made up of repeating sections called sarcomeres. The sarcomere, or more precise the half-sarcomere, is the basic contractile unit of a muscle fibre. It contains thick filaments, which consist primarily of the protein myosin, and thin filaments, which consist primarily of the protein actin. The thick filaments are cross-connected by a fine, filamentous structure at one end of the half-sarcomere, called M-disc. The thick filament's other end is connected to titin filaments, which are fine and very elastic, and link the thick filament to a structure at the other end of the half-sarcomere called Z-disc, see Figure 2.5. The titin filaments act as a molecular spring and keep the thick filament in its position. A hexagonal lattice of thin filaments surrounds each thick filament. The thick and thin filaments interact via cross-bridges (XBs), i. e., myosin molecular heads, that can attach to a neighbouring thin filament. The length of a sarcomere is about 2 μm .

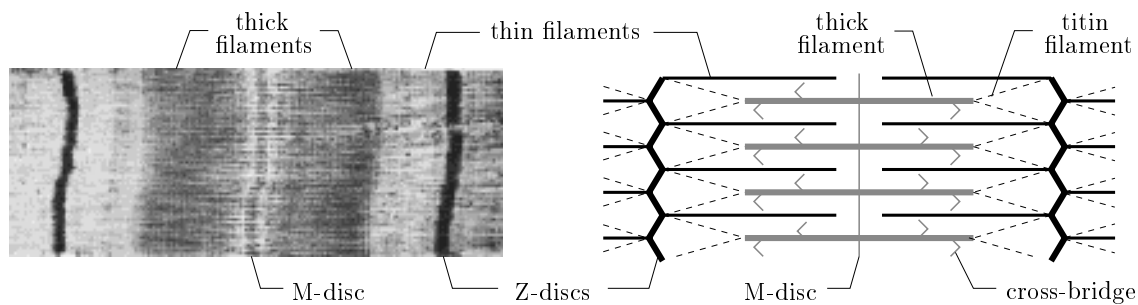


Figure 2.5: *Structure of a sarcomere. On the left side, an image of a sarcomere is shown, while the right side shows the schematic structure of a sarcomere including thick, thin, and titin filaments as well as the Z-discs and M-disc. [Figure modified from Sameerb at <http://en.wikipedia.org/> with permission]*

Passive Behaviour of Skeletal Muscle Tissue

Passive muscle tissue exhibits transversely isotropic material behaviour [181, 189, 256]. The response of the passive muscle tissue is attributed to both the extracellular connective tissue and the myofilaments, especially titin, within the sarcomeres of the muscle fibres, see Prado et al. [209]. While it is often assumed that muscle tissue is stiffer in fibre direction

(see e.g. [181]), Takaza et al. [256] and Nie et al. [189] report a more compliant material behaviour in the fibre direction compared to the cross-fibre directions. Further, passive muscle tissue exhibits slightly viscoelastic behaviour, see e.g. [24, 122, 156, 267, 269], and due to its high content of water, it is commonly considered to behave incompressible within the physiological range [19, 85, 256, 268].

2.5.2 Muscle Fibre Contractions

The complex signaling pathway leading from electrical excitation of a muscle fibre to its contraction is known as excitation-contraction coupling.

Excitation-Contraction Coupling

The excitation-contraction coupling in skeletal muscle fibres, together with the most prominent structures of the muscle fibre, is schematically represented in Figure 2.6.

The AP, generated at the neuromuscular junction, not only propagates along the length of a muscle fibre, but it is also conducted from the surface to the interior of the fibre by numerous, channel-like invaginations of the sarcolemma called T-tubules. Embedded in the membrane of the T-tubules are dihydropyridine receptor (DHPR) channels that are sensitive to changes in the membrane potential. The DHPR channels are mechanically linked via protein structures to the ryanodine receptors (RyR) in the membrane of the SR. The SR is an extensive network of channels in the muscle fibres that stores large amounts of calcium (Ca^{2+}), and the RyR is a Ca^{2+} channel consisting of four subunits. An AP entering the T-tubules activates the DHPR channels, which will then induce the opening of the RyR in the membrane of the SR. When the RyR opens, large amounts of Ca^{2+} will leave the SR and enter the cytosol, following their concentration gradient, since the free concentration of Ca^{2+} in the cytosol is kept at a very low level in the resting state.

Ca^{2+} ions play a key role in muscle contraction. Once released into the cytosol, Ca^{2+} binds to troponin C, which is part of the troponin-tropomyosin regulatory unit. The binding of two Ca^{2+} ions to troponin C yields a conformational change in the troponin molecule that removes the blocking tropomyosin from the thin filaments. This enables the formation of a XB connection between the thick and thin filaments in the sarcomeres.

The contractile, force-producing step is called power stroke and can be figured as a bending mechanism of the myosin heads, which moves the thick and thin filaments relative to each other (sliding filament theory). The energy required for a power stroke is provided by the hydrolysis of one ATP molecule per myosin head. Since each XB acts as an individual molecular motor, i.e., an independent force generator, the force developed during a contraction depends on the number of simultaneous interactions between myosin heads and actin filaments per half-sarcomere (cross-bridge theory).

Length and Velocity Dependence of the Active Force

The maximum isometric force a sarcomere can exert depends on the number of possible XB connections between the thick and thin filaments, which is primarily governed by the regions of overlap between the thick and thin filaments, i.e., by the length of the sarcomere. Figure 2.7a shows the experimentally determined force-sarcomere length relation of

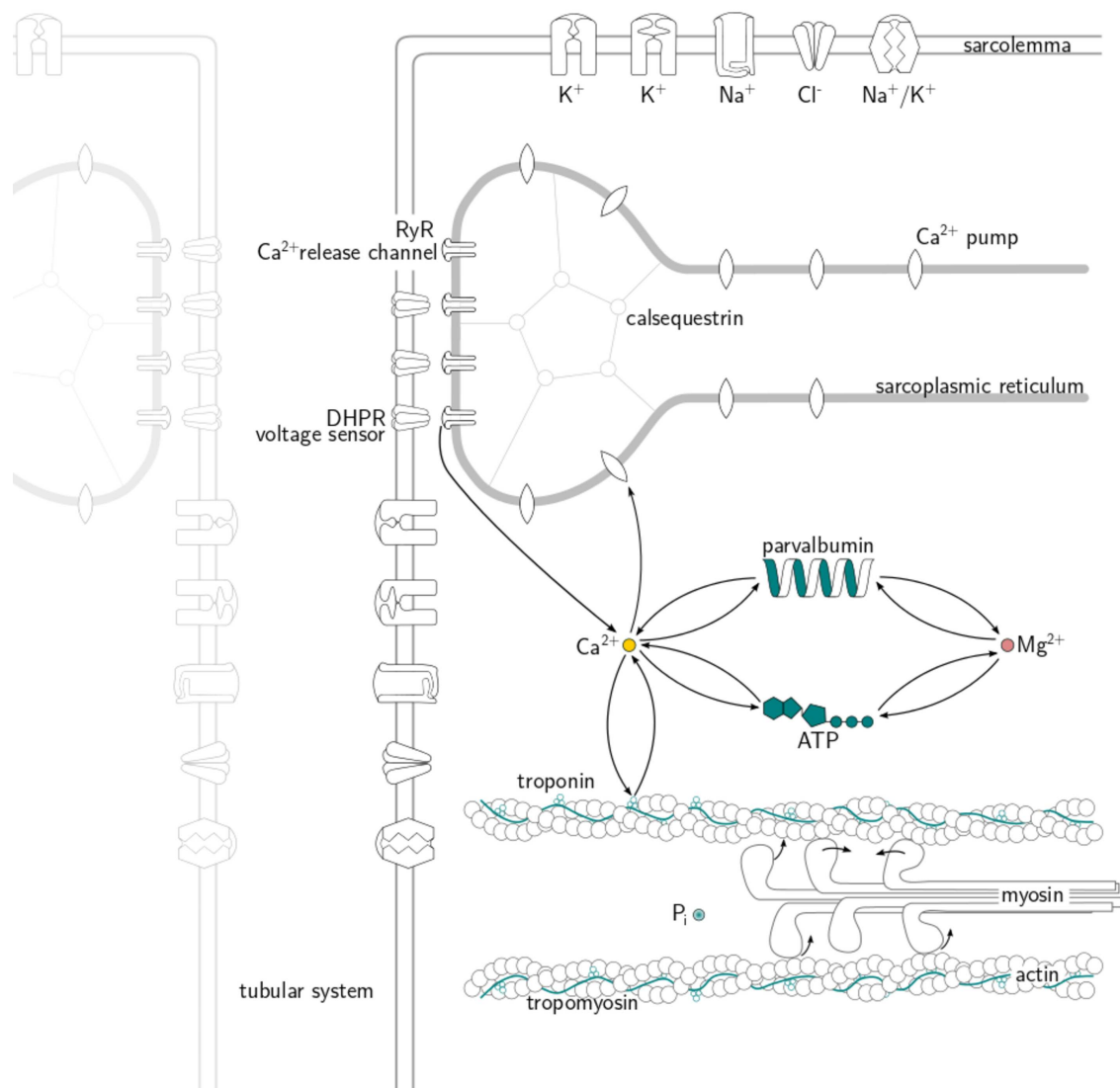


Figure 2.6: Schematic representation of the excitation-contraction coupling in a muscle fibre.
 [Courtesy of Verena Neumann]

Gordon et al. [89], a passive stress-strain relation, and their superposition. Figure 2.7b depicts the regions of overlap between the thick and thin filaments at 5 selected points of Figure 2.7a.

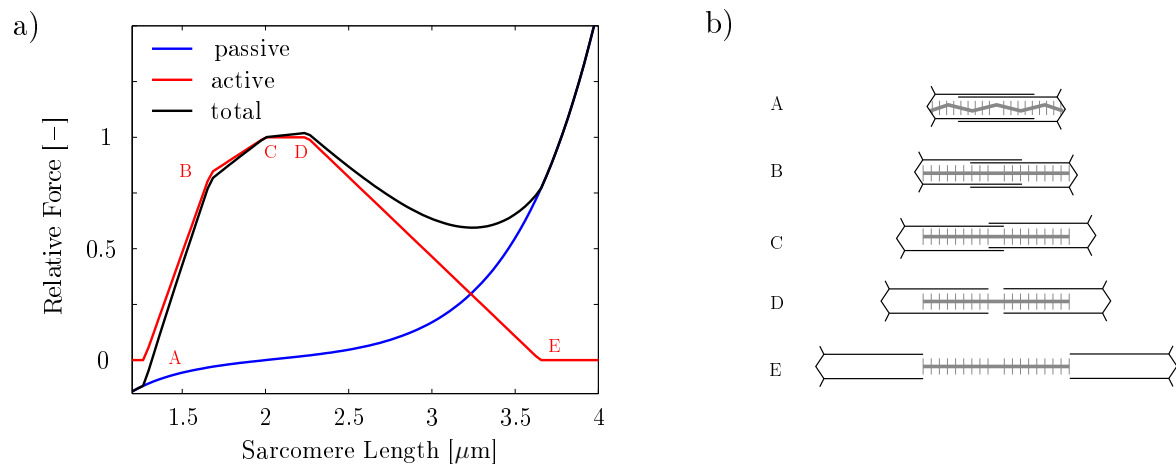


Figure 2.7: (a) Normalised passive, active, and total isometric forces. The active isometric force exerted by a sarcomere depends on (b) the region of overlap between the thick and thin filaments.

Further, the force that a muscle fibre can generate, depends on the fibre's contraction velocity, i. e., the faster the fibre shortens, the less force it can exert [117]. During lengthening contractions, the generated force exceeds the isometric force, cf. Figure 2.8. Note the kink at the transition from shortening to lengthening contractions [141].

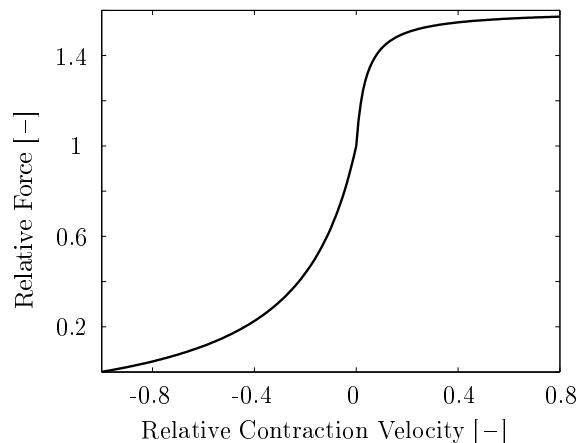


Figure 2.8: The influence of the contraction velocity on the force generation of a skeletal muscle.

2.6 The Motor Unit

Since electrical activation from one muscle fibre to adjacent ones is not observed in skeletal muscle, each fibre must have its own neuromuscular junction. While it is generally assumed that each fibre is innervated by exactly one MN, there is some electrophysiological evidence that a few doubly innervated fibres (fibres with multiple motor endplates and polyneuronal innervation) also exist, see e. g. Lateva et al. [152], McGill & Lateva

[164]. Further, while all muscle fibres belonging to one MU have similar properties, the contractile and metabolic properties of different muscle units vary heavily.

2.6.1 Properties of Motor Units

The differences observed in the contractile and metabolic properties of skeletal muscle fibres inspired the distinction of different MU types. To this end, MUs have been classified based on their speed of contraction, the handling of intracellular Ca^{2+} ions, or their resistance to fatigue during prolonged contractions. For example, muscle fibres can be classified based on the expression of certain isoforms of the myosin heavy chain, which determines the rate of XB cycling, and hence, the speed of contraction. Moreover, based on their metabolic properties, aerobic type-I (slow-twitch) fibres can be distinguished from their fast-twitch counterparts (type-II fibres), which, in addition to the oxidation of fats and carbohydrates, use an anaerobic metabolism. Based on a certain stimulation protocol, Burke et al. [30] distinguished slow-twitch units (type S) and fast-twitch units (type F). The group of type-F units was further split into fatigue-resistant (type FR) and fast-fatigable (type FF) units [30].

In general, the smallest MUs, which are recruited first, exert the smallest forces, exhibit the slowest speed of contraction, and show the least amount of fatigue. Conversely, the largest MUs, which are recruited last, exert the largest forces, have the highest speed of contraction, and are most affected by fatigue. However, the physiological properties of human MUs do not cluster into discrete groups, but rather exhibit a continuous distribution from one extreme to the other [57].

2.6.2 Types of Contractions

The most simple contraction is a single twitch, which is the muscle unit's response to a single AP discharged by the MN. The shape of a twitch can be well described by the impulse response to a critically damped second-order system, cf. Fuglevand et al. [76]. The total duration of a muscular AP, from depolarisation to the point where the resting state is restored, is about 2–5 ms. In contrast, the duration of a twitch from the first rise to complete relaxation varies from about 200 ms to more than 500 ms depending on the MU type. Thus, if subsequent stimulations are applied before the actively generated twitch force of the fibre returned to its initial value, a summation of the resulting twitches is observed (fused twitches). Obviously, the increase in force following subsequent stimulations is not unlimited, but after a number of stimulations, a peak force is reached. The value of the peak force depends on the stimulation frequency – it increases with rising frequency up to a certain optimal frequency, beyond which, no further increase in force can be generated. This form of contraction is referred to as tetanic contraction. Peak firing frequencies during isometric contractions of human muscles are approximately 45 Hz [76].

While single twitches and stimulations with constant frequencies are commonly applied in experimental protocols, actual trains of MN discharges contain a certain degree of variation in the interstimulus interval (time between two successive MN discharges). During isometric contractions, the ratio of the standard deviation of the interstimulus interval to its mean is about 10–30 %. This relation holds for a wide range of mean discharge frequencies.

3 Mathematical and Mechanical Prerequisites

Before introducing the basic concepts of continuum mechanics, this chapter reviews some of the fundamentals of solving differential equations. This is required due to the fact that the mathematical description of biophysical models in general, and the models proposed in this work in particular, is carried out in terms of differential equations. Since analytical solutions to these differential equations are commonly not available, numerical methods are required to approximate the solution. This work uses the finite element method for the numerical treatment of the spatial derivatives occurring in partial differential equations. As the very common (Bubnov-)Galerkin method and Lagrange finite elements are employed, the description of the spatial discretisation is kept rather brief. If the differential equation is a transient PDE, the spatial discretisation yields a set of coupled ordinary differential equations in time, which have to be treated appropriately. Following this, first, the treatment of the spatial derivatives is covered, before discussing numerical methods for solving ODEs. Since some of the presented models are described by stiff ODEs, which impose certain restrictions on the numerical solution scheme, the discussion on ODE solvers is more elaborate.

3.1 Finite Element Method for the Spatial Discretisation of Partial Differential Equations

For the sake of convenience, a linear, vector-valued PDE of second order in space and first order in time is exemplarily considered. The equation is given by

$$\dot{\mathbf{y}}(t, \mathbf{x}) - \operatorname{div} (c(\mathbf{x}) \operatorname{grad} \mathbf{y}(t, \mathbf{x})) = \mathbf{0}, \quad (3.1)$$

where $t \in [0, T]$ is the time, $\mathbf{x} \in \Omega \subset \mathbb{R}^d$ denotes the spatial position vector, $\mathbf{y} \in [0, T] \times \Omega \rightarrow \mathbb{R}^d$ is the vector-valued unknown function, $c(\mathbf{x})$ is a parameter, $\operatorname{grad}(\cdot)$ and $\operatorname{div}(\cdot)$ denote the gradient and divergence operators, respectively, and the superimposed dot denotes a time derivative. Furthermore, for an initial-boundary-value problem, the definition of appropriate initial and boundary conditions is required:

$$\begin{aligned} \text{initial conditions:} & \quad \mathbf{y}(t_0, \mathbf{x}) = \mathbf{y}_0(\mathbf{x}) \in \mathbb{R}^d, \\ \text{Dirichlet boundary conditions:} & \quad \mathbf{y}(t, \mathbf{x}) = \bar{\mathbf{y}}(t) \text{ on } \partial\Omega^D, \\ \text{and Neumann boundary conditions:} & \quad \mathbf{\Lambda}(t, \mathbf{x}) \mathbf{n}(t, \mathbf{x}) = \mathbf{g}(t, \mathbf{x}) \text{ on } \partial\Omega^N, \end{aligned} \quad (3.2)$$

where $\mathbf{n}(t, \mathbf{x})$ denotes the outward-oriented unit normal vector, and $\mathbf{\Lambda}(t, \mathbf{x}) = c(\mathbf{x}) \operatorname{grad} \mathbf{y}(t, \mathbf{x})$. The number of spatial dimensions of the problem is denoted by

$d \in \{1, 2, 3\}$. Further, Ω denotes the domain of the problem, and $\partial\Omega^D$ and $\partial\Omega^N$ are the Dirichlet and Neumann parts of the domain boundary, $\partial\Omega$, respectively, with $\partial\Omega = \partial\Omega^D \cup \partial\Omega^N$ and $\partial\Omega^D \cap \partial\Omega^N = \emptyset$.

3.1.1 The Weak Form

In this work, the FEM (see e. g. Hughes [123], Zienkiewicz et al. [285, 286]) is used to treat the spatial derivatives in Equation (3.1). To this end, Equation (3.1) is first multiplied by an arbitrary test function $\delta\mathbf{y}(\mathbf{x})$ and then integrated over the domain, Ω . This yields the so-called weak form, which is given by

$$\int_{\Omega} \left(\dot{\mathbf{y}}(t, \mathbf{x}) - \operatorname{div} (c(\mathbf{x}) \operatorname{grad} \mathbf{y}(t, \mathbf{x})) \right) \cdot \delta\mathbf{y}(\mathbf{x}) \, dv = 0, \quad (3.3)$$

where dv represents an infinitesimal volume element of the domain. Pointwise satisfaction of the strong form (3.1) is still given by the integral form (3.3) due to the fact that the choice of the test function is arbitrary. In detail, choosing $\delta\mathbf{y} = \delta(\mathbf{x} - \mathbf{x}_i)$, where $\delta(\cdot)$ denotes the Dirac delta function, subsequently for all points $\mathbf{x}_i \in \Omega$ of the domain, yields again the strong form (3.1).

Next, applying integration by parts and the Gaußian integral theorem to Equation (3.3) yields after some tensor algebra a weak form suitable for applying the FEM, viz.:

$$\int_{\Omega} \dot{\mathbf{y}}(t, \mathbf{x}) \cdot \delta\mathbf{y}(\mathbf{x}) \, dv + \int_{\Omega} c(\mathbf{x}) \operatorname{grad} \mathbf{y}(t, \mathbf{x}) \cdot \operatorname{grad} \delta\mathbf{y}(\mathbf{x}) \, dv = \int_{\partial\Omega} \mathbf{g}(t, \mathbf{x}) \cdot \delta\mathbf{y}(\mathbf{x}) \, da, \quad (3.4)$$

where da represents an infinitesimal surface element. Due to the fact that the Neumann boundary term quite naturally occurs in the weak form (3.4), the associated type of boundary condition (Neumann boundary condition) is also called natural boundary condition. It is furthermore noteworthy that the order of PDE (3.1) has been reduced from two to one, as only first-order spatial derivatives occur in its weak form (3.4). Further, all solutions of the strong form (3.1) are also solutions to Equation (3.4).

3.1.2 The Finite Element Method

The FEM relies on approximating the domain, such that it can be subdivided into several smaller, non-overlapping parts called finite elements, i. e.,

$$\Omega \approx \Omega^h = \bigcup_{e=1}^{N_e} \Omega_e. \quad (3.5)$$

Therein, Ω^h denotes the approximated domain, which can be represented by N_e finite elements of element domain size Ω_e . Defining each finite element by N_i nodal points yields a total of $N_n \leq N_e N_i$ nodes in the finite element mesh. A discrete representation of the continuous PDE (3.4) is obtained by approximating the unknown and test functions

by

$$\begin{aligned}\mathbf{y}(t, \mathbf{x}) &\approx \mathbf{y}^h(t, \mathbf{x}) = \bar{\mathbf{y}}^h(t, \mathbf{x}) + \sum_{i=1}^{N_n} \boldsymbol{\varphi}_i(\mathbf{x}) \mathbf{y}_i(t), \\ \delta \mathbf{y}(\mathbf{x}) &\approx \delta \mathbf{y}^h(\mathbf{x}) = \sum_{i=1}^{N_n} \boldsymbol{\psi}_i(\mathbf{x}) \delta \mathbf{y}_i.\end{aligned}\tag{3.6}$$

Therein, $\bar{\mathbf{y}}^h(t, \mathbf{x})$ denotes the discrete version of the Dirichlet boundary conditions. Furthermore, $\mathbf{y}_i(t)$ are the time-dependent nodal degrees of freedom, and $\boldsymbol{\varphi}_i(\mathbf{x}) = \text{diag}[\varphi_{i,1}(\mathbf{x}), \dots, \varphi_{i,d}(\mathbf{x})]$ and $\boldsymbol{\psi}_i(\mathbf{x}) = \text{diag}[\psi_{i,1}(\mathbf{x}), \dots, \psi_{i,d}(\mathbf{x})]$ represent the global basis functions for the approximation of the unknown and test functions, respectively, when using Lagrange finite elements. Following the (Bubnov-)Galerkin approach, the same basis functions are used to approximate the unknown and test functions, i. e., $\boldsymbol{\varphi}_i(\mathbf{x}) \equiv \boldsymbol{\psi}_i(\mathbf{x})$. The decoupling of the temporal and spatial dependencies of the unknown function in Equation (3.6)₁ is obtained by introducing the basis functions, which have not yet been further specified. (The subscript 1 in the notation (3.6)₁ refers to the first equation in (3.6).)

Conveniently, the basis functions are chosen to have compact (local) support. Moreover, the basis functions can be constructed by so-called shape functions that are defined on a simple reference element using a local coordinate system. Thus, the element integrals arising when inserting the approximations (3.6) into the weak form (3.4) can be mapped to the reference element using the Jacobian determinant, where they can be evaluated using a method that is suitable for numerical implementation, such as, for example, Gaussian quadrature. For the sake of brevity, a detailed presentation of these steps is omitted here but can be found in any FEM textbook, see e. g. [123, 286].

Evaluating the resulting equation for each finite element and assembling the resulting element matrices to global matrices finally yields a set of coupled ODEs of the form

$$\mathbf{D} \dot{\mathbf{y}}(t) + \mathbf{K} \mathbf{y}(t) = \mathbf{g}(t),\tag{3.7}$$

where \mathbf{D} and \mathbf{K} are the global damping and stiffness matrices (dimension $N_n \times N_n$), respectively, $\mathbf{y}(t)$ is the global vector of unknown nodal values, and $\mathbf{g}(t)$ is the global right-hand side vector (dimension $N_n \times 1$), which contains the Neumann boundary conditions.

3.2 Numerical Methods for Ordinary Differential Equations

Since analytical solutions to nonlinear ODEs or coupled sets of ODEs, which, for example, arise from the spatial discretisation of a transient PDE, are commonly not available, numerical methods are used to approximate the solution of the governing ODEs. Numerical methods for the integration of ODEs is a research field on its own, and a general presentation of these methods is beyond the scope of this thesis. Instead, a brief discussion is provided, which focuses on a particular group of ODE integrators that will, in the subsequent sections, be used for the solution of stiff ODE systems arising from the mathematical description of biophysical models of the neuromuscular system. Further reading on numerical methods for the solution of ODEs can be found, for example, in Ascher &

Petzold [4], Gupta et al. [95], Hairer et al. [97], Hairer & Wanner [98], Press [210], and Schwarz [231].

The ODEs considered in this work can mathematically be represented by first-order, nonlinear systems of equations of the form

$$\dot{\mathbf{y}}(t) = \mathbf{f}(t, \mathbf{y}(t)), \quad \mathbf{y}(t_0) = \mathbf{y}_0 \in \mathbb{R}^k. \quad (3.8)$$

Therein, $\mathbf{y}(t)$ denotes the vector of unknown functions, \mathbf{y}_0 denotes the vector of given initial values, and \mathbf{f} is a vector-valued, potentially non-linear function of t and $\mathbf{y}(t)$. The dimension of the problem denoted by $k \geq 1$ depends on the specific model under consideration.

3.2.1 Introduction

Numerical methods for the solution of ODEs often approximate the time derivative in Equation (3.8) by a truncated Taylor series. A Taylor series can be used to represent an unknown function value as an infinite sum of terms that are determined from the value and derivatives of the (sufficiently smooth) function at a different point:

$$\mathbf{y}_{n+1} = \mathbf{y}_n + \frac{h}{1!} \mathbf{y}'_n + \frac{h^2}{2!} \mathbf{y}''_n + \dots = \sum_{j=0}^{\infty} \frac{h^j}{j!} \mathbf{y}_n^{(j)}. \quad (3.9)$$

Therein, $\mathbf{y}_n = \mathbf{y}(t_n)$, $\mathbf{y}_n^{(j)} = d^j \mathbf{y} / dt^j |_{t=t_n}$, $h = t_{n+1} - t_n$ denotes the time step size, and $t_n = t_0 + nh$ ($n = 0, 1, \dots$). In the following, the Taylor series (3.9) is considered up to the first-order derivative, and the remaining terms are lumped together in $\mathcal{O}(h^2)$ making use of the big-O notation. Solving the resulting equation for the derivative term yields

$$\left. \frac{d\mathbf{y}}{dt} \right|_{t=t_n} = \dot{\mathbf{y}}(t_n) = \frac{\mathbf{y}_{n+1} - \mathbf{y}_n}{h} + \mathcal{O}(h). \quad (3.10)$$

Approximating Equation (3.10) by neglecting the higher-order terms and inserting the resulting approximation in the ODE system (3.8), yields the explicit forward Euler scheme,

$$\mathbf{y}_{n+1} = \mathbf{y}_n + h \mathbf{f}(t_n, \mathbf{y}_n). \quad (3.11)$$

Similarly, a Taylor series can be used to represent \mathbf{y}_n by \mathbf{y}_{n+1} and its derivatives. Neglecting the higher-order terms, this yields the implicit backward Euler scheme

$$\mathbf{y}_{n+1} = \mathbf{y}_n + h \mathbf{f}(t_{n+1}, \mathbf{y}_{n+1}). \quad (3.12)$$

Since the neglected terms are proportional to h , the forward and backward Euler methods are first-order accurate, i. e., $p = 1$, where p denotes the order of accuracy. The order of a numerical method is a measure of how well it approximates the exact solution of the problem. Note that (3.11) represents an explicit procedure for the evaluation of the unknown values \mathbf{y}_{n+1} . In contrast, the vector of unknown values \mathbf{y}_{n+1} is additionally implicitly contained in the right-hand side of (3.12). Explicit methods are much simpler to implement and are often more efficient than implicit methods, however, their stability

often depends crucially on the time step size. Implicit methods, on the other hand, require the solution of a system of equations in each time step. Moreover, if \mathbf{f} is a nonlinear function of \mathbf{y} , the solution of (3.12) yields a root-finding problem, which has to be solved using an appropriate method. To this end, a modified Newton method (see Section 3.3) is used in this work.

3.2.2 Linear Multistep Methods

The forward and backward Euler methods are one-step methods, i. e., to approximate the solution \mathbf{y}_{n+1} at time t_{n+1} , only values from the previous step \mathbf{y}_n at time t_n are considered. In contrast, a multistep method of order k takes into account the information of the last k time steps, e. g., a multistep method of order 3 uses information from time levels t_{n-2} , t_{n-1} , and t_n to compute \mathbf{y}_{n+1} .

Approximating the derivative in (3.8) by $\mathbf{y}'_{n+1} \approx -\frac{1}{h} \sum_{j=0}^k \bar{a}_j \mathbf{y}_{n+1-j}$ (cf. Brayton et al. [27]), the general form of a k -step linear multistep method is given by

$$\sum_{j=0}^k a_j \mathbf{y}_{n+1-j} = h \sum_{j=0}^k b_j \mathbf{f}(t_{n+1-j}, \mathbf{y}_{n+1-j}) \quad (k \geq 1), \quad (3.13)$$

with coefficients a_j and b_j , where $a_0 \neq 0$. Without loss of generality, one commonly chooses $a_0 = 1$. If $b_0 = 0$, Equation (3.13) denotes an explicit method, otherwise the method is implicit. The coefficients are chosen such that the order of the resulting method is maximal, see Schwarz [231] for details. Note that a k -step linear multistep method requires k initial values, of which only one ($\mathbf{y}(t_0) = \mathbf{y}_0$) is given. To determine the other initial values, one-step methods can be used, which, however, have to be at least of the same order p as the multistep method to achieve an overall method of order p . In the following some particularly popular explicit and implicit linear multistep methods are presented in detail.

Adams-Bashforth, Adams-Moulton, and Adams-Bashforth-Moulton Methods

Using the general form for linear multistep methods (3.13), the explicit Adams-Bashforth ($b_0 = 0$) and implicit Adams-Moulton methods ($b_0 \neq 0$) are obtained when choosing $a_0 = 1$, $a_1 = -1$, and $a_j = 0$ for all other values. This yields

$$\mathbf{y}_{n+1} - \mathbf{y}_n = h \sum_{j=0}^k b_j \mathbf{f}(t_{n+1-j}, \mathbf{y}_{n+1-j}) \quad (k \geq 1). \quad (3.14)$$

As demonstrated in Schwarz [231], the k -step Adams-Bashforth and Adams-Moulton methods are of order $p = k$ and $p = k + 1$, respectively. The methods of Adams-Bashforth are very popular as they only require a single function evaluation per time step, since all other values have previously been determined. Note that the first-order, one-step Adams-Bashforth method is equivalent to the explicit Euler method (3.11).

To avoid the cumbersome solution of an implicit equation in each step when using the Adams-Moulton methods, an Adams-Bashforth method is combined with an Adams-Moulton method to give a predictor-corrector method. The resulting methods are called

Adams-Bashforth-Moulton methods, are explicit, and read

$$\begin{aligned} \mathbf{y}_{n+1}^{\{p\}} - \mathbf{y}_n &= h \sum_{j=1}^k b_{pj} \mathbf{f}(t_{n+1-j}, \mathbf{y}_{n+1-j}), \\ \mathbf{y}_{n+1} - \mathbf{y}_n &= h (b_{c0} \mathbf{f}(t_{n+1}, \mathbf{y}_{n+1}^{\{p\}}) + \sum_{j=1}^k b_{cj} \mathbf{f}(t_{n+1-j}, \mathbf{y}_{n+1-j})). \end{aligned} \quad (3.15)$$

Therein, $\mathbf{y}_{n+1}^{\{p\}}$ is the predictor value, and b_{pj} and b_{cj} are the coefficients of the predictor and corrector step, respectively. The combination of the m -step Adams-Bashforth method (order $p = m$) and the m -step Adams-Moulton method (order $p = m + 1$) yields a method of order $p = m + 1$. A method of the same order but with higher accuracy is obtained when combining the $m+1$ -step Adams-Bashforth method with the m -step Adams-Moulton method [231].

Some of the ODE systems presented in this work are solved using MATLAB's¹ build-in solver ODE113. ODE113 is a multistep variable-order PECE (Predict-Evaluate-Correct-Evaluate) Adams-Bashforth-Moulton solver. Further details on this solver are given in Shampine & Gordon [235].

As it is the case for all explicit methods, predictor-corrector methods are very inefficient for the solution of stiff problems. The most popular linear multistep methods for the solution of stiff ODEs are the so-called backward differentiation formulas.

Backward Differentiation Formulas

The backward differentiation formulas (BDFs), which are also known as Gear's methods, are implicit linear multistep methods. The k -step BDF is derived by differentiating the polynomial that interpolates the previous k values of \mathbf{y} and setting the derivative at t_{n+1} to \mathbf{f}_{n+1} [4]. The family of k -step BDFs can be represented in the general form

$$\sum_{j=0}^k a_j \mathbf{y}_{n+1-j} = h b \mathbf{f}(t_{n+1}, \mathbf{y}_{n+1}) \quad (k \geq 1). \quad (3.16)$$

BDFs are A -stable for $k \leq 2$, $A(\alpha)$ -stable for $3 \leq k \leq 6$, and become unstable for $k > 6$ (not zero-stable), see Section 3.2.3 for related definitions of stability. The accuracy of a k -step BDF is of order $p = k$. The values of the coefficients a_j and $b \neq 0$ for all stable BDFs are provided in Ascher & Petzold [4]. Note that the first-order, one-step BDF is equivalent to the implicit Euler method (3.12). Further details on BDFs can be found, for example, in Gupta et al. [95].

¹<http://www.mathworks.com/products/matlab/>

Numerical Differentiation Formulas

The numerical differentiation formulas (NDFs) are a class of modified BDFs. The NDFs are given by

$$\sum_{j=0}^k a_j \mathbf{y}_{n+1-j} = h b \mathbf{f}(t_{n+1}, \mathbf{y}_{n+1}) + \frac{\kappa}{b} \gamma_k (\mathbf{y}_{n+1} - \mathbf{y}_{n+1}^{(0)}) \quad (1 \leq k \leq 6), \quad (3.17)$$

wherein $\gamma_k = \sum_{j=1}^k 1/j$ are additional coefficients, and κ denotes a scalar parameter. The values of κ can either be chosen to maximise the $A(\alpha)$ -stable region for $3 \leq k \leq 5$ at the price of reduced efficiency or to maximise the efficiency while reducing the stability, cf. Shampine & Reichelt [234]. For $k = 6$, the $A(\alpha)$ -stable region of BDFs and NDFs is so small that often only orders up to $k = 5$ are used [95]. Furthermore, $\mathbf{y}_{n+1}^{(0)}$ denotes the initial guess for the modified Newton iteration, which is found by an extrapolation of the values $\mathbf{y}_n, \mathbf{y}_{n-1}, \dots, \mathbf{y}_{n-k+1}$, cf. Shampine & Reichelt [234].

Some of the ODE systems presented in this work are stiff. In this case, their solution is approximated using MATLAB's build-in solver ODE15s. ODE15s is an implicit, multistep, variable-order solver based on the NDFs. Further details on this solver and its implementation are given in Shampine & Reichelt [234] and Shampine et al. [236].

3.2.3 Convergence, Stability, and Stiffness

The previous sections mentioned the terms convergence, stability, and stiffness. Since these terms have not been discussed yet, they will be briefly explained in this section. The interested reader is referred to Ascher & Petzold [4], Gupta et al. [95], and Schwarz [231] for more in-depth details.

A numerical method is called convergent if it is both consistent and zero-stable. A method is consistent if the local truncation error (the error committed by one step of the method) approaches zero faster than the step size, when considering the limit $h \rightarrow 0$. Multistep methods are consistent if they are at least of order $p = 1$. Further, a linear multistep method is called zero-stable if, within a given time interval, the error of the approximated solution that is induced by a perturbation in the initial values, does not depend on the time step size.

A numerical method is said to be stable if errors in the approximation are damped out or are at least not amplified in subsequent steps of the method. The stability of many methods depends on the time step size. Explicit methods, such as, for example, the Adams-Bashforth methods, have very small regions of absolute stability. Implicit methods have in general larger regions of absolute stability, but not all implicit methods are A -stable. A method is called A -stable if the region of absolute stability of the method contains the complex left half-plane for the model problem $y(t) = \lambda y(t)$ with $\lambda \in \mathbb{C}$. Implicit multistep methods can only be A -stable if their order is at most 2 (second Dahlquist barrier). For example, the first-order backward Euler method and the second-order trapezoidal rule are A -stable, cf. Dahlquist [42]. Implicit multistep methods of order greater than 2 are often $A(\alpha)$ -stable. In this case, the region of absolute stability does not contain the entire complex left half-plane but only a sector with opening angle 2α . The values of α of all stable BDF methods and further details can be found in Hairer & Wanner [98].

A stiff equation is a differential equation for which certain methods lead to numerical instabilities, unless the step size is chosen extremely small. While it is difficult to formulate a precise definition of stiffness, the main idea is that the equation includes some terms that can lead to rapid variations in the solution. Note that A -stable methods do not exhibit the mentioned instabilities.

3.3 Newton's Method

In Section 3.1, for the sake of convenience, a linear PDE was assumed, which yielded the linear space-discrete equation (3.7). For a nonlinear system of equations, the discrete form can be represented by

$$\mathbf{k}(\mathbf{y}) = \mathbf{0}, \quad (3.18)$$

where \mathbf{k} denotes the generalised stiffness vector that nonlinearly depends on the vector of unknowns. Note that, for clarity, the index denoting the time step (if any) is omitted in this derivation. For transient equations, the following procedure has to be carried out in each time step.

The solution of Equation (3.18) corresponds to a root finding problem, which is conveniently carried out using an iterative method, such as, for example, Newton's method. To this end, first the solution increment $\Delta \mathbf{y}^{i+1} := \mathbf{y}^{i+1} - \mathbf{y}^i$ is introduced, where \mathbf{y}^i denotes the approximate solution of the i -th iteration step. The approximate solution of iteration step $i+1$ is then obtained by subsequently solving a linear system of equations for the solution increment, followed by an update of the approximate solution, i. e.,

$$\mathbf{J}^i \Delta \mathbf{y}^{i+1} = -\mathbf{k}(\mathbf{y}^i), \quad \text{and} \quad \mathbf{y}^{i+1} = \mathbf{y}^i + \Delta \mathbf{y}^{i+1}. \quad (3.19)$$

Therein, \mathbf{J}^i denotes the Jacobian matrix of the $i+1$ -st iteration step, which is given by

$$\mathbf{J}^i = \left. \frac{\partial \mathbf{k}(\mathbf{y})}{\partial \mathbf{y}} \right|_{\mathbf{y}=\mathbf{y}^i}. \quad (3.20)$$

For Newton's method the computation of the Jacobian matrix and the steps in (3.19) have to be repeated until a certain tolerance is met. A simplified version of Newton's method is obtained when the Jacobian matrix is not computed in every iteration, but a computed Jacobian matrix is reused in a number of subsequent iteration steps.

To solve the linear system of equations (3.19)₁ for the respective solution increment, the Jacobian matrix is commonly not inverted but an appropriate (direct or iterative) solver is employed. Typical direct solvers are the LU decomposition, the Cholesky decomposition for symmetric positive definite matrices, or some special method for sparse matrices, which arise, for example, from the FEM. For larger systems, iterative methods are commonly more efficient. Typical iterative solvers are, for example, the Jacobi method, the Gauß-Seidel method, Krylov subspace methods such as the conjugate gradient (CG) method or the generalised minimal residual (GMRES) method, or multigrid methods. The interested reader is referred to Press [210] for details.

3.4 Continuum-Mechanical Fundamentals

Continuum mechanics provides a convenient and flexible framework for modelling and simulating the deformation behaviour of a mechanical body as well as the stress and strain distributions that occur within such a body if it is subjected to a load. Being derived from general balance relations, continuum mechanics can be applied to many different problems. Among the numerous applications in the field of biomechanics, skeletal muscle modelling is just one example. Due to the fact that the physiological working range of many muscles involves changes in length of 50% and more [32], a continuum-mechanical skeletal muscle model must be based on the theory of finite deformations. Therefore, a brief introduction to finite-deformation continuum mechanics is provided in the following. For more details, the interested reader is referred to Bonet & Wood [23], Gurtin [96], Holzapfel [121], Truesdell & Noll [263], among many others.

3.4.1 Kinematic Relations

This section presents the kinematic relations required to describe the nonlinear deformation of a body \mathcal{B} , which is defined as the connected manifold of material points \mathcal{P} .

Motion of a Body

In continuum mechanics, the motion or placement function χ assigns a material point with position \mathbf{X} in the reference (undeformed) configuration at time t_0 to a position in the actual (deformed) configuration \mathbf{x} at time t , cf. Figure 3.1, i. e.,

$$\mathbf{x} = \chi(\mathbf{X}, t). \quad (3.21)$$

The displacement vector, \mathbf{u} , is given by the difference of the position of a material point in the actual configuration and its position in the reference configuration, i. e., $\mathbf{u} = \mathbf{x} - \mathbf{X}$. The first and second material time derivatives of the placement function are the velocity and the acceleration fields, $\dot{\mathbf{x}}$ and $\ddot{\mathbf{x}}$, respectively, which are given by

$$\dot{\mathbf{x}} = \frac{d\chi(\mathbf{X}, t)}{dt}, \quad \text{and} \quad \ddot{\mathbf{x}} = \frac{d^2\chi(\mathbf{X}, t)}{dt^2}. \quad (3.22)$$

It is important to note that any physical quantity can be defined in the Lagrangean

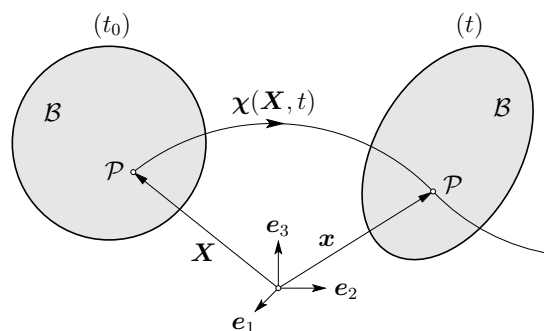


Figure 3.1: Motion of a mechanical body.

and in the Eulerian framework. In the Lagrangean framework, the physical quantities are expressed with respect to the referential coordinates, while in the Eulerian setting, the physical quantities are defined with respect to the spatial (actual) coordinates. The possibility to express quantities in the Eulerian representation requires the existence of the inverse of the placement function. The unique placement function can be uniquely inverted if the Jacobian, J , does not vanish. This yields the following relation

$$\mathbf{X} = \boldsymbol{\chi}^{-1}(\mathbf{x}, t) \quad \text{if} \quad J := \det \frac{\partial \boldsymbol{\chi}}{\partial \mathbf{X}} \neq 0, \quad (3.23)$$

where $\det(\cdot)$ denotes the determinant operator. Following the Lagrangean setting, which is commonly used in solid mechanics, the material time derivatives in (3.22) are equal to their partial time derivatives. In contrast, in the Eulerian framework, which is often conveniently used for fluid-mechanical problems, the material time derivatives in Equation (3.22) contain, in addition to the local time derivative, a convection term that arises due to the fact that the derived function also implicitly depends on the time through the spatial coordinates, which themselves are functions of time, i. e., $\mathbf{x} = \boldsymbol{\chi}(\mathbf{X}, t)$. In detail, the material time derivatives of a scalar-valued function $\Psi(\mathbf{x}, t)$ and a vector-valued function $\boldsymbol{\Psi}(\mathbf{x}, t)$ in the Eulerian framework are given by

$$\dot{\Psi}(\mathbf{x}, t) = \frac{\partial \Psi}{\partial t} + \text{grad } \Psi \cdot \dot{\mathbf{x}}, \quad \text{and} \quad \dot{\boldsymbol{\Psi}}(\mathbf{x}, t) = \frac{\partial \boldsymbol{\Psi}}{\partial t} + (\text{grad } \boldsymbol{\Psi}) \dot{\mathbf{x}}. \quad (3.24)$$

Herein, the gradient operator $\text{grad}(\cdot) = \partial(\cdot)/\partial \mathbf{x}$ denotes the derivative with respect to the spatial variables, whereas $\text{Grad}(\cdot) = \partial(\cdot)/\partial \mathbf{X}$ denotes the derivative with respect to the referential coordinates. Moreover, the dot in (3.24)₁, $(\cdot) \cdot (\cdot)$ indicates a scalar product. Note that in the mathematical sense, the material time derivative equals the total time derivative.

As common in solid mechanics, the Lagrangean description is conveniently used in the following. Thus, the (material) deformation gradient tensor \mathbf{F} is defined as the derivative of the placement function with respect to the material coordinates, i. e.,

$$\mathbf{F} := \frac{\partial \boldsymbol{\chi}(\mathbf{X}, t)}{\partial \mathbf{X}} = \frac{\partial \mathbf{x}(\mathbf{X}, t)}{\partial \mathbf{X}} = \text{Grad } \mathbf{x}(\mathbf{X}, t). \quad (3.25)$$

In the undeformed reference configuration at time t_0 with $\mathbf{X} = \boldsymbol{\chi}(\mathbf{X}, t_0)$, the deformation gradient equals the second-order identity tensor, i. e., $\mathbf{F}(t_0) = \mathbf{I}$ with $\det \mathbf{F}(t_0) = 1$. This and the fact that physically meaningful deformations prohibit the compaction of the material body to a single mathematical point ($\det \mathbf{F} = 0$, cf. also Equation (3.23)), require that a continuous deformation process satisfies

$$J = \det \mathbf{F} > 0. \quad (3.26)$$

Based on this result, one can conclude that the inverse of the deformation gradient exists, which is given by

$$\mathbf{F}^{-1} = \frac{\partial \boldsymbol{\chi}^{-1}(\mathbf{x}, t)}{\partial \mathbf{x}} = \frac{\partial \mathbf{X}}{\partial \mathbf{x}} = \text{grad } \mathbf{X}. \quad (3.27)$$

It follows directly from its definition that the deformation gradient tensor is a dimensionless quantity.

Acting as basic kinematic quantity, the deformation gradient plays a key role in finite-deformation continuum mechanics. This becomes more clear when the transport theorems for differential line, area, and volume elements are considered, which are given by

$$d\mathbf{x} = \mathbf{F} d\mathbf{X}, \quad d\mathbf{a} = (\text{cof } \mathbf{F}) d\mathbf{A}, \quad dv = (\det \mathbf{F}) dV. \quad (3.28)$$

Thus, the deformation gradient itself maps referential line elements $d\mathbf{X}$ to actual line elements $d\mathbf{x}$, its cofactor $\text{cof } \mathbf{F} := (\det \mathbf{F}) \mathbf{F}^{T-1}$ transports referential area elements $d\mathbf{A}$ to area elements of the actual configuration $d\mathbf{a}$, and its determinant relates volume elements of the reference configuration dV to volume elements of the actual configuration dv . Note that area elements are defined as vector-valued quantities using the normal vector \mathbf{n} , i. e., $d\mathbf{a} = \mathbf{n}(\mathbf{x}, t) da$ and $d\mathbf{A} = \mathbf{n}_0(\mathbf{X}, t) dA$, where, in general, the normal vectors in the reference and actual configurations do not coincide, i. e., $\mathbf{n}(\mathbf{x}, t) \neq \mathbf{n}_0(\mathbf{X}, t)$. In fact, a relation between the normal vectors of the reference and actual configurations known as Nanson's formula results from Equation (3.28)₂ and is given by $\mathbf{n}(\mathbf{x}, t) da = J \mathbf{F}^{T-1} \mathbf{n}_0(\mathbf{X}, t) dA$.

Deformation and Strain Measures

To characterise the deformations and strains in a body, it is convenient to derive suitable deformation and strain measures from the deformation gradient. To this end, first a unique polar decomposition of the deformation gradient is introduced, namely

$$\mathbf{F} = \mathbf{R} \mathbf{U} = \mathbf{V} \mathbf{R}, \quad (3.29)$$

where \mathbf{R} denotes the rotation tensor, and \mathbf{U} and \mathbf{V} are the right (or material) and left (or spatial) stretch tensors, respectively. Note that the rotation tensor is a proper orthogonal tensor with $\mathbf{R}^T \mathbf{R} = \mathbf{R} \mathbf{R}^T = \mathbf{I}$ and $\det \mathbf{R} = 1$, and the stretch tensors $\mathbf{K} \in \{\mathbf{U}, \mathbf{V}\}$ are symmetric, positive-definite tensors, i. e., $\mathbf{K} = \mathbf{K}^T$ and $\mathbf{a}^T \mathbf{K} \mathbf{a} > 0$ for any non-zero vector \mathbf{a} . Based on the polar decomposition (3.29), the right and left Cauchy-Green deformation tensors, \mathbf{C} and \mathbf{B} , respectively, are introduced according to

$$\mathbf{C} := \mathbf{F}^T \mathbf{F} = \mathbf{U}^T \mathbf{R}^T \mathbf{R} \mathbf{U} = \mathbf{U} \mathbf{U}, \quad \mathbf{B} := \mathbf{F} \mathbf{F}^T = \mathbf{V} \mathbf{R} \mathbf{R}^T \mathbf{V}^T = \mathbf{V} \mathbf{V}. \quad (3.30)$$

The meaning of the right and left Cauchy-Green deformation tensors is most easily appreciated when expressing the square of line elements of the actual configuration by referential line elements and vice versa, i. e.,

$$\begin{aligned} d\mathbf{x} \cdot d\mathbf{x} &= (\mathbf{F} d\mathbf{X}) \cdot (\mathbf{F} d\mathbf{X}) = d\mathbf{X} \cdot \mathbf{F}^T \mathbf{F} d\mathbf{X} = d\mathbf{X} \cdot \mathbf{C} d\mathbf{X}, \\ d\mathbf{X} \cdot d\mathbf{X} &= (\mathbf{F}^{-1} d\mathbf{x}) \cdot (\mathbf{F}^{-1} d\mathbf{x}) = d\mathbf{x} \cdot \mathbf{F}^{T-1} \mathbf{F}^{-1} d\mathbf{x} = d\mathbf{x} \cdot \mathbf{B}^{-1} d\mathbf{x}. \end{aligned} \quad (3.31)$$

Mapping referential line elements to actual line elements, the deformation gradient must be a two-field tensor with its first basis in the actual and its second basis in the reference configuration. Furthermore, the first basis of the deformation gradient tensor is covariant, while its second basis is contravariant. Covariant and contravariant basis vectors as well as covariant and contravariant transport operations (push-forward and pull-back operations between the reference and the actual configurations for covariant and contravariant vectors and tensors) are briefly described in Appendix A.1, and more comprehensively discussed

in Markert [162]. From the square of line elements (3.31), one can further conclude that the right, contravariant and left, covariant Cauchy-Green deformation tensors are entirely defined in the reference configuration and in the actual configuration, respectively. Moreover, using the definitions of the right and left Cauchy-Green deformation tensors (3.30), one can see that the right and left stretch tensors are also single field tensors, where \mathbf{U} (such as \mathbf{C}) is entirely defined in the reference configuration, and \mathbf{V} (such as \mathbf{B}) is entirely defined in the actual configuration. Since the right and left stretch tensors are single field tensors, the polar decomposition (3.29) reveals that the rotation tensor is a two-field tensor such as the deformation gradient, which transports vectors from the reference configuration to the actual configuration.

Based on these results, it is interesting to further investigate the transport theorem for differential line elements. To this end, the polar decompositions (3.29) are inserted into Equation (3.28)₁ to give

$$d\mathbf{x} = \mathbf{R}(\mathbf{U} d\mathbf{X}) = \mathbf{V}(\mathbf{R} d\mathbf{X}). \quad (3.32)$$

The first part of Equation (3.32) can be interpreted as a stretch of the line element in the reference configuration, followed by a rotation of the stretched line element to the actual configuration. Further, the second part of Equation (3.32) denotes a rotation of the line element from the reference configuration to the actual configuration, followed by a stretch that is carried out in the actual configuration.

Furthermore, relations between the right and left deformation and stretch tensors can be followed from Equations (3.29) and (3.30), such that

$$\begin{aligned} \mathbf{U} &= \mathbf{R}^T \mathbf{V} \mathbf{R}, & \mathbf{V} &= \mathbf{R} \mathbf{U} \mathbf{R}^T, \\ \mathbf{C} &= \mathbf{R}^T \mathbf{B} \mathbf{R}, & \mathbf{B} &= \mathbf{R} \mathbf{C} \mathbf{R}^T. \end{aligned} \quad (3.33)$$

It is noteworthy that the different deformation and stretch tensors are not related to each other through the push-forward and pull-back operations of (A.6) and (A.7) of Appendix A.1, but through the rotation tensor. In fact, both the contravariant push-forward of the right Cauchy-Green deformation tensor as well as the covariant pull-back of the left Cauchy-Green deformation tensor yield the second-order identity tensor.

Equations (3.31) reveal that the deformation measures characterise the squares of line elements. Thus, it is convenient to introduce strain measures relating the squares of line elements of the actual configuration to the squares of line elements of the reference configuration, i. e.,

$$\begin{aligned} d\mathbf{x} \cdot d\mathbf{x} - d\mathbf{X} \cdot d\mathbf{X} &= \\ &= \begin{cases} d\mathbf{X} \cdot \mathbf{C} d\mathbf{X} - d\mathbf{X} \cdot d\mathbf{X} = d\mathbf{X} \cdot (\mathbf{C} - \mathbf{I}) d\mathbf{X} =: d\mathbf{X} \cdot 2\mathbf{E} d\mathbf{X}, \\ d\mathbf{x} \cdot d\mathbf{x} - d\mathbf{x} \cdot \mathbf{B}^{-1} d\mathbf{x} = d\mathbf{x} \cdot (\mathbf{I} - \mathbf{B}^{-1}) d\mathbf{x} =: d\mathbf{x} \cdot 2\mathbf{A} d\mathbf{x}. \end{cases} \end{aligned} \quad (3.34)$$

Therein, \mathbf{E} and \mathbf{A} are the Green-Lagrangean and the Almansian strain tensors, respectively. It follows directly from their definitions

$$\mathbf{E} = \frac{1}{2}(\mathbf{C} - \mathbf{I}), \quad \text{and} \quad \mathbf{A} = \frac{1}{2}(\mathbf{I} - \mathbf{B}^{-1}), \quad (3.35)$$

that the Green-Lagrangean strain tensor describes strains in the reference configuration, while the Almansian strain tensor is defined in the actual configuration. Furthermore, both presented strain tensors are contravariant, and hence, are related to each other through the contravariant transport operations in (A.7) of Appendix A.1. Moreover, as can be directly followed from their definitions, all presented deformation and strain measures are dimensionless quantities. Besides the Green-Lagrangean and the Almansian strains, further strain measures can be defined, cf. Truesdell & Noll [263]. These, however, are not required in the present work.

3.4.2 Stress Measures

Strains can be interpreted as a relative movement of neighbouring material particles of a continuous body, while stresses can be understood as internal forces that these neighbouring particles exert on each other. Stresses and strains are related to each other since a strain in the body induces a stress, and vice versa. The relation between stress and strain can, for example, be observed when compressing elastically a linear spring. The spring reacts to the applied deformation by exerting a resistance to the deformation that is proportional to the applied deformation. The resistance to the deformation and the deformation itself can be measured by means of stresses and strains, respectively. Since stresses are defined as forces per area, their physical dimension is force per unit area.

The concept of a stress tensor goes back to Cauchy, who introduced his lemma and theorem in 1823. Cauchy's lemma states that the traction vectors at a material point on different sides of a surface, which notionally divides the material body into two pieces, have the same value but opposite directions, i. e.,

$$\mathbf{t}(\mathbf{x}, t, \mathbf{n}) = -\mathbf{t}(\mathbf{x}, t, -\mathbf{n}), \quad (3.36)$$

where \mathbf{t} is the traction vector and \mathbf{n} denotes the outward-oriented normal vector of the actual configuration. The surface traction vector is not a usual field function since it depends in addition to position and time on the orientation of the normal vector. In order to replace the traction vector by a more convenient quantity, i. e., a proper field function, Cauchy introduced his theorem, which reads

$$\mathbf{t}(\mathbf{x}, t, \mathbf{n}) = \mathbf{T}(\mathbf{x}, t) \mathbf{n}(\mathbf{x}, t), \quad (3.37)$$

where \mathbf{T} denotes the Cauchy stress tensor. Due to the fact that the Cauchy stress relates incremental surface force elements $d\mathbf{k}_S$ of the actual configuration to actual area elements, i. e.,

$$d\mathbf{k}_S = \mathbf{t} da = \mathbf{T} \mathbf{n} da = \mathbf{T} d\mathbf{a}, \quad (3.38)$$

the Cauchy stress is also called true stress and is obviously a quantity of the actual configuration.

Two further stress measures, namely the Kirchhoff (or weighted) stress and the 1st Piola-Kirchhoff (or nominal or engineering) stress, can be introduced by applying the transport theorem for area elements (3.28)₂ to relate the actual area element to its referential counterpart, i. e.,

$$d\mathbf{k}_S = \mathbf{T} d\mathbf{a} = \mathbf{T} (\text{cof } \mathbf{F}) d\mathbf{A} = \mathbf{T} (\det \mathbf{F}) \mathbf{F}^{T-1} d\mathbf{A} = \boldsymbol{\tau} \mathbf{F}^{T-1} d\mathbf{A} = \mathbf{P} d\mathbf{A}. \quad (3.39)$$

While the Kirchhoff stress tensor $\boldsymbol{\tau}(\boldsymbol{x}, t) := (\det \boldsymbol{F}) \boldsymbol{T}$ is completely defined in the actual configuration, the 1st Piola-Kirchhoff stress $\boldsymbol{P}(\boldsymbol{x}, t) := (\det \boldsymbol{F}) \boldsymbol{T} \boldsymbol{F}^{T-1}$ is a two-field tensor, in which the second basis was pulled-back to the reference configuration by a covariant transport. Thus, the 1st Piola-Kirchhoff stress relates an actual force element to a referential area element.

The interpretation of the 1st Piola-Kirchhoff stress as a partial pull-back of the Kirchhoff stress tensor inspires the definition of the 2nd Piola-Kirchhoff stress. Thus, the 2nd Piola-Kirchhoff (or reference) stress is obtained by also pulling the first basis of the Kirchhoff stress to the reference configuration using a covariant transport, i. e.,

$$\boldsymbol{S}(\boldsymbol{X}, t) := \boldsymbol{F}^{-1} \boldsymbol{\tau} \boldsymbol{F}^{T-1} = \boldsymbol{F}^{-1} \boldsymbol{P} = (\det \boldsymbol{F}) \boldsymbol{F}^{-1} \boldsymbol{T} \boldsymbol{F}^{T-1}. \quad (3.40)$$

Obviously, the 2nd Piola-Kirchhoff stress is entirely defined in the reference configuration, and, similar to the Kirchhoff stress, it has no direct physical interpretation. From Equation (3.40) one can follow that the Kirchhoff and the 2nd Piola-Kirchhoff stresses are related to each other through covariant push-forward and pull-back operations for second-order tensors. Indeed, all of the presented stresses are covariant. It is furthermore noteworthy that if the Cauchy stress is symmetric, the Kirchhoff and the 2nd Piola-Kirchhoff stresses are also symmetric, while the 1st Piola-Kirchhoff stress is not. Further stress measures can be defined, which are, however, not relevant in this work.

The introduction of stress and strain measures of the reference and actual configurations inspires the concept of conjugate variables. To this end, scalar products between (covariant) stresses and (contravariant) strains of the same configuration are computed according to

$$\boldsymbol{S} \cdot \boldsymbol{E} = (\boldsymbol{F}^{-1} \boldsymbol{F}) \boldsymbol{S} \cdot \boldsymbol{E} (\boldsymbol{F}^{-1} \boldsymbol{F}) = (\boldsymbol{F} \boldsymbol{S} \boldsymbol{F}^T) \cdot (\boldsymbol{F}^{T-1} \boldsymbol{E} \boldsymbol{F}^{-1}) = \boldsymbol{\tau} \cdot \boldsymbol{A}, \quad (3.41)$$

yielding the conjugate pair of the reference configuration, $\{\boldsymbol{S}, \boldsymbol{E}\}$, and the conjugate pair of the actual configuration, $\{\boldsymbol{\tau}, \boldsymbol{A}\}$.

3.4.3 Balance Relations

Being based on physical observations, the balance relations are axiomatically introduced within a continuum-mechanical framework. For a mechanical body \mathcal{B} the balance relations combine information given for the body (e. g. motion or deformation) with influences originating from outside the body (e. g. contact or gravitational forces).

In general, the balance relations are introduced as an equation for the entire mechanical body in a global sense. However, in continuum mechanics, one is particularly interested in local relations that are valid for each material point of the mechanical body. To this end, local balance relations valid for the material point are deduced from their global counterparts. Moreover, the balance relations can either be formulated in the reference configuration or in the actual configuration – the latter are presented in this section.

In general, mechanical and thermodynamical balance relations can be introduced. The mechanical balance relations are the balance of mass, the balance of momentum, and the balance of angular momentum. The thermodynamical balance relations are the balance of energy and the balance of entropy. The balance of energy is an important relation when taking into account temperature effects, which are not considered in this work. Further,

the balance of entropy in conjunction with the second law of thermodynamics, which states that the entropy production in a closed system can never be negative, are used to formulate thermodynamic-sound constitutive equations. Similar to Hill-type muscle models, this work assumes a priori a superposition of the active and passive stress contributions. Further, neglecting viscous effects, the passive behaviour of the muscle tissue is modelled as an hyperelastic material. For hyperelastic materials, the result of the evaluation of the second law of thermodynamics is well known. Following this, instead of explicitly introducing the thermodynamical balance relations, their results are directly adopted in this work.

Balance of Mass

The balance of mass states that, in a closed system, the mass of a body does not change in time. This directly yields the global form of the balance of mass

$$\frac{d}{dt} \int_{\mathcal{B}} \rho \, dv = 0, \quad (3.42)$$

where ρ denotes the (mass) density. To derive the local form of the balance of mass, first, the time derivative is carried out, whereby one has to keep in mind that the actual volume element depends on the time. Inserting the time derivative of the volume element, $(dv)' = (\operatorname{div} \dot{\mathbf{x}}) dv$, and dropping the integral yields the local form of the mass balance,

$$\dot{\rho} + \rho \operatorname{div} \dot{\mathbf{x}} = 0. \quad (3.43)$$

Balance of Momentum

The balance of momentum states that the change in time of the momentum of the body equals the sum of the forces acting on the mechanical body at the vicinity and from the distance. In terms of mathematics, this yields the global momentum balance

$$\frac{d}{dt} \int_{\mathcal{B}} \rho \dot{\mathbf{x}} \, dv = \int_{\partial \mathcal{B}} \mathbf{T} \mathbf{n} \, da + \int_{\mathcal{B}} \rho \mathbf{b} \, dv. \quad (3.44)$$

Therein, $\rho \mathbf{b}$ denotes the supply term, which is usually the volume-specific gravitational force. To derive the local form of the momentum balance, one first carries out the time derivative on the left-hand side of (3.44). To simplify the result, the time derivative of the volume element and the local mass balance (3.43) are used. Next, the divergence theorem (or Gauß's theorem) is applied to transform the surface integral into a volume integral. Finally, the integration can be dropped. This yields the local balance of momentum

$$\rho \ddot{\mathbf{x}} = \operatorname{div} \mathbf{T} + \rho \mathbf{b}. \quad (3.45)$$

Equation (3.45), also known as Cauchy's first law of motion, is the most important relation in continuum mechanics.

Balance of Angular Momentum

Within the balance of angular momentum (moment of momentum), the change in time of the body's angular momentum is balanced with the moments acting on the body evoked by internal and external forces with respect to the same arbitrary reference point. This yields the global balance of angular momentum

$$\frac{d}{dt} \int_{\mathcal{B}} (\mathbf{x} \times \rho \dot{\mathbf{x}}) dv = \int_{\partial \mathcal{B}} (\mathbf{x} \times \mathbf{T}) \mathbf{n} da + \int_{\mathcal{B}} (\mathbf{x} \times \rho \mathbf{b}) dv. \quad (3.46)$$

Following the same procedure as before and inserting the local forms of the mass and momentum balances, (3.43) and (3.45), respectively, Equation (3.46) yields the local form of the balance of angular momentum (Cauchy's second law of motion), viz.

$$\mathbf{o} = \mathbf{I} \times \mathbf{T}. \quad (3.47)$$

Using the definition of the axial vector, $\overset{A}{\mathbf{t}} := \frac{1}{2} \overset{3}{\mathbf{E}} \mathbf{T}^T = \frac{1}{2} \mathbf{I} \times \mathbf{T}$, where $\overset{3}{\mathbf{E}}$ denotes the third-order Ricci tensor, the local balance of angular momentum (3.47) yields the symmetry of the Cauchy stress tensor

$$\mathbf{T} = \mathbf{T}^T. \quad (3.48)$$

Note that, according to Section 3.4.2, the symmetry of the Cauchy stress implies the symmetries of the Kirchhoff and 2nd Piola-Kirchhoff stresses.

4 Biophysical Cell Modelling of the Neuromuscular System

The aim of this chapter is to establish a novel model of the neuromuscular system that is biophysical in all main parts. To this end, a biophysical model of the motor neuron pool is coupled to a biophysical model of the muscle units.

An important property of neurons and muscle cells alike is the electrical excitability of their cell membrane, cf. Section 2.3. Biophysical models of cellular membrane dynamics that describe the flow of ions crossing the sarcolemma are often based on the Hodgkin-Huxley formalism. Therefore, this chapter presents the classical Hodgkin-Huxley model in Section 4.1. An extension of this description to a two-compartment model is presented in Section 4.2 by reviewing the model of a motor neuron pool of Negro & Farina [186].

Section 4.3 describes the model of the excitation-contraction coupling in skeletal muscle fibres of Shorten et al. [240] and its extension to non-isometric contractions. Further, the model of Shorten et al. [240] is extended to a description of the motor units of a muscle. To simulate the entire neuromuscular system, Section 4.4 couples the resulting model of the muscle units to the model of the MN pool of Negro & Farina [186]. Representative simulations demonstrate the capacity of the integrated model.

4.1 The Hodgkin-Huxley Model of the Membrane Electrophysiology

In a series of papers published in 1952, Hodgkin and Huxley investigate the flow of electric current through the cell membrane of the giant axon of a squid. They were awarded the Nobel Prize in Physiology or Medicine in 1963 for their discovery of the ionic mechanisms in the cell membrane during an action potential. In a summary paper [120], the authors develop a mathematical description of the membrane behaviour based on their experimental results. Their key idea was to model the membrane of electrically excitable cells as an electrical circuit and to represent currents flowing through a large population of ion channels based on voltage-dependent gating properties [187]. The form of this description has been used as the basis for almost all other ionic current models of excitable tissues. The Hodgkin-Huxley model is briefly presented here, as it builds the foundation for the MN model and the model of the skeletal muscle membrane used in this work.

Cell membranes are selectively permeable to (charged) ions, and consequently they are able to separate electrical charges. In the context of modelling, this can be represented by assigning a capacitance to the cell membrane. The law of capacitance states that the electric charge of a capacitor equals the voltage difference across the capacitor times its capacitance. Taking the time derivative of the law of capacitance, the membrane capacitance, C_m , times the temporal change of the membrane potential, V_m , equals the

(negative) sum of the ionic currents crossing the membrane, I_{ion} :

$$I_m = C_m \frac{\partial V_m}{\partial t} + I_{ion} = 0, \quad (4.1)$$

where I_m denotes the total current flow across the cell membrane. The Hodgkin-Huxley model considers currents through sodium and potassium channels, I_{Na} and I_K , respectively, and a leakage current I_L representing the natural permeability of the membrane to, for example, Cl^- ions. Further, a current I_{stim} is considered that allows to stimulate the model from outside:

$$I_{ion} = I_{Na} + I_K + I_L - I_{stim}. \quad (4.2)$$

Note that, by convention, a positive sign indicates an outward current with the exception of I_{stim} , where a positive sign indicates an inward current. Based on Ohm's law, the membrane current of a given ion type i , with $i \in \{Na, K, L\}$, is proportional to the membrane's conductance for this ion species and to a driving force in the form of the difference between the membrane potential and the ion's equilibrium potential, E_i :

$$I_i = g_i (V_m - E_i), \quad (4.3)$$

where g_i denotes the conductance per unit area for ion species i and is the inverse of the resistance. While the leakage conductance, g_L , is assumed to be constant, the conductances for the potassium and sodium channels depend on the membrane potential:

$$g_K = \bar{g}_K n^4, \quad g_{Na} = \bar{g}_{Na} m^3 h. \quad (4.4)$$

Therein, \bar{g}_K and \bar{g}_{Na} denote the maximum values of the respective conductances, and n , m , and h are gating variables resembling probabilities associated with the potassium channel activation, sodium channel activation, and sodium channel inactivation, respectively [120]. The evolution equations of the gating variables are based on first-order kinetics and can either be expressed using relaxation time constants (cf. [120]), or take the form

$$\frac{\partial \omega}{\partial t} = \alpha_\omega(V_m) (1 - \omega) - \beta_\omega(V_m) \omega, \quad (4.5)$$

for $\omega \in \{n, m, h\}$. The dependence of the forward and backward reaction rates $\eta_\omega \in \{\alpha_\omega(V_m), \beta_\omega(V_m)\}$, respectively, on the membrane voltage can be generalised using the form

$$\eta_\omega = \frac{a_\omega + b_\omega V_m}{c_\omega + d_\omega \exp\left(\frac{V_m + e_\omega}{f_\omega}\right)}, \quad (4.6)$$

with constants a_ω , b_ω , c_ω , d_ω , e_ω , and f_ω [187]. For the sake of brevity, further details are omitted here but can be found, for example, in [120, 187]. Figure 4.1a shows the electrical circuit used in the Hodgkin-Huxley model to represent the cell membrane. Furthermore, parameters for the Hodgkin-Huxley model are summarised in Table 4.1.

In Figure 4.1b the Hodgkin-Huxley model is used to simulate a train of APs at a discharge rate of 50 Hz. For this simulation, a stimulating current of $I_{stim} = 20 \mu\text{A}/\text{cm}^2$ is applied for 0.5 ms at times $t = 0, 20, \dots, 80$ ms. Initial conditions are listed in Table 4.2.

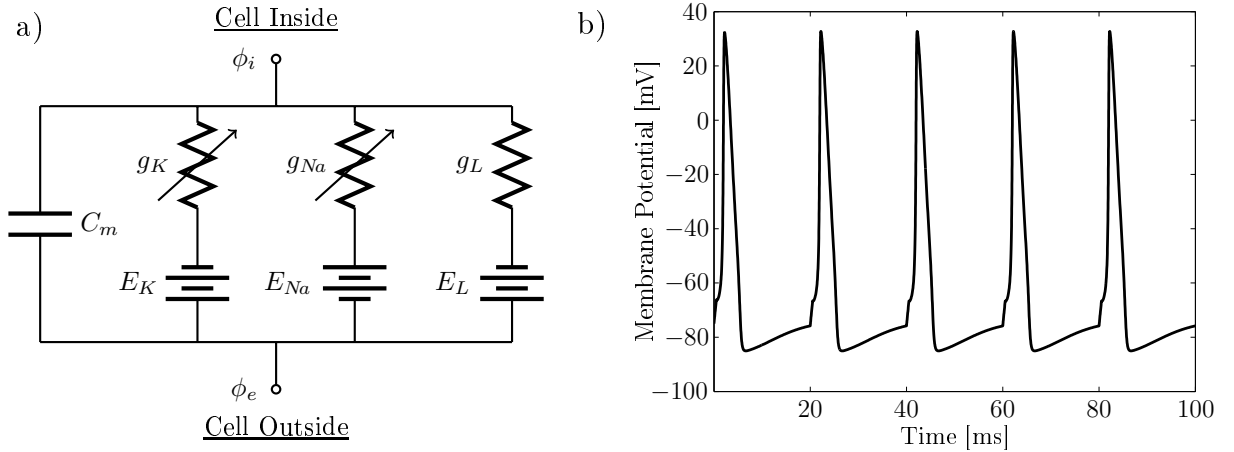


Figure 4.1: Hodgkin-Huxley model. (a) Electrical circuit equivalent to the model. Resistors with an arrow indicate voltage-dependent conductances. The membrane potential, V_m , equals the difference between the intracellular potential, ϕ_i , and the extracellular potential, ϕ_e . The driving forces in the model are the differences between the membrane potential and the corresponding equilibrium potentials, which are represented by batteries. (b) Simulated train of APs due to external stimuli at $t = 0, 20, 40, 60, 80$ ms.

C_m	\bar{g}_{Na}	\bar{g}_K	\bar{g}_L	E_{Na}	E_K	E_L
$1.0 \mu\text{F}/\text{cm}^2$	$120.0 \text{ mS}/\text{cm}^2$	$36.0 \text{ mS}/\text{cm}^2$	$0.3 \text{ mS}/\text{cm}^2$	40.0 mV	-87.0 mV	-64.387 mV

Table 4.1: Parameters for the Hodgkin-Huxley model.

V_m	n	m	h
-75.0 mV	$0.325 [-]$	$0.05 [-]$	$0.6 [-]$

Table 4.2: Initial conditions for the Hodgkin-Huxley model.

The Hodgkin-Huxley model can also be driven by applying a lower, long-lasting stimulation current. For example, an output discharge rate of approximately 50 Hz as in Figure 4.1b, can be achieved by constantly applying $I_{stim} = 4.1 \mu\text{A}/\text{cm}^2$ to the MN model. This type of stimulation is more realistic, as MNs receive permanently synaptic input of varying intensity from different sources. This is commonly simulated by superimposing a mean input current with noisy signals representing, for example, synaptic noise, cf. Section 4.2.3.

Hodgkin-Huxley-type models are commonly formulated as systems of nonlinear ODEs for V_m and the gating variables m , n , and h , cf. Equations (4.1) and (4.5), respectively. Making use of the abstract representation for ODEs (3.8), $\mathbf{y} = [V_m, m, n, h]^T \in \mathbb{R}^4$. The model of Hodgkin & Huxley [120] consists of a single compartment and considers ionic currents for sodium and potassium as well as a leakage current. Based on the same formalism, more detailed models have been proposed in the literature. These models typically distinguish more ionic currents, and/or subdivide the modelled membrane into multiple compartments, which are coupled to each other, see e.g. [2, 232, 272]. Further information on the Hodgkin-Huxley model and its variants can be found, for example, in Nelson [187], Noble [194], and in a critical review of Meunier & Segev [172].

4.2 Modelling Motor Neurons and the Motor Neuron Pool

Based on the Hodgkin-Huxley formalism, Cisi & Kohn [39] proposed a compartmental model for the simulation of spinal cord MNs. The number of simulated compartments for each MN is limited to two in order to balance the biological realism and the computational load [39]. In detail, the dendrites are lumped together in one compartment. The second compartment represents the soma. Somatic APs are assumed to propagate along the axon, which is not modelled explicitly, and are transferred to the muscle fibres at the neuromuscular junctions. To be able to solve Equation (4.5) analytically, Cisi & Kohn [39] approximate the time courses of the reaction rates (4.6) by rectangular pulses. Negro & Farina [186] discard this approximation and solve the ODEs for the gating variables (4.5) using functions of the form (4.6) provided by Traub & Miles [262]. This model of Negro & Farina [186] and its parametrisation are adopted in this work for the simulation of spinal cord MNs.

4.2.1 Mathematical Description of the Motor Neuron Model

The MN model of Cisi & Kohn [39] distinguishes the membrane potential in the dendrites and in the soma, $V_m^d(t)$ and $V_m^s(t)$, respectively, given by

$$C_m^d \frac{\partial V_m^d}{\partial t} = -I_{ion}^d(V_m^d) - I_C^d(V_m^d, V_m^s), \quad C_m^s \frac{\partial V_m^s}{\partial t} = -I_{ion}^s(V_m^s) - I_C^s(V_m^d, V_m^s). \quad (4.7)$$

The two equations are linked to each other through coupling currents I_C^d and I_C^s , where $I_C^s = -I_C^d$ due to the conservation of electric charge. Further, in Equation (4.7), I_{ion}^d and I_{ion}^s are the ionic currents crossing the membrane of the dendrites and the soma, respectively. For the dendrites only a leakage current I_L^d is considered, while for the soma a leakage current I_L^s , a sodium current I_{Na} , a fast and a slow potassium current, I_{Kf} and I_{Ks} , respectively, and an external current I_{stim} are considered:

$$I_{ion}^d = I_L^d, \quad I_{ion}^s = I_L^s + I_{Na} + I_{Kf} + I_{Ks} - I_{stim}. \quad (4.8)$$

Cisi & Kohn [39] reduced the number of ionic currents to a minimum that still enabled the reproduction of a reasonably large set of neuronal properties. The slow potassium current, for example, has been included to incorporate the afterhyperpolarisation, which impedes the generation of subsequent APs, cf. Section 2.3.2. The electrical circuit corresponding to the MN model of Cisi & Kohn [39] is depicted in Figure 4.2.

Similar to the approach of Hodgkin & Huxley [120], the description of the ionic currents is based on Ohm's law, i. e., the currents equal a conductance times a potential difference, i. e.,

$$\begin{aligned} I_L^d &= g_L^d (V_m^d - E_L), & I_L^s &= g_L^s (V_m^s - E_L), \\ I_C^d &= g_C (V_m^d - V_m^s), & I_{Na} &= g_{Na} (V_m^s - E_{Na}), \\ I_{Kf} &= g_{Kf} (V_m^s - E_K), & I_{Ks} &= g_{Ks} (V_m^s - E_K). \end{aligned} \quad (4.9)$$

Therein, E_L , E_{Na} , and E_K are the equilibrium (or Nernst) potentials, g_C denotes the (constant) coupling conductance, g_L^d and g_L^s are the (constant) dendritic and somatic

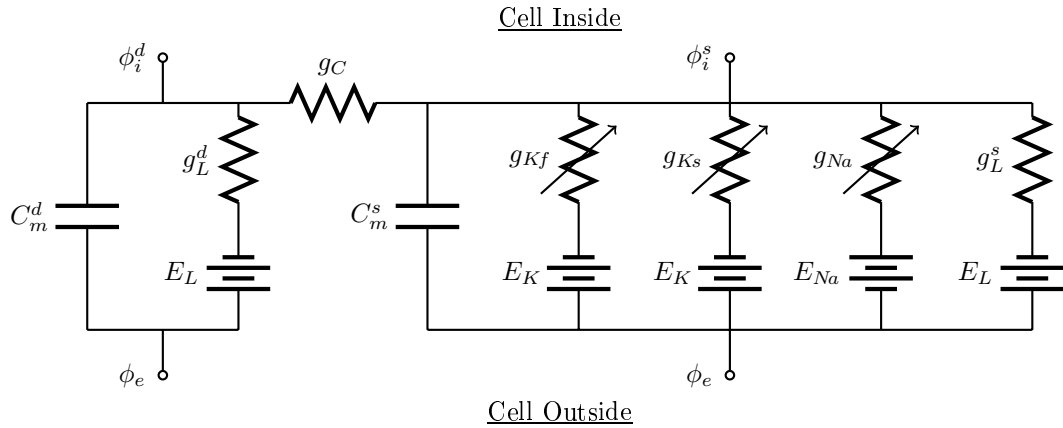


Figure 4.2: Equivalent electrical circuit of the motor neuron model. Resistors with an arrow indicate voltage-dependent conductances. The dendritic membrane potential, V_m^d , equals the difference between the dendritic intracellular potential, ϕ_i^d , and the extracellular potential, ϕ_e . The somatic membrane potential, V_m^s , equals the difference between the somatic intracellular potential, ϕ_i^s , and the extracellular potential, ϕ_e . The driving forces in the model are the differences between the membrane potentials and the corresponding equilibrium potentials, which are represented by batteries.

leakage conductances, respectively, g_{Na} is the sodium channel conductance, and g_{Kf} and g_{Ks} represent the fast and slow potassium channel conductances, respectively. To model the membrane potential dependence of g_{Na} , g_{Kf} , and g_{Ks} gating variables m , n , h , and q are introduced, together with the maximum conductances, \bar{g}_{Na} , \bar{g}_{Kf} , and \bar{g}_{Ks} :

$$g_{Na} = \bar{g}_{Na} m^3, \quad g_{Kf} = \bar{g}_{Kf} n^4, \quad g_{Ks} = \bar{g}_{Ks} q^2 h. \quad (4.10)$$

The evolution of the gating variables, $\omega \in \{m, n, h, q\}$, is given by Equation (4.5) using the respective forward and backward reaction rates given in Equation (4.6). Together with the equations for the dendritic and somatic membrane potentials (4.7), this yields a nonlinear system of six coupled ODEs. Using the abstract representation of (3.8), $\mathbf{y} = [V_m^d, V_m^s, m, n, h, q]^T \in \mathbb{R}^6$. A complete description of the mathematical equations of the MN model of Negro & Farina [186] is included in Appendix B.

4.2.2 Motor Neuron Pool Modelling

To simulate the behaviour of a MN pool, each MN is described by the equations given above. Note that the equations for one MN can be solved independently of all other MNs, since the modelled MNs are not coupled to each other or do exchange information. The MNs of a pool are only related to each other through synaptic input components common to several MNs and the assigned MN parameters, e.g. the excitation threshold. As described in Section 2.4.3, MN excitation thresholds are distributed across a MN pool, whereat many low-threshold MNs and few high-threshold MNs are found, cf. e.g. Powers & Binder [207], Thomas et al. [259]. The MN model of Negro & Farina [186] accounts for this distribution by specifying extreme values for the electrical and geometrical properties of the MNs in a pool, and interpolating exponentially between these extreme values to

find the properties of a given MN. To do so, it is convenient to number the MNs in the pool in an ordered sequence, e. g., starting from the MN with the lowest excitation threshold (MN number 1) to the highest-threshold MN (MN number N , with N being the number of MNs in the pool). Let δ_l and δ_u denote the lower and upper extreme values of a property, respectively. Following Negro & Farina [186], the corresponding value of the i -th MN with $i \in \{1, \dots, N\}$ is determined from

$$\delta_i = \delta_l + \frac{\delta_u - \delta_l}{100} \exp\left(\ln(100) \frac{i}{N}\right). \quad (4.11)$$

The extreme values of the electrical (soma- and dendrite-specific resistances) and geometrical properties (length and diameter of soma and dendrite) used in the interpolation are adopted from Cisi & Kohn [39] and are provided in Appendix B. It is noteworthy that due to the assigned parameter ranges, a size-ordered MN recruitment pattern is observed, when applying a common stimulation current to the entire MN pool [39]. This behaviour is also experimentally observed, cf. Henneman et al. [112, 113]. Further parameters such as equilibrium potentials and membrane capacitance (cf. Appendix B) are also adopted from Cisi & Kohn [39], who based their model on a broad range of experimental data available from the literature.

4.2.3 Input to Motor Neurons

Spinal cord MNs constantly receive excitatory and inhibitory postsynaptic inputs from various sources, for example, from the motor cortex via the corticospinal tract, from the brain stem, from afferent neurons, and from interneurons. Due to the temporal and spatial summation of these postsynaptic potentials, the MN's membrane potential is permanently subject to random fluctuations [35]. To account in the model for these fluctuations, the synaptic input current to each MN contains noise components. Furthermore, components in the input signal can be different for each MN or common to (parts of) the MN pool depending on the origin of the input. In detail, a cortical input current I_{CI} , common to the entire MN pool, is considered. This input consists of two parts, a mean component I_{CI}^m and a noise component I_{CI}^n . The fluctuating component, I_{CI}^n , is modelled as coloured Gaussian noise (bandwidth 0.5–40 Hz), cf. [186]. Gaussian white noise refers to a random signal with zero mean, constant power spectral density, and Gaussian (normal) amplitude distribution. Further, a second common input component I_{SI} is considered representing, for example, signals from the brain stem, interneurons and afferent neurons. This component is modelled as band-limited (0–100 Hz) Gaussian white noise [186]. Additionally, an independent signal I_{IN} for each MN is considered representing synaptic noise, which is modelled as band-limited (0–100 Hz) Gaussian white noise [186]. The specific forms of the components are chosen based on literature data, cf. Negro & Farina [186]. The synaptic input signal for each MN is a linear combination of these components, i. e., $I_{stim} = (I_{CI}^m + I_{CI}^n) + I_{SI} + I_{IN}$. Note that the independent noise component, the secondary common input component, and the fluctuating cortical component contain positive and negative values, representing excitatory and inhibitory signals, and variations from the mean cortical input, respectively.

4.2.4 Behaviour of the Motor Neuron Model

To demonstrate the basic behaviour of the MN model, MATLAB's built in solver ODE113 is employed to approximate the solution to the governing differential equations using optimised time steps within intervals of 1 ms. Figure 4.3a shows a single AP of a high-threshold MN. Figure 4.3b depicts a low-threshold MN discharging a train of APs in response to an input signal as described in Section 4.2.3.

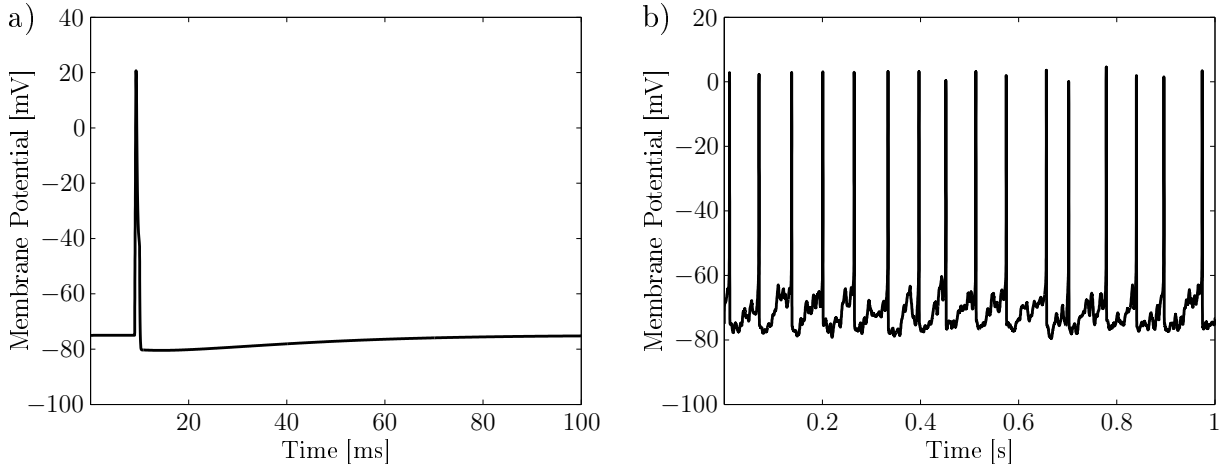


Figure 4.3: (a) Simulated single AP of a high-threshold motor neuron. (b) Simulated train of APs of a low-threshold MN.

The following examples demonstrate the behaviour of a MN pool by considering 100 MNs with geometrical and electrical properties according to Equation (4.11). The simulation time is 10 s, and the sampling rate in all simulations is 1000/s. In the first example, a constant mean cortical input current of $I_{CI}^m = 0.005 \mu\text{A}/\text{cm}^2$ is chosen for all MNs. Further, also common to all MNs of the pool are input components I_{CI}^m and I_{SI} (zero mean, standard deviation $SD=0.00074$). Individual to each MN is the synaptic noise component I_{IN} (zero mean, $SD=0.0021$). All input components are modelled as described in Section 4.2.3. Figure 4.4a shows the coefficient of variation (CoV, defined as the ratio of the standard deviation and the mean multiplied by 100 %) of the input signal for each MN in the pool.

Due to the applied input signal, 85 out of the pool's 100 MNs are recruited. The discharge rates of nine selected MNs are depicted in Figure 4.4c. Figures 4.4b and 4.4d show the temporal mean of the discharge rate and the CoV of the interspike interval (ISI), respectively, of all active MNs.

The average discharge rate of most MNs in the simulation ranges from 10–16 Hz for the applied synaptic input signal (cf. Figure 4.4b), which compares well to experimentally determined MN discharge rates at low force and EMG levels, cf. e.g. Bellemare et al. [13], Farina & Falla [69]. While the CoV of the input signal is approximately 44.5 % for all MNs, cf. Figure 4.4a, the CoV of the ISI is around 20 % for most MNs, and only increases for larger MNs discharging few APs, see, for example, MN number 81 in Figure 4.4c. The CoV of the ISI for isometric contractions of human muscles generally ranges from 10 to 30 %, cf. Nordstrom et al. [195].

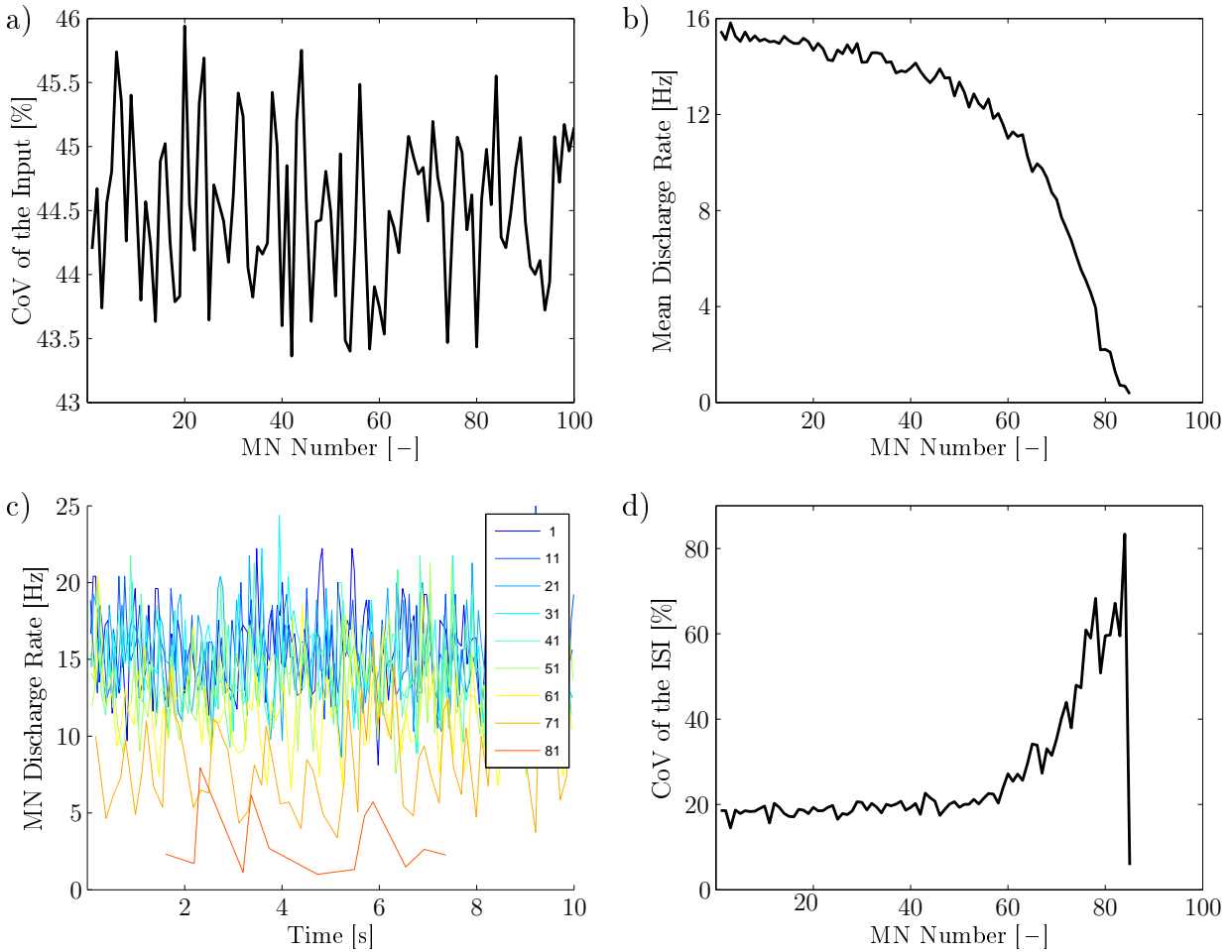


Figure 4.4: Input-output behaviour of the motor neuron model. (a) Coefficient of variation of the input signal. The mean of the input signal is $0.005 \mu\text{A}/\text{cm}^2$ for all MNs. (b) Temporal mean of the discharge rate for all 85 active MNs. (c) Discharge rates of nine selected MNs of a pool consisting of 100 MNs. The numbers of the depicted MNs are displayed in the legend. (d) CoV of the interspike interval for all active MNs.

The second example illustrates the behaviour of the MN model for synaptic input signals of different magnitude. To do so, an input scale factor $\theta_s \in [0, 10]$ is introduced. Similar to the previous example, the considered MN pool consists of 100 MNs, the simulation time is 10 s, the sampling rate is 1000/s, and a mean input current of $I_{CI}^m = 0.005 \mu\text{A}/\text{cm}^2$ (before scaling) is applied. Two scenarios, called *WN* and *NN*, are considered. In scenario *WN* it is assumed that the individual synaptic noise increases when cortical input is increased, while the amplitude of the fluctuations in the cortical signal and the amount of secondary input remain at the same level. Hence, the synaptic input current is modelled by $I_{stim} = \theta_s I_{CI}^m + I_{CI}^n + I_{SI} + \sqrt{\theta_s} I_{IN}$, where the individual input components are modelled as described in Section 4.2.3. Note that this synaptic input current is not necessarily physiological. In reality the fluctuations in the cortical signal and the amount of secondary input to MNs might also increase with increasing mean cortical input. The second scenario, called *NN*, is included to demonstrate the effect of fluctuations in the synaptic input to MNs. To do so, only the mean component of the cortical input is considered, while all fluctuating components are excluded, i. e., $I_{stim} = \theta_s I_{CI}^m$.

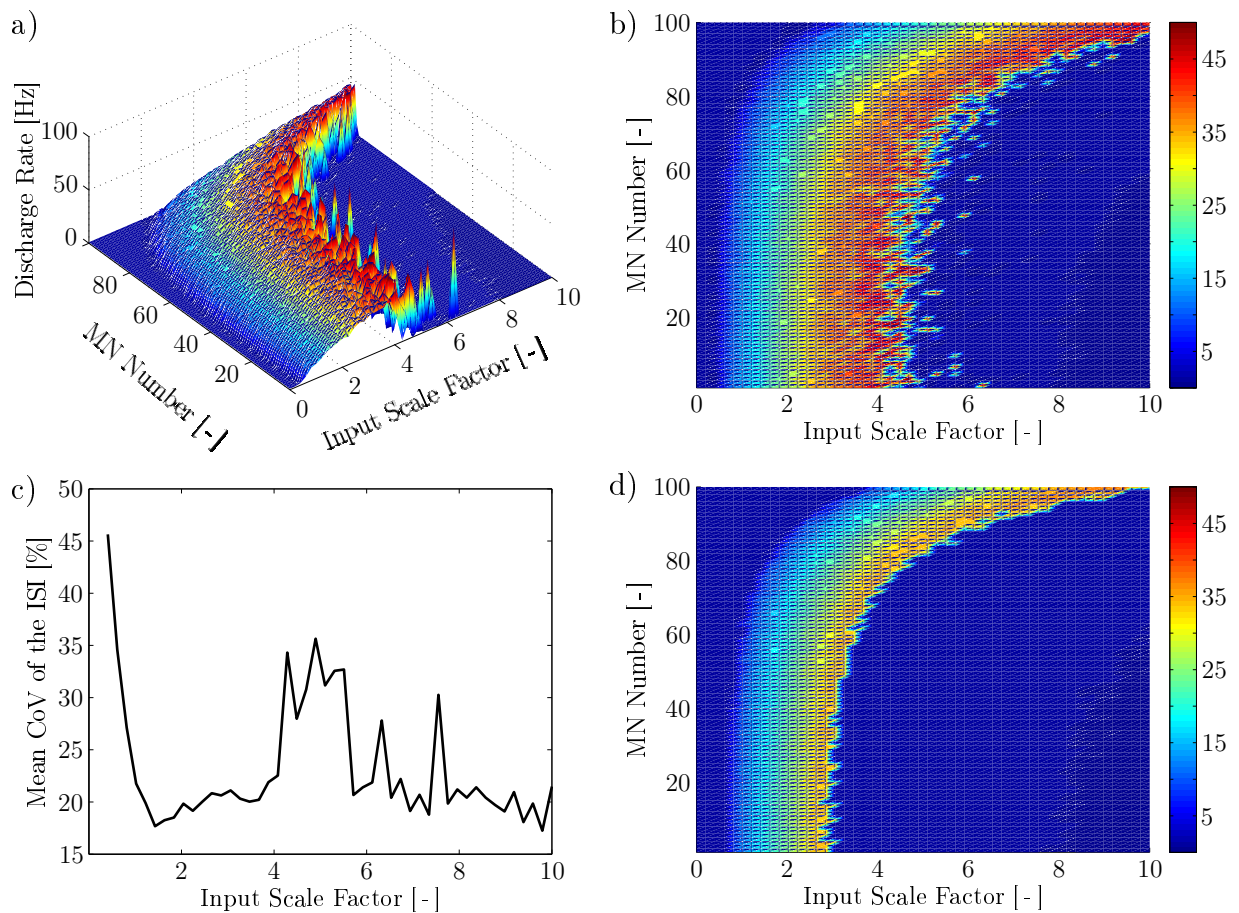


Figure 4.5: Mean discharge rates for each MN in a pool of 100 MNs, and for varying synaptic input current strengths. Colour bars on the right indicating discharge rates in Hz also apply to (a). (a,b) Average MN discharge rates, when fluctuations are present in the synaptic input to MNs (scenario WN). (c) The average CoV of the ISI of all active MNs versus the input scale factor for scenario WN. (d) Average MN discharge rates, when no fluctuations are present in the synaptic input to MNs (scenario NN).

For scenario *WN* Figures 4.5a and 4.5b depict for different combinations of input scale factor and MN number the discharge rates averaged over the 10 s simulation time as surface plot and as contour plot, respectively. For comparison, Figure 4.5d shows the contour plot of the discharge rates for scenario *NN*. Figure 4.5c plots for scenario *WN* the CoV of the ISI averaged over all active MNs versus the input scale factor.

Although not necessarily physiologic, the specific form of the synaptic input current of scenario *WN* has been chosen such that the CoV of the ISI of the MN discharges is approximately 20 % for a wide range of input scale factors, cf. Figure 4.5c. The value of 20 % has been chosen in agreement with data of isometric contractions of human muscles. For example, Nordstrom et al. [195] reported 10–30 % for isometric contractions in humans. In the model, the CoV of the ISI exceeds 30 % only for very low input scale factors and for input scale factors ranging from 4 to 6, which is beyond the physiological range (see further below). For low input scale factors, and hence low synaptic inputs, many MNs are just recruited. The increased CoV of the ISI at low synaptic inputs corresponds to the experimental observation that the variability in the ISI of a MN is marked close to

its recruitment and declines with an increase in contraction intensity, cf. Duchateau & Enoka [57] and references therein.

The mean discharge rates due to existing or non-existing fluctuations in the synaptic input to MNs are only similar for low inputs, cf. Figures 4.5b and 4.5d. In detail, for $\theta_s \leq 2.5$ the mean and standard deviation of the difference between the discharge rates of the two scenarios are 1.92 Hz and 2.37 Hz, respectively. The maximum difference in this region is 11 Hz, and is observed for MN numbers 78, 88, 90, and 91 and for scale factors ranging from 1.4 to 2.5. The mean discharge rates are generally higher when fluctuations are considered in the input signal to MNs for $\theta_s \leq 2.5$. For input scale factors ranging from 2.5 to 4, different behaviours are observed for the different scenarios. When fluctuations are not considered in the input signal (scenario *NN*), low- and medium-threshold MNs stop discharging APs, while the MN discharge rates in scenario *WN* further increase. A decrease in the discharge rates is observed in scenario *WN* only for even higher synaptic inputs ($\theta_s > 4$). The observed behaviour that MNs stop discharging APs at higher injected currents can also be observed in the Hodgkin-Huxley model (result not shown). In experiments, however, this behaviour is not observed. Instead, MN discharge rates reach a plateau, cf. Duchateau & Enoka [57]. It should be noted though, that the range of input scale factors considered here largely exceeds the physiological range of synaptic inputs to MNs (physiological range: $\theta_s \leq 3$, i. e., $\theta_s I_{CI}^m \leq 0.015 \mu\text{A}/\text{cm}^2$). Comparing the mean discharge rates of the two scenarios, one can conclude that fluctuations in the input signal not only introduce variability in the ISI of the MN discharge rates but also influence to a large extent the mean MN discharge rates averaged over the 10 s simulation period. This observation can potentially be explained by nonlinearities in the MN spiking process.

Further, the exponential distribution of parameters is reflected in the shape of the contour plot. This can be observed, for example, in Figure 4.5b at an input scale factor of three. Here, the majority of MNs (those with lower MN numbers) discharge APs at a rate of 30 to 40 Hz, and few MNs with higher MN number discharge APs at lower frequencies. The mean discharge rates of 30 to 40 Hz for $\theta_s \approx 3$ compare well to the peak discharge rates observed in human non-ballistic isometric contractions, which typically range from 20 to 50 Hz, cf. Bellemare et al. [13]. Note that much higher instantaneous discharge rates (>100 Hz) are observed in human muscles at the onset of ballistic contractions, cf. e. g. Duchateau & Baudry [56], Duchateau & Enoka [57], Farina & Falla [69]. Ballistic contractions are characterised by high MN discharge rates, brief contraction times, and high rates of force development [283]. Further, the form of the MN discharge rates implies that most MNs of the pool are recruited at relatively low synaptic inputs. Therefore, at low synaptic input levels, and hence low force levels, force control relies mainly on the recruitment of MUs, while at high synaptic input levels, and hence high force levels, rate modulation remains as the mechanism for varying the force. This behaviour is in agreement with experimental observations, cf. Duchateau & Enoka [57].

It is furthermore noteworthy that, when using the presented MN model, high-threshold MUs cannot reach very high discharge rates, since at the required synaptic input levels ($\theta_s > 8$), low-threshold MNs have already stopped discharging, cf. Figure 4.5. From a physiological point of view, this behaviour is not reasonable, as high-threshold MNs innervate fast-twitch muscle units, whose twitches only fuse at high discharge rates. The actual behaviour of the MN pool at high synaptic inputs remains still unresolved. According

to Duchateau & Enoka [57], this is largely due to technical factors limiting the ability to record the maximal discharge rate of high-threshold MUs, and to follow low-threshold MUs over the full range of contraction forces.

4.3 Modelling the Subcellular Behaviour of Skeletal Muscles

The signaling pathway from electrical excitation to contraction and force generation in skeletal muscles (see Section 2.5.2) is extremely complex and to date not completely understood [161]. Due to this complexity, most research groups specialise on a certain aspect of the excitation-contraction coupling rather than trying to capture the entire pathway. This might explain why a large number of mathematical models exist in the literature describing biophysically a certain component involved in the excitation-contraction coupling, but hardly any model has been proposed that represents the entire signaling pathway. An exception is the model of Shorten et al. [240], which combines several models of components to describe the subcellular processes leading from electrical activation to cross-bridge cycling and isometric force generation in skeletal muscle cells.

The main advantage of the model of Shorten et al. [240] is that it resembles closely the actual cellular biochemical events leading to force generation in skeletal muscle fibres, i. e., the model includes descriptions of the membrane electrophysiology, calcium dynamics, and XB cycling [240]. The model was validated using slow-twitch and fast-twitch skeletal muscles of mice at different stimulation frequencies. Due to its biophysical basis, the model can help to further the understanding of the physiology of skeletal muscles, and it can be applied to investigate pathological conditions.

4.3.1 Mathematical Description of the Skeletal Muscle Model

To represent subcellular processes in skeletal muscles, the present work adopts the model of Shorten et al. [240]. To model the complex nonlinear signaling pathway leading from electrical stimulation to force generation in a skeletal muscle fibre, Shorten et al. [240] combine several models of components of the excitation-contraction pathway representing

- (a) the Hodgkin-Huxley electrophysiology of action potentials via currents in the sarcolemma and T-tubules, cf. Adrian & Peachey [2], Wallinga et al. [272],
- (b) intracellular Ca^{2+} release from the sarcoplasmic reticulum in response to membrane depolarisation through ryanodine receptor Ca^{2+} release channels, cf. Ríos et al. [217],
- (c) calcium dynamics, i. e., the binding of Ca^{2+} to parvalbumin, adenosine triphosphate, troponin, and in the SR to calsequestrin, cf. Baylor & Hollingworth [12],
- (d) force generation via cross-bridge cycling, cf. Campbell et al. [36, 37], Razumova et al. [214, 215], and
- (e) the cellular mechanisms behind muscle fatigue on the basis of phosphate dynamics.

Figure 4.6 schematically depicts an overview of the model of Shorten et al. [240], indicating the individual model components (a–e, see above) and their interactions. Additional details will be provided in the following sections.

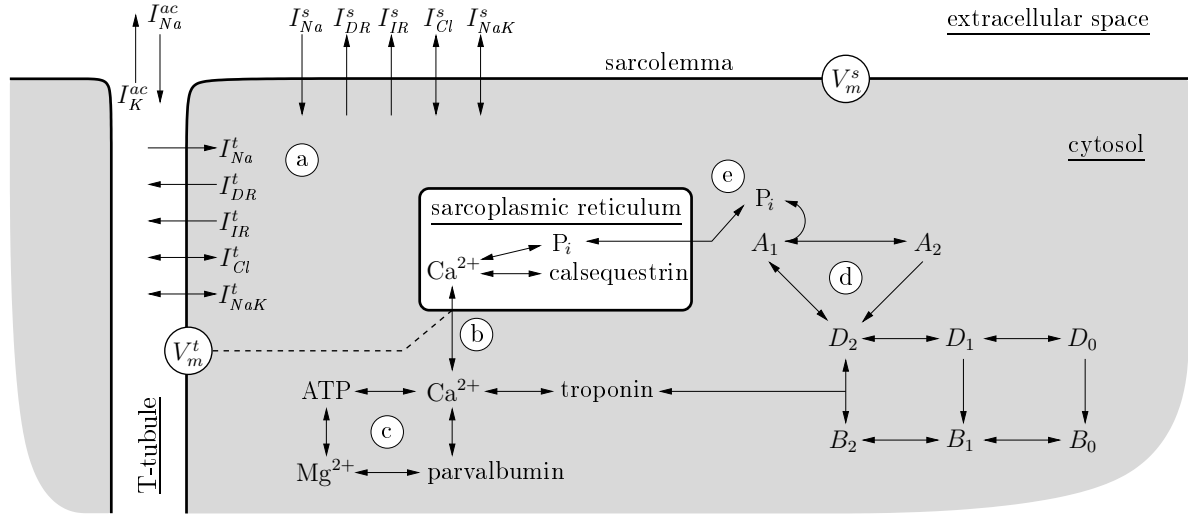


Figure 4.6: Schematic representation of the model of Shorten et al. [240], indicating its components and their interactions. Therein, (a) indicates the model of the membrane ionic currents, (b) is the Ca^{2+} release model, (c) denotes the Ca^{2+} dynamics model, (d) is the model of the XB dynamics, and (e) shows the fatigue model.

The model of Shorten et al. [240] consists of 56 coupled ODEs describing the temporal changes of the unknowns $\mathbf{y} = [\mathbf{y}_{mem}^T, \mathbf{y}_{CaR}^T, \mathbf{y}_{CaD}^T, \mathbf{y}_{XB}^T, \mathbf{y}_p^T]^T \in \mathbb{R}^{56}$. The complete mathematical description of the model is omitted here but can be found in the appendix of Shorten et al. [240]. In the following, a brief summary of each component model is provided. For more details, the interested reader is referred to Shorten et al. [240] and the literature cited therein.

Membrane Electrophysiology

Based on the Hodgkin-Huxley formalism, a two-compartment model of membrane electrophysiology is utilised, cf. Wallinga et al. [272] and Adrian & Peachey [2]. The model distinguishes ionic currents crossing the sarcolemma (superscript s) and the T-tubule membrane (superscript t), I_{ion}^s and I_{ion}^t , respectively, which are given by

$$I_{ion}^s = I_{Na}^s + I_{DR}^s + I_{IR}^s + I_{Cl}^s + I_{NaK}^s, \quad I_{ion}^t = I_{Na}^t + I_{DR}^t + I_{IR}^t + I_{Cl}^t + I_{NaK}^t. \quad (4.12)$$

Both currents consist of the sum of the individual currents through sodium channels (I_{Na}^s, I_{Na}^t), delayed rectifier (I_{DR}^s, I_{DR}^t) and inverse rectifier potassium channels (I_{IR}^s, I_{IR}^t), chloride channels (I_{Cl}^s, I_{Cl}^t), and Na^+ - K^+ pumps (I_{NaK}^s, I_{NaK}^t). Based on Ohm's law, an access current between the T-tubule space and the extracellular space is introduced coupling the two compartments to each other:

$$I_T = \frac{V_m^s - V_m^t}{R_a}. \quad (4.13)$$

Therein, R_a denotes the access resistance at the T-tubule entrance, and V_m^s and V_m^t are the potential differences across the sarcolemma and the T-tubule membrane, respectively. Figure 4.7a shows schematically the individual currents crossing the sarcolemma and the T-tubule membrane.

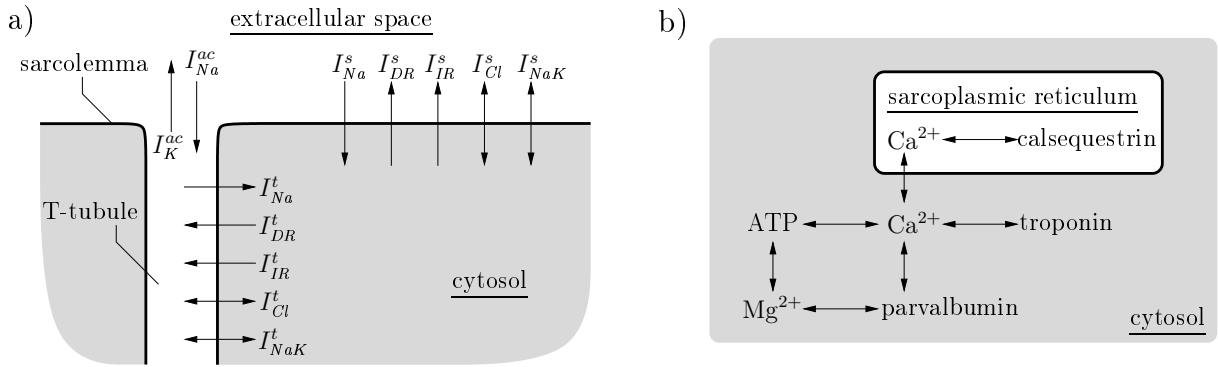


Figure 4.7: (a) The muscle membrane electrophysiological model. Shown are ionic currents crossing the sarcolemma (superscript s) and the T-tubule membrane (superscript t) through sodium channels (I_{Na}^s , I_{Na}^t), delayed rectifier (I_{DR}^s , I_{DR}^t) and inverse rectifier potassium channels (I_{IR}^s , I_{IR}^t), chloride channels (I_{Cl}^s , I_{Cl}^t), and Na⁺-K⁺ pumps (I_{NaK}^s , I_{NaK}^t), as well as the access current (current between the T-tubules and the extracellular space, I_{Na}^{ac} , I_K^{ac}). (b) The calcium dynamics model. Ca²⁺ binds to troponin, parvalbumin, and ATP in the cytosol, as well as to calsequestrin in the sarcoplasmic reticulum.

Both the currents crossing the sarcolemma and the access currents contribute to changes in the sarcolemma's membrane potential, i. e.,

$$C_m^s \frac{\partial V_m^s}{\partial t} = -I_{ion}^s(t, V_m^s) - I_T. \quad (4.14)$$

Being based on the Hodgkin-Huxley formalism, the ionic currents for the sodium channels, delayed rectifier and inverse rectifier potassium channels, and chlorides channels are computed as described in Section 4.1. The component model describing the membrane electrophysiology accounts for 18 of the 56 ODEs of the model of Shorten et al. [240], i. e., $\mathbf{y}_{mem} \in \mathbb{R}^{18}$. Further details are omitted here but can be found in Adrian & Peachey [2], Shorten et al. [240], Wallinga et al. [272].

Intracellular Calcium Release and Calcium Dynamics

Incoming APs enter the T-tubule and depolarise the T-tubule membrane ensuring a simultaneous activation of all sarcomeres in the cross-section of a muscle fibre. Changes in the T-tubule membrane potential are sensed by the dihydropyridine receptor. The dihydropyridine receptor in the T-tubule membrane is linked to the RyR complex in the membrane of the SR, which, upon activation, enables the release of Ca²⁺ ions.

The intracellular release of calcium from the SR to the cytosol is described by a ten-state model originally proposed by Ríos et al. [217], i. e., $\mathbf{y}_{CaR} \in \mathbb{R}^{10}$. In the model, the RyR complex consists of a Ca²⁺ channel and four voltage sensors, which are activated by the T-tubule membrane potential. Each sensor can be in an activated or a deactivated state, and the Ca²⁺ channel can be closed or open. The rate at which the Ca²⁺ channel opens (closes) increases with the number of voltage sensors in the activated (deactivated) state.

The released Ca^{2+} ions in the cytosol bind to buffers such as parvalbumin and ATP along with troponin on the myofilaments to enable XB dynamics. This is described by first-order kinetics. For example, for the binding of Ca^{2+} to ATP,



this yields the following differential equations:

$$\begin{aligned} \frac{\partial[\text{Ca}^{2+}]}{\partial t} &= k_{off}[\text{CaATP}] - k_{on}[\text{Ca}^{2+}][\text{ATP}], \\ \frac{\partial[\text{ATP}]}{\partial t} &= k_{off}[\text{CaATP}] - k_{on}[\text{Ca}^{2+}][\text{ATP}], \\ \frac{\partial[\text{CaATP}]}{\partial t} &= k_{on}[\text{Ca}^{2+}][\text{ATP}] - k_{off}[\text{CaATP}]. \end{aligned} \quad (4.16)$$

Therein, square brackets indicate concentrations.

After being transported back to the SR via Ca^{2+} -ATPase, the Ca^{2+} ions bind to calsequestrin. Intracellular magnesium ions (Mg^{2+}) compete with Ca^{2+} for parvalbumin and ATP binding sites. The Ca^{2+} transport model is depicted in Figure 4.7b. The calcium dynamics model considers two cytosol compartments, one close to the SR and one further away. Considering calcium dynamics in both compartments separately, the calcium dynamics model accounts for 18 ODEs to the biophysical muscle model [240], i. e., $\mathbf{y}_{CaD} \in \mathbb{R}^{18}$.

Force Generation via Cross-Bridge Dynamics

The binding of two Ca^{2+} ions to troponin C leads to a conformational change in the troponin molecule that removes the blocking tropomyosin from the actin filament, which allows the myosin heads to attach to the actin binding sites to form XBs.

An eight-state model of XB dynamics in skeletal muscle based on the generic models of Razumova, Campbell, and co-workers [36, 37, 214, 215] is employed. The eight-state model can be expressed using seven ODEs, as the concentration of XBs in the eighth state can be algebraically determined from the concentration of the seven other states and the total number of XBs available for XB cycling, i. e., $\mathbf{y}_{XB} \in \mathbb{R}^7$. Figure 4.8a shows schematically the XB-cycling scheme. In six of the eight states XBs are detached with either zero, one, or two Ca^{2+} ions bound to troponin (denoted by indices 0, 1, and 2, respectively), and tropomyosin in either the blocking (B) or non-blocking (D) position. Only when two Ca^{2+} ions are bound to troponin, the tropomyosin block can be removed ($B_2 \rightarrow D_2$), and the detached XB can move to a state in which the myosin head is attached. Two attached states are distinguished – the pre-power stroke state, A_1 , and the post-power stroke state, A_2 . The transition from the A_1 to the A_2 state represents the power stroke, i. e., the force producing step. The concentrations of XBs in the detached state D_2 and the attached states A_1 and A_2 are denoted by the respective quantity in

square brackets and are derived from the following differential equations:

$$\begin{aligned}
 \frac{\partial[D_2]}{\partial t} &= k_T^{on} [Ca^{2+}] [D_1] - k_T^{off} [D_2] + k_{Ca}^{on} [B_2] - k_{Ca}^{off} [D_2] - \\
 &\quad - f_0 [D_2] + f' [A_1] + g_0 [A_2], \\
 \frac{\partial[A_1]}{\partial t} &= f_0 [D_2] - f' [A_1] + h' [A_2] - h_0 [A_1], \\
 \frac{\partial[A_2]}{\partial t} &= -h' [A_2] - h_0 [A_1] - g_0 [A_2].
 \end{aligned}
 \tag{4.17}$$

Therein, $[Ca^{2+}]$ denotes the concentration of calcium ions, k_T^{on} and k_T^{off} are the rate coefficients for the binding and unbinding of Ca^{2+} to troponin, respectively, and k_{Ca}^{on} and k_{Ca}^{off} denote the rate coefficients for switching between the blocking and the non-blocking state of the regulatory unit when two Ca^{2+} ions are bound to troponin. Further, f_0, f', h_0, h', g_0 are reaction rate coefficients for XB cycling, where the forward attachment is governed by f_0 , the forward power stroke is governed by h_0 , and XB detachment (from the post-power stroke state) is governed by g_0 , cf. Figure 4.8a. Primes indicate the corresponding reverse reactions, whereat the index $(\cdot)_0$ is omitted. For the sake of brevity, the differential equations for the other states are omitted here but can be found in the appendix of Shorten et al. [240].

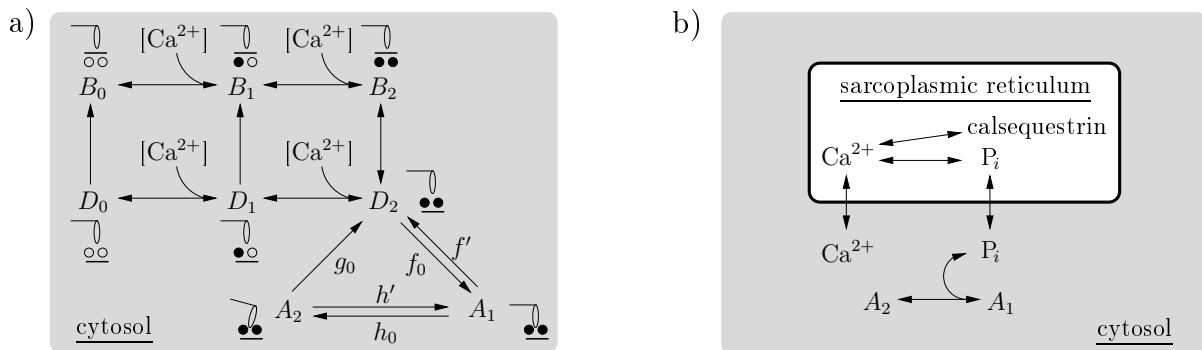


Figure 4.8: (a) The cross-bridge dynamics model. When two Ca^{2+} ions are bound to troponin, and the tropomyosin regulatory unit is removed, XB cycling is enabled. The states in which the tropomyosin regulatory unit is in the blocking position and the non-blocking position are denoted by B and D , respectively. Indices 0, 1, 2 indicate the number of Ca^{2+} ions bound to troponin. A_1 and A_2 are the attached pre-power stroke and attached post-power stroke states, respectively. f_0, f', h_0, h' and g_0 are reaction rate coefficients for the XB cycling. Previously published in [111]. (b) The phosphate dynamics model. P_i is produced during XB cycling and is transported to the SR, where it precipitates with Ca^{2+} .

In the XB dynamics model of Razumova et al. [214], the force generated through XB cycling is represented as the product of the stiffness of all parallel XBs and their average distortion, i. e., the XBs are modelled as parallel aligned linear springs. Under isometric conditions, only the XBs in the post-power stroke state bear loads with their distortion being induced through the power stroke, cf. Figure 4.9. Razumova et al. [214] model the force produced during an isometric contraction, B_{iso} , as proportional to the concentration of XBs in the post-power stroke state and the average distortion induced by the power

stroke, x_0 :

$$B_{iso}(t, f_s) = \eta T_{tot} [A_2] x_0, \quad (4.18)$$

Therein, η is the stiffness of a single XB, and T_{tot} denotes the total number of XBs available for XB cycling, which is assumed to be constant under isometric conditions. Note that under isometric conditions, changes in the concentrations of XBs in the different states exclusively depend on the time (activation history) and stimulation frequency, f_s , at which neural APs are delivered to the muscle fibres, i. e., $B_{iso} = B_{iso}(t, f_s)$. Due to the fact that the concentration of XBs in the post-power stroke state does not vanish in the resting state (assumed at $t = t_0$), the active force in the model of Razumova et al. [214] does not vanish for no activation ($f_s = 0$). In order to have a vanishing active force for no activation, the active force in this work is defined as

$$F(t, f_s) = B_{iso}(t, f_s) - B_{iso}(t_0, 0). \quad (4.19)$$



Figure 4.9: The average distortion x_0 induced through the power stroke in an isometric contraction. In the pre-power stroke state, A_1 , the cross-bridge is attached to the myosin binding site (small filled circle) and does not experience an elastic distortion. The power stroke converts the A_1 to the A_2 state by transducing chemically stored energy into mechanical energy, which is stored in the elastically distorted XBs. Note that the length of the sarcomere does not change during the isometric contraction. Previously published in [111].

The model of Shorten et al. [240] was designed for the simulation of isometric muscle contractions. An extension of the model to non-isometric conditions will be presented in Section 4.3.4.

Fatigue via Phosphate Dynamics

The accumulation of phosphate (P_i) is believed to be the primary mechanism behind metabolic fatigue [240]. P_i is formed from the energy-providing reaction of ATP to adenosine diphosphate (ADP) during SR Ca^{2+} pumping and XB cycling when weakly bound XBs isomerise into strongly bound XBs. The accumulation of phosphate has been proposed to slow XB cycling by decreasing XB isomerisation, which results in a decreased proportion of XBs in the force-producing state.

The model of Shorten et al. [240] only considers the P_i production during XB cycling but not the P_i production that results from the pumping of Ca^{2+} into the SR. The produced P_i can passively be transported into the SR, where it can precipitate with Ca^{2+} . Thereby, the amount of Ca^{2+} that is released from the SR during activation decreases, and, as a result, less troponin regulatory units can be removed from their blocking state. With more regulatory units in the blocking state, less active force can be generated through

XB cycling. In summary, sustained muscle contraction causes an accumulation of P_i ions, which slow-down muscle contraction through feedback. The phosphate transport model is shown in Figure 4.8b and accounts for three ODEs in the model of Shorten et al. [240], i. e., $\mathbf{y}_p \in \mathbb{R}^3$.

4.3.2 Parametrisation

Shorten et al. [240] provide two parametrisations for their muscle model – one parametrisation to simulate mouse soleus muscle, and one to simulate mouse extensor digitorum longus (EDL) muscle. Both parametrisations are based on experimental data of mainly mice and rats taken from the literature. Unfortunately, not all parameters could be taken from a single source and not even all parameters were available for a single species. It is assumed that the parameters are compatible and that the model is also applicable to other mammals due to identical underlying biophysics.

Soleus muscle in many species has the highest portion of slow-twitch muscle fibres of all muscles, reaching up to 100 % in some animals such as guinea pig and cat, cf. Ariano et al. [3], Burke et al. [31]. For rat soleus muscle, Soukup et al. [244] and Augusto et al. [5] report that almost all fibres are of type I. Therefore, it is assumed that the parametrisation of the mouse soleus muscle of Shorten et al. [240] can be identified with a slow-twitch (type-I) muscle fibre. In contrast to the soleus muscle, the EDL muscle is composed of mainly fast-twitch fibres. For example, Bobinac et al. [17] and Soukup et al. [244] found only 4-6 % type-I fibres within the EDL muscle of the rat. Further, Augusto et al. [5] report that mouse and rat EDL muscles predominantly consist of type-II fibres. Thus, the parametrisation for the mouse EDL muscle of Shorten et al. [240] is assumed to be consistent with a fast-twitch (type-II) muscle fibre. Only 30 out of the 105 parameters of the model of Shorten et al. [240] are different in the two parametrisations. They include, amongst others, parameters describing the membrane electrophysiology, the calcium dynamics, and the XB dynamics.

According to Heckman & Enoka [106], the mechanical properties of the muscle units match the electrical properties of their corresponding MNs. For example, the duration of the neuronal AHP duration and the duration of the twitch in the corresponding muscle unit are positively correlated, cf. e. g. Gardiner & Kernell [80], Meehan et al. [166]. In general, the MNs with low recruitment threshold innervate muscle units with high contraction times (slow-twitch units), while MNs with high recruitment threshold innervate muscle units with low contraction times (fast-twitch units). The properties of human MUs, however, do not cluster into discrete groups of type-I and type-II fibres but are distributed continuously within a MU population [106]. Thus, to realistically simulate a human muscle, a description of the mechanical behaviour of each muscle unit is required. The methodology to extend the model of Shorten et al. [240] to a description of the individual muscle units of a muscle is presented in the following. To this end, the human first dorsal interosseous (FDI) muscle is representatively simulated. This hand muscle comprises approximately 120 MUs [106].

Many of the parameters of the model of Shorten et al. [240] cannot be determined and few are readily available for the MUs of the human FDI muscle. Thus, it is assumed that the basic principles of the subcellular processes are similar in different mammalian muscles, and that the reaction rates determining these processes are comparable in mice

and humans. Accordingly, the parameters of Shorten et al. [240] are adopted. To account for the slower XB dynamics in human compared to mouse (cf. Campbell et al. [37]), the reaction rates in the XB dynamics model of Razumova et al. [214] are adjusted. The values originally proposed by Razumova et al. [214] are adopted for the simulation of the slowest MU in the human FDI muscle. These values correspond to 0.1-times the values used in Shorten et al. [240] for the mouse soleus muscle. Accordingly, the XB dynamics rate constants for the mouse EDL muscle [240] are multiplied by a factor of 0.1 for the simulation of the fastest MU in the human FDI muscle. The resulting XB dynamics reaction rate constants are summarised in Table 4.3.

	f_0 [ms^{-1}]	f' [ms^{-1}]	h_0 [ms^{-1}]	h' [ms^{-1}]	g_0 [ms^{-1}]
slow twitch	0.05	0.5	0.008	0.006	0.004
fast twitch	0.15	1.5	0.024	0.018	0.012

Table 4.3: Reaction rates for the cross-bridge dynamics model of the human FDI muscle. Here, f_0 denotes the rate of XB attachment, f' is the rate of pre-power stroke XB detachment, h_0 denotes the forward rate of the power stroke, h' is the reverse rate of power stroke, and g_0 is the rate of post-power stroke XB detachment.

The XB dynamics rate constants determine, among others, the shape of a single twitch, cf. Campbell et al. [36]. Based on the parameters given in Table 4.3, Figures 4.10a and 4.10c depict normalised twitches of a slow-twitch MU and a fast-twitch MU, respectively. Instead of comparing the simulated twitches to experimental data, they are compared to the impulse responses of a critically damped, second-order system, which has been proposed by Fuglevand et al. [76] to simulate the twitch shape. Fuglevand et al. [76] build their model on a wide range of experimental data. The twitch rise times (contraction times) are set as identical in the two models for this comparison. They are 93.7 ms and 30.5 ms for the slow-twitch and the fast-twitch MUs, respectively. The half-relaxation times (time elapsed from peak twitch force to 50 % of this value) for the slow-twitch and fast-twitch models are 155.6 ms (proposed biophysical model) and 159.2 ms (impulse response; 2.3 % relative difference), and 44.5 ms (proposed biophysical model) and 51.1 ms (impulse response; 12.9 % relative difference), respectively. The largest relative differences between the two models occurs in the beginning of the rise of the MU twitches. Therefore, Figures 4.10b and 4.10d highlight the initial phases of the twitch shapes. Note the delayed and hence more physiological rise of the MU twitches in the proposed biophysical model. A major advantage of the biophysical description compared to phenomenological relations is that quantities of the modelled signaling pathway can be investigated. To illustrate this, Figures 4.10b and 4.10d additionally depict the corresponding intracellular free calcium concentrations as predicted by the proposed biophysical model.

The mechanical properties of MUs are distributed continuously across the motor pool [105, 106]. Thus, it is assumed that the parameters of a muscle unit can be determined from the parameter sets of the slowest MU and the fastest MU. Since data are available for the contraction times of the individual MUs, this property is a convenient measure for the distribution of the muscle unit parameters across the pool, cf. [76, 106, 266]. The frequency distribution based on contraction time (time elapsed from stimulation to peak twitch force) is nonlinear across a MU pool, i. e., small MUs have contraction times that

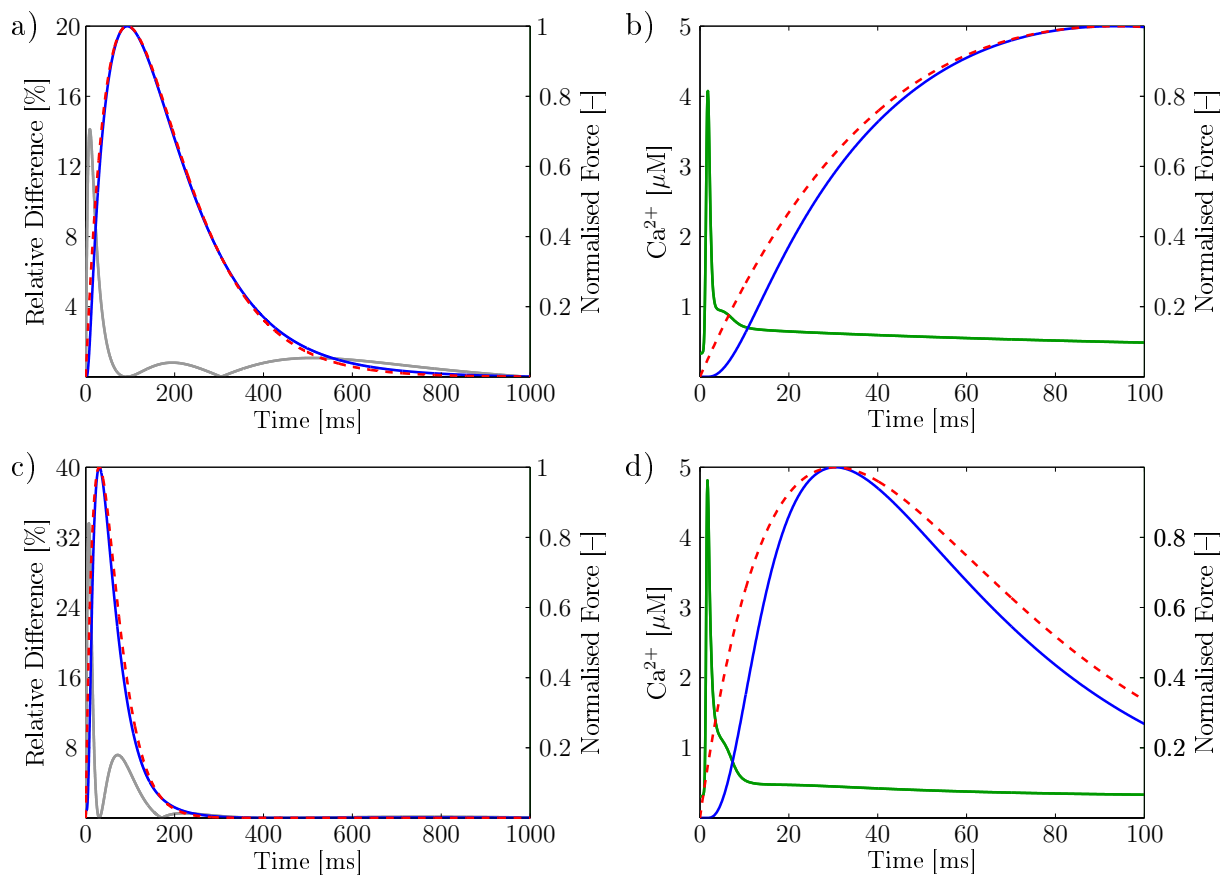


Figure 4.10: *Twitch forces in the proposed model (blue solid line) and the model of Fuglevand et al. [76] (red dashed line). (a,c) Comparison of normalised twitch forces of (a) a slow MU (contraction time: 93.7ms) and of (c) a fast MU (contraction time: 30.5 ms), and their relative differences (grey line). (b,d) First 100ms of the normalised twitch forces of (b) a slow MU and of (d) a fast MU, and corresponding myoplasmic free calcium concentration (green line) in the proposed model.*

vary over most of the range of observed values, while intermediate and large MUs are generally fast contracting and exhibit little variation in contraction time [76]. Similarly to the approach chosen for the parameters of the MN model, an exponential distribution across the MU pool, cf. Equation (4.11), is first applied. However, the resulting distribution of contraction times is not in agreement with experimental findings. Linear interpolation of the parameter sets generates a much more realistic distribution of contraction times across the MU pool, cf. Figure 4.11a. Note that although the parameter sets are linearly interpolated, the distribution of contraction times across the MU pool is clearly nonlinear. Additionally, Figure 4.11a shows the distribution of contraction times used in the model of Fuglevand et al. [76]. Parameters for this simulation are directly adopted from Fuglevand et al. [76], i.e., the contraction time of the slowest MU is set to 90 ms and a three-fold range in contraction times is assigned. The maximum relative difference between the two models is 14.4%. For the majority of MUs, the proposed biophysical model predicts shorter contraction times than the model of Fuglevand et al. [76]. This is in accordance with the experimental findings of Van Cutsem et al. [266].

The increase in force from slow-twitch to fast-twitch MUs primarily depends on the MU innervation number [106]. Slow-twitch and fast-twitch mammalian muscle fibres do not show significant differences in generated active stresses [106]. Further, only minor differences in muscle fibre diameters are observed. Assuming that the model of Shorten et al. [240] represents a single muscle fibre, the predicted twitch forces should be approximately equal for the different model parametrisations. However, the MU force model predicts approximately four times larger twitch forces for a slow-twitch fibre than for a fast-twitch fibre. Using a least-squares fit, a straight line is approximated to the distribution of maximum twitch forces of single muscle fibres across the MU pool. Dividing the fibre force of each MU by the corresponding value of the approximated line yields a much more uniform distribution of the single-twitch forces across the MU pool. To take into account the MU innervation number, the resulting single fibre forces are multiplied by an exponential function, as in Fuglevand et al. [76], to obtain physiological MU forces. Therefore, the MU force is given by

$$F_{MU_i} = F_i \exp\left(\ln(r_f) \frac{i}{N}\right), \quad (4.20)$$

where F_{MU_i} denotes the force of the i -th MU, F_i is the single fibre force, r_f is the range of twitch forces, and N is the number of MUs in the pool, i. e., $N = 120$ for the human FDI. Although MU force summation is nonlinear at low force levels (cf. Clamann & Schelhorn [40]), the simulated MU forces are linearly summed up to obtain the total muscle force, F , i. e.,

$$F = \sum_{i=1}^N F_{MU_i}. \quad (4.21)$$

Based on the linear interpolation of the parameters of the muscle unit force model, Figure 4.11 compares the distribution of maximum twitch forces across the MU pool to the distribution obtained from the model of Fuglevand et al. [76]. In the model of Fuglevand et al. [76], the maximum twitch force of the slowest MU is set to 1 [AU] (arbitrary unit) and the range in twitch force is set to 100 [76]. As the same exponential distribution in the MU innervation number is used in both models, the twitch-force distribution shows good agreement. A maximum difference of 6.3 % is observed.

4.3.3 Behaviour of the Isometric Skeletal Muscle Model

In the following, a number of representative simulations are presented to demonstrate the capability of the proposed muscle model.

Response to Trains of Discharges with Constant Frequency

Previous examples focused on the properties of isolated twitches. From a physiological point of view, it is more relevant to investigate the effect of multiple subsequent stimuli under conditions leading to fused twitches. Figure 4.12a shows the simulated force response of the slowest muscle unit to trains of stimuli at 5, 10, 20, 40, and 50 Hz. Additionally, Figure 4.12a depicts the force response of the same muscle unit using the model of Fuglevand et al. [76] with a 20 Hz stimulation frequency. As expected for slow-twitch, low-force muscle units, a high resistance to fatigue is observed, see Burke et al. [30]. The

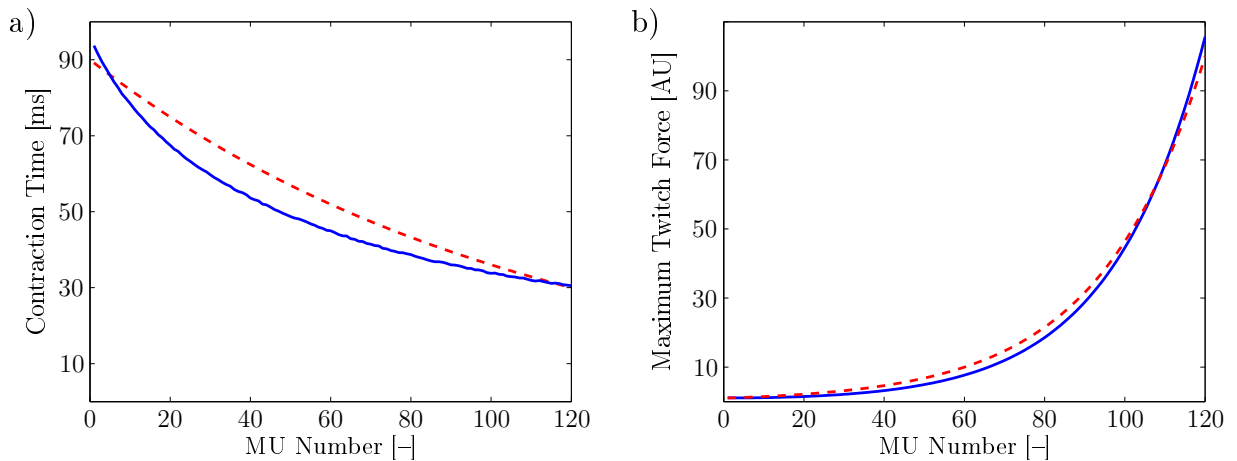


Figure 4.11: Basic twitch properties in the proposed biophysical model (blue solid line) and in the model of Fuglevand et al. [76] (red dashed line) for a MU pool consisting of 120 MUs. (a) Contraction times. (b) Maximum twitch forces.

slow-twitch muscle unit reaches full force output at stimulation rates of approximately 50 Hz. The model of Fuglevand et al. [76] reaches its maximum force at a stimulation frequency of 20 Hz. The ratio of twitch force to maximum tetanic force (twitch-tetanus ratio) of the biophysically modelled muscle unit is 0.07 (at 50 Hz stimulation frequency). Figure 4.12b shows the simulated force responses of the fastest muscle unit to trains of stimuli at 10, 20, 40, 50, and 100 Hz. The force output clearly shows sag, i. e., a decrease of the force. Burke et al. [30] used the property to develop sag to differentiate fast-twitch from slow-twitch muscle units. Slow-twitch muscle units do not develop sag. For the fast-twitch muscle unit, the model reaches full force output at a stimulation frequency of approximately 100 Hz. The twitch-tetanus ratio is 0.12 (determined at 50 Hz stimulation frequency before the force decreases). In addition, Figure 4.12b shows the force response of the model of Fuglevand et al. [76] due to a 50 Hz stimulation frequency. At this stimulation frequency the model of Fuglevand et al. [76] reaches full force output. Since Fuglevand et al. [76] do not model fatigue, no force decrease is observed. The twitch-tetanus ratio in the model of Fuglevand et al. [76] is 0.11 for all MUs. The frequency of tetanic contractions for the computation of the twitch-tetanus ratios of the proposed model is chosen as 50 Hz, since MU discharge rates increase with increasing excitatory synaptic input up to a certain value beyond which the discharge rate does not further increase. Experimentally determined peak discharge frequencies in human MUs during isometric contractions are approximately 45 Hz [76].

While Figure 4.12 compares the behaviour of the proposed model only to the reference model [76], Shorten et al. [240] also validated their model to force responses at different stimulation frequencies. Moreover, the reader is referred to Shorten et al. [240] for more sustained contractions demonstrating further effects of fatigue on the force in the model. As demonstrated by the fatiguing fast-twitch MUs, nonlinearities in the force response due to the activation history are an important feature of the proposed model. In the following a second nonlinearity of the model is discussed in detail.

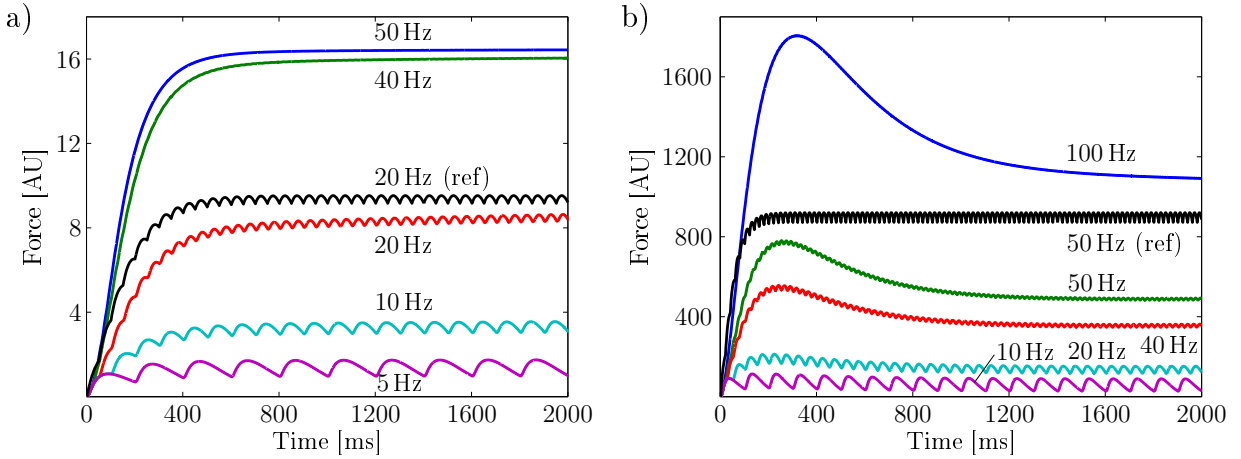


Figure 4.12: Force responses to stimulation trains at various frequencies of (a) the slowest MU and (b) the fastest MU of a pool of 120 MUs. Additionally, for the same MUs in the model of Fuglevand et al. [76] the frequency leading to maximum tetanic force in each case is plotted (traces indicated by (ref)).

Doublet Potentiation

It is well known that two consecutive stimuli with a short interstimulus interval yield contractile forces that are larger than twice the twitch force (nonlinear sum) [137]. This effect is termed doublet potentiation. Doublets are frequently observed at the onset of MU firing, i. e., at the recruitment of a MU, especially during ballistic contractions [49].

Doublet potentiation has been attributed to an enhanced free calcium concentration in the myoplasm resulting from the summation of residual calcium due to the first stimulus and the calcium release due to the second stimulus [58, 59, 137]. The higher concentration of free calcium allows the formation of a larger number of XBs that contribute to the force as independent motors, cf. Huxley [128].

Using the muscle unit force model, doublets are simulated for interstimulus intervals ranging from 5 ms to 500 ms in 5 ms steps. Figure 4.13a shows for the slowest muscle unit the twitch responses due to a single stimulus (thick line) and due to a selection of doublet stimulations (thin lines). Figure 4.13b shows the twitch peak recovery function (*TPRF*) for the doublets. To calculate the *TPRF*, first, the force response of the singlet, $F_s(t)$, is subtracted from the force response of a doublet, $F_d(t)$, and then, the ratio of the maximum value of the resulting function and the maximum value of the singlet is determined, i. e.,

$$TPRF = \frac{\max [F_d(t) - F_s(t)]}{\max [F_s(t)]}. \quad (4.22)$$

As the proposed model contains a description of calcium release and dynamics, it is used to investigate if doublet potentiation is caused by an enhanced free calcium concentration in the myoplasm. Figure 4.13c shows for a singlet (thick line) and for the doublets (thin lines) depicted in Figure 4.13a the respective myoplasmic calcium concentrations for a slow-twitch muscle unit. Furthermore, a calcium recovery function (*CaRF*) is introduced. The *CaRF* is defined as the ratio of the difference of the integrated calcium concentrations of a doublet and the singlet and the baseline-corrected, integrated calcium concentration

of the singlet, i. e.,

$$CaRF = \frac{\int_{t_0}^{t_e} F_d(t) dt - \int_{t_0}^{t_e} F_s(t) dt}{\int_{t_0}^{t_e} F_s(t) dt - F_s(t_e)(t_e - t_0)}. \quad (4.23)$$

Therein, t_0 is the time of stimulation of the first stimulus and t_e denotes a time at which the calcium concentration resumed again its baseline value ($t_e = 1000$ ms). Figure 4.13d plots the calcium recovery function versus the interstimulus interval. Equivalently to Figure 4.13, Figure 4.14 shows the same quantities for a fast-twitch muscle unit.

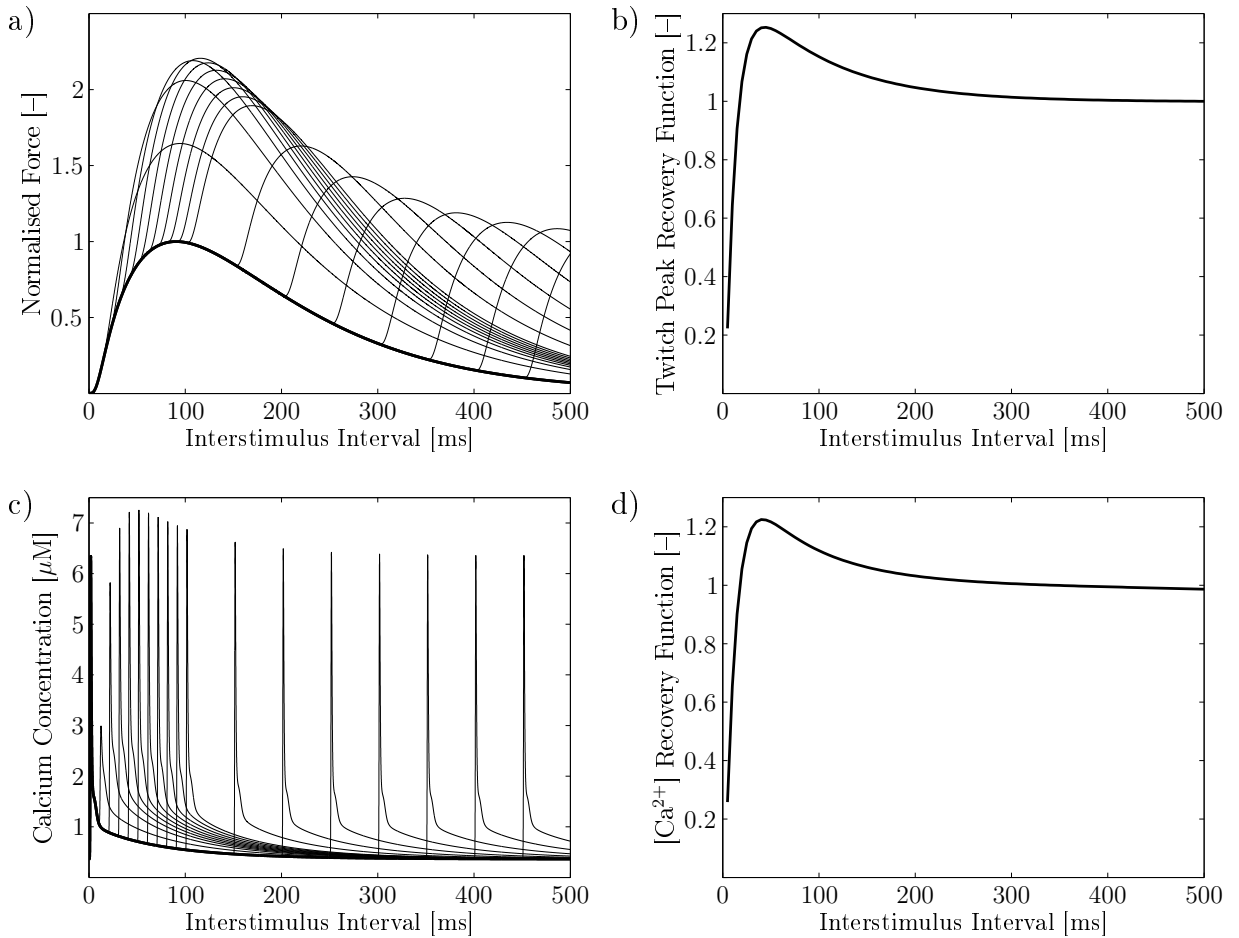


Figure 4.13: Doublet stimulations in a slow-twitch MU. (a) The normalised force of a singlet (thick line) and a selection of doublets with different ISIs (thin lines; for ISIs up to 100 ms the ISI is increased in steps of 10 ms, after 100 ms in steps of 50 ms). (b) Twitch peak recovery function for doublets with ISI ranging from 5 ms to 500 ms in 5 ms steps. (c) Myoplasmic free calcium concentrations of a singlet (thick line) and the doublets (thin lines) shown in (a). (d) Calcium concentration recovery function (see text for definition) for doublets with ISI ranging from 5 ms to 500 ms in 5 ms steps.

Figures 4.13 and 4.14 demonstrate that the proposed model is able to reproduce a marked enhancement in the force response when two consecutive stimuli with a short interstimulus interval are applied. It is remarkable that no parameter optimisation is required to evoke the doublet potentiation. Further, the simulations suggest that the force enhancement is in fact due to an increased calcium concentration, which results

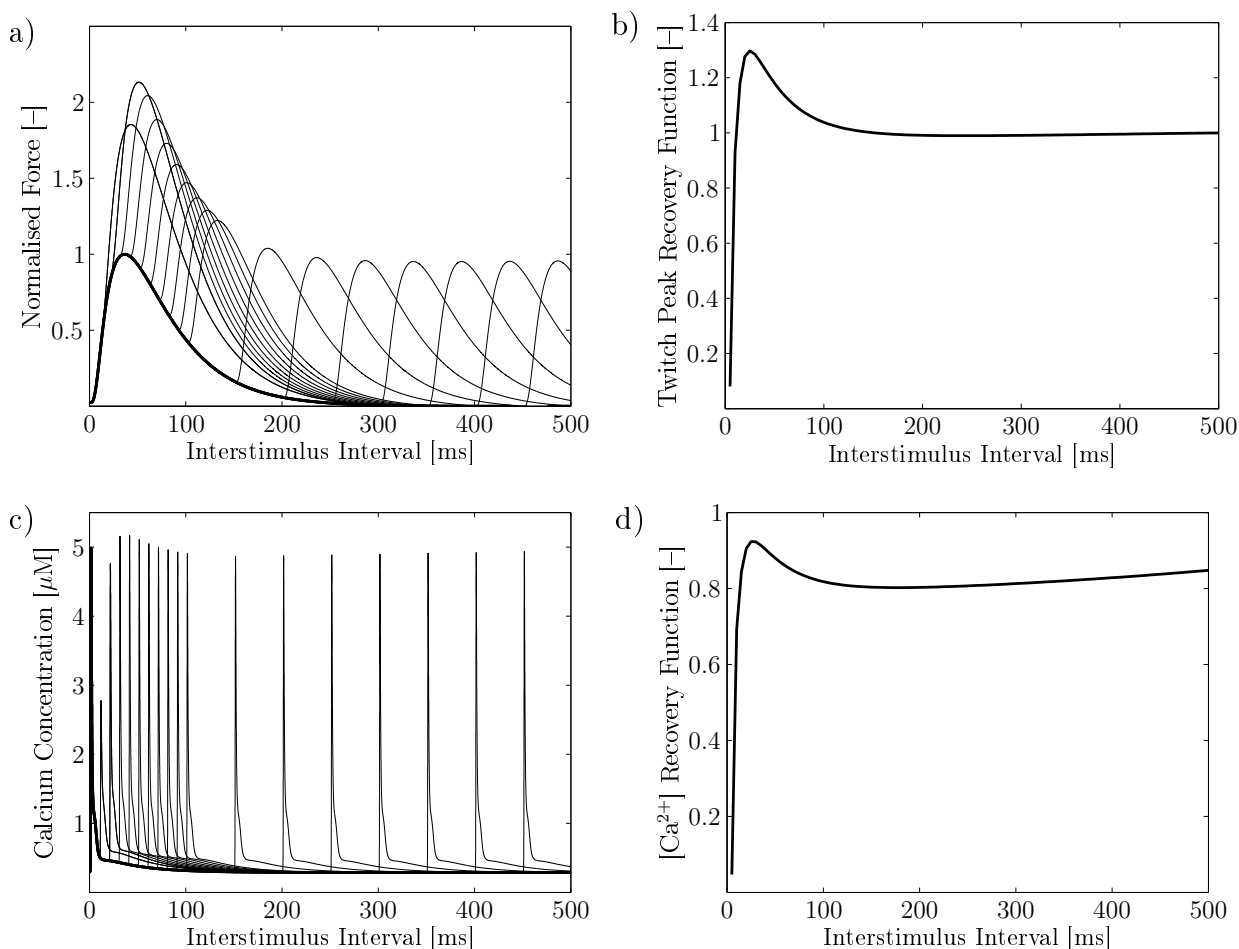


Figure 4.14: Doublet stimulations in a fast-twitch MU. (a) The normalised force of a singlet (thick line) and a selection of doublets with different ISIs (thin lines; for ISIs up to 100 ms the ISI is increased in steps of 10 ms, after 100 ms in steps of 50 ms). (b) Twitch peak recovery function for doublets with ISI ranging from 5 ms to 500 ms in 5 ms steps. (c) Myoplasmic free calcium concentrations of a singlet (thick line) and the doublets (thin lines) shown in (a). (d) Calcium concentration recovery function (see text for definition) for doublets with ISI ranging from 5 ms to 500 ms in 5 ms steps.

from the summation of residual calcium due to the first stimulus and the additional calcium injection due to the second stimulus. Considering the evolution of the calcium concentrations and the calcium recovery function of the fast-twitch MU (Figures 4.14c and 4.14d), the model furthermore predicts that the force enhancement is due to a raised peak calcium concentration and is not due to an increased total amount (integrated values) of calcium. Experimentally determined doublet potentiations of whole muscle are much larger than those predicted by the model, see, for example, Kamavuako & Farina [137]. It is possible that the additional force increase is related to the muscle-tendon complex, i.e., the system is already under tension when the second stimulus is applied. Moreover, Nishikawa et al. [193] measured 20 % higher doublet potentiations in the soleus muscle of wild type mice, than in the mdm (muscular dystrophy with myositis) mouse, with a 779 base-pair deletion in the N2A region of the titin gene. Based on these experiments,

Nishikawa et al. [193] hypothesized that the calcium activation of titin contributes to the active force generation. Hill-type or 3D continuum-mechanical muscle models need to be developed to investigate this phenomenon in more detail.

4.3.4 Extension to Non-Isometric Contractions

Due to the fact that the original model of Shorten et al. [240] is limited to isometric conditions, it is extended in this section to simulate non-isometric contractions of skeletal muscle. To this end, changes in myofilament overlap are incorporated, and a distortion dependence and cooperative effects are added to the XB-dynamics component model [214] within the model of the excitation-contraction coupling of Shorten et al. [240].

Incorporating the Force-Sarcomere Length Relation

The force that can be exerted by a half-sarcomere depends on the number of XB connections between the actin and myosin filaments, cf. Section 2.5.2 and Huxley [128]. The number of possible XB connections in turn depends on the filament overlap and hence on the sarcomere length, see Gordon et al. [89]. Based on analytical considerations of the filament overlap, Campbell et al. [37] proposed a piecewise linear relation between the sarcomere half-length and the number of possible XB connections. The relation is depicted in Figure 4.15a (green dashed line) assuming a direct relation between the number of possible XB connections and the isometric active force at full activation. Experiments on single sarcomeres, however, suggest a steeper decline of the force on the ascending limb of the active force-length (F - ℓ) curve at sarcomere lengths below $1.7 \mu\text{m}$ and no active force production at lengths below $1.27 \mu\text{m}$ [89]. This is attributed to an interaction of the myosin filament with the Z-disks at low sarcomere lengths. The red solid line in Figure 4.15a shows the experimentally determined relation between the sarcomere length and the isometric active force at full activation. The present work uses a fourth-order polynomial, cf. Figure 4.15a (dot-dashed blue line), given by

$$f_\ell(\ell_S) = \max \{ -1.2 \ell_S^4 + 11.5 \ell_S^3 - 41.7 \ell_S^2 + 67.6 \ell_S - 40.3, 0 \} . \quad (4.24)$$

Therein, ℓ_S denotes the sarcomere length and $f_\ell(\ell_S)$ is the normalised isometric active force-length relation at full activation. The polynomial in (4.24) is symmetric with respect to the optimal sarcomere length $\ell_S^{\text{opt}} = 2.4 \mu\text{m}$ [32], and can be seen as an approximation to the experimentally determined force-sarcomere length relation, where the largest deviations occur at very long sarcomere lengths. In this work, the behaviour at very long sarcomere lengths plays a minor role since the passive stiffness of the muscle tissue prevents for the most part such sarcomere lengths, cf. Section 6.3.3. Note that the fourth-order polynomial in (4.24) is a generic description of a muscle's F - ℓ behaviour, cf. [287]. This approximation can be easily replaced by a different F - ℓ curve that was fitted to experimental data of a specific muscle. The advantage of using a closed-form polynomial rather than a piecewise linear function is the smooth transition between the different regions leading to improved computational efficiency.

To account for length changes in the model during a contraction, the approach proposed by Campbell et al. [37] is followed. At this, average distortions (or elastic deformations) of XBs in a sarcomere are introduced into the XB-dynamics component model. The

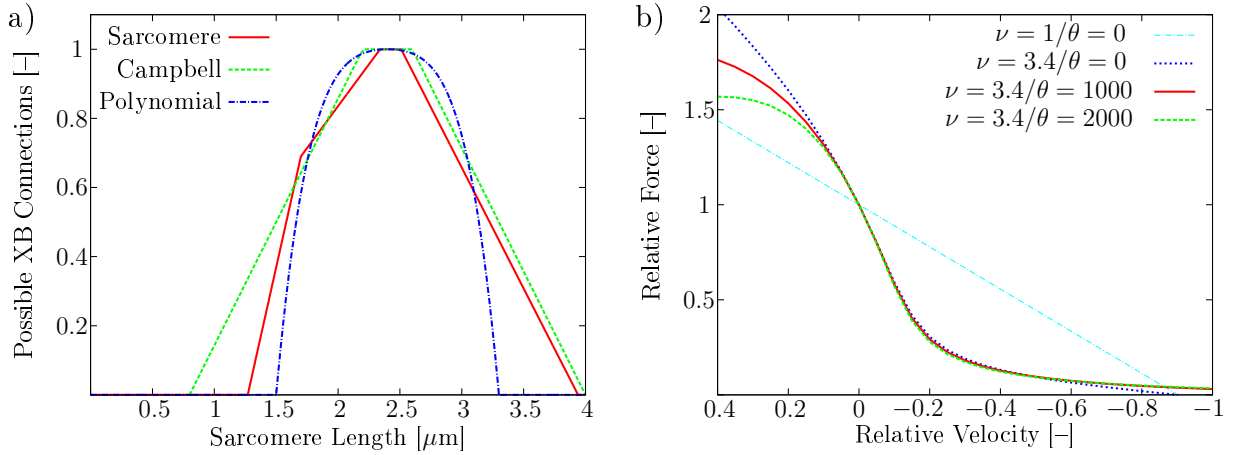


Figure 4.15: (a) Normalised relation between the number of possible XB connections and sarcomere length. Sarcomere denotes the actual relation determined from length-clamp experiments. Campbell denotes the relation proposed by Campbell et al. [37]. This work uses the fourth-order polynomial denoted by Polynomial (cf. Equation (4.24)). (b) Normalised force-velocity relations for different combinations of ν and θ . Figure previously published in [111].

average elastic deformations among XBs in the pre-power and post-power stroke states are denoted by x_1 and x_2 , respectively, and are schematically represented in Figure 4.16.

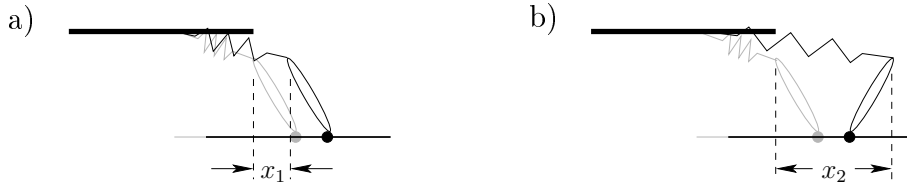


Figure 4.16: Average distortions (a) x_1 and (b) x_2 induced through filament sliding during non-isometric contractions on the cross-bridges in the A_1 and A_2 states, respectively. Figure previously published in [111].

While the average distortion induced by the power stroke, x_0 , is assumed to be constant, x_1 and x_2 account for distortions entering and leaving due to XB cycling and for distortions imposed by shearing between thick and thin filaments [37]. From the distortional balances, Campbell et al. [37] derived the following ODEs:

$$\begin{aligned} \frac{\partial x_1}{\partial t} &= -\left(f_0 \frac{[D_2]}{[A_1]} + h' \frac{[A_2]}{[A_1]}\right)x_1 + h' \frac{[A_2]}{[A_1]}(x_2 - x_0) + \frac{\dot{\ell}_S}{2}, \\ \frac{\partial x_2}{\partial t} &= -h_0 \frac{[A_1]}{[A_2]}(x_2 - (x_1 + x_0)) + \frac{\dot{\ell}_S}{2}, \end{aligned} \quad (4.25)$$

where $\dot{\ell}_S$ denotes the sarcomere contraction velocity.

Further, the actively generated force is proportional to the product of the stiffness of

all parallel XBs and their average distortions [37, 214], i. e.,

$$B(t, f_s, \dot{\ell}_S) = \eta T_{tot} ([A_1] x_1 + [A_2] x_2). \quad (4.26)$$

In Equation (4.26), $[A_1]$ and $[A_2]$ depend only on the stimulation frequency, f_s , while x_1 and x_2 are functions of f_s and $\dot{\ell}_S$. Note that in the original XB-dynamics model [36, 37, 214, 215] the number of XBs in a certain state is given in absolute values, while here, in compliance with the model of Shorten et al. [240], concentrations are used. Hence, in the equations for the active force (4.18) and (4.26), the concentrations are multiplied by the number of possible attachment sites. To account for the resting concentrations of XBs in the pre-power and post-power stroke states as well as the F - ℓ relation, the active force is defined as

$$F(t, f_s, \ell_S, \dot{\ell}_S) = f_\ell(\ell_S) [B(t, f_s, \dot{\ell}_S) - B(t_0, 0, 0)]. \quad (4.27)$$

The F - ℓ relation dominates the active behaviour of skeletal muscles under isometric conditions at a specified level of stimulation. Under non-isometric conditions, the force-velocity relation (F - v), i. e., the dependence of the force on the shortening or lengthening velocity, has to be considered additionally.

Incorporating the Force-Velocity Relation

To reproduce the hyperbolic F - v relation of Hill [117], Razumova et al. [214] introduce two modifications into their four-state XB-dynamics model: (i) Considering nearest-neighbour cooperative effects within the forward rate of XB attachment, f_0 , i. e., increased XB-attachment probabilities due to neighbouring XBs in the force-bearing state, and (ii) incorporating a distortion dependence in the XB-detachment rate, g_0 , lead to the following rules within the XB-dynamics model [214]:

$$\begin{aligned} f_0 &= \bar{f} \left(1 + \frac{[A_1]}{T_{tot}} \left[\exp\left(\frac{x_1}{x_0}(\nu - 1)\right) - 1 \right] + \frac{[A_2]}{T_{tot}} \left[\exp\left(\frac{x_2}{x_0}(\nu - 1)\right) - 1 \right] \right), \\ g_0 &= \bar{g} \exp(\vartheta(x_2 - x_0)^2), \end{aligned} \quad (4.28)$$

where \bar{g} is the XB-detachment rate of an isometric contraction, and ϑ controls the distortion dependence. Further, \bar{f} is the forward rate of XB attachment if no neighbour is in the force-bearing state, and ν controls the influence of the cooperative effects.

To show that the extended model exhibits a F - v relation as muscles fibres do, the sensitivity of the model to the newly introduced parameters ν and ϑ is analysed. To do so, in-silico experiments using the fast-twitch version of the extended model at a stimulation frequency of $f_s = 100$ Hz are carried out. For different prescribed constant velocities, the corresponding normalised active forces are computed at optimal sarcomere length.

For constant rate coefficients f_0 and g_0 ($\vartheta = 0$, $\nu = 1$), the model predicts a linear F - v relation, cf. Figure 4.15b. When considering nearest-neighbour cooperative effects in f_0 ($\vartheta = 0$, $\nu = 3.4$), the model is able to predict a hyperbolic relation for shortening contractions, but unreasonable high forces occur for lengthening contractions. The distortion dependence in g_0 ($\nu = 3.4$, $\vartheta = 1000, 2000$) mainly influences lengthening contractions.

In the next example, three shortening contractions are simulated to demonstrate the influence of the F - ℓ and the F - v relations on the active force profiles. To this end,

the extended model is stimulated at a frequency of 100 Hz. After 500 ms of isometric contraction at the optimal length, the fibre shortens at a constant prescribed velocity. Three different velocities are considered: 5, 10, and 15% of the maximum shortening velocity, v_{max} .

Figure 4.17 shows the evolution of the normalised active forces (top) and the sarcomere length (ℓ_S , bottom). The profiles show, for the first part, which is identical for all three traces, an increase in the active force due to the stimulation. After 500 ms, when the force approximately saturates and the shortening starts, the model shows an instantaneous drop of the force, which is due to the shortening velocity. As expected, the magnitude of the drop increases with the shortening velocity, cf. Figure 4.15b. The model further predicts a decrease in the force, which is due to the F - ℓ relation. In detail, as the sarcomere shortens along the ascending limb of the F - ℓ relation (from the optimal length towards smaller sarcomere lengths, cf. Figure 4.15a), the region of filament overlap reduces, and hence, the force decreases.

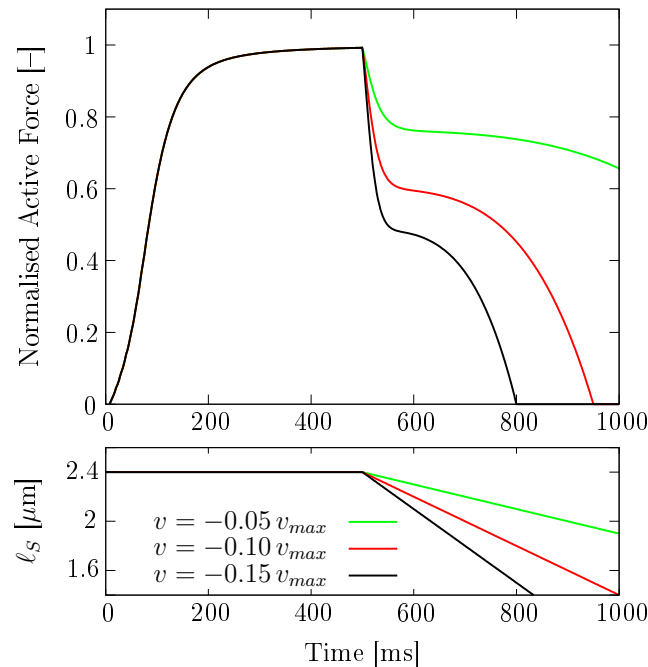


Figure 4.17: Evolution of the normalised active force of the extended model for three different shortening velocities at a stimulation frequency of 100 Hz (top). The shortening contraction is preceded by an isometric contraction of 500 ms duration at optimal length. Additionally, the actual sarcomere length (ℓ_S) is shown for each of the force profiles (bottom). Figure previously published in [111].

4.4 Modelling of the Neuromuscular System

The numerical experiments presented in the previous sections focused on the behaviour of a MN pool (Section 4.2) or the behaviour of a muscle unit under idealised conditions (Section 4.3). In this section, the muscle unit force model is coupled to the MN model of Negro & Farina [186] to establish an integrated model of the neuromuscular system that is biophysical in all its main parts. Figure 4.18 provides an overview of the integrated model, where the discharge trains predicted by the MN model are used to drive the muscle unit force model (cf. Section 4.4.1 for details).

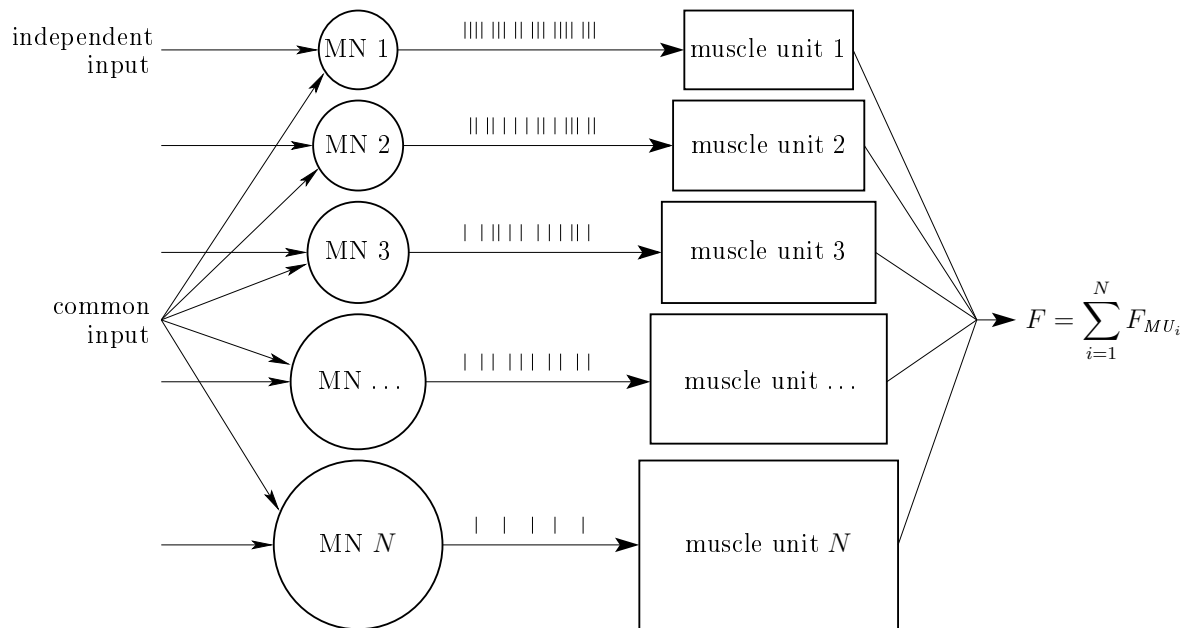


Figure 4.18: Schematic representation of the structure of the biophysical model of the neuromuscular system. The discharge trains (indicated by the vertical bars above the arrows) predicted by the motor neuron model are used to drive the muscle unit force model. The input to the coupled model is the synaptic input to the motor neurons, and the output of the model is the muscle force, which is the sum of the MU forces.

Without loss of generality, the following sections consider representatively the human FDI muscle. The presented simulations are chosen to demonstrate the capacity of the integrated model to be applied to many scenarios, such as, for example, physiological and pathological tremor.

4.4.1 Coupling the Motor Neuron Model and the Muscle Unit Force Model

The skeletal muscle model of Shorten et al. [240] is mathematically represented by a system of stiff, nonlinear ODEs. Its numerical solution requires a much smaller time step than the solution of the ODEs describing the MN model. Further, in this thesis, proprioceptors that generate afferent signals are not considered explicitly, and thus, the flow of information is unidirectional from the MN model to the muscle model. Hence, the MN model and the MU force model are not integrated into a single model that is

solved with a common time step. Instead, the models are solved successively. For each MN discharge, a stimulating current of $150 \mu\text{A}/\text{cm}^2$ and 0.5 ms duration is applied to the corresponding muscle unit model. This stimulation leads to a muscle fibre membrane depolarisation and the corresponding force generation [240]. Both models are implemented in MATLAB. For the integration of the MN model, the Adams-Bashforth-Moulton solver ODE113 is used, while ODE15s for stiff differential equations is used to solve the muscle unit model.

It is noteworthy that the MN model and the muscle unit force model can also be integrated into a single framework and solved concurrently. Such an approach is necessary when proprioceptors are considered, and hence, the muscle unit force model feeds back to the MN model. Proprioceptors, such as e. g. muscle spindles and Golgi tendon organs, are sensory organs providing the central nervous system with information about the state of the muscles. Although proprioceptors can be considered as a part of the neuromuscular system, they are not explicitly modelled in this work. If, however, a certain application requires a more detailed description of afferent signals, models of proprioceptors [173, 174] can be integrated in the presented models of the neuromuscular system.

4.4.2 Linear Ramp Increase and Decrease

Comparing Different Models

An advantage of the decoupled approach is that individual parts of the model can easily be replaced. This provides the basis to quantify the effect that each model part has on the behaviour of the whole system. Following this idea, the next case study compares parts of the proposed model of the neuromuscular system to the corresponding parts of the model of Fuglevand et al. [76]. Similarly to the proposed model, the model of Fuglevand et al. [76] consists of a MN model to determine the MN discharge times and a muscle unit force model to predict the force. In contrast to the proposed model, however, the model of Fuglevand et al. [76] is a completely phenomenological approach. In the following, the model of the neuromuscular system of Fuglevand et al. [76] is termed reference model.

An isometric contraction of the human FDI muscle is exemplarily simulated. The effective synaptic input and the excitation function used as input to the MN model of Negro & Farina [186] and the reference model, respectively, are chosen to have a ramp profile. To this end, the mean input first linearly increases up to a peak value. Symmetrically, after reaching the peak value, the mean input decreases linearly to zero with the same slope. The peak value of the input functions is chosen such that all 120 MUs of the FDI are just recruited.

The MN discharge times predicted by the biophysical model of Negro & Farina [186] are used to drive the proposed biophysical muscle unit force model and the muscle unit force model of the reference model. Similarly, the MN discharge times predicted by the MN part of reference model are used to drive both muscle unit force models.

Figure 4.19a shows the excitation function that is used as input to the MN part of the reference model. The discharge rates of twelve selected MNs as predicted by this model are depicted in Figure 4.19c. Based on these discharge rates, Figures 4.19e and 4.19g show the resulting forces of these twelve muscle units (different colours) and the total muscle force (thick black line) of the force part of the reference model [76] and the muscle unit force part of the proposed model, respectively. Note that although the simulated forces

are in arbitrary units (AU), the forces are comparable, since the twitch forces are similar in the two muscle models, cf. Figure 4.11b.

Figure 4.19b shows a representative synaptic input function that is used to drive the MN model of Negro & Farina [186]. The ramp-shaped synaptic input is common to all MNs and can be associated with an idealised cortical input to the motor nucleus. The ramp profile is superimposed by independent synaptic noise (Gaussian distributed, bandwidth 0–50 Hz) for each individual MN. The standard deviation of the independent synaptic noises is selected to generate a coefficient of variation of the interstimulus interval of approximately 15% when a steady level of synaptic current equal to the peak value of the ramp is simulated. The resulting discharge rates of twelve selected MNs as predicted by this model are depicted in Figure 4.19d. Based on these MN discharge rates, Figures 4.19f and 4.19h show the resulting forces of these twelve muscle units (different colours) and the total muscle force (thick black line) of the reference model [76] and the proposed muscle unit force model, respectively.

The predicted discharge rates demonstrate that both MN models account for Henneman’s size principle of recruitment [112, 113], i. e., the number of recruited MUs increases with increasing mean synaptic input. Further, both models show the “onion-skin” property [46, 47], i. e., earlier-recruited low-threshold MNs have for a certain level of synaptic input higher discharge rates than later-recruited high-threshold MNs. Figures 4.19c and 4.19d suggest that the model of Negro & Farina [186] predicts higher discharge rates than the MN model of Fuglevand et al. [76]. This behaviour, however, is not observed for the entire MN pool as shown in Figure 4.20. In fact, for the largest MUs, which contribute the highest forces, the MN model of Fuglevand et al. [76] predicts higher mean discharge rates than the model of Negro & Farina [186]. This might explain the fact that the reference model predicts higher forces for the discharge rates of Figure 4.19c, cf. Figure 4.19e, than for those in Figure 4.19d, cf. Figure 4.19f.

The difference between the forces of the reference model and the proposed model, cf. Figures 4.19f and 4.19h, respectively, are less pronounced for the discharge rates predicted by the model of Negro & Farina [186] shown in Figure 4.19d. This can potentially be explained by the fact that force saturation in the proposed model only occurs at discharge rates above 50 Hz, which do not occur in this simulation, cf. Figure 4.19d.

Influence of the Rate of Change of the Input

Similar to the previous example, a ramp-shaped mean synaptic input function is applied to the model of Negro & Farina [186]. While the peak synaptic input is identical in all simulations, different slopes are considered. In detail, the mean synaptic input rises from zero to its maximum value in 4, 2, and 1 s and decreases afterwards back to zero within the same times. The resulting discharge rates are used as input to the proposed muscle unit force model.

The force responses for twelve selected MUs (different colours) and the total resulting force (thick black line) are shown in Figures 4.21a–4.21c for three different slope values. Figure 4.21d compares the total forces of the three different slopes. Although the peak synaptic input is the same for all cases, the maximum total forces of the simulations with medium and high slopes are 8.2% and 18.2% higher, respectively, than the total force achieved with the lowest slope.

Although the peak synaptic input is identical for the different ramps, the integrated

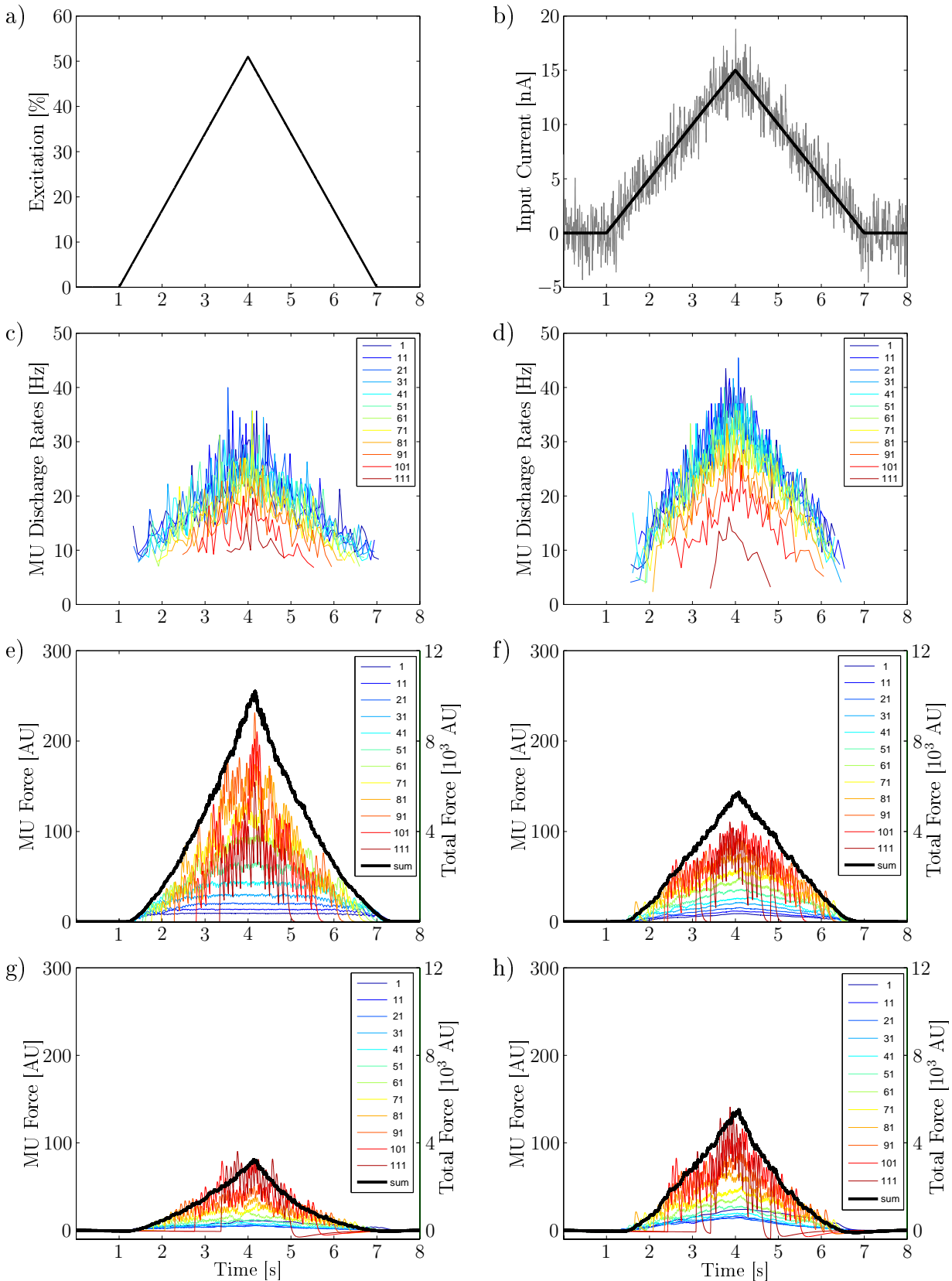


Figure 4.19: Comparison of the proposed model and the reference model [76]. (a) Ramp-shaped excitation function used as input to the reference model. (c) MN discharge rates of twelve selected MNs as predicted from the reference model. The force predicted by (e) the reference muscle unit force model and (g) the proposed muscle unit force model for the MN discharge rates in (c). (b) Ramp-shaped effective synaptic current used as input to the proposed MN model. (d) MN discharge rates predicted by the proposed MN model. The force predicted from the muscle unit force part of (f) the reference model and (h) the proposed model for the MN discharge rates in (d).

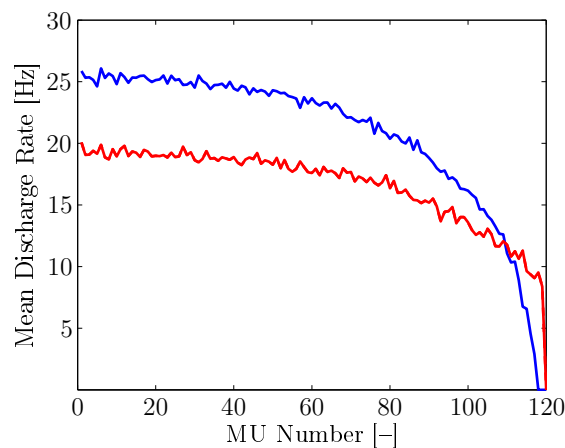


Figure 4.20: Comparison of the mean discharge rates for each motor neuron in the model of Negro & Farina [186] (blue line) and in the model of Fuglevand et al. [76] (red line).

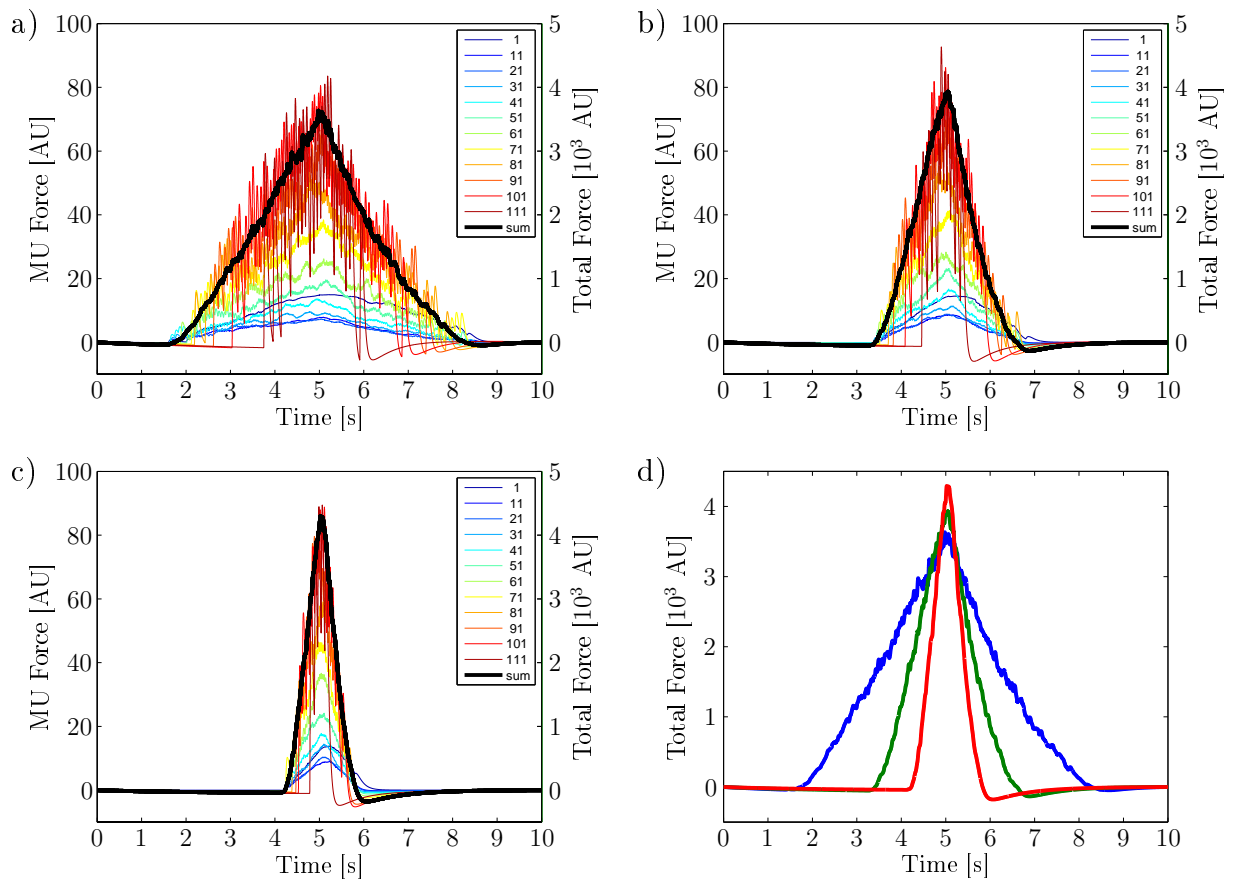


Figure 4.21: Behaviour of the model for slow and fast synaptic inputs. Forces generated by a subgroup of individual MUs and total force (black thick line) for (a) slow, (b) medium velocity, and (c) fast ramp contractions. (d) Comparison between the three total force profiles generated by simulations (a-c).

model shows a nonlinear behaviour, whereat a higher slope in the mean synaptic input current yields a higher peak force. Note that in reality an increase in the rate of change of

a voluntary contraction also causes a change in the neural drive to the muscle. However, this is not included in the model, and the predicted differences in the force response are entirely due to the muscle unit model. Therefore, the results of the ramp example cannot directly be compared to experimental data of voluntary contractions. Nonlinearities in the force response that are independent of changes in the neural drive are known from experiments, e. g., in the context of postactivation potentiation [11, 176] or early depression and potentiation, which occur when two or more stimuli are applied with a short interstimulus interval, cf. [200, 249, 250] and Section 4.3.3. In phenomenological models of skeletal muscle, these nonlinearities are often neglected (cf. e. g. Fuglevand et al. [76]), which might lead to inaccurate model predictions.

4.4.3 Force Variability

To confirm the physiological behaviour of the proposed model, the coefficient of variation of the simulated force is calculated for different net synaptic input levels. The simulated input is a steady level of current common to all MNs with an additional independent Gaussian noise in the bandwidth 0–50 Hz. The standard deviation is simulated as a function of the mean current in order to generate a coefficient of variation of the interstimulus interval of approximately 15 % for all synaptic input levels. Figure 4.22 shows the simulated results, which are in good agreement with the experimental findings of Moritz et al. [180].

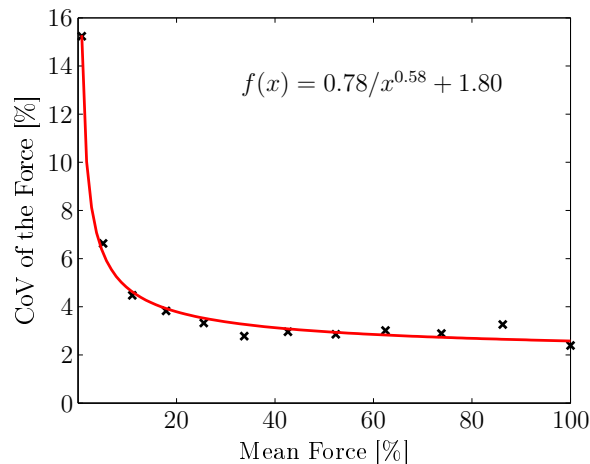


Figure 4.22: Coefficient of variation of the force versus mean force. Simulated data are shown as black crosses. Best fit $f(x)$ to the data points is shown as red line.

A function of the form

$$f(x) = \frac{a}{x^b} + c, \quad (4.29)$$

with coefficients a , b , and c is used to approximate the computed pairs of mean force (x) and coefficient of variation of the force ($f(x)$). Using a least-squares fitting algorithm, the coefficients a , b , and c are determined as 0.78, 0.58, and 1.80, respectively.

Besides the cortical input [153], common input signals are delivered to the motor nucleus by afferent neurons [134], brain stem neurons [148], and other pathways. Synaptic input components common to the MN population generate correlations between MN spike trains

that are transmitted unaltered to the force output, cf. Farina et al. [73].

The aim of the next example is to investigate the effects of common synaptic input components on the modelled force output. Two cases are considered. In the first case, the noise in the synaptic input to the MNs is completely independent (no common synaptic input other than the cortical input). In the second case, 50 % of the noise in the synaptic input is common to all MUs. Different levels of excitation, i. e., 5 % and 50 %, are simulated for both cases. The independent noise and the common synaptic noise have both Gaussian distribution and a bandwidth of 0–50 Hz.

Figure 4.23 shows the force output for the different scenarios (left column) and the corresponding power spectra of the force output (right column). In both cases, the introduction of the shared noise increases significantly the force oscillations as demonstrated by the increase of the power spectrum of the force in all frequencies. The power spectrum of a signal describes how the variance of the signal is distributed over the frequency components into which the signal may be decomposed. It indicates the portion of a signal's power (energy per unit time) falling within given frequency bins. Furthermore, the coefficient of variation of the interstimulus interval and the coefficient of variation of the force are listed in Table 4.4 for the different scenarios.

common synaptic noise	5 % excitation		50 % excitation	
	CoV-ISI	CoV-force	CoV-ISI	CoV-force
0 %	15.98 %	7.34 %	16.91 %	3.44 %
50 %	12.10 %	14.35 %	12.14 %	6.82 %

Table 4.4: *The coefficient of variation of the interstimulus interval (CoV-ISI) and the coefficient of variation of the force (CoV-force) for 5 % and 50 % excitation without common synaptic noise and with 50 % common synaptic noise.*

Considering the variation in force fluctuations across a large range of mean synaptic inputs, the present model predicts a hyperbolic relation between the coefficient of variation of the force and the mean force. While the predicted force fluctuations agree well with the experimental findings of Burnett et al. [33], Galganski et al. [79], and Laidlaw et al. [149, 150], the coefficients of variation in the simulated force are approximately twice as large as those reported by Moritz et al. [180]. If, furthermore, input components that are common to all MNs but different from the mean cortical input (e.g. afferent inputs) are included in the input currents, the modelled coefficient of variation of the force will even further increase. However, while Moritz et al. [180] measured exponentially decreasing coefficients of variation of the interstimulus interval for each MU from an average of 30 % to 13 % as force increased, an approximately constant coefficient of variation of the interstimulus interval of about 15 % is assumed in the proposed model. Furthermore, Moritz et al. [180] reported that the maximal discharge rates of MNs across the pool increases with recruitment threshold, while the present model predicts a decreasing maximal discharge rate, which is in agreement with the findings of De Luca & Hostage [46], De Luca et al. [47], Duchateau & Hainaut [60], and Tanji & Kato [257]. In summary, the behaviour of the proposed biophysical model of the neuromuscular system is in agreement with the existing experimental data.

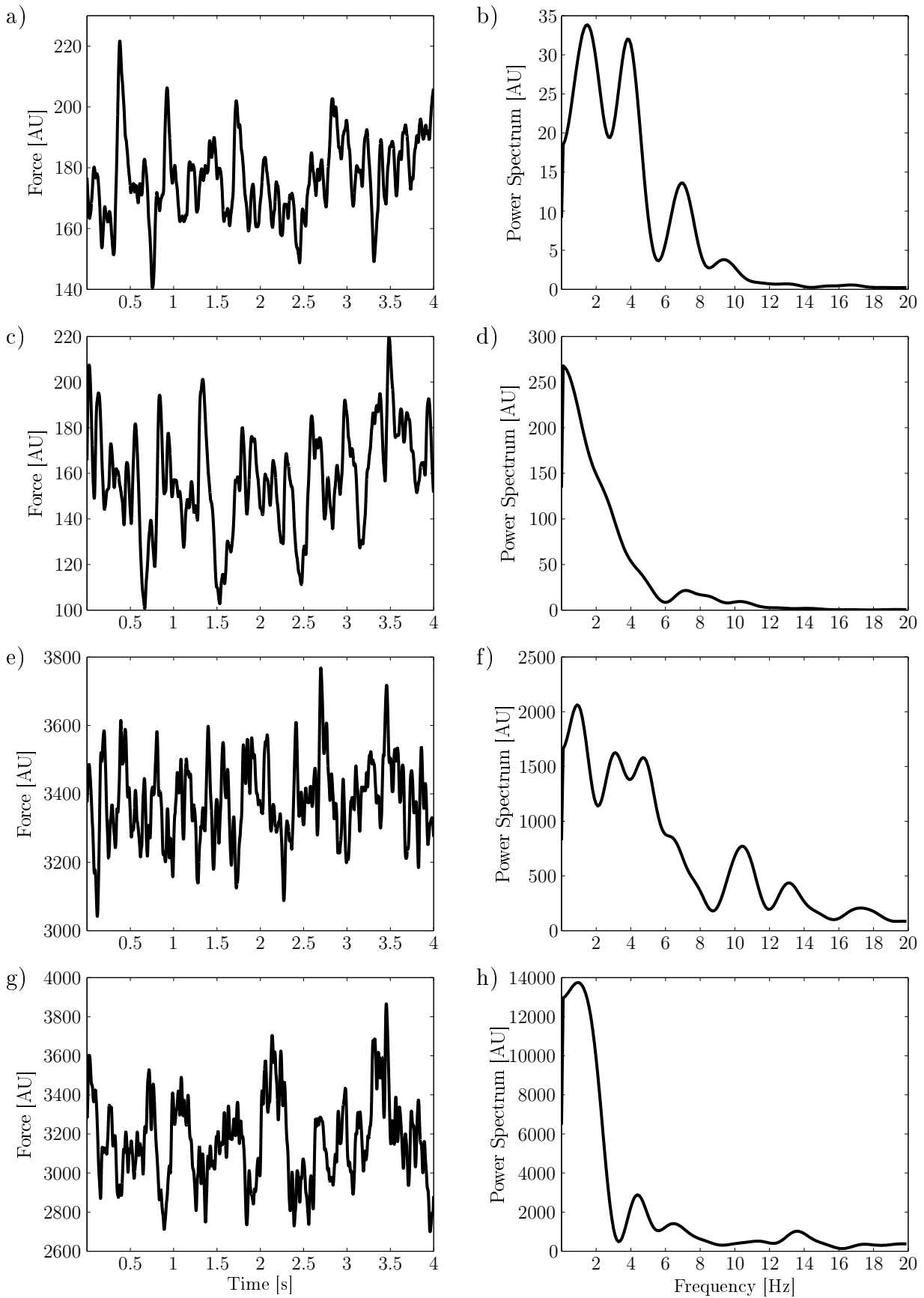


Figure 4.23: Total force (left column) and power spectrum (right column) of the force variability example. (a, b) 5% excitation, no common synaptic input; (c, d) 5% excitation, 50% common synaptic input; (e, f) 50% excitation, no common synaptic input; (g, h) 50% excitation, 50% common synaptic input.

4.4.4 Tremor

This case study demonstrates the ability of the proposed model to simulate physiological and pathological conditions. This is done by including a narrow frequency band around 8 Hz of common synaptic noises in the synaptic input to the MNs resembling tremor. The aim of this case study is to use the proposed biophysical model to quantify the influence of common synaptic noise, which resembles physiological tremor, on the force output. The mean synaptic input current is set to 5 nA and the standard deviation of the total synaptic noise (common and independent) is fixed at 1 nA in all cases. Three cases with different proportions of common synaptic noise (25 %, 35 %, and 45 % of the total synaptic noise) are considered.

Figure 4.24a shows the power spectrum of the common synaptic noise components for the three cases. For each case, the level of coherence is estimated from pairs of MU spike trains and is depicted in Figure 4.24b. Furthermore, a short segment of the total force responses is shown in Figure 4.24c.

Table 4.5 lists for each of the three cases the mean discharge rate, the mean coefficient of variation of the interstimulus interval, and the coefficient of variation of the force. To quantify the sensitivity of these quantities with respect to the amount of common synaptic input, a linear regression is carried out. The slopes of the linear regression lines are -1.5 ($R^2 = 0.998$), 2.7 ($R^2 = 0.72$), and 20.35 ($R^2 = 0.97$) for the mean discharge rates, the mean coefficients of variation of the interstimulus interval, and the coefficients of variation of the force, respectively.

common noise	Mean Discharge Rate	CoV-ISI	CoV-force
25 %	10.63 Hz	16.89 %	10.25 %
35 %	10.47 Hz	17.45 %	11.71 %
45 %	10.33 Hz	17.43 %	14.32 %

Table 4.5: Mean discharge rate, mean coefficient of variation of the interstimulus interval (CoV-ISI), and the coefficient of variation of the force (CoV-force) for the tremor example with increasing amplitude of the common synaptic noise.

With increasing common synaptic noise, the level of coherence estimated from pairs of MN spike trains increases significantly. Furthermore, linear regression demonstrates that the mean discharge rate and the mean coefficient of variation of the interstimulus interval do not change significantly with the amount of common synaptic noise, while the coefficient of variation of the force increases significantly with the amount of common synaptic noise (approximately 10-times higher slope of the linear regression line).

4.5 Discussion

A novel model of the neuromuscular system, which is biophysical in all main parts has been presented. The new model arose from coupling the MN model of Negro & Farina [186] to the model of the excitation-contraction coupling in skeletal muscle fibres of Shorten et al. [240]. In contrast to previous, biophysical models, the proposed model accounts for nonlinearities in the force response that result from the activation history.

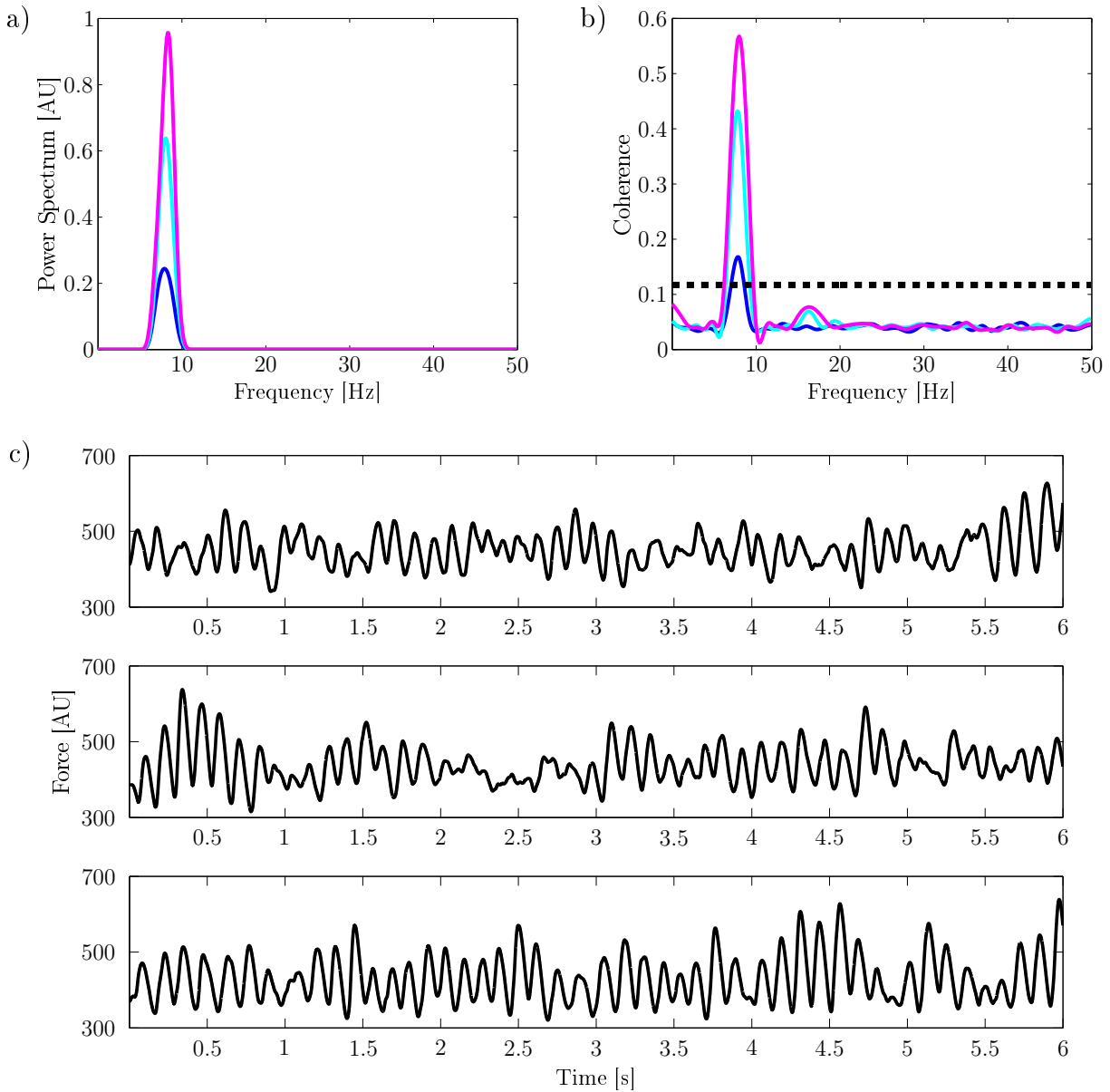


Figure 4.24: Tremor example. (a) Power spectrum of the motor neuron input when 25% (dark blue), 35% (light blue), and 45% (magenta) of the total synaptic noise is common to all motor neurons. (b) Coherence estimated from MU firing times. The dashed line shows the 95% confidence level. (c) Total simulated forces when 25% (top), 35% (middle), and 45% (bottom) of the total synaptic noise is common to all motor neurons.

To account for the different contractile properties of the muscle units in a MU pool, the slow-twitch and fast-twitch parametrisations of Shorten et al. [240] were linearly interpolated. While this simple approach is sufficient to reproduce a frequency distribution of contraction times that is similar to experimental data, it is justified to assume that the linear interpolation yields an oversimplification compared to the actual parameter distribution. In fact, certain properties of muscle units are not continuously distributed, but can be classified into discrete groups, such as, for example, the myosin heavy chain iso-

forms. Moreover, the muscle unit model of Shorten et al. [240], which has been validated for mouse muscles, has been applied to simulate human muscle. To this end, only the reaction rates within the XB dynamics model have been modified. While this simplification was necessary due to a lack of experimental data of human subcellular properties, one can easily imagine that other reaction rates in human muscles also differ from those in mouse muscles. To summarise, while the proposed model closely resembles the underlying biophysical processes of the neuromuscular system leading to force generation, there exist significant uncertainties regarding its parameters.

Wherever applicable, the behaviour of the proposed model has been compared to the model of Fuglevand et al. [76]. The model of Fuglevand et al. [76] has been chosen as reference, due to the fact that it is build on a broad range of experimental data. Although the shape of the single twitch is similar in both models, there are significant differences in the generated muscle forces, when a ramp-shaped synaptic input is applied to the motor nucleus. This also applies when recombining the individual parts (MNs and muscle units, see Figure 4.19) of the two models. It would be very interesting to see, which of the combinations yields the most accurate result, when compared to experimental data. Unfortunately, this comparison is not possible at this point, since, to date, it is not possible to completely decompose the neural drive to muscles (e. g. from the EMG) or to precisely extract the individual MU forces from the total force.

Due to its simplified, phenomenological formulation, the model of Fuglevand et al. [76] cannot be applied to more complex examples, and thus, no comparison with the proposed model can be performed. Although a quantitative analysis is not possible in each case, the qualitative behaviour of the proposed model is in agreement with experimental findings.

In conclusion, the presented examples demonstrate the capabilities of the proposed model to simulate different scenarios of normal and pathological conditions.

5 Propagation of Electrical Signals Through Biological Tissues

The previous chapter demonstrated that many properties of the neuromuscular system can be modelled using a description that is independent of the spatial components of the underlying system. Many other interesting applications, however, depend on the spatial dimensions of the musculo-skeletal system. Spatial dimensions of the tissue are essential, for example, for simulating the propagation of electrical signals through biological tissues. In skeletal muscle the propagation of action potentials along muscle fibres induces the contraction, and the resulting electrical potentials can be measured at the skin surface using a surface electromyograph.

The aim of this chapter is to extend the muscle model of Chapter 4 to take into account the spatial dimensions of the muscle. To this end, a description of the cellular membrane electrophysiology (e.g. the Hodgkin-Huxley model [120] or the model of Shorten et al. [240]) is linked to a propagation equation. This is schematically represented in Figure 5.1.

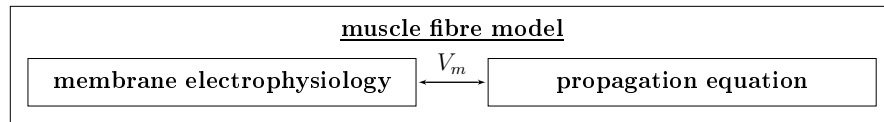


Figure 5.1: Overview of the model of a muscle fibre. The model of the membrane electrophysiology is coupled to the propagation equation through the membrane potential, V_m .

In brief, the previous chapter described the rise and fall of the AP by solving

$$I_m = C_m \frac{\partial V_m}{\partial t} + I_{ion}, \quad (5.1)$$

for $I_m = 0$, cf. Equations (4.1), (4.7), and (4.14). Considering spatial components of the muscle tissue, however, current can also flow from one point of the cell membrane to another point, and hence, the total current across the membrane does not necessarily vanish locally [185]. Based on this consideration, Hodgkin & Huxley [120] proposed the cable equation to simulate the propagation of APs along a 1D structure. Although Hodgkin & Huxley [120] considered the giant axon of the squid, the cable equation is equally applicable to muscle fibres [211]. In this work, the cable equation will be introduced as a special case of the more general bidomain equations, which will be derived in the following.

5.1 The Bidomain Model

Based on the simulation of the AP propagation in the heart [211], Röhrle et al. [220] suggested to use the bidomain equations to model the spreading of the change of the membrane potential in skeletal muscle tissue. The bidomain model is a continuum approximation of the electrophysiology of excitable biological tissues. The model describes how currents from one region of a cell interact with other regions [211].

In electrically active biological tissue, such as muscle, the bidomain model considers two interpenetrating domains representing the intracellular space (i.e., the muscle cells or fibres) and the extracellular space (i.e., the space surrounding the fibres). Since the bidomain model is a continuum model, these two spaces coexist at each point of the muscle region, Ω^M , at all times. The intracellular and extracellular domains can interact with each other through currents crossing the cell membrane, I_m . Further, each domain is assigned its own conductivity tensor and its own potential. The conductivities in the intracellular domain and the extracellular domain are denoted by σ_i and σ_e , respectively, and the intracellular potential and the extracellular potential are denoted by ϕ_i and ϕ_e , respectively. A schematic representation of the bidomain model is given in Figure 5.2.

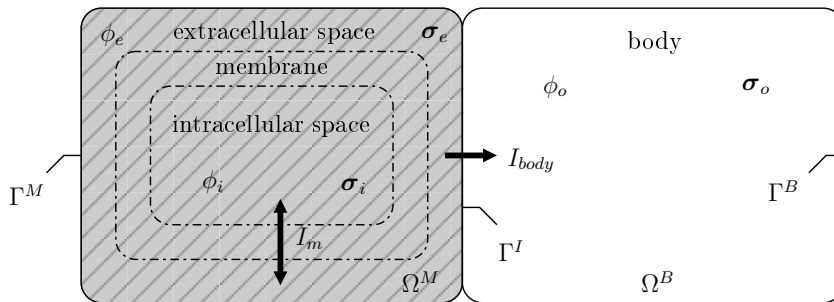


Figure 5.2: Schematic representation of the bidomain model. The bidomain model distinguishes between the electrically inactive body region, Ω^B , and the electrically active muscle region, Ω^M . At each point of the muscle region the intracellular (subscript i) and extracellular (subscript e) domains coexist at all times. While the intracellular and the extracellular domains of the muscle region interact with each other through currents crossing the cell membrane, I_m , muscle-body interactions are considered through currents between the extracellular domain of the muscle region and the body region, I_{body} . The reader is referred to the text for further details.

Besides the electrically active muscle tissue, the bidomain model allows to consider electrically inactive tissues in the body region, Ω^B , representing, for example, skin and subcutaneous fat tissue. While there is no direct interaction between the intracellular domain of the muscle region and the body region, the extracellular domain of the muscle region can interact with the body region through a current I_{body} crossing the muscle-body interface, $\Gamma^I := \partial\Omega^M \cap \partial\Omega^B$. Further, the conductivity tensor and potential in the body region are denoted by σ_o and ϕ_o , respectively. Neglecting the conductivity of the surrounding air and other adjacent tissues (e.g. bone), there is no current crossing the outer surface of the body region, $\Gamma^B := \partial\Omega^B \setminus \Gamma^I$, or the outer muscle boundary, $\Gamma^M := \partial\Omega^M \setminus \Gamma^I$.

5.1.1 Derivation of the Bidomain Equations

Several formulations of the bidomain equations exist, which differ in the dependent variables used. The formulation presented here, which can also be found, for example, in Pullan et al. [211], is in terms of the extracellular potential, ϕ_e , and membrane potential,

$$V_m := \phi_i - \phi_e. \quad (5.2)$$

This formulation has the advantage that it can interface in a straightforward manner with the cell models presented in Chapter 4, as these also rely on the membrane potential.

Describing an electric field problem, the bidomain equations can be derived from Maxwell's equations, given by

$$\begin{aligned} \operatorname{div} \mathbf{e} &= \frac{v}{\epsilon_0}, & \operatorname{rot} \mathbf{e} &= -\frac{\partial \mathbf{b}}{\partial t}, \\ \operatorname{div} \mathbf{b} &= 0, & \operatorname{rot} \mathbf{b} &= \mu_0 \left(\mathbf{q} + \epsilon_0 \frac{\partial \mathbf{e}}{\partial t} \right). \end{aligned} \quad (5.3)$$

Therein, \mathbf{e} denotes the electric field density, \mathbf{b} is the magnetic flux density, \mathbf{q} is the current density, and v denotes the electric charge density. Further, ϵ_0 and μ_0 are the permittivity and permeability of free space, respectively, and $\operatorname{rot}(\cdot)$ represents the rotation or curl operator. In addition to Maxwell's equations, a balance equation is employed to ensure continuity of current, i. e.,

$$\frac{\partial v}{\partial t} = -\operatorname{div} \mathbf{q} + S_v, \quad (5.4)$$

where S_v denotes a current source. Commonly, quasi-static conditions are assumed for muscle tissue, since the frequencies of the generated electric and magnetic fields are relatively low (less than 100 Hz), cf. e. g. Mesin [169]. Following this assumption, the time derivatives in Equations (5.3) and (5.4) can be neglected [211]. For Maxwell's equations this yields a decoupling of the electric field and the magnetic field. Since for the derivation of the bidomain equations only the electric field is required, the equations for the magnetic field are not further considered. This yields the following equations

$$\operatorname{div} \mathbf{e} = \frac{v}{\epsilon_0}, \quad \operatorname{rot} \mathbf{e} = 0, \quad \operatorname{div} \mathbf{q} = S_v. \quad (5.5)$$

Considering first the electrically active muscle region, in the absence of other sources, the current entering the extracellular domain must be equal to the current that leaves the intracellular domain. Furthermore, currents between the intracellular and extracellular domains have to cross the muscle cell membrane, and hence, the current source equals the total current crossing the membrane multiplied by the surface-area-to-volume¹, A_m , i. e.,

$$-\operatorname{div} \mathbf{q}_i = \operatorname{div} \mathbf{q}_e = A_m I_m. \quad (5.6)$$

¹Neglecting the lateral surface areas, a cylindrical-shaped fibre with length l and radius r has a surface-area-to-volume ratio of

$$A_m = \frac{2\pi r l \theta_m}{\pi r^2 l} = \frac{2\theta_m}{r},$$

where a membrane folding factor θ_m is included to account for the roughness of the fibre surface that can increase the effective membrane area by a factor of ten, cf. DiFrancesco & Noble [53].

Ohm's law states that the current density equals the ratio between the electric field density and the resistivity. Using instead of the resistivity, its inverse, the conductivity, Ohm's law reads

$$\mathbf{q} = \boldsymbol{\sigma} \mathbf{e}, \quad (5.7)$$

where $\boldsymbol{\sigma}$ is the conductivity tensor. Furthermore, Equation (5.5)₂ states that the electric field density is curl free, and hence, it can be derived from a scalar potential field, ϕ , i. e.,

$$\mathbf{e} = -\text{grad } \phi, \quad (5.8)$$

where the minus sign ensures that current flows from regions of higher potential to regions of lower potential. Combining Equations (5.6), (5.7), and (5.8), and using the definition of the membrane potential (5.2), the second bidomain equation is found, which, in rearranged form, is given by

$$\text{div}((\boldsymbol{\sigma}_i + \boldsymbol{\sigma}_e) \text{grad } \phi_e) = -\text{div}(\boldsymbol{\sigma}_i \text{grad } V_m) \quad \forall \mathbf{x} \in \Omega^M. \quad (5.9)$$

Inserting the definition of the current crossing the cell membrane (5.1) into the current balance (5.6), and again using the definition of the membrane potential (5.2) to eliminate the intracellular potential yields the first bidomain equation

$$\text{div}(\boldsymbol{\sigma}_i \text{grad } V_m) + \text{div}(\boldsymbol{\sigma}_i \text{grad } \phi_e) = A_m \left(C_m \frac{\partial V_m}{\partial t} + I_{ion} \right) \quad \forall \mathbf{x} \in \Omega^M. \quad (5.10)$$

Equations (5.9) and (5.10) are a system of two coupled partial differential equations. The first bidomain equation (5.10) relates changes in the membrane potential and the extracellular potential to currents crossing the cell membrane. From a mathematical point of view, Equation (5.10) is a parabolic PDE in the membrane potential that links to a system of ODEs, $\dot{\mathbf{y}} = \mathbf{f}(t, \mathbf{y})$, required to determine the ionic currents crossing the cell membrane, i. e., $I_{ion} = I_{ion}(t, V_m)$, where V_m is an entry of \mathbf{y} that depends on other entries of \mathbf{y} . The second bidomain equation (5.9) relates changes in the membrane potential to changes in the extracellular potential. Equation (5.9) is an elliptic PDE that is solved for the extracellular potential.

Inserting Equation (5.7) into Equation (5.5)₃ and assuming that there exists no current source in the electrically inactive body region yields a generalised Laplace equation that describes the potential distribution in the body region, i. e.,

$$\text{div}(\boldsymbol{\sigma}_o \text{grad } \phi_o) = 0 \quad \forall \mathbf{x} \in \Omega^B. \quad (5.11)$$

Note that the body region has only one domain, which corresponds to the extracellular domain of the muscle region. This is due to the fact that there are no active cellular responses but only passive electric properties in the electrically inactive body region.

Analytical solutions to the bidomain equations are not generally available and their numerical solution is computationally complex. This complexity results from the coupling between the PDEs and the system of stiff ODEs, cf. Pathmanathan et al. [201], Vigmond et al. [270]. To simplify this complexity, approximations to the bidomain equations have been developed. The most common approximation is the monodomain equation (see Sundnes et al. [255]), which will be presented in Section 5.2.

Interface and Boundary Conditions

Since the potential in the body region is the continuation of the extracellular potential of the muscle region, continuity of potential and continuity of current flow must be satisfied at the muscle-body interface. This can be achieved by demanding

$$\phi_e = \phi_o \quad \forall \mathbf{x} \in \Gamma^I, \quad (\boldsymbol{\sigma}_e \text{grad } \phi_e) \cdot \mathbf{n}^M = -(\boldsymbol{\sigma}_o \text{grad } \phi_o) \cdot \mathbf{n}^B \quad \forall \mathbf{x} \in \Gamma^I, \quad (5.12)$$

where \mathbf{n}^M and \mathbf{n}^B denote the outward-oriented unit normal vectors of the muscle region and the body region, respectively, and $\mathbf{n}^M = -\mathbf{n}^B$ at the muscle-body interface. Note that the interface conditions ensuring continuity of potential and continuity of current at the muscle-body interface (5.12) are automatically satisfied when using the finite element method.

The assumptions that there is no current flow between the intracellular domain of the muscle region and the body region and that current cannot flow across the outer muscle boundary yield the boundary condition

$$(\boldsymbol{\sigma}_i \text{grad } \phi_i) \cdot \mathbf{n}^M = 0 \quad \longrightarrow \quad (\boldsymbol{\sigma}_i \text{grad } V_m) \cdot \mathbf{n}^M = -(\boldsymbol{\sigma}_i \text{grad } \phi_e) \cdot \mathbf{n}^M \quad \forall \mathbf{x} \in \Gamma^I \cup \Gamma^M. \quad (5.13)$$

In (5.13) a change in variables has been carried out using the definition of the membrane potential, since the intracellular potential is not a primary variable of the presented formulation of the bidomain equations. Note that boundary condition (5.13) has to be applied also at the muscle-body interface, since the intracellular potential has no continuation in the body domain within the bidomain model.

Boundary condition (5.13), however, only restricts the flow of current from the intracellular domain across the outer muscle boundary. To ensure that no current can flow across the outer muscle boundary, additionally a no-flow (homogeneous Neumann) boundary condition is required for the extracellular potential, which takes the form

$$(\boldsymbol{\sigma}_e \text{grad } \phi_e) \cdot \mathbf{n}^M = 0 \quad \forall \mathbf{x} \in \Gamma^M. \quad (5.14)$$

Further, to ensure that current cannot flow over the outer boundary of the body region, a no-flow boundary condition is applied at the body surface. This condition is given by

$$(\boldsymbol{\sigma}_o \text{grad } \phi_o) \cdot \mathbf{n}^B = 0 \quad \forall \mathbf{x} \in \Gamma^B. \quad (5.15)$$

The extracellular bidomain equation (5.9) is essentially a Poisson equation, and the equation for determining the potential in the body region, Equation (5.11), is a generalised Laplace equation. Since only Neumann-type boundary conditions for a Laplace-type or a Poisson-type equation yield an ill-conditioned matrix [211], an additional boundary condition is required. Dirichlet boundary conditions far away from the electrical source, as proposed, for example, by Pullan et al. [211] for the heart/torso, are too restrictive for the EMG. Hence, a zero-mean condition, as proposed by Austin et al. [6], is applied to the extracellular bidomain equation in the muscle domain and to the generalised Laplace equation in the body domain. The zero-mean condition is given by

$$\int_{\Omega^M} \phi_e \, dv + \int_{\Omega^B} \phi_o \, dv = 0 \quad \forall \mathbf{x} \in \Omega^M \cup \Omega^B, \quad (5.16)$$

where dv denotes an infinitesimal volume element. The constraint in (5.16) can conveniently be applied in a post-processing step.

5.2 The Monodomain Model

Assuming that the intracellular and extracellular conductivity tensors have equal anisotropy ratios, i. e., $\boldsymbol{\sigma}_i = k \boldsymbol{\sigma}_e$ for some scalar $k > 0$, the bidomain equations (5.9) and (5.10) can be simplified to the monodomain equation, cf. Keener & Sneyd [144]. To this end, the second (extracellular) bidomain equation (5.9) is first rearranged

$$\begin{aligned} \operatorname{div}((\boldsymbol{\sigma}_i + \boldsymbol{\sigma}_e) \operatorname{grad} \phi_e) &= -\operatorname{div}(\boldsymbol{\sigma}_i \operatorname{grad} V_m), \\ \operatorname{div}\left(\left(1 + \frac{1}{k}\right) \boldsymbol{\sigma}_i \operatorname{grad} \phi_e\right) &= -\operatorname{div}(\boldsymbol{\sigma}_i \operatorname{grad} V_m), \\ \frac{k+1}{k} \operatorname{div}(\boldsymbol{\sigma}_i \operatorname{grad} \phi_e) &= -\operatorname{div}(\boldsymbol{\sigma}_i \operatorname{grad} V_m), \\ \operatorname{div}(\boldsymbol{\sigma}_i \operatorname{grad} \phi_e) &= -\frac{k}{k+1} \operatorname{div}(\boldsymbol{\sigma}_i \operatorname{grad} V_m), \end{aligned} \quad (5.17)$$

and then inserted into the first bidomain equation (5.10) yielding

$$\begin{aligned} \operatorname{div}(\boldsymbol{\sigma}_i \operatorname{grad} V_m) - \frac{k}{k+1} \operatorname{div}(\boldsymbol{\sigma}_i \operatorname{grad} V_m) &= A_m \left(C_m \frac{\partial V_m}{\partial t} + I_{ion} \right), \\ \frac{1}{k+1} \operatorname{div}(\boldsymbol{\sigma}_i \operatorname{grad} V_m) &= A_m \left(C_m \frac{\partial V_m}{\partial t} + I_{ion} \right), \\ \operatorname{div}((k+1)^{-1} \boldsymbol{\sigma}_i \operatorname{grad} V_m) &= A_m \left(C_m \frac{\partial V_m}{\partial t} + I_{ion} \right), \\ \operatorname{div}((k \boldsymbol{\sigma}_e + \boldsymbol{\sigma}_e)^{-1} \boldsymbol{\sigma}_i \boldsymbol{\sigma}_e \operatorname{grad} V_m) &= A_m \left(C_m \frac{\partial V_m}{\partial t} + I_{ion} \right), \\ \operatorname{div}((\boldsymbol{\sigma}_i + \boldsymbol{\sigma}_e)^{-1} \boldsymbol{\sigma}_i \boldsymbol{\sigma}_e \operatorname{grad} V_m) &= A_m \left(C_m \frac{\partial V_m}{\partial t} + I_{ion} \right). \end{aligned} \quad (5.18)$$

Introducing the effective conductivity $\boldsymbol{\sigma}_{eff} := (\boldsymbol{\sigma}_i + \boldsymbol{\sigma}_e)^{-1} \boldsymbol{\sigma}_i \boldsymbol{\sigma}_e$, the monodomain equation reads

$$\operatorname{div}(\boldsymbol{\sigma}_{eff} \operatorname{grad} V_m) = A_m \left(C_m \frac{\partial V_m}{\partial t} + I_{ion} \right) \quad \forall \mathbf{x} \in \Omega^M. \quad (5.19)$$

The monodomain equation, essentially a transient reaction-diffusion equation, is a parabolic PDE coupled to a system of ODEs, which are needed to determine I_{ion} . Comparing Equation (5.19) with the equations that describe the ionic current crossing the cell membrane in the models of Chapter 4, i. e., Equations (4.1), (4.7), and (4.14), the monodomain equation contains additionally a diffusive term. The diffusion of the membrane potential depolarises the membrane potential of adjacent segments of a fibre. If the threshold value is reached, voltage gated channels in these segments will produce the AP and restore the impulse shape of the propagating AP.

Although the monodomain model is an exact representation of the bidomain model only if the extracellular and intracellular conductivity tensors are equally anisotropic, the monodomain model is also often employed in other cases as an approximation [191]. To this end, Nielsen et al. [191] present mathematically optimal monodomain approximations

to the bidomain model.

Within the limits of this approximation, it is sufficient to solve the monodomain equation (5.19) if one is only interested in the membrane potential. If one is also interested in the extracellular potential, one needs to solve the second bidomain equation (5.9) for the extracellular potential, after solving the monodomain equation (5.19) for the membrane potential. Since the monodomain equation (5.19) does not rely on the extracellular potential, these calculations can be carried out in a decoupled fashion, which enables a simple parallel execution.

To accurately simulate the propagation of APs through muscle tissue, a detailed knowledge of the underlying material parameters is required. Here, especially the conductivities of the intracellular and extracellular domains in lateral and transversal directions of the muscle are of interest. As often in biomechanics, however, these parameters are not readily available. In fact, the experimentally determined values for muscle conductivities vary by at least a factor of five, cf. Gielen et al. [84], Lowery et al. [160]. However, due to the fact that gap junctions do not exist in skeletal muscle tissue, the AP is not transferred between adjacent fibres. Gap junctions are specialised intercellular connections between two cells that are present in most tissues, e.g. the myocardium (cardiac muscle tissue) of the heart. Since electrical stimulation from one fibre to adjacent ones does not occur, it is pertinent to consider the propagation of APs along a muscle fibre as a 1D problem. The 1D representation of the monodomain equation reads

$$\frac{\partial}{\partial s} \left(\sigma_{eff} \frac{\partial V_m}{\partial s} \right) = A_m \left(C_m \frac{\partial V_m}{\partial t} + I_{ion} \right), \quad (5.20)$$

where s is the spatial variable along the muscle fibre, and σ_{eff} denotes the conductivity, which is a scalar for 1D problems. Further, for 1D problems, the monodomain approximation (the conductivity tensors have equal anisotropy ratios) is always satisfied (cf. Nielsen et al. [191]), and thus, the monodomain model is equivalent to the bidomain model. It is furthermore noteworthy that the 1D monodomain equation with constant conductivities coincides with the cable equation proposed by Hodgkin & Huxley [120].

Boundary Conditions

Similar to the bidomain model, the most common boundary condition for the monodomain model is the no-flow boundary condition. Neglecting the conductivity of adjacent structures, current cannot flow out of the muscle domain. Thus, for the membrane potential of the monodomain model, no-flow (homogeneous Neumann) boundary conditions are applied at all muscle domain boundaries, yielding

$$(\sigma_{eff} \text{grad } V_m) \cdot \mathbf{n}^M = 0 \quad \forall \mathbf{x} \in \Gamma^M. \quad (5.21)$$

If, in addition to the membrane potential, the extracellular potential is of interest, one can first solve the monodomain equation (5.19) for the membrane potential, and then solve the extracellular bidomain equation (5.9) in the muscle domain, and, if appropriate, the generalised Laplace equation (5.11) in the body domain. To this end, the appropriate boundary conditions for these equations are applied, see Section 5.1.1.

5.2.1 Numerical Methods for Solving the Monodomain Equation

Analytic solutions to the monodomain equation are restricted to low dimensional problems and very simple phenomenological cell models, e.g. the cubic polynomial ionic current model, cf. Hunter et al. [126]. For complex, nonlinear biophysical cell models, such as the model of Hodgkin & Huxley [120] or the model of Shorten et al. [240], however, analytic solutions are generally not available.

Numerical methods for the solution of PDEs typically rely on a discrete representation of its differential terms, see Section 3.1. To this end, it is often convenient to first treat the spatial derivatives yielding a system of coupled ODEs, before treating the time derivatives. Discretising the monodomain equation in space, a reaction term $I_{ion,i} = I_{ion}(t, V_{m,i})$ occurs at each spatial discretisation point i of the space-discrete, time-continuous equation. For a problem with n spatial discretisation points and a cell model of dimension m , this yields a system of coupled nonlinear ODEs of dimension $m \times n$ that has to be solved using a Newton iteration in every time step. Furthermore, biophysical cell models are often mathematically represented by stiff differential equations, requiring very small time steps to resolve the steep gradients and rapid changes occurring in these models [211].

Although it is certainly possible to follow this approach, it is not very efficient from a computational point of view. Instead, operator splitting methods [155] that allow to treat the cell models separately from the diffusion term are frequently used for the solution of the monodomain and bidomain equations, cf. e.g. Qu & Garfinkel [212], Sundnes et al. [254], Whiteley [275].

Operator Splitting Methods

In contrast to the approach discussed above, the presented operator splitting methods rely on first discretising the temporal derivatives, and then treating the spatial derivatives. These methods can be represented using the abstract notation

$$\frac{\partial u}{\partial t} = \sum_{i=1}^N \mathcal{L}_i(u), \quad (5.22)$$

where \mathcal{L}_i represents an operator, such as, for example, a spatial derivative, u is the unknown function, and N denotes the number of steps of the splitting method. Two common operator splitting techniques are presented in the following, the Godunov splitting and the Strang splitting. The reader is referred to LeVeque [155] and Strang [251] for further details.

Godunov Operator Splitting The simplest differential operator splitting technique is called Godunov splitting and is obtained for $N = 2$. Its splitting error is of first order, i.e., $\mathcal{O}(h)$. Since the overall order of a numerical method can never be higher than its submethods lowest order, it is sufficient to use first-order time-stepping schemes for the resulting subproblems. Applying the Godunov splitting to the monodomain equation (5.19)

and employing finite differences for the time discretisation, Equation (5.22) yields

$$\begin{aligned}\mathcal{L}_1(V_m) &:= \frac{V_m^* - V_m^k}{h} = -\frac{1}{C_m} I_{ion}, & h = t^{k+1} - t^k, \\ \mathcal{L}_2(V_m) &:= \frac{V_m^{k+1} - V_m^*}{h} = \frac{1}{A_m C_m} \operatorname{div}(\sigma_{eff} \operatorname{grad} V_m), & h = t^{k+1} - t^k,\end{aligned}\quad (5.23)$$

where V_m^k and V_m^{k+1} are the discrete solutions at times t^k and t^{k+1} , respectively, and V_m^* denotes an intermediate step introduced through the operator splitting method. Note that each equation in (5.23) is solved over the interval $[t^k, t^{k+1}]$. Figure 5.3a graphically represents the Godunov operator splitting method.

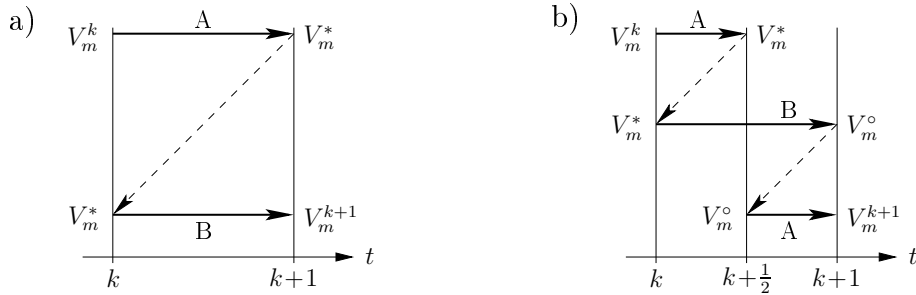


Figure 5.3: Schematic representation of the time stepping in operator splitting methods, where A denotes the solution of the reaction term I_{ion} , and B marks the solution of the transient diffusion equation. (a) Godunov splitting. (b) Strang splitting.

Strang Operator Splitting The Strang splitting [251] obtained for $N = 3$ yields second-order accuracy assuming each subproblem is solved using a method of at least this accuracy. The Strang splitting of the monodomain equation is given by

$$\begin{aligned}\mathcal{L}_1(V_m) &:= \frac{V_m^* - V_m^k}{\frac{1}{2}h} = -\frac{1}{C_m} I_{ion}, & \frac{1}{2}h = t^{k+1/2} - t^k, \\ \mathcal{L}_2(V_m) &:= \frac{V_m^circ - V_m^*}{h} = \frac{1}{A_m C_m} \operatorname{div}(\sigma_{eff} \operatorname{grad} V_m), & h = t^{k+1} - t^k, \\ \mathcal{L}_3(V_m) &:= \frac{V_m^{k+1} - V_m^circ}{\frac{1}{2}h} = -\frac{1}{C_m} I_{ion}, & \frac{1}{2}h = t^{k+1} - t^{k+1/2},\end{aligned}$$

where a further intermediate step V_m^circ has been introduced. The Strang splitting scheme is graphically represented in Figure 5.3b.

Employing operator-splitting methods to the monodomain and bidomain equations provides several advantages. The most obvious advantage results from the fact that the reaction term, I_{ion} , at one discretisation point can be evaluated completely independent of all other discretisation points. Thus, instead of solving one huge nonlinear system, many small systems are solved. This is typically much faster and can easily be done in parallel, potentially employing a massively parallel GPGPU (general-purpose computing graphics processing units), cf. Rocha et al. [218]. Moreover, due to the separation of the reaction term from the diffusion term, the most suitable numerical method can be used for each subproblem. Hence, the transient diffusion equation (5.23)₂, a linear parabolic PDE, can

be treated differently than the nonlinear ODE in (5.23)₁. This also includes that different time step sizes can be used to solve the equations within the interval $[t^k, t^{k+1}]$, e. g., subcycling can be performed. This is particularly interesting for the integration of biophysical cell models, which are commonly described by stiff equations and require very small time step sizes to resolve the rapid changes and steep gradients that are occurring especially during the rising phase of an AP.

5.3 Simulating the Action Potential Propagation

The first part of this section demonstrates that for the presented applications the monodomain model is a good approximation to the more complex bidomain model. Based on this result, the subsequent parts of this section investigate the effect that the choice of material and discretisation properties of the monodomain model have on the AP propagation.

5.3.1 Comparing the Monodomain and Bidomain Models

As previously mentioned, the monodomain model equals the bidomain model only if the assumption of equal anisotropy ratios of the intracellular and extracellular conductivity tensors is satisfied. Appendix C presents numerical examples demonstrating this behaviour. The aim of this section is to investigate how well the monodomain model approximates the bidomain model for the present applications if the assumption of equal anisotropy ratios is not satisfied.

The investigation is carried out on a simple two-dimensional (2D) test problem of size $\Omega^M = [x_1, x_2] = [0, 0.0625 \text{ cm}]^2$. The domain is discretised using the finite difference method and 10 discretisation points in each direction. No body domain is considered. The Godunov operator splitting is employed for both the monodomain equation (5.19) and the bidomain equations. The coupled PDEs representing the bidomain model (5.9) and (5.10) are solved in a monolithic fashion. The fast-twitch parametrisation of the cell model of Shorten et al. [240] is used to represent the ionic currents crossing the cell membrane. Furthermore, the surface-area-to-volume ratio, A_m , and the membrane capacitance, C_m , are chosen to be 500 cm^{-1} and $1.0 \mu\text{F}/\text{cm}^2$, respectively, [221, 240]. Both models are implemented in MATLAB. The (implicit) backward Euler method and a time step size of 0.01 ms are used to solve the PDEs. MATLAB's build-in solver ODE15s is employed to integrate the stiff ODEs of the cell model of Shorten et al. [240] using optimised internal time steps within intervals of 0.01 ms. To evoke an AP, a stimulating current sufficiently high to depolarise the membrane potential is injected close to a corner of the domain, one grid point away from the boundary in each direction.

It is interesting to note that for the very small examples considered in this section, there is almost no difference in the computation time required to solve the monodomain and the bidomain problems. This can partially be explained by the fact that the solution of the cell model of Shorten et al. [240], which needs to be carried out in both models, requires most of the computing time, while the solution of the linear matrix system, which contains twice as many equations for the bidomain model than for the monodomain model, requires only very little time. Furthermore, it is noteworthy that the $m \times m$ matrix arising from the discretisation of the bidomain model has rank $m - 1$, i. e., it is singular (2-norm

condition number $1.37 \cdot 10^{17}$). The singularity arises from exclusively using Neumann boundary conditions for the extracellular bidomain equation, which is a Poisson-type equation. For the resulting system of equations, an infinite number of solutions for the extracellular potential exists. MATLAB still solves the linear system of equations. The zero-mean condition (5.16) is applied in a post-processing step to determine a reasonable solution for the extracellular potential.

Conductivity Tensors with Unequal Anisotropy Ratios

Two different test cases are considered. The first test case assumes an anisotropy ratio of 10 for the intracellular conductivity tensor and an isotropic extracellular conductivity tensor (anisotropy ratio of 1), cf. Mordhorst et al. [178]. In detail, the following conductivity tensors are considered:

$$\boldsymbol{\sigma}_i = 8.93 \begin{bmatrix} 1 & 0 \\ 0 & 0.1 \end{bmatrix} \mathbf{e}_k \otimes \mathbf{e}_l, \quad \boldsymbol{\sigma}_e = 6.7 \begin{bmatrix} 1 & 0 \\ 0 & 1 \end{bmatrix} \mathbf{e}_k \otimes \mathbf{e}_l. \quad (5.24)$$

Based on the conductivity tensors in (5.24), Figures 5.4a – 5.4c compare the evolution of the membrane potential of the monodomain and bidomain models at three different grid points. Furthermore, the distribution of the difference between the monodomain and bidomain models is depicted in Figure 5.4d 0.5 ms after stimulation has been applied at node $(x_1, x_2) = (9, 9)$.

While the membrane potentials based on the monodomain and the bidomain models are quite similar, one can observe that the difference between the two models increases with increasing distance from the stimulation point. This is due to the fact that for the conductivity tensors in (5.24) the propagation velocity in the bidomain model is slightly higher than in the monodomain model. The higher propagation velocity can be explained by an interaction of the membrane potential with the extracellular potential in the bidomain model, which is neglected when using the monodomain model. Furthermore, the differences between the two models are significantly larger than in the previous test cases and are now of the order of several millivolts, cf. Figure 5.4d. The maximum difference between the models is 24.04 mV and occurs at node $(x_1, x_2) = (9, 10)$ 0.03 ms after stimulation. It is however noteworthy that except for grid points close to the stimulation point at times briefly after stimulation, the difference between the two models is less than 10 mV, cf. Figure 5.4. Although differences exist between the two models, it can be concluded that for the conductivity tensors in (5.24), the monodomain model approximates the bidomain model quite well.

It is furthermore noteworthy that for these conductivity tensors propagation of the AP is fast in the x_1 -direction but also occurs at a slower rate in the x_2 -direction, due to the assumed intracellular conductivity in this direction. In skeletal muscle, however, the APs only propagate along the muscle fibres but not perpendicular to them. This is due to the fact that gap junctions do not exist in skeletal muscle tissue.

The absence of gap junctions in skeletal muscle tissue inspired the choice of conductivities used in the second test case. Here, for the intracellular domain, conductivity exists only in one direction, i. e., the fibre direction, which is assumed to coincide with the x_1 -direction. The values of the extracellular conductivity tensor are chosen such that the resulting conductivity tensor on the left-hand side of the extracellular bidomain equa-

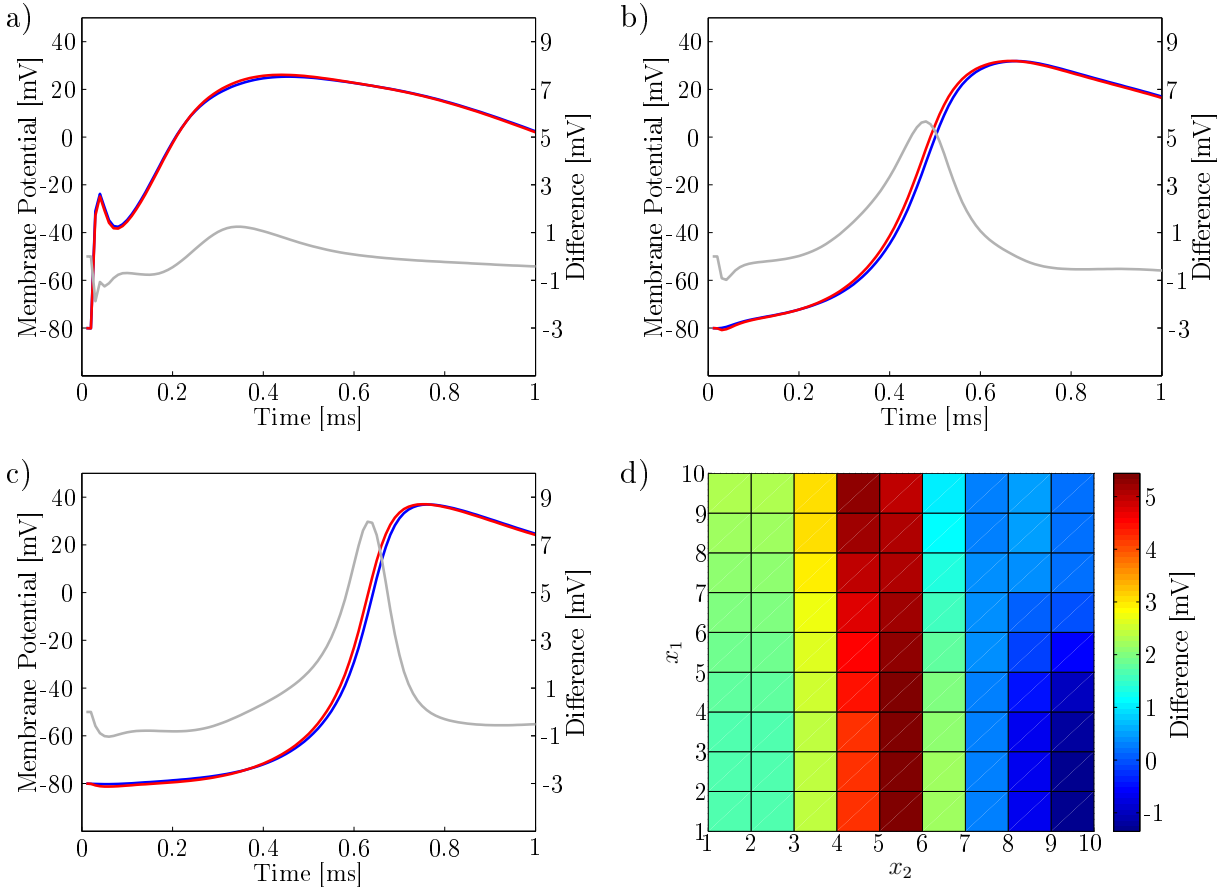


Figure 5.4: Difference of the membrane potential of the monodomain and bidomain models for an anisotropic intracellular conductivity tensor and an isotropic extracellular conductivity tensor. The evolution of the membrane potential of the bidomain model (red) and the monodomain model (blue) is shown (a) at node $(x_1, x_2) = (8, 8)$, (b) at node $(x_1, x_2) = (5, 5)$, and (c) at node $(x_1, x_2) = (2, 2)$. In addition, (a–c) show the difference between these two models (gray, right y-axis). (d) The distribution of the difference (in mV) between the bidomain and the monodomain models is depicted 0.5 ms after stimulation has been applied at node $(x_1, x_2) = (9, 9)$.

tion (5.9), i. e., $\sigma_i + \sigma_e$, has an anisotropy ratio of 5, cf. e. g. Mesin [170]. In detail, the following conductivity tensors are used:

$$\sigma_i = \begin{bmatrix} 8.93 & 0 \\ 0 & 0 \end{bmatrix} \mathbf{e}_k \otimes \mathbf{e}_l, \quad \sigma_e = \begin{bmatrix} 6.7 & 0 \\ 0 & 3.126 \end{bmatrix} \mathbf{e}_k \otimes \mathbf{e}_l. \quad (5.25)$$

Based on these conductivity tensors, Figures 5.5a – 5.5e compare the evolution of the membrane potential of the monodomain and bidomain models at five different grid points. Furthermore, Figure 5.5f depicts the distribution of the difference between the monodomain and bidomain models 0.25 ms after stimulation has been applied at node $(x_1, x_2) = (9, 9)$.

To interpret the results of Figure 5.5, it is pertinent to consider also the distribution of the extracellular potential. For the bidomain model, the extracellular potential is a primary variable. After applying the zero-mean condition (5.16), the extracellular potential can directly be stated. The extracellular potential, however, is not a variable of the mono-

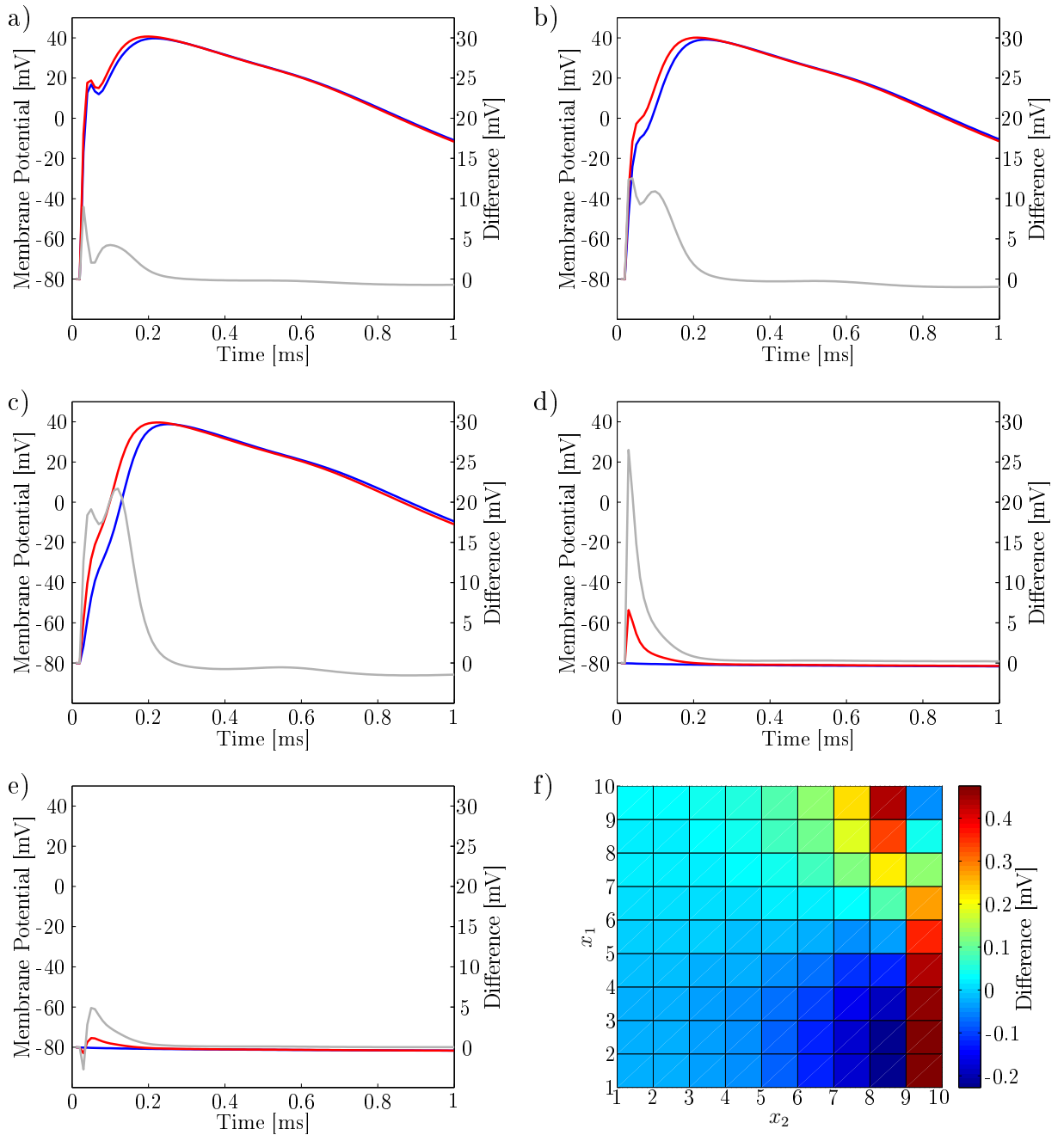


Figure 5.5: *Difference of the membrane potential of the monodomain and bidomain models for an intracellular conductivity only in fibre direction and an anisotropic extracellular conductivity tensor. The evolution of the membrane potential of the bidomain model (red) and the monodomain model (blue) is shown (a) at node $(x_1, x_2) = (6, 9)$, (b) at node $(x_1, x_2) = (5, 9)$, (c) at node $(x_1, x_2) = (3, 9)$, (d) at node $(x_1, x_2) = (9, 8)$, and (e) at node $(x_1, x_2) = (9, 7)$. In addition, (a–e) show the difference between these two models (gray, right y-axis). (f) The distribution of the difference (in mV) between the bidomain and the monodomain models is depicted 0.25 ms after stimulation has been applied at node $(x_1, x_2) = (9, 9)$.*

domain model, and hence, based on the computed membrane potential distribution, the extracellular bidomain equation has to be solved for the extracellular potential. Again, the zero-mean condition (5.16) is applied in a post-processing step.

For the conductivity tensors in (5.25), Figure 5.6 compares the distribution of the bidomain-based extracellular potential with the monodomain-based extracellular potential 0.2 ms after stimulation has been applied at node $(x_1, x_2) = (9, 9)$.

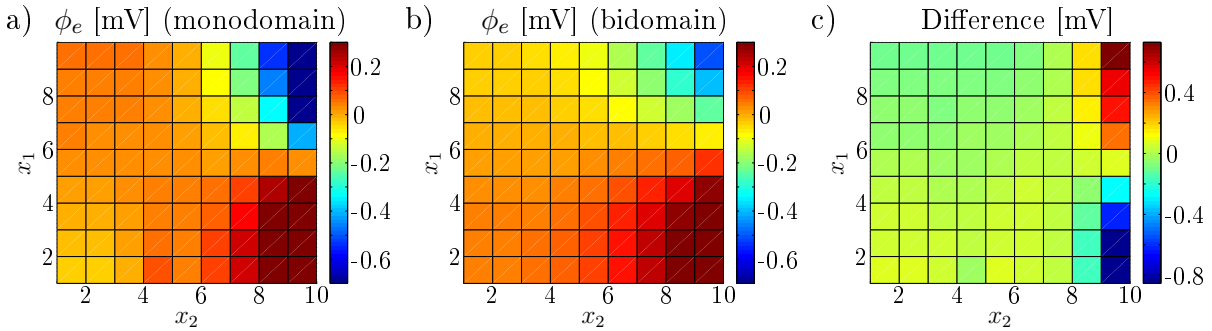


Figure 5.6: Distribution of (a) the monodomain-based extracellular potential (in mV), (b) the bidomain-based extracellular potential (in mV), and (c) the difference between the models (in mV) for intracellular conductivity only in x_1 -direction and an anisotropic extracellular conductivity tensor. The results are shown 0.2 ms after stimulation has been applied at node $(x_1, x_2) = (9, 9)$.

Considering the membrane potential in Figure 5.5, it can be observed that for the conductivity tensors in (5.25), the AP propagates almost exclusively in the fibre direction. Along this direction, the membrane potential of the monodomain and bidomain models are comparable, whereas the bidomain model again shows a slightly higher propagation velocity (cf. Figures 5.5a–c). Normal to the fibre direction, there is no propagation of the membrane potential in the monodomain model (cf. Figures 5.5d and 5.5e). In contrast, in the bidomain model, propagation of the membrane potential also occurs normal to the fibre direction due to a non-zero entry in the extracellular conductivity tensor in this direction. This is due to the fact that the extracellular potential propagating normal to the fibre direction induces a change in the membrane potential at grid points that are located at a distance in x_2 -direction from the stimulation point, cf. Figure 5.6. Solving successively the monodomain and the extracellular bidomain equations, the extracellular potential does not influence the membrane potential, and hence, the extracellular potential distribution in Figure 5.6a has no influence on the membrane potential. It is, however, noteworthy that the propagation equation for the extracellular potential is a Poisson equation, describing diffusion processes, and hence, the potentials rapidly decline with increasing distance in x_2 -direction. The induced membrane potential at grid points next to those along which the AP propagates is low enough that the membrane potential in the cell models associated with these grid points does not reach the threshold potential, and hence, no AP is generated at these points.

The maximum difference in the membrane potential between the models is 36.16 mV and occurs 0.03 ms after stimulating node $(x_1, x_2) = (9, 10)$. Except for grid points close to those along which the AP propagates, the difference between the two models is much smaller, cf. Figure 5.5. Thus, differences between the extracellular potentials of the two models are of the order of the extracellular potential close to the propagating AP but vanish with increasing distance from the AP, cf. Figure 5.6. It can be concluded that, for the conductivities in (5.25), the monodomain model approximates well the AP propagation along the fibres, while it exhibits significant differences in the normal-to-fibre (cross-fibre) direction. The most important property of the propagation equations, however, is the AP propagation along the muscle fibres.

5.3.2 Propagation of the Action Potential Along Muscle Fibres

The previous section demonstrated that the monodomain model is a good approximation to the bidomain model for the considered applications. Based on this result, the 1D monodomain equation (5.20) is now used to simulate the propagation of APs along muscle fibres. As before, the model of Shorten et al. [240] is employed to represent the ionic currents crossing the cell membrane.

Making use of the Godunov operator splitting method, Equation (5.23)₁ is integrated using the forward Euler method. For the time discretisation of the transient diffusion equation (5.23)₂ the backward Euler method is employed. In the following, a 6 cm long fibre is considered. The fibre is spatially discretised using linear Lagrange finite elements. Unless otherwise stated, the material parameters listed in Table 5.1 are used for the simulations.

Symbol	Description	Value (slow/fast)	Unit	Ref.
σ_{eff}	effective conductivity	3.828	mS/cm	[221]
A_m	surface-area-to-volume ratio	500	cm ⁻¹	[221]
C_m	membrane capacitance	0.58/1.0	μF/cm ²	[240]

Table 5.1: *Material parameters for the monodomain equation.*

The weak form of the monodomain equation is provided in Appendix D.1, and its finite element formulation has been implemented in the open-source software library `OpenCMISS`². For the integration of the cell model use is made of the CellML API (application programmer interface). Further implementational details are provided in Bradley et al. [26].

5.3.3 Influence of the Time Step Size

The aim of this section is to investigate the influence of the time step sizes used for the solution of the ODE and PDE models, which result from the operator splitting. To this end, the 6 cm long muscle fibre is homogeneously discretised using 1152 one-dimensional, linear Lagrange finite elements. All simulations employ the fast-twitch parametrisation of the model of Shorten et al. [240]. The fibre is stimulated by injecting a current of 9600 μA/cm² for 0.1 ms into the intracellular domain at the leftmost node of the finite element mesh. To avoid boundary and stimulation effects, the propagation time is measured between two nodes that are 5 cm apart from each other and remain away from both boundaries. The times at which the AP reaches its maximum value at each of the two nodes are used to compute the propagation speed.

First, the effect of the time step size used for the solution of the cell model is investigated. To this end, the time step size for the transient diffusion equation is fixed at $h^{DEQ} = 0.0005$ ms. Table 5.2 (left) lists the resulting AP propagation times required to travel the 5 cm long distance and the corresponding propagation velocities for different cell model time step sizes. It can be observed that the propagation speed converges towards approximately 1.95 m/s.

²<http://physiomeproject.org/software/opencmis>

Having investigated the effect of the cell model time step size, now the influence of the time step size for the solution of the diffusion equation is analysed. To this end, the cell model time step size is fixed at $h^{ODE} = 0.0001$ ms. Table 5.2 (right) summarises the propagation times and velocities for different time step sizes of the diffusion equation.

h^{ODE} [ms]	time [ms]	velocity [m/s]	h^{DEQ} [ms]	time [ms]	velocity [m/s]
0.001	no convergence		0.01	26.6	1.88
0.0001	23.6	2.12	0.005	26.0	1.92
0.00001	25.4	1.97	0.001	24.8	2.02
0.000001	25.6	1.95	0.0005	23.6	2.12

Table 5.2: Propagation times and velocities required by the AP to travel a 5 cm long distance for (left) different cell model time step sizes, h^{ODE} , and a fixed time step size of $h^{DEQ} = 0.0005$ ms for the transient diffusion equation, and (right) different time step sizes for the transient diffusion equation, h^{DEQ} , and a fixed time step size for the cell model of $h^{ODE} = 0.0001$ ms.

Interestingly, decreasing the time step size of the cell model, h^{ODE} , yields a decrease in the propagation velocity, while a decrease of the time step size of the diffusion equation, h^{DEQ} , yields an increase in the propagation velocity. In detail, reducing the cell model time step size by an order of magnitude caused an 8.7% decrease of the propagation velocity. Further, a reduction of the time step size of the diffusion equation by an order of magnitude yielded a 9.4% increase in the propagation velocity. Furthermore, it should be mentioned that a decrease of the time step size comes at the cost of increased computing time. This applies, in particular, to the cell model, where a reduction caused a dramatic increase of the total computing time (result not show). This can be explained by the fact that the solution of the nonlinear cell models is much slower than the solution of the linear diffusion equation.

5.3.4 Influence of the Element Size

This example investigates the influence that the element size has on the propagation velocity. The investigation is carried out for both the fast-twitch and the slow-twitch parametrisation of the cell model of Shorten et al. [240]. Similar to the previous examples, a 6 cm long 1D muscle fibre is stimulated at the leftmost node, and the propagation time between two nodes that are 5 cm apart from each other is measured. The time step sizes for the cell model and the transient diffusion equation are $h^{ODE} = 0.0001$ ms and $h^{DEQ} = 0.0005$ ms, respectively.

Initially, the 6 cm long fibre is discretised using 144 linear Lagrange finite elements. Successively, the number of elements is doubled until convergence of the propagation velocity is achieved. Following Pathmanathan et al. [201], the stimulation current has to be adjusted when changing the discretisation. For the discretisation with the fewest elements, here 144 elements, the injected currents equal $1200 \mu\text{A}/\text{cm}^2$ and $2000 \mu\text{A}/\text{cm}^2$ for the slow-twitch and the fast-twitch parametrisations, respectively. These values double when the number of elements are doubled, since the amount of injected current is proportional to the number of elements, when injecting current at a single node.

Table 5.3 summarises for the different discretisations the AP propagation times required for the 5 cm long distance and the resulting AP propagation velocities using the fast-twitch (left) and slow-twitch (right) parametrisations of Shorten et al. [240].

N_e	time [ms]	velocity [m/s]	N_e	time [ms]	velocity [m/s]
144	24.6	2.03	144	35.8	1.40
288	25.4	1.97	288	37.0	1.35
576	26.2	1.91	576	37.4	1.34
1152	26.4	1.89	1152	37.6	1.33
2304	26.4	1.89	2304	37.6	1.33

Table 5.3: Action potential propagation times required to travel a 5 cm long distance and resulting conduction velocities in fast-twitch (left) and slow-twitch (right) muscle fibres for different number of elements, N_e .

For both parametrisations, the propagation velocity converges when decreasing the element size. The converged propagation velocities are 1.89 m/s and 1.33 m/s for the fast-twitch and the slow-twitch parametrisations, respectively. Experimentally determined AP propagation velocities usually range from approximately 2 m/s to 6 m/s, cf. e. g. McGill & Lateva [164]. The fact that the AP propagation velocities predicted by the model are smaller than literature values might be attributed to inaccurate material parameters. Hence, the influence of the material parameters is investigated in the following section.

5.3.5 Influence of Material Parameters

The 1D monodomain equation (5.20) depends on three material parameters – the effective conductivity, σ_{eff} , the membrane capacitance, C_m , and the surface-area-to-volume ratio, A_m . However, assuming a homogeneous conductivity, the formulation reduces to two effective parameters – the membrane capacitance and the ratio between the conductivity and the surface-area-to-volume ratio. To investigate the effect these parameters have on the AP propagation, and to analyse the sensitivity of the propagation velocity to changes in these parameters, a systematic variation of the parameters is carried out. The fast-twitch parametrisation of the model of Shorten et al. [240] is used for the investigation. Time steps sizes are $h^{ODE} = 0.0001$ ms for the cell model and $h^{DEQ} = 0.0005$ ms for the diffusion equation. Further, 1152 linear Lagrange finite elements are used for the spatial discretisation of the 6 cm long fibre.

Table 5.4 summarises for different values of the material parameters the time an AP requires to propagate along a 5 cm long segment of a muscle fibre and the corresponding propagation velocity. The results indicates that both a lower membrane capacitance and a higher ratio between the conductivity and the surface-area-to-volume ratio yield a higher conduction velocity. Since the aim of this work is not to model a specific muscle but rather the development of methods for the simulation of any skeletal muscle, the material parameters of Table 5.1, which are based on literature values, are still used in the following simulations.

σ_{eff}/A_m [μS]	C_m [$\mu\text{F}/\text{cm}^2$]	time [ms]	velocity [m/s]	Remarks
1.914	1.0	48.2	1.04	
3.828	1.0	33.4	1.50	
7.656	1.0	23.6	2.12	<i>C</i>
15.312	1.0	16.8	2.98	
30.624	1.0	–	–	<i>A</i>
7.656	0.25	13.3	3.76	<i>B</i>
7.656	0.5	16.8	2.98	
7.656	2.0	33.4	1.50	
7.656	4.0	–	–	<i>A</i>

Table 5.4: Propagation times and velocities required by the AP to travel a 5 cm long distance for different values of the material parameters. Remarks: *A* – no propagating AP is generated. *B* – besides the propagation velocity, also the amplitude of the AP is affected, i. e., an approximately 14 % higher AP amplitude is observed. *C* – this simulation corresponds to the reference case of Table 5.1.

5.3.6 Influence of the Activation History

From experiments it is known that the AP propagation velocity and the amplitude of the AP depend on the activation history, cf. Juel [136], Milner-Brown & Miller [175]. Of particular interest are the reduced AP amplitude and the reduced propagation velocity observed during sustained contractions at high frequency. This phenomenon is termed membrane fatigue and is attributed to an accumulation of potassium ions and a depletion of sodium ions within the T-tubules as a result of high-frequency stimulation. Due to a change in the ionic concentration gradient across the T-tubule membrane in response to sustained high-frequency AP discharges (cf. Green [90], Sejersted & Sjøgaard [233]), the amplitude of the membrane potential decreases and the AP propagation velocity is reduced, cf. Juel [136], Milner-Brown & Miller [175].

Due to the fact that the biophysical cell model of Shorten et al. [240] includes a description of T-tubule ionic currents, the presented model of a muscle fibre is used to investigate the effect of membrane fatigue on the AP amplitude and propagation velocity. For the analysis, the model setup described in Section 5.3.4 is used. In agreement with the results of Table 5.3, the 6 cm long fibre is discretised using 2304 finite elements. The fast-twitch model is stimulated using a frequency of 100 Hz. Due to the fact that the stimulation frequency of 100 Hz is too high for the slow-twitch parametrisation (APs were not reliably generated), a stimulation frequency of 50 Hz is considered for the slow-twitch model.

Stimulating the fast-twitch model at 100 Hz for 500 ms, the propagation velocity decreases from 1.89 m/s to 1.58 m/s, which corresponds to a decrease of 16.4 %. Employing the slow-twitch parametrisation, the AP propagation velocity decreases within 500 ms from 1.33 m/s to 1.25 m/s, which corresponds to a 6.0 % decrease. The model predicted decreases of the AP propagation velocity of 6.0 % and 16.4 % within 500 ms can be compared to the experimentally determined decrease of about 30–50 % obtained after 2 min of stimulation, cf. Juel [136].

Besides a reduction of the AP propagation velocity, changes in the AP amplitude are observed. Figure 5.7a shows the evolution of the membrane potential at a point far from the stimulation point in the fast-twitch model as a result of 100 Hz stimulation. Figure 5.7b shows the same quantity for the slow-twitch model due to 50 Hz stimulation.

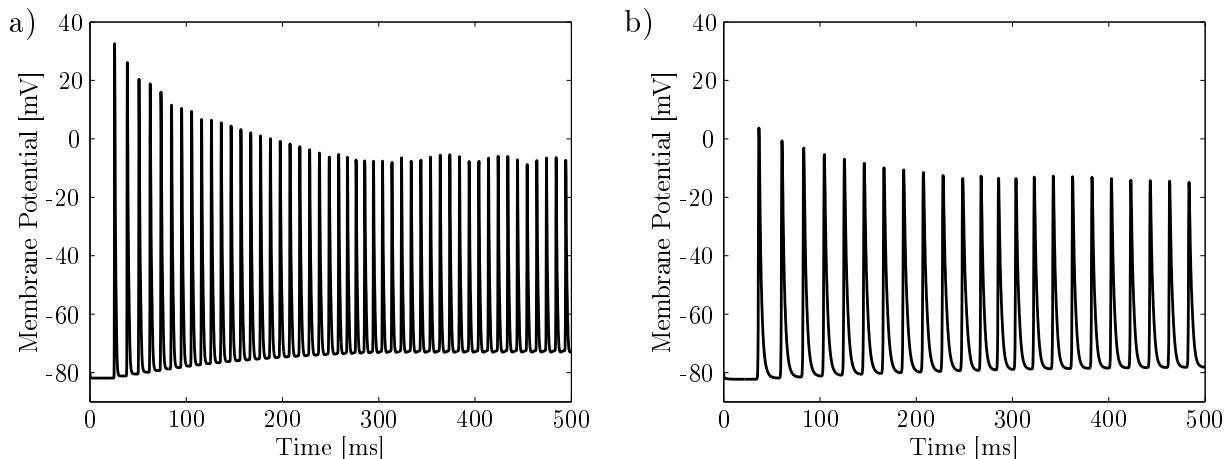


Figure 5.7: Evolution of the membrane potential (a) in the fast-twitch model during 100 Hz stimulation, and (b) in the slow-twitch model during 50 Hz stimulation at a point far away from the stimulation point.

In Figure 5.7 it can be observed that for both parametrisations, the AP amplitude decreases rapidly to an approximately steady level. Due to a 500 ms long stimulation at 100 Hz, the fast-twitch model predicts an amplitude reduction of 44.9 %, while the slow-twitch model at 50 Hz stimulation predicts an amplitude reduction of 27 %. Due to the fact that the direct measurement of changes of the AP amplitude of a single fibre is difficult, instead, the amplitude reduction of the surface-detected potential is commonly reported in experimental studies. Therefore, the predicted AP amplitude reductions are not compared to experimental data at this point, but a comparison will be provided, when investigating surface-detected potentials in Section 5.4.3.

The predicted decreases in the AP amplitude and the AP propagation velocity due to high-frequency stimulation demonstrate that the model is capable of simulating membrane fatigue. As previously mentioned, membrane fatigue is attributed to potassium accumulation and sodium depletion in the T-tubules. Therefore, Figure 5.8 shows the evolution of the potassium and sodium concentrations in the T-tubules of a fast-twitch muscle fibre due to a high-frequency stimulation of 100 Hz.

The model predicts that potassium concentration saturates at a level almost twice as high as its resting concentration, when the fibre is stimulated for approximately 300 ms at 100 Hz, cf. Figure 5.8a. It is noteworthy that the steady level of the AP amplitude during high-frequency stimulation is also reached after approximately 300 ms, cf. Figure 5.7a. The decrease in the concentration of sodium in the T-tubules is less pronounced than the increase of the potassium concentration, cf. Figure 5.8b. After 500 ms of high-frequency stimulation, the model predicts a T-tubule sodium concentration that is about 10 % lower than the resting concentration.

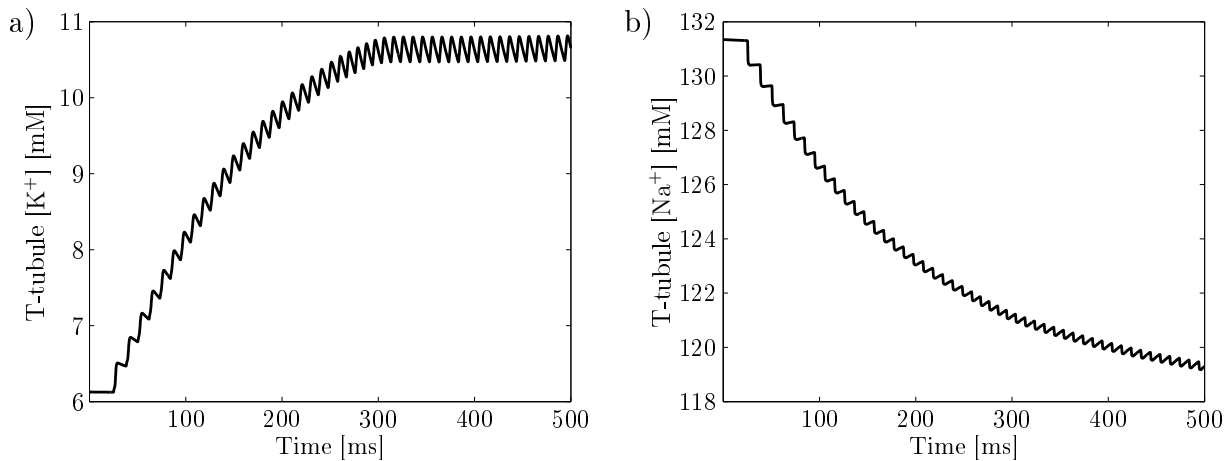


Figure 5.8: Evolution of (a) the potassium concentration and (b) the sodium concentration in the T-tubules during 100 Hz stimulation in a fast-twitch muscle fibre.

5.4 Simulating Electromyographic Signals

The electrical activity of a muscle is the superposition of the APs generated by its muscle units, each of which consists of many fibres that are simultaneously activated by their corresponding motor neuron. The electrical activity of a muscle can be recorded either at the skin surface above the muscle or within the muscle using needle electrodes. These experimentally recorded signals are generally termed EMG signals, or more specifically, surface EMG (sEMG) and intramuscular EMG, depending on the electrode placement. Providing information on healthy and pathological conditions of a muscle, EMG signals are widely used as source of data in rehabilitation medicine but also in scientific research such as movement analysis, neurology, or the development of biofeedbacks. Due to the fact that EMG signals are the result of cascades of complex biophysical processes, they are often hard to interpret and analyse. Therefore, computational models predicting the EMG have great potential to improve comprehension of recorded signals.

Building on the results of Sections 5.1 and 5.2, the electrical activity of muscle tissue consisting of many fibres is modelled in this section. Further, to predict the EMG signals, the muscle tissue model is linked to a volume conductor. In addition, the MN model of Negro & Farina [186] is included in the model to evoke the MUAPs. A schematic representation of the resulting model is shown in Figure 5.9.

Some of the results presented in this section have previously been published in Mordhorst et al. [178]³.

5.4.1 Propagation of Electrical Signals Through a Volume Conductor

The propagation of electrical signals through the 3D muscle tissue can be modelled at the macroscale using the bidomain model, cf. Section 5.1. Neglecting the effect that the extracellular potential has on the membrane potential, the bidomain model can be

³The methods and results presented in this section have been developed in close collaboration with Mylena Mordhorst, M. Sc., during her master thesis and thereafter. The work of Mylena is greatly acknowledged.

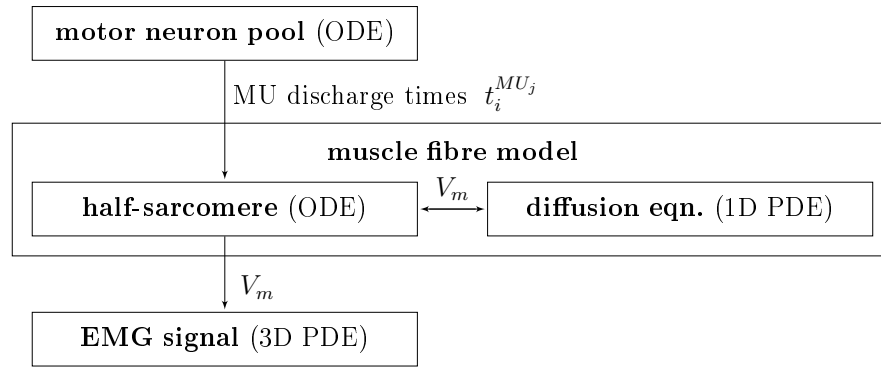


Figure 5.9: Overview of the model of the EMG. Each box indicates a model part. The couplings between the parts are indicated through arrows together with the transferred information.

simplified to the monodomain model, cf. Section 5.2. While both the bidomain and the monodomain models are well established for simulating the electrical activity of the heart (cf. Pullan et al. [211]), these approaches have not yet been applied to model EMG signals. The activation of skeletal muscle, however, is much more complex than the activation of the heart. The contraction of the heart is initiated by a single continuous wave front propagating through the myocardium. In contrast, in skeletal muscle, the fibres belonging to a MU are activated through their corresponding MN independent of all other MUs, and electrical activation from one fibre to adjacent ones does not occur. Hence, the individual fibres can be considered as electrically isolated and can be modelled as 1D objects. Following this argumentation, the distribution of the membrane potential can be determined from the 1D monodomain equation (5.20), similarly to the approach presented in Section 5.3.2.

Once the membrane potential has been determined by solving the monodomain equation (5.19), the extracellular potential distribution can be computed in the muscle tissue using the extracellular bidomain equation (5.9) and in the electrically inactive tissues using the generalised Laplace equation (5.11). Due to the fact that the extracellular potential not only propagates along the fibre direction but also in directions perpendicular to it, Equation (5.9) has to be discretised on a 3D domain. To this end, the nodes of the 1D muscle fibre meshes are connected such that a 3D linear Lagrange finite element mesh is obtained, see Figure 5.10. The weak forms of the extracellular bidomain equation (5.9) and the generalised Laplace equation (5.11) are provided in Appendix D.2. The spatial derivative terms in the extracellular bidomain equation (5.9) are discretised and solved using the resulting fine-spaced 3D finite element mesh. Note that this straightforward approach is chosen due to its simplicity but other methods are also possible. For example, a computationally more efficient method that uses a coarser finite element mesh for the solution of the extracellular bidomain equation than for the monodomain equation is used in Vigmond et al. [270] for modelling the electrical activity of the heart. Due to the fact that skeletal muscle fibres are electrically isolated, the distribution of the membrane potential in the 3D muscle tissue, which enters the extracellular bidomain equation (5.9) as a source term, is highly irregular and non-smooth. The projection of such a fluctuating signal to a different grid is not straightforward, which further complicates the usage of different discretisations.

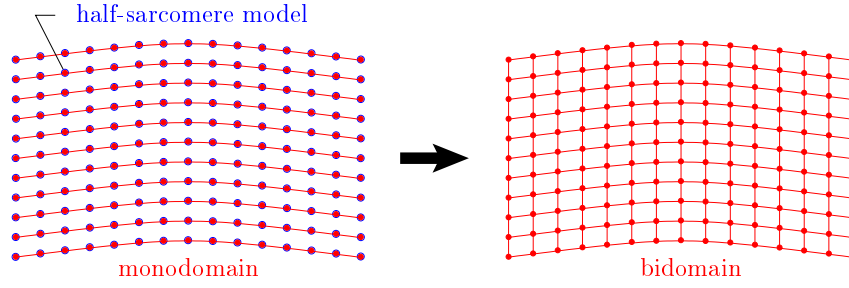


Figure 5.10: A 2D schematic representation of the 3D problem highlighting the connection of the nodes of the 1D fibre meshes (red, left) to the 3D mesh for the solution of the extracellular bidomain equation (red, right). Each finite element node point of the 1D muscle fibre meshes requires the solution of the biophysical half-sarcomere model (blue, left).

To summarise, the steps used in this work to compute the EMG signal are: (i) The 1D monodomain equation (5.20) is solved for the membrane potential distribution along the muscle fibres. (ii) The extracellular bidomain equation (5.9) and the generalised Laplace equation (5.11) are solved for the extracellular potential in the muscle region and for the potential in the body region, respectively. The weak forms of these equations have been implemented into the open-source software library `OpenCMISS` [26].

While the electrically inactive body region is assumed to behave electrically isotropic, an anisotropy ratio of 5 is assumed for the overall conductivity of the extracellular bidomain equation ($\sigma_i + \sigma_e$), cf. Epstein & Foster [66], Gielen et al. [84], Mesin [170]. Further, in agreement with the previous findings, the intracellular conductivity tensor has a non-zero component only in fibre direction. To model an arbitrary distribution of the fibre directions, it is convenient to introduce a local, orthonormal fibre coordinate system (cf. Pullan et al. [211]), denoted by $\boldsymbol{\nu}_j$, such that

$$\boldsymbol{\sigma}_i = \begin{bmatrix} \sigma_i & 0 & 0 \\ 0 & 0 & 0 \\ 0 & 0 & 0 \end{bmatrix} \boldsymbol{\nu}_k \otimes \boldsymbol{\nu}_l, \quad \boldsymbol{\sigma}_e = \begin{bmatrix} \sigma_e^l & 0 & 0 \\ 0 & \sigma_e^t & 0 \\ 0 & 0 & \sigma_e^t \end{bmatrix} \boldsymbol{\nu}_k \otimes \boldsymbol{\nu}_l, \quad \boldsymbol{\sigma}_o = \begin{bmatrix} \sigma_o & 0 & 0 \\ 0 & \sigma_o & 0 \\ 0 & 0 & \sigma_o \end{bmatrix} \boldsymbol{\nu}_k \otimes \boldsymbol{\nu}_l,$$

and a local fibre direction can be assigned at each material point of the considered body. Here, the $\boldsymbol{\nu}_1$ -direction is chosen to coincide with the direction of the muscle fibres. The material parameters used in the presented simulations are summarised in Table 5.1 and Table 5.5.

Symbol	Description	Value [mS/cm]	Ref.
σ_i	longitudinal intracellular conductivity	8.93	[28]
σ_e^l	longitudinal extracellular conductivity	6.7	[228]
σ_e^t	transversal extracellular conductivity	3.126	[170]
σ_o^{fat}	fat conductivity	0.4	[228]
σ_o^{skin}	skin conductivity	0.2	[78]

Table 5.5: Electrical conductivities.

5.4.2 Surface and Intramuscular EMG in a Rectangular Cuboid

This section demonstrates that the proposed method can simulate realistic intramuscular and sEMG signals. To this end, a rectangular cuboid of length $l = 6$ cm (x_1 -direction), width $w = 2.9$ cm (x_2 -direction), and overall height $h = 1.4$ cm (x_3 -direction) is considered. The lower 1.2 cm are defined as transversely isotropic muscle region that is covered by a 0.2 cm thick isotropic fat layer. (This simulation does not explicitly account for the skin.) Within the muscle region, a total of $30 \times 13 = 390$ muscle fibres are equally distributed. The 390 fibres are randomly assigned to 10 MUs. The resulting distribution is shown in Figure 5.11a. To simulate a parallel-fibred muscle, all fibres are chosen to run in parallel with the cuboid's long edge and span over its entire length. Further, each muscle fibre is meshed using 144 finite elements, and the cell model assigned to each node of the resulting mesh uses the fast-twitch parametrisation of Shorten et al. [240]. This leads to the same AP propagation velocity along all fibres. The innervation zone is assumed to be located at the middle of the muscle cuboid. To model the innervation zone, a Gaussian distribution around the middle of the fibres with a standard deviation of two nodes is assigned to the stimulation point. The maximum deviation is 7 nodes, which corresponds to a 0.5 cm wide spread of the innervation zone.

The MU discharge times are determined using the biophysical model of the MNs of Negro & Farina [186], which has been described in Section 4.2. The input to the MN model is a constant mean synaptic current of $0.005 \mu\text{A}/\text{cm}^2$ superimposed by two Gaussian-distributed high-frequency oscillating signals, one common to the entire MN pool and one independent for each MN, see Negro & Farina [186] for details. Due to the total synaptic input signal, 8 out of the 10 MUs are recruited. The mean discharge frequencies of the recruited MUs are approximately 10–15 Hz, and the interstimulus interval exhibits a coefficient of variation of approximately 20%. Figure 5.11b shows the MU discharge times as predicted by the MN model.

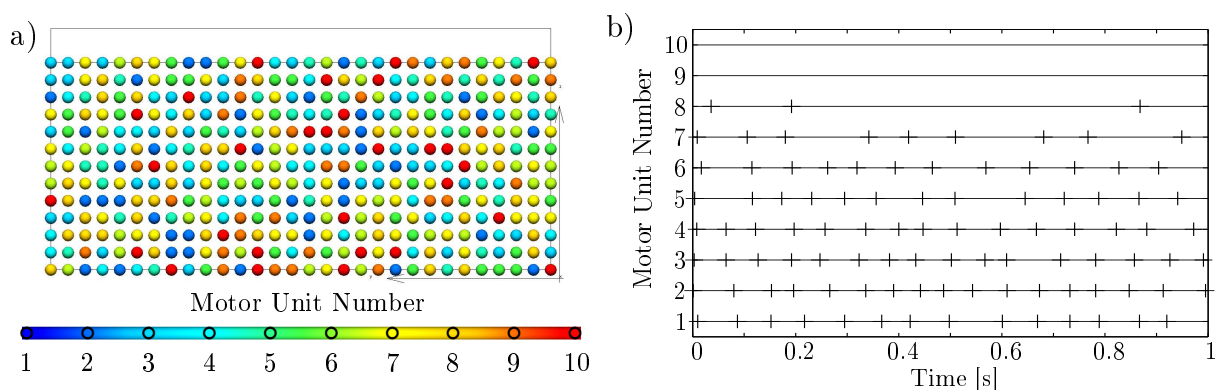


Figure 5.11: (a) The attribution of the fibres to the 10 MUs. (b) The motor neuron discharge times. Figure previously published in [178].

Figure 5.12 shows the APs propagating along the muscle fibres and the resulting sEMG signals at the beginning of the simulation (0–13 ms). While in experimental studies often differential EMG signals are recorded, all EMG signals presented in this thesis result from monopolar detections. Due to the fact that the proposed method determines the potential at each point of the domain, differential signals can easily be computed from the difference of two monopolar signals if necessary.

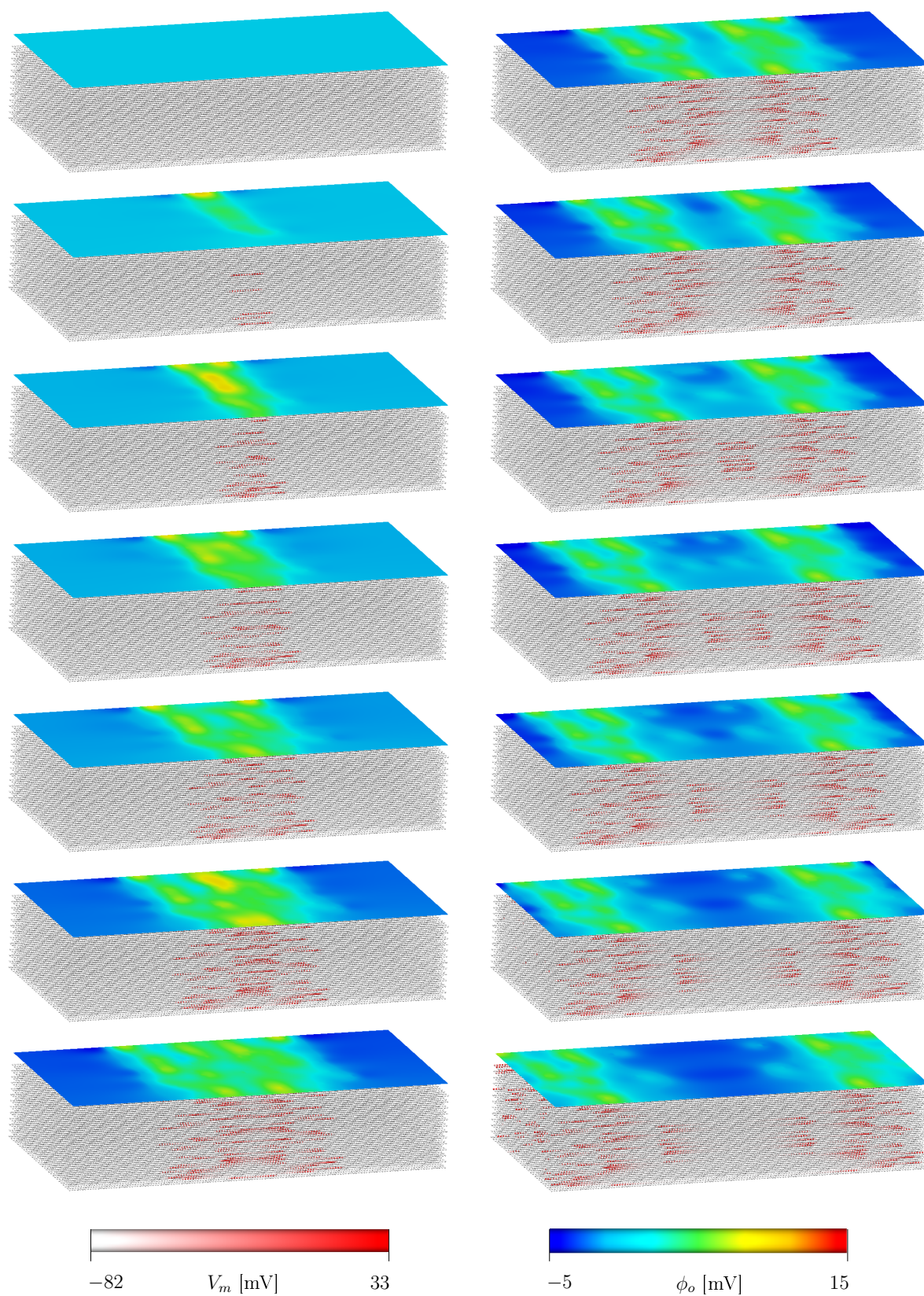


Figure 5.12: Muscle fibre APs and the resulting sEMG signals at times $t = 0-6$ ms (left, from top to bottom) and $t = 7-13$ ms (right) in steps of size 1 ms.

Figure 5.13 shows a short segment of the virtual sEMG signal at 25 (5×5) selected points. In both directions, the distance between the points is chosen to be 5 mm, which is in agreement with the interelectrode distance (IED) of high-density sEMG electrodes.

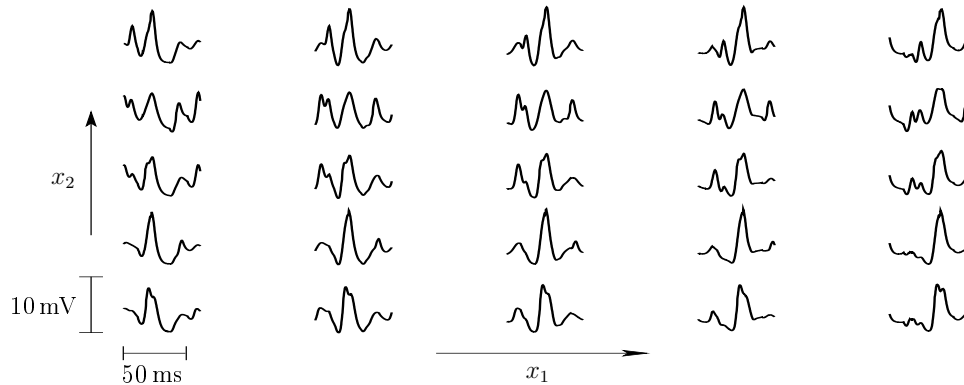


Figure 5.13: High-density sEMG signals. The x_1 -direction coincides with the muscle fibre direction, and the x_2 -direction is perpendicular to the fibre direction. In both directions, the interelectrode distance (IED) is 5 mm.

Figure 5.14 shows the computed EMG signals at 7 selected positions within the muscle (different depths) and one position at the outer surface of the fat tissue. This representation reveals that the intramuscular EMG depends heavily on the electrode position, picking up signals from only few fibres, which is in agreement with experimental observations [138]. Furthermore, Figure 5.14 demonstrates the effect of the low-conductivity fat tissue on the EMG signal.

Despite the simplified example set-up (cuboid geometry, unrealistic MU territories), the predicted EMG signals compare qualitatively well with the experimental sEMG data of Farina et al. [70] and Barbero et al. [9]. A quantitative comparison is difficult as experimental EMG signals depend heavily on properties that are difficult to control in experiments, such as, for example, the MU territories and the thickness of the subcutaneous tissue [54]. It is furthermore noteworthy that no noise has been added to the computed EMG signals. Experimental EMG recordings, in contrast, always contain noise, for example, electrode-electrolyte noise, the noise of the electronic amplifiers, line interference, biological noise and the interference activity of MUs far from the detection point [68, 168].

5.4.3 Effect of Membrane Fatigue on the EMG

The aim of this test case is to investigate the effect of membrane fatigue on the EMG signal. Changes of the AP amplitude and propagation velocity of a single skeletal muscle fibre due to membrane fatigue have been analysed in detail in Section 5.3.6. Due to the fact that the direct measurement of changes of the AP amplitude of a single fibre is difficult, the resulting amplitude reductions of the surface-detected potential are now investigated.

For the numerical experiments the cuboid of Section 5.4.2 is extended by a 1 mm thick layer of skin tissue on top of the fat layer. The conductivity of the isotropic skin layer is provided in Table 5.5. As before, the fast-twitch parametrisation of the model of Shorten

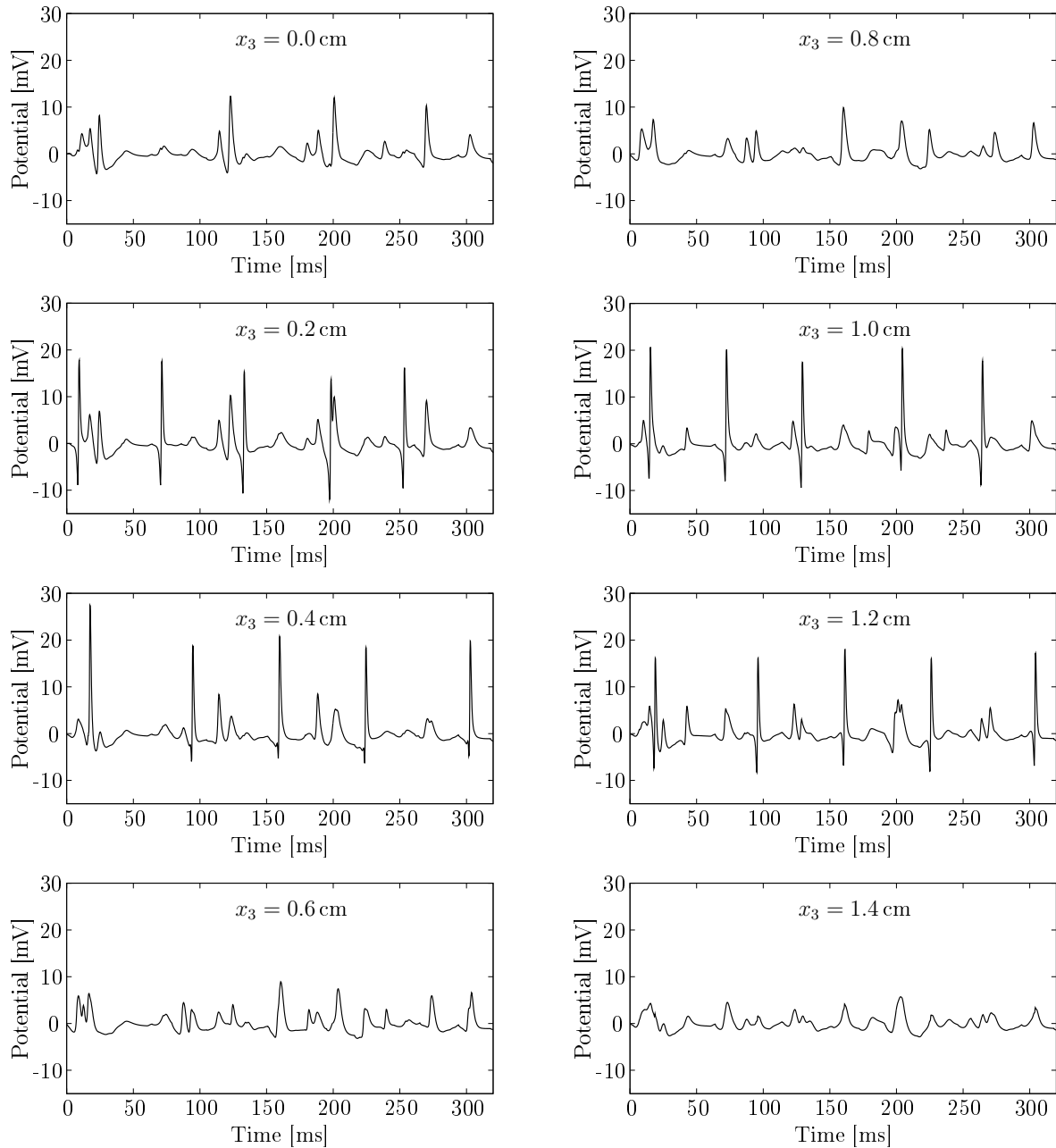


Figure 5.14: Intramuscular and *sEMG* signals at position $(x_1, x_2) = (3.92 \text{ cm}, 1.25 \text{ cm})$ and different depths (x_3) , where $x_3 = 1.4 \text{ cm}$ is at the outer surface of the fat tissue, and $x_3 = 1.2 \text{ cm}$ is at the muscle-fat interface.

et al. [240] is used. To clearly demonstrate the effect of fatigue on the sEMG signal, only a single fibre in the tissue block is activated. The activated fibre is located in the middle of the cuboid and 0.4 cm below the skin surface. Stimulation of this fibre occurs at its left end at a frequency of 100 Hz.

Figure 5.15 shows the first simulated APs propagating along the stimulated fibre and the resulting sEMG signal on top of the skin surface. The decrease in the amplitude of the potential from the first to the second AP is clearly visible in the sEMG signal. Note that this decrease is due to the high stimulation frequency and becomes less pronounced with larger interstimulus intervals (not shown).

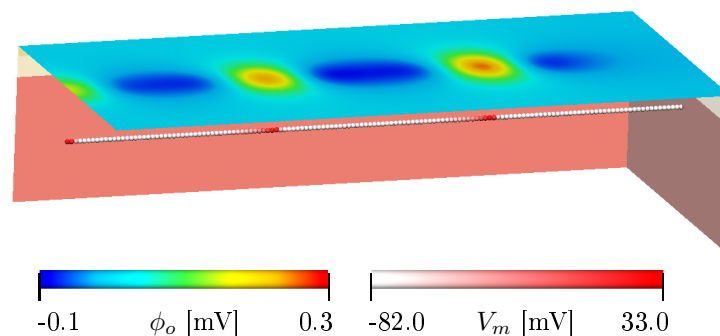


Figure 5.15: Single fibre APs propagating from left (point of stimulation, stimulation frequency 100 Hz) to right and resulting sEMG at time $t = 30.4$ ms. Note that for illustrational purposes only the activated fibre is depicted in the muscle tissue. Additionally, two sides of the cuboid indicate the muscle and fat tissues. Previously published in [178].

To quantify the decrease in the amplitude of the EMG signal over a larger number of APs, Figure 5.16a displays the sEMG signal recorded at a position in the middle of the skin surface versus time. Within 500 ms, the amplitude of the EMG decreases from 0.37 mV to 0.22 mV, which corresponds to a decrease of 40 %.

Furthermore, to illustrate changes in the propagation velocity due to membrane fatigue, Figure 5.16 depicts the potential distribution in fibre direction at the surface along the cuboid's centre line at times 30.4 ms and 500.4 ms. These time instants are chosen such that in both cases the next stimulation occurs at the left end of the fibre. Comparing the sEMG of the non-fatigued state ($t = 30.4$ ms) with the fatigued state ($t = 500.4$ ms), one observes that both the propagation velocity and the amplitude of the signal decrease with time.

The model predicted AP amplitude reduction of 40 % compares well to the experimentally determined surface-detected mean amplitude reduction of 32 %, see Milner-Brown & Miller [175]. Experimental data reflecting changes in the AP amplitude exist only based on the sEMG. In contrast, changes in the conduction velocity due to membrane fatigue can be analysed intramuscularly from single fibres or from surface-detected potentials, cf. Juel [136], McGill & Lateva [164]. Since the intramuscular recordings of the propagation velocity are probably more reliable than the values obtained from the sEMG, and since the model predicted changes of the AP propagation velocity in single fibres have already been discussed in detail in Section 5.3.6, a comparison of the predicted surface-detected potentials with experimental recordings is omitted here.

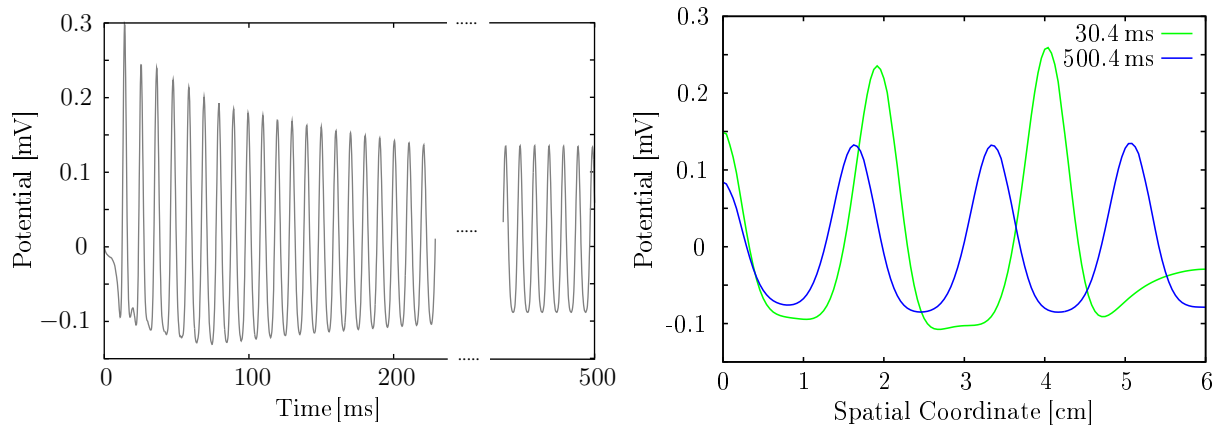


Figure 5.16: (a) The surface potential versus time captured at position $(x_1, x_2, x_3) = (3.0, 1.4, 1.5)$ cm. (b) The surface potential versus the spatial coordinate for times 30.4 ms and 500.4 ms. Figure previously published in [178].

5.5 Discussion

The presented model for simulating the intramuscular and surface EMG is based on the bidomain model, which is a continuum approximation of the electrophysiological behaviour of electro-active biological tissue [211]. The continuum character of the bidomain model is reflected by the fact that not each half-sarcomere of a muscle fibre is represented, but instead a continuous distribution of the subcellular quantities is assumed. Furthermore, assuming homogeneous conditions in the cross-section of the muscle fibre, only one half-sarcomere model in the cross-section is used to determine the AP propagation along the muscle fibre.

A monolithic coupling of the bidomain model with a detailed biophysical cell model in the muscle and the generalised Laplace equation in the surrounding tissues leads to computational expensive simulations. One common approach to decrease the computational complexity of the bidomain model is to use the less complex monodomain model, cf. Nielsen et al. [191], Sundnes et al. [255]. This approach yields an exact method if the assumption of equally anisotropic intracellular and extracellular conductivity tensors is satisfied, and an approximation if not [191]. Therefore, it has been demonstrated that the monodomain model approximates well the bidomain model for the presented applications.

Using the monodomain model, the equations for the membrane potential and for the extracellular potential are decoupled from each other, and hence, can be solved successively. The successive solution of the monodomain equation and the extracellular bidomain equation essentially corresponds to the approach used in previous models of the EMG [72, 160, 168, 171]. These phenomenological models prescribe the shape (e.g. the Rosenfalck approximation) and propagation velocity of the AP, and solve a Poisson equation for the extracellular potential to predict the EMG.

By successively solving the monodomain equation and the extracellular bidomain equation, the effect that the extracellular potential has on the membrane potential is neglected. However, it has been demonstrated that this approximation has a minor effect on the AP propagation velocity. In fact, the monodomain model predicts slightly lower AP propagation velocities than the bidomain model. This is also reflected in the discrepancy

between the monodomain-based AP propagation velocities reported in Section 5.3.4 and those reported by Davidson [45] for the bidomain model.

The AP propagation velocities obtained from the monodomain or bidomain models for the material parameters given in Table 5.1, however, are rather small compared to experimentally determined AP propagation velocities, which in skeletal muscle are commonly about 4 m/s, cf. Mesin [170]. Although there is also variability in the experimental data (for example, McGill & Lateva [164] assumed 2–6 m/s), it is pertinent to assume that the given set of material parameters is inaccurate. Following this, it has been shown that both a lower membrane capacitance and a higher ratio between the conductivity and the surface-area-to-volume ratio yield a higher conduction velocity.

In contrast to previous models of the EMG, which prescribe the shape and propagation velocity of the AP as part of the model constitution, the generation and propagation of the AP in the presented model is based on a transient diffusion equation in conjunction with a biophysical Hodgkin-Huxley-type model of the membrane electrophysiology. One of the major advantages of the biophysical description is that it intrinsically accounts for physiological effects such as, for example, membrane fatigue that causes changes in the amplitude and conduction velocity of the AP during sustained contractions. Thus, using the presented biophysical model, one can analyse their effect on the EMG signal, which might improve signal interpretation and lead to a better understanding of recorded EMG signals. Moreover, changes in the EMG that might occur, for example, in pathological conditions, can potentially be investigated using the presented model due to its biophysical description. A further potential application of the model is the *in-silico* testing of drugs. For example, knowing the effect a certain medication has on the conduction of a species of ion channels, its effect on the AP shape and conduction velocity can be studied, and the simulation results can be validated using EMG measurements. No previous model of the EMG could combine all these processes within one framework.

Other drawbacks of existing models also apply to the presented model, e.g., a lack of reliable experimental data such as accurate descriptions of the fibre directions, material parameters, heterogeneities, and MU territories. This and the fact that recorded EMG signals vary a lot, for example, due to differences in the thickness of the subcutaneous tissue (cf. Dimitrov et al. [54]), make a quantitative validation of the EMG computation difficult. The bidomain model and its simplification, the monodomain model, however, are well established within the field of biosignal modelling, in particular for simulating the electrical activity of the heart, see Pullan et al. [211]. In this context, Vigmond et al. [270] demonstrated that a coarser mesh can be used for the (elliptic) extracellular bidomain equation than for the (parabolic) monodomain equation and still maintain reasonable accuracy. Choosing the same mesh size for the extracellular bidomain equation would not have been necessary but appeared to be, from an implementational point of view, the simplest choice.

Commonly, as also described in Section 3.2, implicit methods are used for the integration of the stiff ODEs describing the cellular behaviour. This is due to the fact that, when using explicit methods to solve stiff equations, the time step size is often restricted by stability issues. Employing an implicit method, such as, for example, the backward Euler method, a larger time step can be used, however, a nonlinear system of equations has to be solved in each time step. Independent of the solution method, however, a very small time step size is required to resolve the rapid changes and steep gradients occurring during

the rising phase of an AP. Despite the fact that the cell model of Shorten et al. [240] is mathematically represented by a system of stiff ODEs, the advantage of using an implicit method and a larger time step is balanced by the additional computational cost of solving a nonlinear system of equations in every time step. Indeed, the forward Euler method, an explicit, first-order accurate method, turned out to be efficient to solve the nonlinear cell model of Shorten et al. [240]. It is, however, noteworthy that the small time step size required to resolve the rising phase of an AP is not required during other phases. To simulate these phases an implicit method and a larger time step size might be much more efficient than an explicit method. Therefore, an implicit method using an adaptive time step size might be ideal for the solution of the cell models. Such methods have been used to solve the examples in Chapter 4 and Section 5.3.1 using MATLAB, however, they are currently not implemented in `OpenCMISS`.

The Hodgkin-Huxley-type model of the membrane electrophysiology used within the monodomain model is part of the biophysical half-sarcomere model of Shorten et al. [240]. Since the half-sarcomere model describes the entire excitation-contraction coupling, i. e., the signaling pathway from AP generation via calcium release and calcium dynamics to stress generation, the model can, in addition to the EMG, also predict the force that is generated by the muscle. This, amongst others, will be comprehensively discussed in the next chapter.

6 A Multiscale Skeletal Muscle Model

Previous chapters presented modelling approaches that either completely neglected the spatial components of the underlying system (Chapter 4) or considered spatial components of the muscle only with respect to the propagation of electrical signals through the tissue (Chapter 5). The activation-induced contraction of skeletal muscles, however, causes also a deformation of the muscle, which in turn affects the force-generating capacity of the muscle (cf. the force-length and force-velocity relations in Figures 2.7 and 2.8) and the action potential propagation (mechano-electric feedback). To simulate the deformation, as well as the total force that is exerted during contraction, a continuum-mechanical description of skeletal muscle behaviour is introduced in the following. In this regard, continuum mechanics provides a flexible framework for modelling and simulating isometric and non-isometric muscle contractions.

6.1 Constitutive Modelling

The continuum-mechanical balance relations presented in Section 3.4.3 are universally valid, independent of the material of the body under consideration. However, due to the fact that the presented system contains more unknowns than equations, further relations have to be developed to close the system of equations. To this end, suitable assumptions have to be constitutively introduced, which will also characterise the behaviour of the material.

6.1.1 Preliminary Assumptions and Resulting Equations

Proceeding from the local forms of the continuum-mechanical balance relations of Section 3.4.3, assumptions are made towards adapting the generally valid balance relations to the special case of skeletal muscle modelling. Furthermore, simplifying assumptions are introduced to decrease the computational complexity of the model such that the resulting model can be solved within a reasonable time on today's hardware architecture. For the sake of convenience, all basic assumptions are first summarised before they are comprehensively discussed and applied to the balance relations.

- Material incompressibility,
- quasi-static conditions,
- negligible body forces,
- isothermal conditions,
- the superposition of passive and active stress contributions,
- hyperelastic material behaviour.

Due to its high content of water, skeletal muscle tissue is generally considered to behave materially incompressible under physiological conditions, cf. e.g. Böhl et al. [19], Gindre et al. [85], Takaza et al. [256], Van Loocke et al. [268]. In incompressible materials the mass density does not change during a deformation process. Hence, the time derivative of the density in the local form of the mass balance (3.43) vanishes and the resulting relation yields

$$\operatorname{div} \dot{\boldsymbol{x}} = (\operatorname{grad} \dot{\boldsymbol{x}}) \cdot \boldsymbol{I} = \boldsymbol{L} \cdot \boldsymbol{I} = \boldsymbol{D} \cdot \boldsymbol{I} = 0. \quad (6.1)$$

Therein, $\boldsymbol{D} := \operatorname{sym} \boldsymbol{L} = \frac{1}{2}(\boldsymbol{L}^T + \boldsymbol{L})$ denotes the spatial rate of deformation tensor, which is defined as the symmetric part of the spatial velocity gradient, $\boldsymbol{L} := \operatorname{grad} \dot{\boldsymbol{x}}$. The mass balance, such as all other balance relations, is stated in Section 3.4.3 in the actual configuration. Of course, the balance relations can similarly well be expressed in the referential frame. In the reference configuration, the condition of incompressibility states that the material density of the body at all times equals its density in the reference state, i. e., $\rho = \rho_0$. Assuming material incompressibility, the local form of the mass balance in the reference configuration leads to

$$\rho_0 = \rho \det \boldsymbol{F} \quad \longrightarrow \quad \det \boldsymbol{F} = 1. \quad (6.2)$$

Equation (6.2) restricts the set of admissible deformations to the subset of volume preserving deformations. To take this restriction into account, the product of a Lagrange multiplier p (the hydrostatic pressure) and the incompressibility constraint (6.1) is added to the entropy inequality, which is obtained when the balance of entropy is inserted into the second law of thermodynamics. Evaluation of the entropy inequality then yields that the total stress consists of two parts, i. e.,

$$\boldsymbol{T} = -p \boldsymbol{I} + \boldsymbol{T}_E, \quad \boldsymbol{S} = -p J \boldsymbol{C}^{-1} + \boldsymbol{S}_E, \quad (6.3)$$

where \boldsymbol{T}_E and \boldsymbol{S}_E are the so-called extra stresses of the actual and reference configurations, respectively. Since the treatment of incompressible materials is well-known in continuum-mechanics, further details are omitted here but can be found, for example, in Bonet & Wood [23] and Holzapfel [121].

Further, the assumption of quasi-static conditions for the continuum-mechanical model implies that the inertia term in the balance of momentum (3.45) vanishes. This assumption is obviously only valid for slow deformations. Deformations involving large accelerations have to be excluded. For example, the model will not necessarily produce accurate results for quick-release experiments, cf. e.g. Hill [117, 118], Siebert et al. [243]. Restricting the application of the model to more physiological and slow contractions, however, one can assume that the inertia terms are small in comparison to the forces exerted by the muscle. The same assumption holds for the body (gravitational) forces. Following these assumptions, the local form of the balance of momentum (3.45) reduces to

$$\operatorname{div} \boldsymbol{T} = \boldsymbol{o}. \quad (6.4)$$

Furthermore, the local form of the balance of angular momentum (3.47) directly yielded the symmetry of the Cauchy stress tensor, which implies the symmetries of the Kirchhoff and the 2nd Piola-Kirchhoff stresses. While these results will be used in the following, the balance of angular momentum will not be considered any further.

Next, the assumption of isothermal conditions is considered. In reality, muscle contractions generate heat, cf. Epstein [67], Hill [117], which is released to adjacent body parts and the environment. Furthermore, it is known from experiments that the temperature has an effect on the force-producing capabilities of the muscle and the AP propagation velocity, see [14, 164]. Moreover, the temperature of a muscle depends on its position in the body, the temperature of the environment, and the level of muscle activity. Following the idea of isothermal conditions used in experimental studies, temperature effects are neglected in this work. Therefore, the energy balance drops out and is not further considered.

Muscle tissue resists external loads like any other material but can, in addition, also actively contract and generate force. To incorporate the active contractile behaviour within the continuum-mechanical framework, the stress tensor of the muscle tissue is a priori constitutively assumed to consist of two parts describing the passive and active behaviours, \mathbf{S}_E^{pas} and \mathbf{S}_E^{act} , respectively, i. e.,

$$\mathbf{S}_E = \mathbf{S}_E^{pas} + \mathbf{S}_E^{act}. \quad (6.5)$$

The rheological model corresponding to the superposition of the passive and active stresses is shown in Figure 6.1.

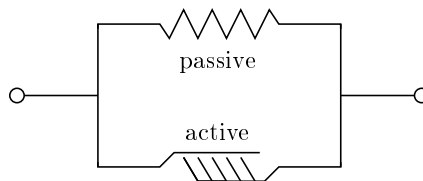


Figure 6.1: *Rheological model for the superposition of passive and active stresses.*

While the superposition of the passive and active stresses is inspired from Hill-type muscle modelling, Hill-type models typically consist of three elements. In addition to the contractile and the parallel elastic elements, they include an elastic element in series to the active element or in series to the parallel arrangement depicted in Figure 6.1, cf. Siebert et al. [242]. The series elastic element represents the series elasticity of the muscle-tendon complex. Since the series elasticity can mainly be attributed to tendon, which is not considered in this work, the third element is omitted here.

In this work, only the passive part of the stress tensor is derived from a strain energy (see below), while the form of the active part is constitutively assumed, and hence, does not necessarily satisfy the second law of thermodynamics. Recently, a few researchers also derived the active part of the stress tensor from a strain energy, which allows to demonstrate the thermodynamic consistency of the overall model, cf. e.g. Gizzi et al. [86], Rossi et al. [224], Sharifimajd & Stålhand [239], Stålhand et al. [246, 247].

While details regarding the thermodynamic consistent formulation of constitutive models are omitted here, Appendix A.2 provides additional information on this subject. For more details, the reader is referred to Wang & Truesdell [273] and references therein.

Neglecting viscous effects and assuming hyperelastic material behaviour of the passive muscle tissue, the second law of thermodynamics yields that the stress tensor can be

derived from a strain energy function \mathcal{W} according to

$$\mathbf{S}_E^{pas} = 2 \frac{\partial \mathcal{W}}{\partial \mathbf{C}}. \quad (6.6)$$

For a transversely isotropic material, the strain energy depends on the right Cauchy-Green deformation tensor, \mathbf{C} , and a structural tensor, \mathcal{M}_a . Commonly, however, the strain energy is formulated in terms of its principal and mixed invariants (cf. Appendix A.2), i. e.,

$$\mathcal{W}(\mathbf{C}, \mathcal{M}_a) = \mathcal{W}(I, II, III, IV, V). \quad (6.7)$$

Therein, the principal invariants are given by

$$\begin{aligned} I &= \operatorname{tr} \mathbf{C} = \operatorname{tr} \mathbf{B} = \mathbf{F} \cdot \mathbf{F}, \\ II &= \operatorname{tr} (\operatorname{cof} \mathbf{C}) = \operatorname{tr} (\operatorname{cof} \mathbf{B}) = \operatorname{cof} \mathbf{F} \cdot \operatorname{cof} \mathbf{F}, \\ III &= \det \mathbf{C} = \det \mathbf{B} = (\det \mathbf{F}) \cdot (\det \mathbf{F}), \end{aligned} \quad (6.8)$$

and the mixed invariants, which are only required for anisotropic materials and vanish for isotropic materials, are given by

$$\begin{aligned} IV &= \operatorname{tr} (\mathcal{M}_a \mathbf{C}) = (\mathbf{a}_0 \otimes \mathbf{a}_0)^T \cdot \mathbf{C} = \mathbf{a}_0 \cdot \mathbf{F}^T \mathbf{F} \mathbf{a}_0 = \mathbf{F} \mathbf{a}_0 \cdot \mathbf{F} \mathbf{a}_0 = \mathbf{a} \cdot \mathbf{a}, \\ V &= \operatorname{tr} (\mathcal{M}_a \mathbf{C}^2) = \mathbf{a}_0 \cdot \mathbf{C}^2 \mathbf{a}_0. \end{aligned} \quad (6.9)$$

Herein, \mathbf{a}_0 is a unit vector pointing in the materials preferred direction in the reference configuration, and the structural tensor is given by $\mathcal{M}_a = \mathbf{a}_0 \otimes \mathbf{a}_0$. Moreover, $IV = \lambda_f^2$ is the squared fibre stretch in the direction of the mapped fibre orientation $\mathbf{a} = \mathbf{F} \mathbf{a}_0$, where $\lambda_f = |\mathbf{a}|$ denotes the fibre stretch (length). Invariant V has no direct physical meaning.

6.1.2 Resulting Strain Energy Functions

Based on the findings of the previous section, suitable strain energy functions are defined for the passive muscle tissue and the tissue of the subcutaneous layer. Hereby, the strain energy function for the isotropic subcutaneous tissue is included as a special case of the anisotropic passive muscle tissue.

Further, due to the fact that muscles consist of muscle fibres and extracellular connective tissue, the muscle derives its passive response from a combination of these structures [85]. Within the fibres, the titin filament, which connects the myosin filament to the Z-discs, is believed to contribute most of the passive response, cf. e. g. Prado et al. [209]. Besides the titin filaments, the hierarchical organisation of the extracellular connective tissue, with its various filament orientations and cross-connections, gives rise to an anisotropic, or more precisely, transversely isotropic passive material behaviour, cf. e. g. Böl et al. [20], Gindre et al. [85], Takaza et al. [256]. Based on the description of fibre-reinforced materials, the passive part of the energy function is decomposed into an isotropic part and an anisotropic part,

$$\mathcal{W}(I, II, III, IV, V) = \mathcal{W}^{iso}(I, II, III) + \mathcal{W}^{ani}(IV, V). \quad (6.10)$$

Therein, the isotropic part of the energy function depends on the principal invariants and represents a fictitious ground matrix, whereas the anisotropic part is assumed to depend only on the mixed invariants and represents the fibre reinforcements. Note that in this

macroscopic continuum-mechanical formulation, neither does the isotropic ground matrix reflect the behaviour of the extracellular connective tissue, nor do the fibre reinforcements represent the mechanical behaviour of the muscle fibres (although the direction of the fibre reinforcements coincides with the muscle fibre direction). For example, there is no reason for assuming that the extracellular connective tissue behaves mechanically isotropic.

Isotropic Contribution to the Passive Behaviour

A group of isotropic material models that is well-known in continuum mechanics, is the generalised Rivlin or polynomial hyperelastic material. This group is characterised by the strain energy functions

$$\mathcal{W}^{iso}(I, II) = \sum_{i,j=0}^N c_{ij}(I-3)^i(II-3)^j. \quad (6.11)$$

Therein, $c_{ij0} \geq 0$ are material parameters and $a_{00} = 0$ to satisfy the normalisation condition. The strain energy in (6.11) does not depend on the third principal invariant $III = \det \mathbf{C} = (\det \mathbf{F})^2$, which is unity due to the incompressibility constraint. Interestingly, the incompressible form of the generalised Rivlin models (6.11) does not satisfy the condition of a stress-free reference configuration, cf. Ogden [197]. However, due to the fact that the residual stresses are identical normal stresses, they cause no deformation of the incompressible material, similar to the penalty terms resulting from the incompressibility constraint. Note that the compressible form of the generalised Rivlin model is constructed in such a way that it a priori satisfies the requirement of a stress-free reference configuration.

Several commonly used material models, such as, for example, the Neo-Hookean solid ($N = 1, c_{01} = c_{11} = 0$), can be derived from this group. In this work, the Mooney-Rivlin model is adopted [121]. The strain energy of the Mooney-Rivlin model is given by

$$\mathcal{W}^{iso}(I, II) = c_{10}(I-3) + c_{01}(II-3). \quad (6.12)$$

To obtain a completely stress-free reference configuration, which is advantageous for the numerical solution process, the initial condition of the undetermined Lagrange multiplier is chosen to be $p = -(c_{10} + 2c_{01})$, cf. Ogden [197]. Note that the Mooney-Rivlin material a priori satisfies the requirements of polyconvexity and coercivity (see Appendix A.2.6).

From the strain energy function in (6.12) the isotropic part of the extra stress can be derived according to Equation (6.6), i. e.,

$$\mathbf{S}_E^{iso} = 2 \frac{\partial \mathcal{W}^{iso}}{\partial \mathbf{C}} = 2 \frac{\partial \mathcal{W}}{\partial I} \frac{\partial I}{\partial \mathbf{C}} + 2 \frac{\partial \mathcal{W}}{\partial II} \frac{\partial II}{\partial \mathbf{C}}. \quad (6.13)$$

Making use of the derivatives of the principal invariants,

$$\frac{\partial I}{\partial \mathbf{C}} = \mathbf{I}, \quad \frac{\partial II}{\partial \mathbf{C}} = (\text{tr } \mathbf{C}) \mathbf{I} - \mathbf{C}^T, \quad \frac{\partial III}{\partial \mathbf{C}} = \text{cof } \mathbf{C}, \quad (6.14)$$

the symmetry of the right Cauchy-Green deformation tensor, and the definition of the first principal invariant, the isotropic part of the 2nd Piola-Kirchhoff stress tensor results

in

$$\mathbf{S}_E^{iso}(I, II) = 2c_{10}\mathbf{I} + 2c_{01}(II - \mathbf{C}). \quad (6.15)$$

This stress tensor is not only used for representing the isotropic part of the muscle tissue, but also to model the material behaviour of the subcutaneous layer. Due to the fact that subcutaneous tissue is isotropic and does not actively contract, the terms derived in the following vanish for this material.

Anisotropic Contributions to the Passive Behaviour of Muscle Tissue

Skeletal muscle tissue is generally considered to behave transversely isotropic, i.e., the material has a single preferred direction, which coincides with the local muscle fibre direction. While many experiments indicate that muscle tissue is stiffer in fibre direction than normal to the fibre direction (cf. e.g. Böhl et al. [19], Morrow et al. [181]), a more compliant behaviour of the fibre direction compared to the cross-fibre direction is reported by others, cf. Nie et al. [189], Takaza et al. [256]. Due to the fact that different muscles and different species are considered in the different experiments, it is possible that both behaviours exist in different muscles. Following this, first a strain energy function is introduced to represent the more common case with stiffer fibre direction. For this case, the energy function describing the anisotropic behaviour of the muscle tissue is adopted from Markert et al. [163]. This strain energy depends only on the fourth (mixed) invariant and is given by

$$\mathcal{W}^{ani}(IV) = \begin{cases} \sum_{i=1}^M \left(\frac{b_i}{d_i} (IV^{d_i/2} - 1) - b_i \ln(IV^{1/2}) \right) & \text{if } IV \geq 1, \\ 0 & \text{otherwise.} \end{cases} \quad (6.16)$$

Therein, b_i and d_i are material parameters (see Markert et al. [163] for their restrictions), and M specifies the number of terms. The form in (6.16) satisfies a priori the normalisation condition and the condition of a stress-free reference configuration. For further details on this anisotropic strain energy function, the interested reader is referred to Karajan [140] and Markert et al. [163].

Since the energy in (6.16) depends only on the fourth invariant, Equation (6.6) yields

$$\mathbf{S}_E^{ani} = 2 \frac{\partial \mathcal{W}^{ani}}{\partial \mathbf{C}} = 2 \frac{\partial \mathcal{W}^{ani}}{\partial IV} \frac{\partial IV}{\partial \mathbf{C}}, \quad \text{where} \quad \frac{\partial IV}{\partial \mathbf{C}} = \mathcal{M}_a. \quad (6.17)$$

Proceeding from this result, the anisotropic portion of the extra stress describing a material with stiffer behaviour in fibre direction is given by

$$\mathbf{S}_E^{ani}(IV) = \begin{cases} \sum_{i=1}^M b_i (IV^{(d_i-2)/2} - IV^{-1}) \mathcal{M}_a & \text{if } IV \geq 1, \\ \mathbf{0} & \text{otherwise.} \end{cases} \quad (6.18)$$

The stress tensor of a transversely isotropic material with stiffer behaviour in the directions normal to the fibre direction is, for the sake of brevity, not derived from a strain energy, but directly stated. The derivation follows ideas presented by Markert et al. [163].

First, additional unit vectors, \mathbf{b}_0 and \mathbf{c}_0 , describing directions normal to the fibre direction are introduced, together with their corresponding squared stretches, I_{V_b} and I_{V_c} , and structural tensors, \mathcal{M}_b and \mathcal{M}_c :

$$\begin{aligned} \mathbf{b}_0 &\perp \mathbf{a}_0 & I_{V_b} &= \mathbf{b}_0 \cdot \mathbf{C} \mathbf{b}_0 & \mathcal{M}_b &= \mathbf{b}_0 \otimes \mathbf{b}_0, \\ \mathbf{c}_0 &= \mathbf{a}_0 \times \mathbf{b}_0 & I_{V_c} &= \mathbf{c}_0 \cdot \mathbf{C} \mathbf{c}_0 & \mathcal{M}_c &= \mathbf{c}_0 \otimes \mathbf{c}_0. \end{aligned} \quad (6.19)$$

Note that for the sum of the structural tensors, the relation $\mathcal{M}_a + \mathcal{M}_b + \mathcal{M}_c = \mathbf{I}$ holds. Using the quantities defined in (6.19), the anisotropic portion of a stress tensor describing a stiffer behaviour in the directions normal to the fibre direction (i. e., in cross-fibre direction, XF) can be given by

$$\begin{aligned} \mathbf{S}_{E, XF}^{ani}(I_{V_b}, I_{V_c}) &= \left\{ \begin{array}{ll} \sum_{i=1}^K \bar{b}_i (I_{V_b}^{(\bar{d}_i-2)/2} - I_{V_b}^{-1}) \mathcal{M}_b & \text{if } I_{V_b} \geq 1 \\ \mathbf{0} & \text{otherwise} \end{array} \right\} + \\ &+ \left\{ \begin{array}{ll} \sum_{i=1}^K \bar{b}_i (I_{V_c}^{(\bar{d}_i-2)/2} - I_{V_c}^{-1}) \mathcal{M}_c & \text{if } I_{V_c} \geq 1 \\ \mathbf{0} & \text{otherwise} \end{array} \right\}. \end{aligned} \quad (6.20)$$

Of course, a superposition of the two anisotropic tensors, \mathbf{S}_E^{ani} and $\mathbf{S}_{E, XF}^{ani}$, is also possible, where the choice $\bar{b}_i = b_i$ and $\bar{d}_i = d_i$ for all $i = 1, \dots, K = M$ yields again an isotropic material behaviour.

Active Contribution

The focus of this section is on the continuum-mechanical description of the key property of skeletal muscle to actively contract and generate force. Muscle contraction originates from the interaction and relative movement of the actin and myosin filaments in the sarcomeres of the muscle fibres, see Section 2.5.2.

Two approaches are commonly used to incorporate the active contractile behaviour of muscle within a continuum mechanical framework. The first approach is inspired from the field of Hill-type muscle modelling, cf. e. g. Günther et al. [92], Günther & Schmitt [93], Siebert et al. [242], Till et al. [261], and assumes a priori a superposition of the energies or stress tensors describing the passive and active behaviour. This approach is often used in continuum and multiscale muscle mechanics, cf. e. g. Blemker et al. [16], Böl [18], Böl & Reese [21], Dal et al. [43], Göktepe & Kuhl [87, 87], Johansson et al. [135], Murtada et al. [182], Nash & Hunter [184], Niederer & Smith [190], Odegard et al. [196], and Röhrle and co-workers [219–223, 274].

The second approach is based on the multiplicative split of the deformation gradient tensor, which was initially developed to model processes involving elastic and inelastic deformations (viscoelasticity, elastoplasticity), cf. Lee [154]. In the context of muscle mechanics, the deformation gradient is decomposed into an active (contractile) and a passive (elastic) part, cf. e. g. Gizzi et al. [86], Göktepe et al. [88], Rossi et al. [224, 225], Sharifimajd & Stålhand [239], Stålhand et al. [246, 247]. Note that the multiplicative split of the deformation gradient tensor also yields an additive strain energy (cf. [86, 110, 224]),

but the method requires to identify and solve an additional equation for the evolution of an internal variable.

To avoid the additional complexity involved with the second approach, the present work follows the first method. Thus, the active stress contribution is not formally derived from a strain energy but is constitutively assumed to take the form

$$\mathbf{S}_E^{act}(t, IV, \gamma) = \frac{1}{\lambda_f} P^{max} \gamma(t, \alpha, \lambda_f, \dot{\lambda}_f) \mathbf{M}_a. \quad (6.21)$$

Therein, P^{max} denotes the maximum isometric active force per unit reference area (nominal or engineering stress), and γ is a normalised measure of the local active stress in the muscle, which depends on the activation, α , the sarcomere length expressed through the fibre stretch, λ_f , and the contraction velocity, $\dot{\lambda}_f$, cf. Section 2.5.2. Although the active stress tensor in (6.21) is not derived from a strain energy function, the form is chosen to comply with such an approach. Assuming that an active strain energy $\mathcal{W}^{act}(\lambda_f)$ exists, the active stress tensor can be derived from

$$\mathbf{S}_E^{act} = 2 \frac{\partial \mathcal{W}^{act}}{\partial \mathbf{C}} = 2 \frac{\partial \mathcal{W}^{act}}{\partial \lambda_f} \frac{\partial \lambda_f}{\partial IV} \frac{\partial IV}{\partial \mathbf{C}}, \quad \text{where} \quad \frac{\partial \lambda_f}{\partial IV} = \frac{1}{2\lambda_f}. \quad (6.22)$$

This yields the active stress tensor in (6.21) for $\partial \mathcal{W}^{act} / \partial \lambda_f = P^{max} \gamma$ [110].

As commonly, the active stress tensor in (6.21) only acts in the direction of the muscle fibres, \mathbf{M}_a . This assumption is based on the observation that, when muscles contract, they shorten along their fibre direction, and, due to their incompressibility, they expand in the cross-fibre directions. Although one can easily imagine that activated muscle tissue exhibits also a higher stiffness in the cross-fibre direction than non-activated muscle tissue, no experimental data exist that investigate this effect. Hence, the values of material parameters of the additional stiffness in cross-fibre direction cannot be determined. Despite this lack of experimental data, active stress tensors considering additional components in the cross-fibre direction have been proposed by Baillargeon et al. [7], Rossi et al. [224], Usyk et al. [265] in the context of modelling the mechanical behaviour of the heart.

Different formulations for the normalised active stress in (6.21) are possible. A purely macroscopic description could, for example, be based on the active contractile element in Hill-type muscle models, cf. e.g. Blemker et al. [16]. This leads to $\gamma(t, \alpha, \lambda_f, \dot{\lambda}_f) = \alpha(t) f_\ell(\lambda_f) f_v(\dot{\lambda}_f)$, where $\alpha(t) \in [0, 1]$ is a measure of the activation of the muscle, $f_\ell(\lambda_f)$ is the force-length relation, and $f_v(\dot{\lambda}_f)$ denotes the force-velocity relation, cf. Gordon et al. [89], Hill [117], Katz [141], Siebert et al. [242].

A different approach yielding a multiscale model is obtained when the normalised active stress in the macroscopic continuum-mechanical formulation is derived from a microscopic model, such as, for example, the biophysical half-sarcomere model of Shorten et al. [240]. When the normalised active stress is derived from a microscopic cell model, it is often more convenient to express the fibre stretch in terms of the sarcomere length, ℓ_S , which is directly related to the fibre stretch via $\lambda_f = \ell_S / \ell_S^0$ with $\ell_S^0 = 2.0 \mu\text{m}$ being the sarcomere resting length [61], i.e., the sarcomere length of the reference configuration. Following this and using the definition of the cell-model-based active stress in Equation (4.26), the

normalised active stress in the multiscale chemo-electro-mechanical model is given by

$$\gamma(t, \alpha, \ell_S, \dot{\ell}_S) = f_\ell(\ell_S) \frac{B(t, f_s, \dot{\ell}_S) - B(t_0, 0, 0)}{B(t_s, f_s^{max}, 0) - B(t_0, 0, 0)}. \quad (6.23)$$

Therein, the stimulation frequency, f_s , is used as a measure of the activation, α , and the F - ℓ relation is denoted by $f_\ell(\ell_S)$, cf. Equation (4.24). Moreover, t_s is the time, at which the cell model develops its maximum force, and f_s^{max} denotes the maximum stimulation frequency.

The form in (6.23) accounts for the resting concentrations of XBs in the pre-power stroke and post-power stroke states and normalises the active stress using its value at full activation, at optimal sarcomere length, and under isometric conditions. While the minimal value of the active stress is zero, its maximal value can exceed the value of one during lengthening contractions, cf. Zajac [282].

Note that the forces obtained from the 0D model introduced in Chapter 4 are here interpreted as stresses. Justification for this is given by the fact that normalised nominal stresses are considered; since the nominal stress is defined as the ratio between the force and the referential area element, the normalisation process cancels out the referential area elements, which do not change in time, and the resulting normalised nominal stress is identical to the normalised force.

Summary

In summary, the resulting overall 2nd Piola-Kirchhoff stress tensor of the anisotropic and active skeletal muscle tissue is given by

$$\mathbf{S} = -p J \mathbf{C}^{-1} + \mathbf{S}_E^{iso} + \mathbf{S}_E^{ani} + \mathbf{S}_{E, XF}^{ani} + \mathbf{S}_E^{act}. \quad (6.24)$$

On the right hand side of Equation (6.24), the first term results from the incompressibility constraint, the second term describes the isotropic part of the passive material response, and the third and fourth terms represent the additional passive stress contributions in fibre and cross-fibre directions, respectively. Further, the fifth term describes the active stress contribution that is due to cross-bridge cycling and vanishes if purely passive material behaviour is considered.

6.2 Numerical Treatment of the Multiscale Model

The previous section demonstrated that the formulation of the active part of the stress tensor of the continuum-mechanical muscle model relies on the biophysical half-sarcomere model of Shorten et al. [240], which has been introduced in Section 4.3. Further, Chapter 5 presented the extension of the description of the membrane electrophysiology to spatial conditions. Together, these models constitute a multiscale skeletal muscle model.

The major drawback of the presented multiscale muscle model is its extreme computational complexity. To deal with this, methods are developed in this section to biophysically simulate muscle behaviour from the cellular level to the whole organ level on today's hardware architectures.

6.2.1 Overview of the Multiscale Muscle Model

Figure 6.2 provides an overview of the proposed modelling framework. The individual parts of the framework have been presented in previous sections (the model of the half-sarcomeres in Section 4.3, the AP propagation model in Chapter 5, and the continuum-mechanical model in Section 6.1). Here, the interactions and couplings between the individual model parts are reviewed and highlighted.

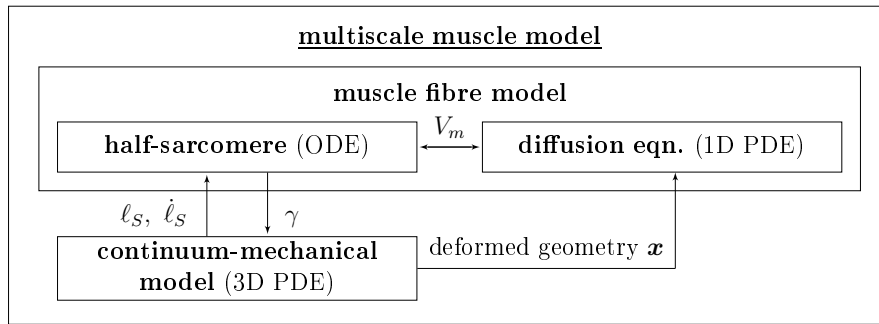


Figure 6.2: Overview of the multiscale muscle model. Each box indicates a part of the model. The couplings between the parts are indicated through arrows together with the transferred information.

To induce the contraction of a muscle fibre, a stimulating current is injected into the half-sarcomere model [240] that is located at the neuromuscular junction. The location of the neuromuscular junction is assumed to be, for example, at the middle of the muscle fibres. Starting from the neuromuscular junctions, the APs propagate along the muscle fibres. This process is described by the diffusion term of the monodomain model, cf. Section 5.2. For the solution of the monodomain model, use is made of the operator splitting approach, which has been presented in Section 5.2.1. The aim of the operator splitting is to separate the biophysical cell model of Shorten et al. [240] from the transient diffusion equation, which are coupled to each other through the membrane potential (cf. Section 5.2.1). Besides the membrane potential and many other biophysical quantities, the cell model of Shorten et al. [240] provides the active stress, γ , that is generated in each half-sarcomere, cf. Equation (6.23).

The normalised active stress enters the active part of the continuum-mechanical constitutive equation through a mapping (homogenisation), which will be discussed in detail in Section 6.2.3. The continuum-mechanical muscle model predicts the stress and strain distributions, as well as the actual (deformed) geometry of the muscle. From the strain distribution, the changes in the sarcomere lengths are determined and, via a finite difference approximation, the local contraction velocities are computed. The contraction velocities directly enter the model of the half-sarcomere, while the sarcomere lengths are used to scale the generated active stresses at the half-sarcomere level, cf. Section 4.3.4. Hence, at a point in space, the half-sarcomere model and the continuum-mechanical model are bidirectionally coupled.

In contrary to Röhrle et al. [220], the governing equations describing the bioelectrical fields and 3D finite elasticity theory are solved in a strongly coupled way, where the solution of the mechanics influences the bioelectrical fields and vice versa. Furthermore, to take into account length changes that arise from the deformation of the muscle tissue,

the monodomain equation is solved on a deforming/moving domain. The adjustments required to take into account the deformation of the domain when solving the equations describing the AP propagation along the muscle fibres will be presented in detail in the next section.

6.2.2 Monodomain Model on a Deforming Domain

This section investigates changes that have to be applied to the monodomain model when taking into account a deformation of the conducting tissue. In a general setting, the conductivity tensor, the membrane capacitance, the surface-area-to-volume ratio, and the ionic currents crossing the cell membrane can depend on the deformation, i. e., $\boldsymbol{\sigma}_{eff} = \boldsymbol{\sigma}_{eff}(\mathbf{C})$, $C_m = C_m(\mathbf{C})$, $A_m = A_m(\mathbf{C})$, and $I_{ion} = I_{ion}(\mathbf{C})$, respectively, cf. Nash & Panfilov [185]. Furthermore, the deformation of the domain has to be taken into account when evaluating the diffusive term on the left-hand side of the monodomain equation (5.19). Moreover, stretch-activated ion channels could be added to a Hodgkin-Huxley-type description of the membrane ionic currents or in a phenomenological model of the AP generation, cf. Guharay & Sachs [91], Panfilov et al. [199].

Without loss of generality, the conductive, capacitive, and ionic dependencies are neglected in the following. Further, since the surface-area-to-volume ratio depends to a large extent on the membrane folding factor (cf. Pullan et al. [211]), changes of this quantity due to the contraction of muscle fibres are expected to be negligible. Here, the focus is on modelling the changes introduced through the deformation of the domain. Distinguishing between derivatives with respect to the actual coordinates and those with respect to referential coordinates, and using the short-hand notation $\mathbf{q} = -\boldsymbol{\sigma}_{eff} \text{grad } V_m$, the monodomain equation can be formulated in the actual configuration by

$$-\text{div } \mathbf{q} = A_m \left(C_m \frac{\partial V_m}{\partial t} + I_{ion} \right). \quad (6.25)$$

Equation (6.25) can either be directly solved in the actual configuration, or it can be solved in the reference configuration by pulling back the respective geometric quantities. To this end, the local formulation in (6.25) is first transformed into the global representation, i. e.,

$$\int_{\Omega} -\text{div } \mathbf{q} \, dv = \int_{\Omega} A_m \left(C_m \frac{\partial V_m}{\partial t} + I_{ion} \right) \, dv, \quad (6.26)$$

and then shifted to the reference configuration. Making use of the transport theorem for the volume element, $dv = (\det \mathbf{F}) \, dV = J \, dV$, the right-hand side of Equation (6.26) can be rewritten in the reference configuration according to

$$\int_{\Omega} A_m \left(C_m \frac{\partial V_m}{\partial t} + I_{ion} \right) \, dv = \int_{\Omega} J A_m \left(C_m \frac{\partial V_m}{\partial t} + I_{ion} \right) \, dV. \quad (6.27)$$

Using Gauß's divergence theorem and Nanson's formula, $d\mathbf{a} = J \mathbf{F}^{T-1} \, d\mathbf{A}$, the left-hand side of Equation (6.26) can be reformulated to obtain

$$\int_{\Omega} -\text{div } \mathbf{q} \, dv = \int_{\partial\Omega} -\mathbf{q} \cdot d\mathbf{a} = \int_{\partial\Omega} -J \mathbf{q} \cdot \mathbf{F}^{T-1} \, d\mathbf{A} = \int_{\Omega} -\text{Div} (J \mathbf{F}^{-1} \mathbf{q}) \, dV. \quad (6.28)$$

While the divergence operator and the integral have been pulled-back to the reference configuration, the current flux, \mathbf{q} , is still defined with respect to the actual configuration. Following Holzapfel [121], the spatial gradient is related to the material gradient by $\text{grad}(\cdot) = \mathbf{F}^{T-1} \text{Grad}(\cdot)$. Furthermore, the referential conductivity tensor, $\boldsymbol{\sigma}_{eff}^0$, is introduced through a covariant pull-back operation, i. e., $\boldsymbol{\sigma}_{eff}^0 = \mathbf{F}^{-1} \boldsymbol{\sigma}_{eff} \mathbf{F}^{T-1}$. This yields for the current flux vector

$$\mathbf{q} = -\boldsymbol{\sigma}_{eff} \text{grad} V_m = -\boldsymbol{\sigma}_{eff} \mathbf{F}^{T-1} \text{Grad} V_m = -\mathbf{F} \boldsymbol{\sigma}_{eff}^0 \mathbf{F}^T \mathbf{F}^{T-1} \text{Grad} V_m. \quad (6.29)$$

Inserting Equations (6.27), (6.28), and (6.29) into (6.26), and returning to a local formulation yields the monodomain equation in the reference configuration, which is given by

$$\frac{1}{J} \text{Div} (J \boldsymbol{\sigma}_{eff}^0 \text{Grad} V_m) = A_m (C_m \frac{\partial V_m}{\partial t} + I_{ion}). \quad (6.30)$$

For further details, the reader is referred to, for example, Dorfmann & Ogden [55], Gizzi et al. [86], Nash & Panfilov [185].

6.2.3 High-Performance Computing

Previous sections discussed the individual modelling parts and their interactions within the multiscale modelling framework. This section focuses on implementational and high-performance computing aspects of the resulting multiphysics discretisation schemes. To this end, efficient solution strategies are developed for the resulting complex and computationally very demanding multiphysics model describing phenomena on different length and time scales. To achieve this, various concepts of software engineering, for example, advanced discretisation schemes for multiphysics problems, parallelisation, or staggered solution schemes are adopted. These concepts have been implemented within the open-source software library `OpenCMISS`, cf. Bradley et al. [26], Heidlauf & Röhrle [109].

Discretisation in Space and Time

The numerical solutions of both the continuum-mechanical model, presented in Section 6.1, and the monodomain equation, presented in Section 5.2, rely on the finite element method. The weak forms of the governing equations of the bioelectrical and continuum-mechanical models, required for a finite element implementation, are provided in Appendix D. A straightforward implementation would use the same mesh for the solution of both problems. However, the solution of the bioelectrical field equations requires an extremely small time step and a very fine mesh due to the rapid changes and steep gradients occurring in physiological cell models, see Section 5.3 and Pullan et al. [211]. On the other hand, using the same spatial and temporal discretisation for the solution of the 3D nonlinear continuum-mechanical model is prohibitively expensive and unnecessary, as changes on the scale of an entire muscle occur at considerably larger time scales.

Following the idea of different characteristic length scales, a multiphysics discretisation scheme is proposed, which uses a much finer mesh for the bioelectrical model than for the continuum-mechanical system. To this end, first, a relatively coarse 3D finite element mesh of the muscle's geometry is generated. Then, relatively fine 1D finite element muscle fibre meshes are embedded within the 3D elements, cf. Röhrle et al. [221]. This

is schematically represented in Figure 6.3. The governing equations of the continuum-mechanical model are discretised using the coarse 3D mesh, while the diffusion part of the bioelectrical field equation is solved on the 1D muscle fibre meshes.

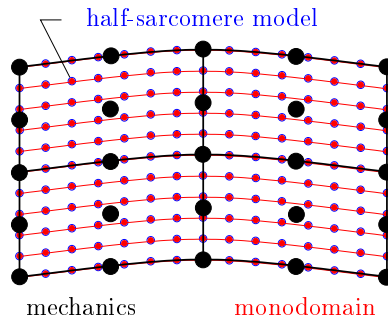


Figure 6.3: A 2D schematic representation of the 3D problem highlighting the use of the different meshes for the different subproblems of the multiscale model. First, the geometry of the muscle is discretised using 3D quadratic Lagrange finite elements (black mesh). This mesh is used for the solution of the continuum-mechanical model. Embedded in these 3D finite elements are 1D muscle fibre meshes (red) used for the solution of the monodomain equation. Each finite element node point of the 1D muscle fibre meshes requires the solution of the biophysical half-sarcomere model (blue).

Since some variables exist on both meshes, transfer operations between the two meshes are required. The transfer from the coarse 3D finite element mesh to the fine 1D fibre meshes is called interpolation, while the transfer in the opposite direction is termed homogenisation. The homogenisation and interpolation operations are discussed for each affected variable further below.

Due to the different characteristic time scales of the different physical phenomena, a staggered solution scheme with three different time step sizes is applied in this work. A schematic representation of the time-stepping scheme is shown in Figure 6.4. First, the half-sarcomere models are solved for 50 time steps with time step size h^{ODE} , cf. Section 4.3.1. The symbol A in Figure 6.4 denotes the solution process for computing the states of the half-sarcomere model for time $t + h^{ODE}$. Note that for simplicity and readability of Figure 6.4 only a fractional number of time steps are depicted. In case of computing the cellular states, which will be used within the next time step of the diffusion equation, only 5 instead of the 50 time steps typically used are depicted in Figure 6.4. Each discretisation point of the monodomain equation is associated with its own half-sarcomere model. The half-sarcomere model is mathematically described by ODEs in

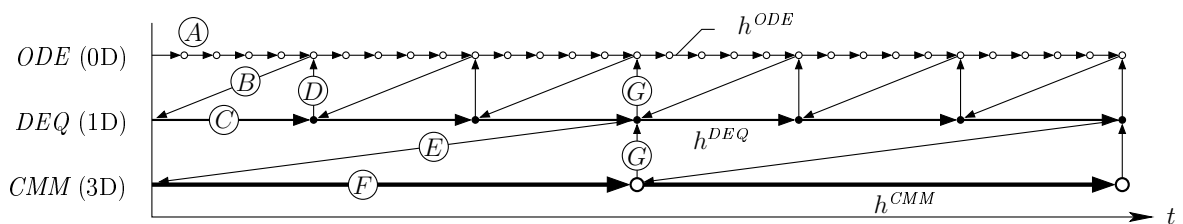


Figure 6.4: Schematic representation of the time-stepping scheme. Therein, h is the time step, ODE denotes the half-sarcomere model, DEQ is the diffusion equation, and CMM is short for continuum-mechanical model. Previously published in [109].

time, which do not rely on any spatial quantities. Therefore, each half-sarcomere model can be solved independently of all other half-sarcomere models. The final values of the membrane potential computed in these steps are used as starting values for the diffusion equation, cf. Section 5.2. This process is denoted by B in Figure 6.4. Following the solution of the diffusion equation with time step h^{DEQ} (indicated by C), the updated values of the membrane potential are used as initial conditions for the next solution step of the half-sarcomere model (indicated by D). This procedure is repeated a number of times (3 times in Figure 6.4, typically 1000 times in the actual computations) before the values of the active stress, γ , are homogenised ($\Gamma : \gamma \rightarrow \bar{\gamma}$). The homogenisation process is denoted in Figure 6.4 by E . The homogenised values, $\bar{\gamma}$, enter the continuum-mechanical model through the active stress tensor, cf. Section 6.1.2. The continuum-mechanical model is only solved in time increments of size h^{CMM} (cf. step F). Further, the values of the sarcomere lengths and sarcomere velocities are interpolated and applied to the half-sarcomere models, see G in Figure 6.4. At the same time, the position of the nodes of the 1D fibre meshes are updated based on the calculated deformation. The described steps are repeated until the final time is reached.

Homogenisation and Interpolation

As described above, some variables are shared between the different discretisations. For example, the values of the active stress field are determined in the model of the half-sarcomere, i. e., at the nodes of the 1D fibre meshes. In order to include the sarcomere-based active stresses in the continuum-mechanical constitutive equation, which is evaluated at the integration points (e. g. the Gauß points) of the 3D finite elements associated with the weak formulation of the mechanical model (see Appendix D.3), the values need to be homogenised. Like in Röhrle et al. [220], the homogenisation is achieved by computing the arithmetic mean of all 1D nodal values that are closest to a certain Gauß point of the continuum-mechanical 3D finite element mesh. Other elaborate homogenisation techniques could be adopted but are not further considered in this work.

The positions of the nodes of the 1D fibre meshes are defined in terms of the local element coordinate system of the 3D geometric finite elements. Following this, the actual positions of the nodes of the 1D fibre meshes can be determined from the deformation of the muscle's geometry, i. e., from the actual configuration. For the interpolation the basis functions of the 3D finite elements are used. The nodal positions of the 1D fibre meshes are updated after each solve of the mechanical submodel.

Further, information about the sarcomere lengths and sarcomere velocities is required in the half-sarcomere models located at the nodes of the 1D fibre meshes. The sarcomere lengths and velocities cannot be determined in the biophysical model of the half-sarcomere, as they also rely on the boundary conditions of the continuum-mechanical model of the entire muscle. Therefore, the local sarcomere velocity, $\dot{\lambda}_f$, is approximated by a backward finite difference scheme: $\dot{\lambda}_f = (\eta_i^{k+1} - \eta_i^k) / h^{CMM}$, where η_i represents the distance between two adjacent nodes, and k and $k + 1$ denote two consecutive time steps of the continuum-mechanical model. To avoid unrealistic high variations in the sarcomere velocity, the average of the velocity is calculated over a patch of seven sequential nodes of one fibre.

Data Structure

The open-source software library `OpenCMISS` [26] provides a highly flexible framework for the simulation of coupled multiphysics problems. Being arranged in a hierarchical fashion, the concepts of regions, meshes, fields, etc. (see Bradley et al. [26] for details) allow for couplings between different physical problems at different length and time scales. The presented skeletal muscle model is built on two regions that occupy the same physical space (volume-coupled problem). Note that the model just as well could have been built on a single region that contains two meshes, as shown in Figure 6.5. When the interaction of a skeletal muscle with neighbouring structures such as other muscles, bone, fat, or skin is of interest, these structures have to be added to the model as additional regions. To couple different regions, their interaction can be defined via interface conditions, e.g. contact.

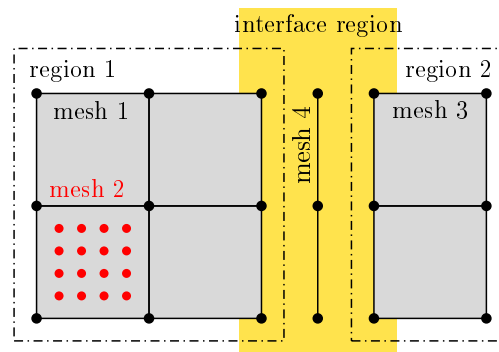


Figure 6.5: Schematic drawing of regions and meshes in `OpenCMISS`. Different regions can be coupled via interface conditions. Several meshes can be associated with a region. Previously published in [109].

Although a region can contain an arbitrary number of meshes, each region used for the chemo-electro-mechanical muscle model contains only one mesh. The region used for the 3D representation of the geometry and the continuum-mechanical model uses a 3D mesh, while the region used for the bioelectrical model contains a mesh that consists of a number of 1D fibres. The 1D fibre meshes are embedded in the 3D finite elements, cf. Figure 6.3.

Fields are a key data structure in `OpenCMISS`. Any quantity that can be associated with a mesh is represented in `OpenCMISS` as a field. A field variable can be constant across the mesh, it can vary from element to element, from node to node, from interpolation point (e.g. Gauß point) to interpolation point, or from data point (arbitrarily located) to data point. The representation of fields in `OpenCMISS` is based on `FieldML`¹ [38], which provides field transfer operators (homogenisation or interpolation) to handle different spatial scales, cf. Section 6.2.3.

Further, `OpenCMISS` employs nested control loops to handle different temporal scales. In the presented model, two separate control loops for the continuum-mechanical model and the bioelectrical problem, each with its own time step size, are linked to a superior main control loop. The control loop for the mechanical model is only associated with a single solver, while the bioelectrical control loop is connected to a solver for the diffusion

¹<http://physiomeproject.org/software/fieldml/>

equation and a second solver for the half-sarcomere model.

The half-sarcomere model is provided in CellML format [82, 107, 158]. CellML is a markup language for the description of subcellular models based on XML (Extensible Markup Language). In a multiscale model, CellML can be used to conveniently describe the physical processes occurring at a single point within a model at a larger spatial scale, cf. Bradley et al. [26], Nickerson et al. [188]. Within OpenCMISS, CellML files are converted to Fortran code, compiled, and linked to the multiscale model at runtime. CellML models can be downloaded from the CellML repository², which contains more than 500 models, among them the biophysical model of a half-sarcomere of Shorten et al. [240]. In OpenCMISS, the time step sizes for the CellML models can be chosen independently of the time step sizes used to solve equations representing different physics. For example, the half-sarcomere model requires a much smaller time step than the diffusion equation, and hence, subcycling of the CellML model is employed. Mathematical justification for doing this is given by the operator splitting technique, cf. Section 5.2.1.

Parallelisation

OpenCMISS is developed for parallel computations in a heterogeneous multiprocessing environment [26], where the MPI (Message Passing Interface) standard³ is used for distributed memory parallelisation, and the OpenMP standard⁴ is used for shared memory parallelisation.

The implementation of the distributed memory parallelisation in OpenCMISS builds on the concept of domain decomposition. For the presented chemo-electro-mechanical skeletal muscle model, the domain is decomposed in such a way that each embedded 1D fibre mesh is uniquely assigned to a processor, see Figure 6.6. This approach reduces the amount of communication between the individual processors to a minimum for the bioelectrical model. Parallel efficiency is hereby guaranteed by the fact that the diffusion part of the bioelectrical model is usually evaluated 1000 times more often than the continuum-mechanical model ($h^{CMM} = 1000 h^{DEQ}$). Hence, a user-defined domain decomposition, rather than a computed decomposition based on the graph partitioning packages ParMETIS⁵ or Scotch⁶, which is typically used within OpenCMISS, is optimal with respect to the entire chemo-electro-mechanical model.

Although currently not implemented, the individual muscle fibre meshes within a single computational domain could be further parallelised using an OpenMP shared memory parallelisation. Further, the integration of the ODEs describing the half-sarcomere model is highly suitable for parallel execution on GPGPUs.

6.3 Applications of the Multiscale Model

This section demonstrates the capability of the proposed multiscale and multiphysics model to biophysically simulate muscle contractions. First, the parameters of the multi-

²<http://www.CellML.org>

³<http://mpi-forum.org>

⁴<http://openmp.org/wp/>

⁵<http://glaros.dtc.umn.edu/gkhome/metis/parmetis/overview>

⁶<http://www.labri.fr/perso/pelegrin/scotch/>

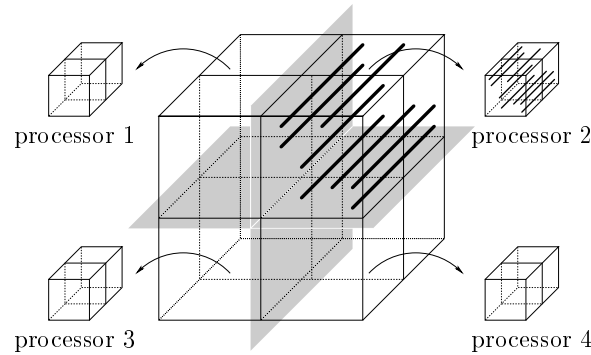


Figure 6.6: *Schematic drawing of the domain decomposition as realised for the chemo-electro-mechanical skeletal muscle model. The decomposition of the 3D mesh of the muscle geometry does not split any of the muscle fibre meshes. Previously published in [109].*

scale model introduced in the previous sections are determined from experimental data. Further, the performance of the computational model is investigated, and a computational validation of the multiscale model is provided. Finally, different applications of the multiscale and multiphysics model are presented.

6.3.1 Parameter Identification

This section deals with the identification of the material parameters that have been introduced in the previous sections. For this purpose, experimental data obtained from the literature are used.

The two parametrisations for the model of the excitation-contraction pathway of Shorten et al. [240] are based on mouse muscles. To simulate human muscle fibres, a partial reparametrisation has been carried out in Section 4.3.2. Within the multiscale muscle model, however, the cell model of Shorten et al. [240] is used to represent individual half-sarcomeres. When modelling fibres that consist of individual half-sarcomeres, the fibre length significantly influences the twitch shape and duration, see Section 6.3.3. Therefore, the reparametrised version will not lead to twitch durations similar to those observed in human muscles. Instead of introducing yet another reparametrisation, the original parametrisations of Shorten et al. [240] are used in this section. While this approach is considered to be sufficient for the generic model developed in this chapter, the simulation of a specific muscle might require a fine tuning of the model. This, however, is beyond the scope of this work.

Being part of the monodomain equation, the description of the membrane ionic currents within the half-sarcomere model of Shorten et al. [240] significantly affects the AP propagation velocity, cf. Pullan et al. [211]. Furthermore, the parameters describing the diffusive part of the monodomain model govern the AP propagation velocity, cf. Section 5.3.5. The parameters for the diffusive part of the monodomain equation are based on literature values and are provided in Table 5.1.

Passive Material Parameters

The anisotropic continuum-mechanical description of the passive muscle tissue is based on several parameters that need to be identified. Unfortunately, the majority of experimen-

tal data existing in the literature have been determined with the macroscopic Hill-type model in mind. Therefore, the experimentally reported stretches are either given in absolute lengths or they are normalised with respect to the optimal length of the muscle. Furthermore, experimental data almost exclusively exist for the muscle's along-fibre direction, since Hill-type muscle models are 1D descriptions that do not consider the cross-fibre directions.

Following the Lagrangean description of continuum mechanics, all quantities are expressed with respect to the reference configuration, which, by definition, has to be stress free. Therefore, the muscle's resting length plays a crucial role in the description of continuum mechanical models. Unfortunately, the resting length of muscles is rarely reported in the literature. Following this, it is difficult to identify valid continuum-mechanical stress-strain relations of passive muscle tissue from the experimental literature. Among the few existing stress-strain data, Hawkins & Bey [102] carried out uniaxial extension tests only in fibre direction. Morrow et al. [181], Nie et al. [189], and Takaza et al. [256] considered, in addition to the fibre direction, the tensile behaviour of muscle tissue in cross-fibre direction. Due to the fact that extension experiments require a non-destructive fixation of the tissue samples, which is extremely difficult to achieve, several researchers investigated the properties of the 3D muscle tissue under compression, see Böl et al. [20], Bosboom et al. [24], Van Loocke et al. [267, 268, 269], and Zheng et al. [284]. Furthermore, Böl et al. [19] investigated the behaviour of passive muscle tissue under pure shear.

In this work, the characterisation of the passive material behaviour is based on the description of fibre-reinforced materials, where one commonly assumes that the fibres bear load only under tension but not under compression [163]. Following this, the parameters of the isotropic Mooney-Rivlin model are determined from the data of the compression experiments of Zheng et al. [284] using a least-squares fit. Compared to other experiments (see Van Loocke et al. [268]), the data of Zheng et al. [284] describe muscle tissue exhibiting intermediate stiffness. Figure 6.7a demonstrates that the resulting material behaviour nicely fits the experimental data [284].

Comparing the resulting isotropic material behaviour to data obtained from tension experiments in fibre direction, the model's behaviour is much too compliant (result not shown). Following this, the parameters of the anisotropic material model of Markert et al. [163] are determined from the experimental data of Hawkins & Bey [102] by performing a least-squares fit. Figure 6.7b shows the resulting behaviour of the model in fibre direction together with the experimental data of Hawkins & Bey [102]. A single term of the model of Markert et al. [163] is sufficient to fit the experimental data. The fitted parameters of the isotropic and anisotropic models (parameter set *A*) are summarised in Table 6.1.

Symbol	Description	Value (slow/fast)	Unit	Reference
c_{10}	1 st Mooney-Rivlin parameter	$6.352e^{-11}$	N/cm ²	[284]
c_{01}	2 nd Mooney-Rivlin parameter	0.3627	N/cm ²	[284]
b_1	1 st anisotropy parameter	$2.756e^{-6}$	N/cm ²	[102]
d_1	2 nd anisotropy parameter	43.373	[-]	[102]

Table 6.1: *Passive material parameters of the mechanical model (A).*

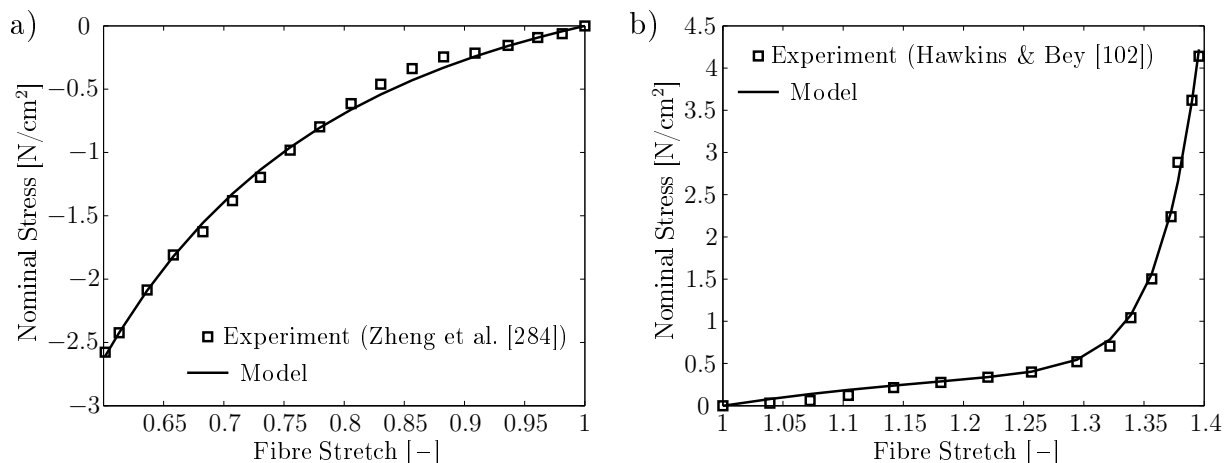


Figure 6.7: Comparison of the model and passive experimental data. (a) The parameters of the isotropic Mooney-Rivlin material, c_{10} and c_{01} , are fitted in a least-squares sense to the experimental data of passive skeletal muscle under compression of Zheng et al. [284]. (b) The parameters of the anisotropic material in fibre direction, b_1 and d_1 , are fitted in a least-squares sense to the experimental data of Hawkins & Bey [102].

While parameter set *A* nicely fits the experimental data of Zheng et al. [284] and Hawkins & Bey [102], it shows less agreement with the passive behaviour of other muscles. This can be explained by the fact that the passive properties of skeletal muscles vary heavily from muscle to muscle, subject to subject, and species to species, cf. e.g. Gareis et al. [81]. To demonstrate that the presented model is flexible enough to simulate muscles with different mechanical behaviour, now a muscle is considered that has a more compliant mechanical behaviour in fibre direction than in cross-fibre direction, cf. Nie et al. [189], Takaza et al. [256]. Furthermore, this muscle has a quite different behaviour in fibre direction than normal to the fibre direction. Hence, while the parameters of the isotropic Mooney-Rivlin material are retained, an alternative set of anisotropic parameters is determined from the experimental data of Takaza et al. [256] using a least-squares fit (parameter set *B*). Figure 6.8 demonstrates that the model can nicely fit the experimental data [256] in fibre direction (Figure 6.8a) and in cross-fibre direction (Figure 6.8b). In each direction, a single term of the respective material model was sufficient to fit the experimental data. The resulting material parameters (parameter set *B*) are listed in Table 6.2.

Symbol	Description	Value (slow/fast)	Unit	Reference
c_{10}	1 st Mooney-Rivlin parameter	$6.352e^{-11}$	N/cm ²	[284]
c_{01}	2 nd Mooney-Rivlin parameter	0.3627	N/cm ²	[284]
b_1	1 st anisotropy parameter	0.3554	N/cm ²	[256]
d_1	2 nd anisotropy parameter	12.6605	[-]	[256]
\bar{b}_1	1 st cross-fibre anisotropy parameter	5316.3722	N/cm ²	[256]
\bar{d}_1	2 nd cross-fibre anisotropy parameter	$1.499e^{-2}$	[-]	[256]

Table 6.2: Passive material parameters of the mechanical model (*B*).

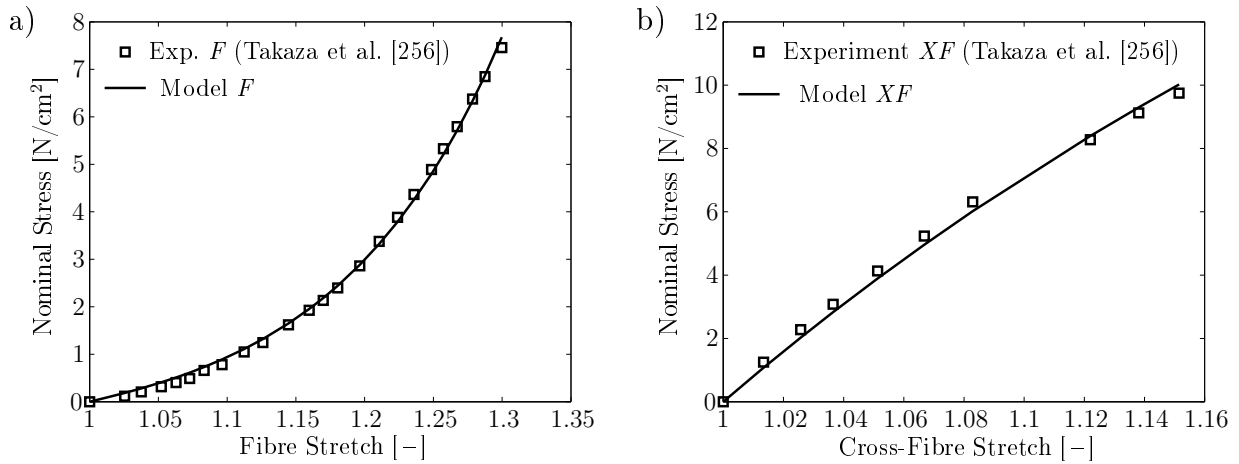


Figure 6.8: Comparison of the model and passive anisotropic experimental data. The parameters of the anisotropic material (a) in fibre (F) direction, b_1 and d_1 , and (b) in cross-fibre (XF) direction, \bar{b}_1 and \bar{d}_1 , are fitted in a least-squares sense to the experimental data of Takaza et al. [256].

Due to the fact that Takaza et al. [256] only report passive material properties but do not investigate the active behaviour of the muscle, the passive material parameters of Table 6.1, i.e., parameter set A , are used in the following. These parameters are based on the data of Hawkins & Bey [102], who also investigated the active behaviour of the muscle.

Active Material Parameters

Having identified the parameters of the passive material description, the active behaviour is considered next. The description of the active part of the continuum-mechanical model depends on the parameter P^{max} and via $\bar{\gamma}$ on the F - ℓ and the F - v relations. For the description of the F - ℓ relation, the fourth-order polynomial of Section 4.3.4 is used. Further, the maximum isometric stress, P^{max} , can directly be obtained from experimental data. For example, Hawkins & Bey [102] report a maximum isometric stress of approximately 7.3 N/cm² for the tibialis anterior muscle of the rat. Although values of 20–25 N/cm² are reported by other researchers, this work adopts the value of Hawkins & Bey [102], since the passive anisotropic material parameters are also determined from this source. Of course, for the simulation of a different muscle, the maximum isometric stress can easily be changed in the model, just as well as all other parameters. While one can easily find the value of the maximum isometric stress, the stretch or strain at which this stress can be generated is more difficult to determine. Following the direct relation between the sarcomere length and the fibre stretch and adopting the value of the resting sarcomere length $\ell_S^0 = 2.0 \mu\text{m}$ [61], the stretch at the optimal sarcomere length of $\ell_S^{opt} = 2.4 \mu\text{m}$ [32] is found to be $\lambda_f^{opt} = 1.2$. Finally, the parameters required in the cell model to obtain a F - v relation that is similar to experimental data, are directly adopted from Section 4.3.4. For the sake of convenience, the parameters of the active mechanical model are summarised in Table 6.3.

Symbol	Description	Value (slow/fast)	Unit	Ref.
P^{max}	maximum isometric stress	7.3	N/cm ²	[102]
x_0	average distortion induced through the power stroke	0.05	μm	[240]
f'	XB-detachment rate (from A_1)	5/15	ms ⁻¹	[240]
h_0	power stroke forward rate	0.08/0.24	ms ⁻¹	[240]
h'	power stroke backward rate	0.06/0.18	ms ⁻¹	[240]
\bar{f}	XB-attachment rate of an isometric contraction	0.5/1.5	ms ⁻¹	[240]
\bar{g}	XB-detachment rate if no neighbour is in the A_2 state	0.04/0.12	ms ⁻¹	[240]
ν	influence of cooperative effects	3.0/3.4	[-]	[213]
ϑ	level of distortion dependence	1700/1000	[-]	[213]
ℓ_S^0	resting sarcomere length	2.0	μm	[61]
ℓ_S^{opt}	optimal sarcomere length	2.4	μm	[32]

Table 6.3: Material parameters of the active mechanical model.

6.3.2 The Multiscale Computational Model

This section deals with the computational model that results from the discretisation of the multiscale muscle model. First, as a proof of concept, the multiscale model is used to simulate key parameters of macroscopic muscle behaviour. Furthermore, critical discretisation parameters and the parallel performance of the multiscale computational model are investigated. The results presented in this section have previously appeared in Heidlauf & Röhrle [109, 111].

Verification of the Multiscale Computational Model

The presented multiscale approach is based on the assumption that key properties of skeletal muscle behaviour, namely the F - ℓ and F - v relations, can be recovered at the macroscale although they are completely defined at the microscopic half-sarcomere level. Following this, the multiscale model is first compared to experimental F - ℓ data to demonstrate that the chemo-electro-mechanical muscle model can reproduce typical mechanical behaviour of whole muscle under isometric conditions on the macroscale. For the comparison, the experimental F - ℓ data of Hawkins & Bey [102] are used, from which the parameters of the anisotropic material parameters and the value of the maximum isometric stress have been determined.

Hawkins & Bey [102] analysed the rat TA muscle, which consists of about 97.5% type-II fibres [248]. Therefore, all fibres within the model are assumed to be of type II. The numerical specimen used for the comparison is chosen as a rectangular cuboid with dimensions 4 cm \times 2 cm \times 2 cm. The fibres are aligned with the long edge of the cuboid. Starting from the stress-free reference configuration, the muscle specimen is first passively stretched along the fibre direction to the desired muscle length. After passively stretching, displacement in the direction of the fibres is constrained at both ends of the specimen in order to simulate fixed-end contractions. Moreover, displacement at two fur-

ther non-parallel faces of the specimen is constrained in the direction perpendicular to the respective face (symmetry boundary conditions). Note that the lengths of the individual half-sarcomeres are not constrained but only the total length of the muscle. To simulate a fully activated muscle, a stimulation frequency of $f_s = 100$ Hz is applied to the central half-sarcomere model of each muscle fibre model. The simulation output is the nominal stress, which is defined as the ratio of the resulting reaction forces in fibre direction and the initial cross-sectional area of the specimen. The peak nominal stress of the chemo-electro-mechanical model induced through the passive stretch and the applied stimulation provides the value of the total model. The determined passive and total nominal stresses at different muscle stretches are shown in Figure 6.9a together with the experimental stress-stretch data of Hawkins & Bey [102].

After establishing realistic mechanical behaviour under isometric conditions, the coupled chemo-electro-mechanical model is now tested for its capacity to reproduce experimental F - v data of whole muscle. The hyperbolic F - v relation of Hill [117] can be expressed by

$$\frac{v}{v_{max}} = \frac{1 - \bar{F}/\bar{F}_{iso}}{1 + \bar{F}/(\kappa\bar{F}_{iso})}, \quad (6.31)$$

where \bar{F}_{iso} denotes the maximum isometric force, v_{max} is the maximum shortening velocity at $\bar{F} = 0$, and κ is a dimensionless parameter. In the literature, κ ranges from 0.15 to 0.25 [165]. Ranatunga [213], for example, reports a mean value of $\kappa = 0.24$ for rat soleus muscle. Since rat soleus muscle consists mainly of type-I fibres [244], all half-sarcomere models in the multiphysics model use now the type-I parametrisation of Shorten et al. [240].

Within the numerical experiments the model specimen is first passively stretched to the optimal length. Then, the length of the specimen is kept fixed, and all fibres are fully activated ($f_s = 100$ Hz). For a prescribed velocity the corresponding reaction force is computed. The resulting F - v data are depicted in Figure 6.9b, where the force values have been normalised to the value at isometric conditions and the velocity has been normalised to the maximum shortening velocity. Fitting the parameter κ in Equation (6.31) in a least-squares sense to the simulation results obtained for shortening contractions yields $\kappa = 0.241$, cf. Figure 6.9b.

For lengthening contractions, the chemo-electro-mechanical model predicts a maximum force of 1.77 times the isometric force. In the literature, different behaviours are reported for lengthening contractions of skeletal muscles, see Morgan [179]. The bounded increase predicted by the model is in agreement with the findings of Zajac [282], who reports a maximum of 1.8 times the isometric force. Since the model behaviour for lengthening contractions proved to be sensitive to a single parameter, the presented model can easily be adapted to a different shape. However, the non-continuously differentiable behaviour at the transition from shortening to lengthening contractions, observed in experimental F - v relations (see Katz [141]), is not predicted by the model. Once the origin of this unique feature is completely understood, it could potentially be included in the XB-dynamics component model.

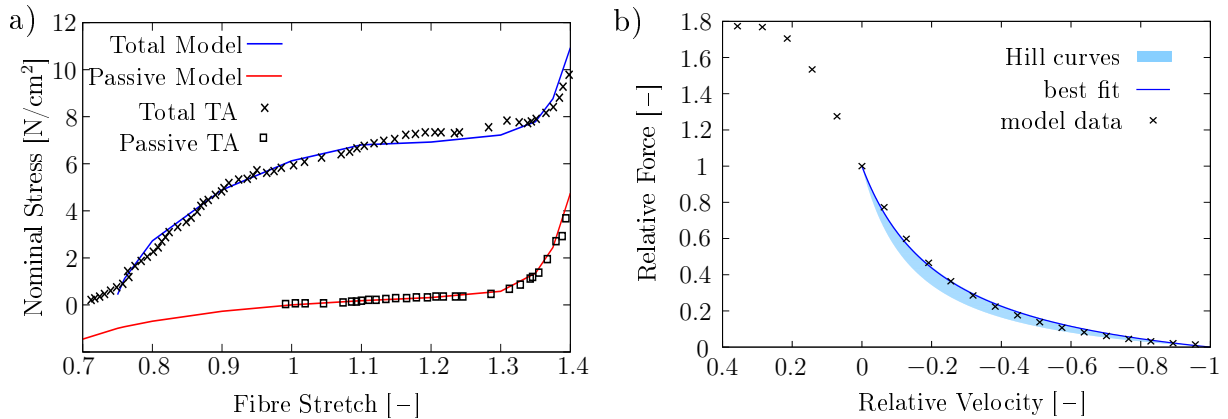


Figure 6.9: F - ℓ and F - v relations of the multiscale muscle model compared to experimental data. (a) The passive and total stresses of the model, and the experimental data of rat TA muscle [102]. Simulations are carried out at stretches varying from 0.8 to 1.4 in steps of size 0.1 and at $\lambda_f = 0.75, 0.76, 1.35,$ and 1.375 . (b) The F - v data of the model (black crosses), the corresponding fit of Hill's hyperbolic relation ($\kappa = 0.241$, blue line), and the region of typical muscle F - v curves ($0.15 \leq \kappa \leq 0.25$, light-blue shaded area). Figure previously published in [111].

Investigation of Critical Discretisation Parameters

The presented multiscale model is built on a staggered solution scheme that uses different time step sizes for the solution of the different submodels. Critical time step sizes for the bioelectrical model have already been discussed in Section 5.3.3. Here, the model behaviour for different time step sizes of the continuum-mechanical model, h^{CMM} , is investigated. Figure 6.10 shows the stress evolution of a shortening contraction ($v = -0.1 v_{max}$) of a muscle that is uniformly stimulated at 50 Hz. The results for three different time step sizes ($h^{CMM} = 0.1$ ms, 0.5 ms, and 2.0 ms) are shown, whereof the solutions for the smaller two time steps almost coincide (red dashed line and blue crosses), and the solution for the largest time step size ($h^{CMM} = 2.0$ ms) depicts significant deviations and oscillatory behaviour.

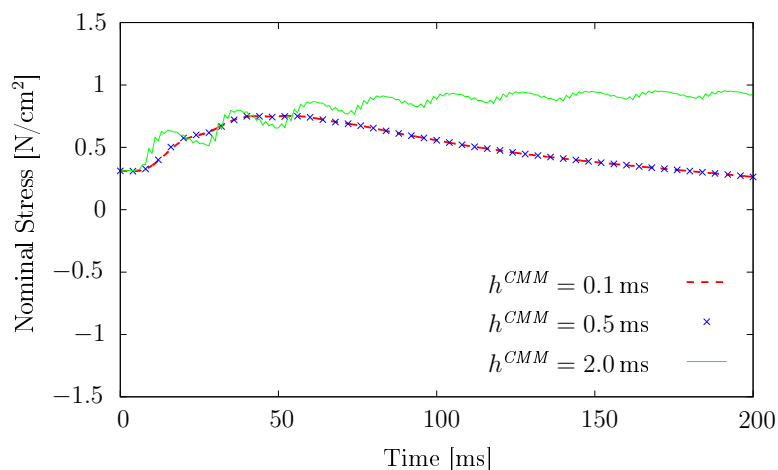


Figure 6.10: Model behaviour for different time step sizes of the continuum-mechanical model, h^{CMM} . The solutions for the smaller two time steps almost coincide (red dashed line and blue crosses), while the solution for the largest time step size shows a non-physical, oscillatory behaviour. Previously published in [111].

Moreover, within this framework the active stresses determined in the half-sarcomere models are homogenised and included in the continuum-mechanical constitutive equation. The homogenisation is required for computational efficiency. A skeletal muscle model that would use the same number of elements for the bioelectrical and the mechanical problem does no longer require any homogenisation, however, this approach results in a computational model that is no longer feasible for any practical application. The homogenisation process has little effect on the convergence behaviour of the mechanical problem, as has been demonstrated by Röhrle et al. [220]. In Röhrle et al. [220], the number of embedded fibre models remained constant, while the number of 3D mechanical elements was successively refining until homogenisation is no longer required. The investigation showed very good convergence properties if compared to the mechanical-only problem, see Röhrle et al. [220].

Performance Analysis

To analyse the parallel performance of the computational framework, a simple geometric model is considered. A cubic geometry with 2 cm edge length is generated and discretised using eight tri-quadratic/tri-linear Lagrange finite elements, cf. Appendix D.3. A uniform fibre direction parallel to an edge of the cube is defined, and a total of 400 muscle fibres are evenly distributed in the cubic geometry. Each fibre is discretised using 60 linear Lagrange finite elements. At each discretisation point of the 1D muscle fibre meshes, the fast-twitch version of the model of Shorten et al. [240] is solved.

First, the muscle is passively stretched in fibre direction by 20 % to reach the optimal fibre stretch of $\lambda_f^{opt} = 1.2$. Under isometric conditions (the muscle specimen is fixed at the optimal length), a 100 Hz tetanic stimulation is applied to the central half-sarcomere model of all fibres in the model. To analyse the speed-up in a parallel environment, the described model is executed on 1, 2, and 4 processors. A speed-up of 2.18 is achieved when going from 1 to 2 processors, while a speed-up of 1.95 is achieved when comparing 2 to 4 processors. Further, the simulations are repeated using only 36 fibres instead of 400. In this case, speed-ups of 1.44 and 1.50 are achieved, when increasing the number of processors from 1 to 2 and from 2 to 4, respectively. Table 6.4 lists the timing results and speed-up factors for a Intel® Xeon® Processor E5520 and 8 GB of RAM.

# of procs	36 fibres		400 fibres	
	time [s]	speed-up [-]	time [s]	speed-up [-]
1	10004.32		177759.11	
2	6940.91	1.441	81360.24	2.185
4	4625.88	1.500	41763.99	1.948

Table 6.4: Execution time in seconds and resulting speed-up for 1, 2, and 4 processors. Previously published in [111].

In the example with 400 fibres, the solution of the bioelectrical model dominates the total computing time. Here, a speed-up factor of 2.18 occurs, which exceeds the theoretically achievable value of 2. This can be explained by a significantly higher number of cache misses on 1 processor than on multiple processors, as the size of the bioelectrical

model for each processor scales down proportionally to the number of processors. (Ghost elements do not exist and no communication between the processors is required in the bioelectrical model.) The other end of the spectrum is marked by the example using only 36 fibres, i. e., 3×3 fibres per 3D element, leading to a one-by-one correspondence between the number of Gauß points in the plane perpendicular to the fibres and the number of embedded fibres. (The 3D elements use $3 \times 3 \times 3$ Gauß points.)

Note that the discretisation for the mechanics is independent of the number of embedded fibres and is identical in both cases. In the case of 36 fibres, the speed-up factors are rather poor, since the solution of the continuum-mechanical problem claims a larger fraction of the total computing time. The poor scaling of the continuum-mechanical model is due to the few 3D elements. Together with the ghost elements required for the mechanical model, each processor has to compute (i) 8 finite elements when 1 processor is used, (ii) 8 finite elements when 2 processors are used, and (iii) 6 finite elements when 4 processors are used. (All elements that share a surface with an actual element of the domain are ghost elements.) For practical applications, however, finer discretisations of the continuum-mechanical model are desirable since they provide a better approximation of the muscle's geometry and a higher accuracy. Furthermore, including more muscle fibres within the chemo-electro-mechanical model is preferable for more realistic muscle simulations.

6.3.3 Investigating Different Muscle Fibre Arrangements

While previous sections investigated the general behaviour of the multiscale computational model, this section presents a specific application of the chemo-electro-mechanical muscle model. To this end, differences in the muscle contraction and force generation that result from the arrangement of the muscle fibres in the muscle are investigated. The results presented in this section have previously been published in Heidlauf & Röhrle [111].

Introduction

The fascicles in parallel-fibred muscle are aligned with the muscle's line of action and run almost the entire length of the muscle [159]. The fascicles either consist of long fibres spanning the entire length of the fascicles (in the following termed "spanning-fibred muscle"), or they are composed of several shorter in-series arranged fibre compartments (in the following termed "series-fibred muscle"), cf. Heron & Richmond [115], Young et al. [277]. The fibre compartments in series-fibred muscle can either be separated by tendinous inscriptions, as, for example, in cat and human semitendinosus muscle, or the muscle fibres are arranged in short overlapping arrays, see Loeb et al. [159], Paul [202], Woodley & Mercer [276].

The advantages and disadvantages of series-fibred and spanning-fibred muscle arrangements on the force generation have not yet been systematically analysed. Experiments provide only limited information on which effects are due to the fibre arrangement and which effects are due to other anatomical or physiological properties, e. g. the muscle geometry. Mathematical models instead can be used to investigate the influence of a specific property on the overall behaviour. Previous modelling works focused on the influences of the muscle geometry and the fibre direction on the force generation [229, 288]. In this section, the presented chemo-electro-mechanical skeletal muscle model is used to compare series-fibred and spanning-fibred muscles. The aim of this comparison is to reveal

differences in the mechanical behaviour of the different muscle fibre arrangements.

Loeb et al. [159] hypothesize that there exists a stability problem in spanning-fibred muscles when the AP propagation time exceeds the twitch rise time of a single sarcomere. This implies that sarcomeres located at a long fibre's neuromuscular junction produce their peak twitch force before sarcomeres located at the fibre's ends are activated, and hence, activated sarcomeres might shorten against non-activated parts of the fibre [159]. As a result, mechanical instabilities and damage might occur [159], since sarcomeres located at the fibre ends might be passively stretched to beyond myofilament overlap, a state, from which the sarcomere can not independently recover through activation. It has therefore been suggested that the AP propagation time might impose a limit on the fibre length [159]. In series-fibred muscle, a similar stability problem is believed to exist when activation of series-arranged compartments is unbalanced or asynchronous, i. e., if muscle fibres in an activated compartment shorten against fibres in non-activated compartments [159, 216].

Methods

In all of the following numerical experiments, a rectangular cuboid with dimensions $12\text{ cm} \times 2\text{ cm} \times 2\text{ cm}$ is considered. The fascicle direction is assumed to be aligned with the cuboid's long edge. To mimic series-fibred skeletal muscle arrangements, the long side of the muscle specimen is subdivided into compartments of equal length. The muscle fibres in adjacent compartments are aligned end-to-end and do not interdigitate with each other. As in real muscle, electrical activation from one muscle fibre to adjacent ones does not occur, neither between adjacent compartments nor in lateral direction within a compartment. The neuromuscular junction of each muscle fibre is assumed to be located in the middle of the respective fibre. All half-sarcomeres are assumed to be of type II. The mechanical behaviour of the chemo-electro-mechanical muscle model is investigated for simultaneously stimulating all muscle fibres. Before stimulating the muscle specimen, it is passively stretched to the optimal length ($\lambda_f^{opt} = 1.2$, $\ell_S^{opt} = 2.4\ \mu\text{m}$).

Results

First, fixed-end contractions and shortening contractions at 10 % of the maximum shortening velocity at $f_s = 50\text{ Hz}$ and 100 Hz are considered. A muscle model with fibres that span the entire length of the fascicles (referred to as *SPA*) and a model consisting of four fibre compartments in series (referred to as *SER·4*) are compared to each other. The resulting nominal stresses are depicted in Figure 6.11. Fixed-end contractions predict differences of almost up to 80 % between the different muscle fibre arrangements. The largest differences occur at the beginning of the contraction, i. e., during the first twitch but decline rapidly to approximately 10 % and less. Moreover, the results show that the initial differences are less pronounced in shortening contractions independent of the stimulation frequency. At $f_s = 50\text{ Hz}$, twitches tend to be more fused for model *SPA* than for model *SER·4*. This applies to both fixed-end and shortening contractions. Completely fused twitches are observed for both models for $f_s = 100\text{ Hz}$.

Independent of the stimulation frequency, model *SER·4* shows higher peak forces than model *SPA* in fixed-end and shortening contractions. At $f_s = 100\text{ Hz}$, the maximum force of model *SER·4* is 3.29 % and 6.61 % higher than the maximum force of model *SPA* in

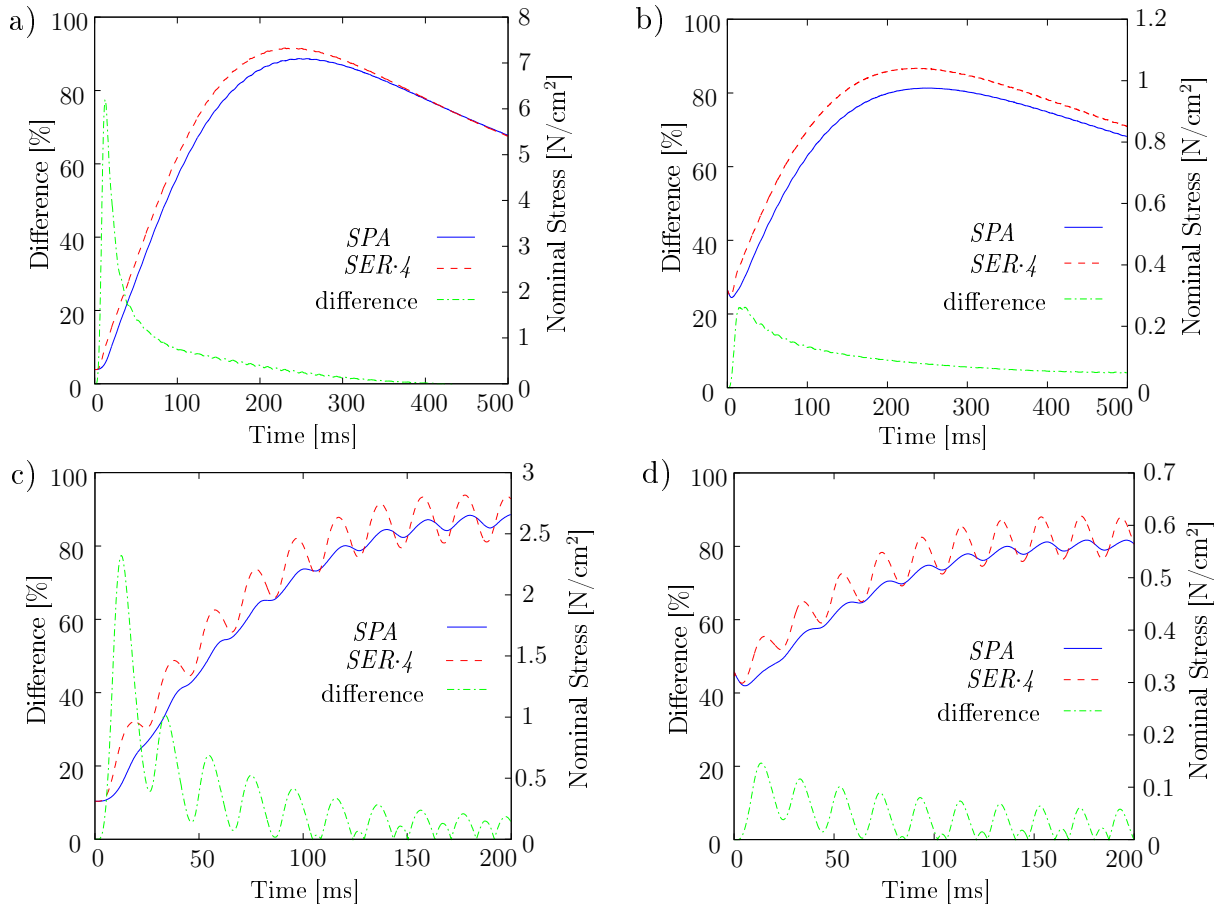


Figure 6.11: Comparison of a spanning-fibred muscle model (*SPA*) and a series-fibred muscle model consisting of four in-series arranged fibre compartments (*SER.4*) stimulated with (a, b) $f_s = 100$ Hz and (c, d) $f_s = 50$ Hz in (a, c) fixed-end and (b, d) shortening contractions at $v = 0.1 v_{max}$, and their differences in percent. Figure previously published in [111].

fixed-end and shortening contractions, respectively. The observed decrease after reaching the maximal value in all simulations with $f_s = 100$ Hz is due to fatigue, which is contained in the half-sarcomere model of Shorten et al. [240].

The results reveal that the largest differences between spanning-fibred and series-fibred muscle models occur during the first twitch in fixed-end contractions. Hence, fixed-end single twitch experiments are further investigated in the following. The aim is to reveal a potential relation between the twitch shape and the fibre length. In addition to the model with spanning fibres (termed *SPA*), muscle specimens consisting of two, four, six, and twelve fibre compartments of equal length are considered. The series-fibred models are termed *SER.2*, *SER.4*, *SER.6*, and *SER.12* indicating the respective number of compartments. Furthermore, two different scenarios are considered. In the first scenario, all fibres in all compartments receive a stimulus at the same time to simulate a coordinated single twitch contraction. The second scenario appeals to the model with six in-series arranged compartments, in which only the fibres within the first compartment are stimulated. (Note that the choice which of the compartments is stimulated does not influence the resulting reaction forces.) This model is referred to as *SER.6a*.

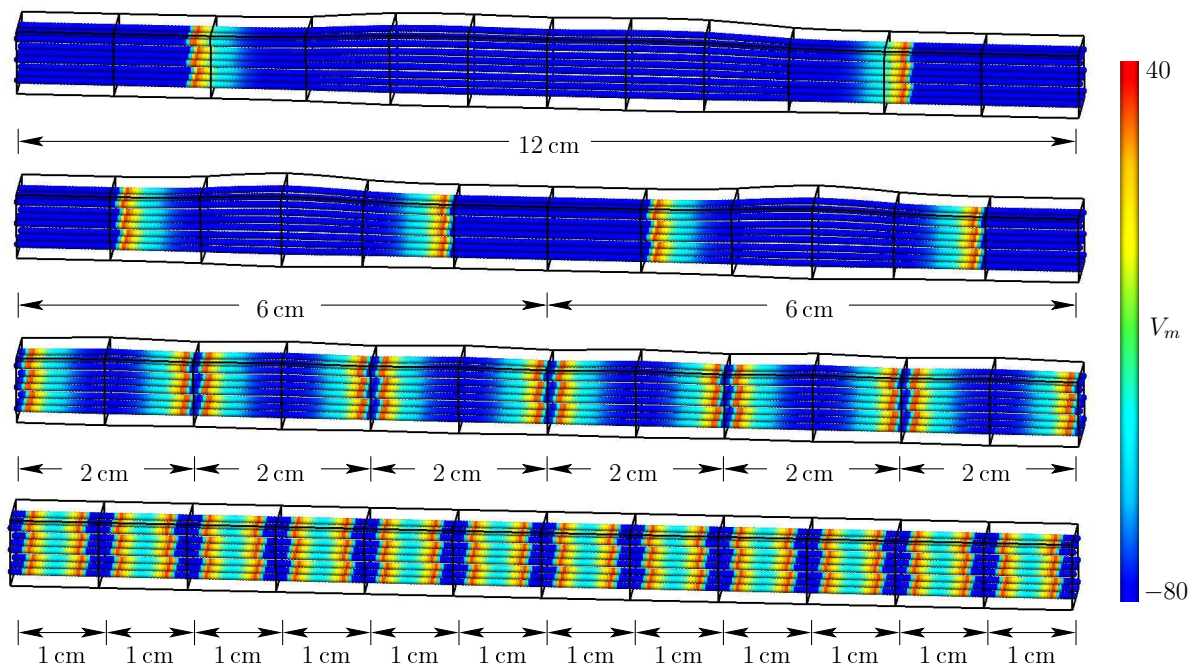


Figure 6.12: Distribution of the membrane potential (V_m in [mV]) and contraction-induced deformation during single twitch contractions of models *SPA* ($t = 22$ ms after stimulation), *SER.2* ($t = 10$ ms), *SER.6* ($t = 5$ ms), and *SER.12* ($t = 2$ ms) (from top to bottom). Previously published in [111].

Figure 6.12 shows the distribution of the membrane potential and the contraction-induced deformation of the muscle in the different models of the first scenario. Further, Figure 6.13 demonstrates that the twitch rise time of a muscle depends on the length of its muscle fibres, i. e., the twitch rise time increases with increasing muscle fibre length. Thus, model *SER.12* has the lowest twitch rise time of 17.2 ms, while the maximum twitch rise time occurs in model *SPA*, where the peak stress occurs 38.2 ms after stimulation. The computed AP propagation speed of the models is 2.186 m/s. In model *SPA*, where the AP propagates 6 cm from the motor end-plates to each end of the fibres, this propagation speed yields an AP propagation time of 27.45 ms. In comparison, a half-sarcomere model considered in isolation shows a twitch rise time of 16.1 ms. Hence, the AP propagation time in model *SPA* exceeds the twitch rise time of a single half-sarcomere. In other words, the sarcomeres located at the motor end-plates reach their peak twitch force before the sarcomeres located at the ends of the fibres are activated.

While the twitch rise time increases, the peak twitch stress of the muscle model decreases with increasing muscle fibre length. In detail, the peak twitch stresses are 0.82 N/cm^2 and 0.98 N/cm^2 in models *SPA* and *SER.12*, respectively, which corresponds to an increase of 19.4 %. Integrating the area below the stress curve over 200 ms, i. e., to a point where the active stress has declined and only passive stress components remain, yields $84.95 \text{ N}\cdot\text{ms/cm}^2$ and $83.25 \text{ N}\cdot\text{ms/cm}^2$ for models *SPA* and *SER.12*, respectively. Further, deducting from the total stresses the respective passive stresses, which are due to the initial stretch to the optimal length, the peak twitch force obtained in model *SER.6a* is 6.5 times smaller than the peak twitch force of model *SER.6*.

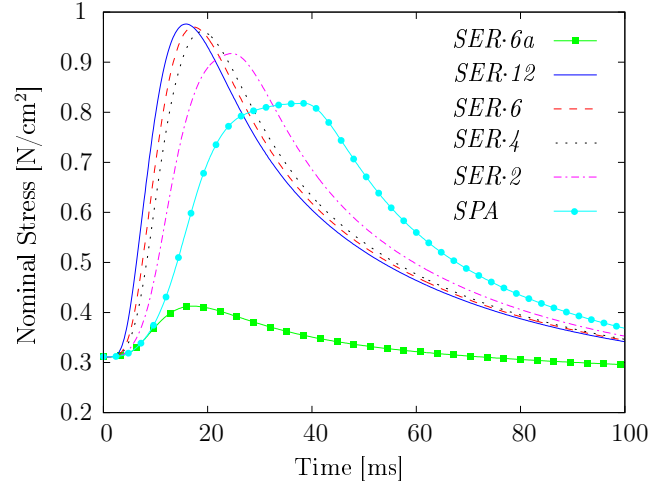


Figure 6.13: Comparison of single twitch contractions in a spanning-fibred model and in series-fibred models with different fibre lengths and number of compartments. The reader is referred to the text for model definitions. Previously published in [111].

Besides the contraction-induced stresses, changes in local sarcomere length during fixed-end single twitch contractions are analysed. The aim is to investigate if activation-induced stretches of passive sarcomeres to beyond myoflament overlap occur. The resulting maximum and minimum sarcomere lengths are reported in Table 6.5.

	Min. sarcomere length		Max. sarcomere length	
<i>SER-12</i>	2.39 μm	99.59 %	2.41 μm	100.41 %
<i>SER-6</i>	2.26 μm	93.96 %	2.54 μm	105.95 %
<i>SER-4</i>	2.16 μm	90.05 %	2.63 μm	109.68 %
<i>SER-2</i>	2.03 μm	84.52 %	2.64 μm	109.84 %
<i>SPA</i>	1.81 μm	75.49 %	2.66 μm	111.02 %
<i>SER-6a</i>	1.74 μm	72.51 %	2.58 μm	107.38 %

Table 6.5: Minimum and maximum sarcomere lengths in fixed-end single twitch contractions absolute and in percent of their length prior to stimulation, i. e., $\ell_S^{\text{opt}} = 2.4 \mu\text{m}$. Previously published in [111].

Considering the first scenario, the shortest and largest sarcomere lengths of 1.81 μm and 2.66 μm , respectively, occur for model *SPA*. Changes in sarcomere length decrease with an increasing number of in-series fibre compartments. In the second scenario, a minimum sarcomere length of 1.74 μm is observed for model *SER-6a*.

Discussion

First, the computational results obtained for the different muscle fibre arrangements are discussed, before using this data to analyse its implications on stability. The presented model predicts the largest differences between series-fibred and spanning-fibred muscles in the rise time, shape, and peak force of single twitches. During sustained contractions, twitches tended to fuse at lower stimulation frequencies in spanning-fibred muscles, while

series-fibred muscles showed higher peak forces. Since the basic descriptions of passive and active material behaviour are identical in the different models, the observed differences in the force responses must result from the differences in the muscle fibre arrangement. Although the same half-sarcomere model is used in all simulations, single twitches are more dispersed in muscle models with longer fibres, which can be explained by longer AP propagation times. Experimentally observed differences in the twitch shape in different fibres of the same twitch type might therefore be largely governed by the fibre length. This might partially explain the different twitch shapes observed in different species. For example, the twitch rise time in mouse soleus muscle consisting purely of type-I fibres is approximately 35 ms [240], while 90 ms are observed in human type-I MUs [76]. Further, the simulations demonstrated that a fascicle consisting of end-to-end terminating fibres does functionally not perform like a single muscle fibre of equivalent length, as hypothesized by Lieber & Fridén [157].

According to Harris et al. [101], long fibres are less efficient than short fibres since sarcomere shortening cannot be well synchronised along the length of a fibre. Harris et al. [101] speculate that a twitch in a long fibre will produce much less force than a more synchronous contraction of the sarcomeres. The presented results confirm that the peak twitch force in spanning-fibred muscle is lower than in series-fibred muscle of the same length, however, it is also more dispersed, such that the stress induced through a single twitch integrated over time is similar in series-fibred and spanning-fibred muscles. This can be attributed to the fact that the number of sarcomeres contributing to the active force is identical in both models. The non-activated parts of the fibres behave as series elastic elements, i. e., they store contractile energy. It is believed that the minor differences observed in the integrated stress values stem from local changes in sarcomere length due to the F - ℓ relation and from different sarcomere contraction velocities due to the F - v relation. At this point, however, one has to bear in mind that the modelling assumption of hyperelastic passive material behaviour neglects viscous effects, which exist in passive muscle, see Hoyt et al. [122], Van Loocke et al. [267].

The model further predicts that the peak force exerted by a synchronous activation of all in-series arranged compartments exceeds the product of the number of in-series arranged compartments and the peak force produced when stimulating only the fibres in one compartment. This might be explained by the fact that an additional series compliance is introduced through inactive compartments against which the activated fibres contract [25]. It is hypothesized that the effect will be more pronounced at shorter muscle lengths than at the optimal length (at which the numerical experiments are carried out), cf. Mutungi & Ranatunga [183], or in muscles with passive forces appearing only at long muscle length (see further below).

Changes in sarcomere length due to the contraction of activated parts of the fibres against non-activated parts are reported for spanning-fibred and series-fibred muscle models. Fixed-end single twitch contractions, in which the fibres of all compartments are simultaneously activated, show that changes in sarcomere length increase with increasing fibre length. Shorter sarcomere lengths are only observed if one out of six compartments is activated (model *SER-6a*). This is not surprising as the five non-activated compartments act as series elastic elements. Comparing the extreme values of the sarcomere length with Figure 4.15a reveals that the range of sarcomere lengths of the numerical experiments is limited to a rather narrow region with considerable filament overlap. Mutungi &

Ranatunga [183] report experimental sarcomere length changes in fixed-end single twitch contractions that are considerably smaller than those found in the present numerical investigations. The difference can be explained based on the fact that Mutungi & Ranatunga [183] simultaneously stimulated the entire fibre bundle using plate electrodes, and hence, almost all sarcomeres shortened concurrently against a small region at the fibre ends.

The fact that the model predicts rather small changes in sarcomere length during fixed-end single twitch contractions might be explained by the following considerations. A resting sarcomere length of $2.0\ \mu\text{m}$ [61] is assigned to the model's stress-free reference configuration ($\lambda_f = 1$). Thus, the longest observed sarcomere length of $2.66\ \mu\text{m}$ corresponds to a local fibre stretch of $\lambda_f = 1.33$. Comparing this value with the F - ℓ relation in Figure 6.9a, one observes that considerable passive forces start to appear at this fibre stretch. This can be explained by the fact that at every instant in time, the contractile forces in the activated parts of the muscle need to be matched by the stretch-induced passive forces in the non-activated, in-series arranged parts. Sarcomere length changes will therefore be more pronounced in muscles with passive forces appearing at long muscle length.

A limitation of the model is that it does not include tendons. Since tendinous tissue is much stiffer than passive muscle tissue [103], the series compliance added to the system by including tendons is considered to be small. Therefore, the effect of neglecting tendons in this study is expected to have a minor effect on the force generation and the sarcomere length changes.

The study of compartmentalisation is particularly interesting with regard to analysing stability issues. The model results demonstrate that activated parts of a muscle can contract against non-activated parts. It has been hypothesized that in long spanning-fibred muscle, in which the AP propagation time exceeds the twitch rise time, activation-induced stresses might stretch non-activated sarcomeres to beyond myofilament overlap potentially leading to instabilities [159]. Loeb et al. [159] therefore speculate that the twitch rise time might impose a limit on the length of the muscle fibres. The presented results, however, demonstrate that a muscle model, in which the AP propagation time exceeds the twitch rise time of a single sarcomere, does not necessarily show any instabilities. In series-fibred muscle a similar stability problem is believed to exist when activation of series-arranged compartments is unbalanced or asynchronous, i. e., if muscle fibres in an activated compartment shorten against fibres in non-activated compartments [159, 216]. This instability was not observed either in the numerical experiments (model *SER-6a*) using the presented model settings.

The fact that instabilities are observed neither in the spanning-fibred model nor in the series-fibred model might be due to the fact that in the present model passive forces appear already at short muscle length. According to Hawkins & Bey [102], this corresponds to the behaviour of rat TA muscle, which shows even at full activation a monotonically increasing isometric F - ℓ relation, cf. Figure 6.9a. The passive stiffness of the muscle tissue might therefore prevent an overextension of non-activated sarcomeres. However, in muscles with passive forces appearing at long muscle length, sarcomere extensions to beyond myofilament overlap might be possible, and this might lead to stability problems and damage [159].

7 A Multiscale Model of the Neuromuscular System

The previous chapter introduced a multiscale model of skeletal muscle. Assuming simplified stimulations, this model was used to simulate idealised muscle contraction. To simulate more realistic muscle contractions, this chapter enhances the multiscale muscle model to a model of the neuromuscular system.

7.1 Overview of the Multiscale Model of the Neuromuscular System

To simulate the behaviour of the neuromuscular system, the multiscale muscle model of Chapter 6 is coupled to the model of the motor neuron pool of Negro & Farina [186], which has been described in Section 4.2. Furthermore, the model of the neuromuscular system is coupled to the EMG model of Section 5.4, to simulate muscle contractions and the EMG signal under isometric and non-isometric conditions. The resulting model of the neuromuscular system is schematically shown in Figure 7.1.

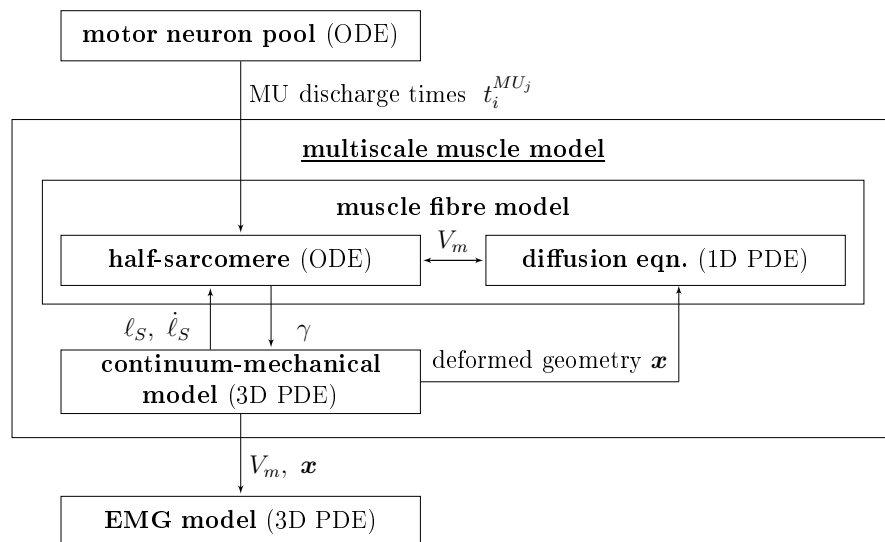


Figure 7.1: Overview of the multiscale model of the neuromuscular system. Each box indicates a model part. The couplings between the parts are indicated through arrows together with the transferred information.

To determine the discharge times of each MN, the biophysical model of Negro & Farina [186] is solved, cf. Section 4.2 and Appendix B. The coupling of the MN pool model to the muscle model is unidirectional, i. e., the flow of information between the models only

occurs from the model of the MN pool to the muscle model. Therefore, theoretically, one could precompute the motor unit recruitment and firing times independent of the muscle model. However, in order to integrate in the framework proprioceptors, such as muscle spindles and Golgi tendon organs, which provide the MN pool with information about the state of the muscle, at a later time, the model of the MN pool is integrated in the framework and is not solved decoupled from the muscle model. To realise the integrated formulation, the MN model of Negro & Farina [186] is coupled to the half-sarcomere model that is located at the neuromuscular junction (e.g. at the middle of each fibre).

The MU discharge times are used to drive the multiscale chemo-electro-mechanical muscle model. The multiscale model predicts the actively generated force and the deformation of the muscle, see Chapter 6 for details.

In Section 5.4, the bidomain model has been proposed to simulate EMG signals. Here, this technique is further developed to take into account the activation-induced deformation of the tissue to accurately predict the EMG signal also under non-isometric conditions. To this end, the EMG model requires information about the deformed geometry, \mathbf{x} , in addition to the membrane potential, V_m , cf. Figure 7.1. The modifications required in the EMG model are explained in detail in the following section.

7.2 Modelling Electromyographic Signals Under Non-Isometric Conditions

Following the monodomain approximation (see Section 5.2), the equations for determining the EMG signals are decoupled from the multiscale muscle model. Thus, the multiscale model and the extracellular bidomain equation can be solved successively.

Following the approach of Section 5.4, the nodes of the 1D muscle fibre meshes, which are used for the solution of the monodomain equation, are connected to form a 3D mesh of linear Lagrange finite elements, see Figure 7.2. This fine-spaced 3D mesh is used to discretise the extracellular bidomain equation and to compute the EMG signal.

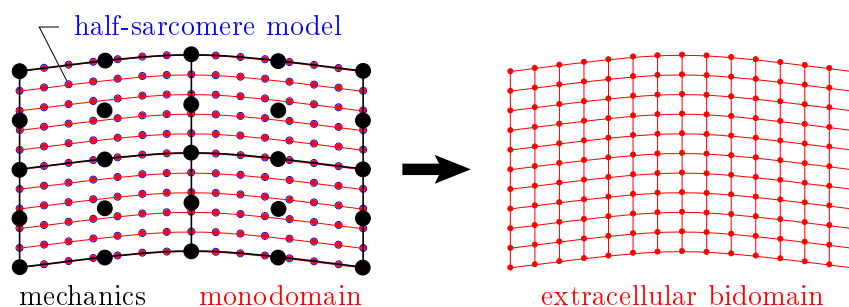


Figure 7.2: A 2D schematic representation of the 3D problem highlighting the use of the different meshes for the different subproblems of the multiscale model. First, the geometry of the muscle is discretised using 3D quadratic Lagrange finite elements (black mesh). This mesh is used for the solution of the continuum-mechanical model. Embedded in these 3D finite elements are 1D muscle fibre meshes (red, left), used for the solution of the monodomain equation. Each finite element node point of the 1D muscle fibre meshes requires the solution of the biophysical half-sarcomere model (blue). Connecting the nodes of the 1D meshes yields a fine-spaced 3D finite element mesh (right) for solving the extracellular bidomain equation. Previously published in [178].

The multiscale skeletal muscle model takes into account the mechano-electric feedback by applying the deformation of the 3D muscle geometry to the 1D muscle fibre meshes, cf. Section 6.2.2. The computation of the EMG takes advantage of the same technique, i. e., the solution of the extracellular bidomain equation accounts for the tissue deformation. Similar to the monodomain equation, the extracellular bidomain equation either can be solved on the actual configuration, or it can be solved in the reference configuration by pulling back the geometric quantities. Following the approach of Section 6.2.2, the extracellular bidomain equation reads in the reference configuration

$$\text{Div} (J (\boldsymbol{\sigma}_i^0 + \boldsymbol{\sigma}_e^0) \text{Grad} \phi_e) = -\text{Div} (J \boldsymbol{\sigma}_i^0 \text{Grad} V_m), \quad (7.1)$$

where $\boldsymbol{\sigma}_i^0 = \mathbf{F}^{-1} \boldsymbol{\sigma}_i \mathbf{F}^{T-1}$ and $\boldsymbol{\sigma}_e^0 = \mathbf{F}^{-1} \boldsymbol{\sigma}_e \mathbf{F}^{T-1}$ are the referential conductivity tensors of the intracellular and the extracellular domains, respectively. In this work, however, the EMG is computed on the deformed (actual) configuration, where the nodal positions of the fine-spaced 3D mesh (Figure 7.2 right) are updated in every step. Here, the step size of the EMG model is taken in accordance with the time step size of the continuum-mechanical model.

7.3 Applications of the Multiscale Model of the Neuromuscular System

Two examples are presented in the following, demonstrating the capability of the proposed model of the neuromuscular system. While the first example considers an idealised geometry, the second example simulates the tibialis anterior muscle.

7.3.1 Isometric and Non-Isometric Contractions of a Rectangular Cuboid

Introduction and Methods

For the simulation, the cuboid geometry and the MU fibre distribution of the example of Section 5.4.2 is adopted. While the formulation in Section 5.4.2 is restricted to isometric conditions, the chemo-electro-mechanical model can simulate any kind of contraction and, additionally, allows to predict the generated force.

Two scenarios are considered. In the first scenario, the cuboid muscle specimen is fixed at both ends to simulate a fixed-length contraction. In the second scenario, only one end of the muscle specimen is fixed, while deformation of the other end is left unconstrained to simulate a non-isometric contraction. Furthermore, in both scenarios, displacement at two further non-parallel faces of the specimen is constrained in the direction perpendicular to the respective face (symmetry boundary conditions). For the computation of the bio-electrical fields, homogeneous Neumann (no-flow) boundary conditions are applied. Note that in the non-isometric case, the force-length and force-velocity relations are omitted to obtain larger deformations of the muscle specimen.

Results

To drive the model of the neuromuscular system, a constant mean synaptic current of $0.005 \mu\text{A}/\text{cm}^2$ superimposed by two Gaussian-distributed high-frequency oscillating signals (see Negro & Farina [186] for details) is applied to the MN model of Negro & Farina [186]. The resulting discharge times are shown in Figure 7.3a, together with the generated nominal stresses. The nominal stresses are computed from the reaction forces of the muscle model of the first scenario (fixed-length contraction). Due to the small number of MUs included in the simulation, the generated stresses are accompanied by large fluctuations.

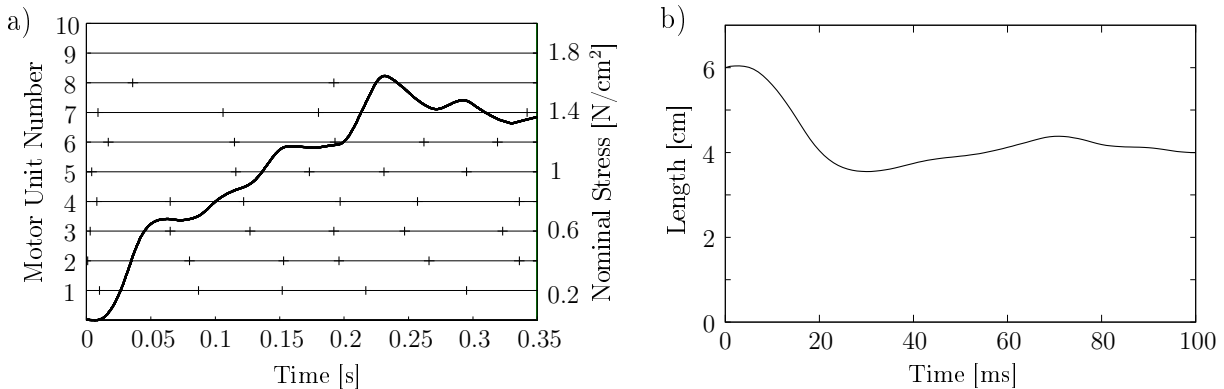


Figure 7.3: (a) Motor unit discharge times and induced nominal stresses during a fixed-length contraction, and (b) total length of the specimen during a non-isometric muscle contraction in the cuboid example.

If only one end of the specimen is fixed (as in the second scenario), the contraction induces a deformation of the muscle specimen. This is shown in Figure 7.3b, where the total length of the cuboid is plotted versus the time. According to Figure 7.3b, the specimen shortens significantly in the beginning of the simulation, but little changes are observed at later simulation times.

Following this, Figure 7.4 shows the action potentials propagating along the muscle fibres and the resulting sEMG signals at the beginning of the simulation (0–26 ms) for the non-isometric contraction. The contraction-induced deformation of the cuboid is clearly visible.

Discussion

In contrast to previous models of the EMG, the proposed multiscale chemo-electro-mechanical can take into account the tissue deformation. This allows to predict, for example, the effect of changes in the local fibre orientation or a shift of the innervation zone with respect to the skin surface on the sEMG signal, cf. DeFreitas et al. [48], Nishihara et al. [192], Piitulainen et al. [206].

Further, while previous models of the EMG are restricted to isometric conditions, the present approach allows to study the EMG also during non-isometric contractions. This enhances significantly the applicability of EMG models. For example, lengthening contractions of skeletal muscles require a neural activation strategy that is different from that during isometric contractions, see Enoka [64]. Using the presented framework, recruitment and rate coding strategies based on neurophysiological hypotheses can be tested and the

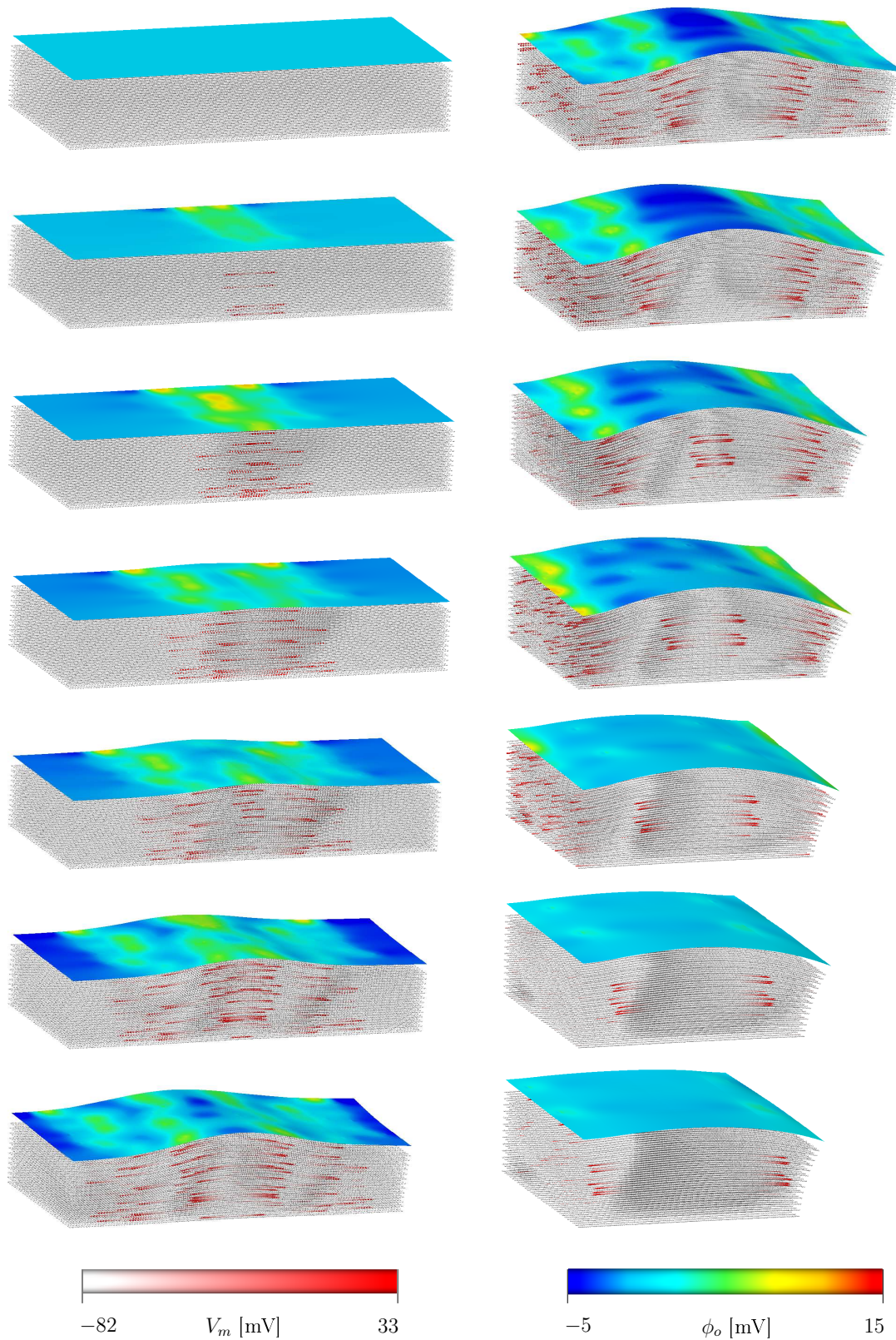


Figure 7.4: Deformation, muscle fibre APs, and the resulting *sEMG* signals at times $t = 0-12$ ms (left, from top to bottom) and $t = 14-26$ ms (right) in steps of size 2 ms.

simulation results can be compared to EMG recordings during lengthening contractions. This might help to reveal the neural strategy underlying lengthening contractions.

7.3.2 Modelling the Tibialis Anterior Muscle

Although the finite element method allows for arbitrary geometries, the examples presented in the previous sections were all based on simplified geometries. This section demonstrates that the proposed model is capable of simulating muscle contractions and EMG signals also for non-trivial, realistic geometries. To this end, the human TA muscle is considered. Some of the results of this section have previously appeared in Mordhorst et al. [178].

Introduction and Methods

The geometry of the TA and the fat/skin tissue is based on the visible human male dataset [245]. The TA's bipennate muscle fibre directions are based on DT-MRI data [151]. The geometry of the muscle without the fat/skin tissue has previously been used, see [109, 219, 221]. For the discretisation of the 3D geometry of the muscle and the subcutaneous tissue 39 tri-quadratic/tri-linear Lagrange finite elements are used. To reduce complexity and computational time, only 2700 muscle fibres are considered. The 1D muscle fibres are discretised using 140 400 linear Lagrange finite elements and 144 000 nodes. Each of these nodes is associated with a biophysical half-sarcomere model of Shorten et al. [240].

The muscle fibres are grouped into 10 MUs. The general assumption that a muscle typically consists of many type-I and few type-II MUs [76] is reflected within the model by choosing the first six MUs to use the slow-twitch parametrisation, while the other four MUs (MUs 7–10) use the fast-twitch parametrisation of the cell model of Shorten et al. [240]. Note that the different parametrisations of the biophysical half-sarcomere model lead to different AP propagation velocities, which are also observed in real muscles and significantly influence the sEMG. Further, following Fuglevand et al. [76], an exponential distribution of the innervation number was assumed, where the largest MU had 100 times as many fibres as the smallest MU. The MU fibre distribution is depicted in Figure 7.5, where a different colour is chosen for each MU.

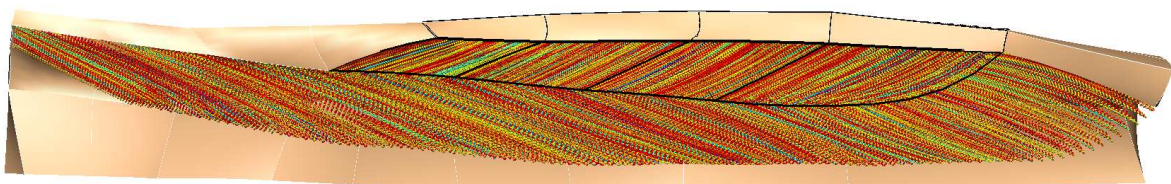


Figure 7.5: *The geometry of the TA and the surrounding fat/skin tissue. Additionally, the (randomly assigned) MU fibre distribution is illustrated, where the colours of the fibres display the 10 MUs. The resulting EMG signals are simulated based on the superficial TA and adjacent fat/skin layer, i. e., the region highlighted with bold black lines. Previously published in [178].*

While the MU territories in real muscles are spatially confined to small regions within the muscle's cross-sectional area, this model assumes a random distribution of the fibres. This assumption is made to simplify the model setup and is not due to any framework-

inherent limitations. An algorithm to distribute the MU fibres within the muscle volume can be found in Röhrle et al. [221].

The MU discharge times are adopted from the example in Section 5.4.2. These discharge times have been determined using the biophysical MN model of Negro & Farina [186], and are depicted in Figure 5.11b. To model the innervation zone, a Gaussian distribution around the middle of the fibres with a standard deviation of two nodes was assigned to the stimulation point. The maximum deviation was 7 nodes, which corresponds to a 0.56 cm wide spread of the innervation zone. To simulate a fixed-length contraction, all finite element nodes at the proximal and distal ends of the muscle are fixed in the mechanical model.

While the activation-induced contraction of the TA is based on the entire muscle and the surrounding fat/skin tissue, the subsequent EMG computation is only based on the superficial part of the TA covered by a layer of fat and a layer of skin tissue (black lines in Figure 7.5). Along the superficial TA, the thickness of the fat and the skin layer varies slightly, i. e., the fat layer has a thickness of approximately 6 mm and the skin layer thickness is approximately 1.5 mm. Due to its larger distance to the skin surface, the deep TA is considered to have a minor contribution to the sEMG signal. It is, however, noteworthy that the presented modelling approach is not limited to the superficial part of the TA. The TA's superficial part contains 900 embedded fibres. The finite element mesh for the computation of the EMG consists of 47 908 elements. The conductivities in Table 5.5 are used for computing the EMG signal.

Results

Figure 7.6 shows for six selected times the distribution of the membrane potential along the muscle fibres and the contraction-induced deformation of the TA muscle and the surrounding tissue.

The resulting sEMG signal at the skin covering the superficial part of the TA muscle is visualised in Figure 7.7 for five different times.

Since the TA is a pennate muscle, the generated EMG signal is different from the one shown in the previous section, where the fibres are parallel to the skin. Due to the fibre angle, no pronounced propagation of the potential at the surface can be detected. Rather, the signals propagating along the fibres towards the surface lead to an increase in the surface potential. In agreement with the findings of Barbero et al. [9], the sEMG of the simulated pennate muscle is dominated by the end-of-fibre effect and the extinction of the AP. While these experimental findings are qualitatively reflected by the model results, they make a quantitative comparison difficult. This likewise holds for the mechanical deformation. Experiments using ultrasound together with EMG measurements are performed, for example, by Hodges et al. [119], Ruiz-Muñoz & Cuesta-Vargas [226] to study the relation between the EMG signal and architectural parameters, such as the pennation angle. As expected from the experimental findings of Hodges et al. [119], the pennation angle increases during the simulated isometric contraction. However, while the model considers the isolated TA, the experiments are performed in vivo including interactions of the TA with adjacent tissue, which makes further comparisons within the scope of this work impossible.

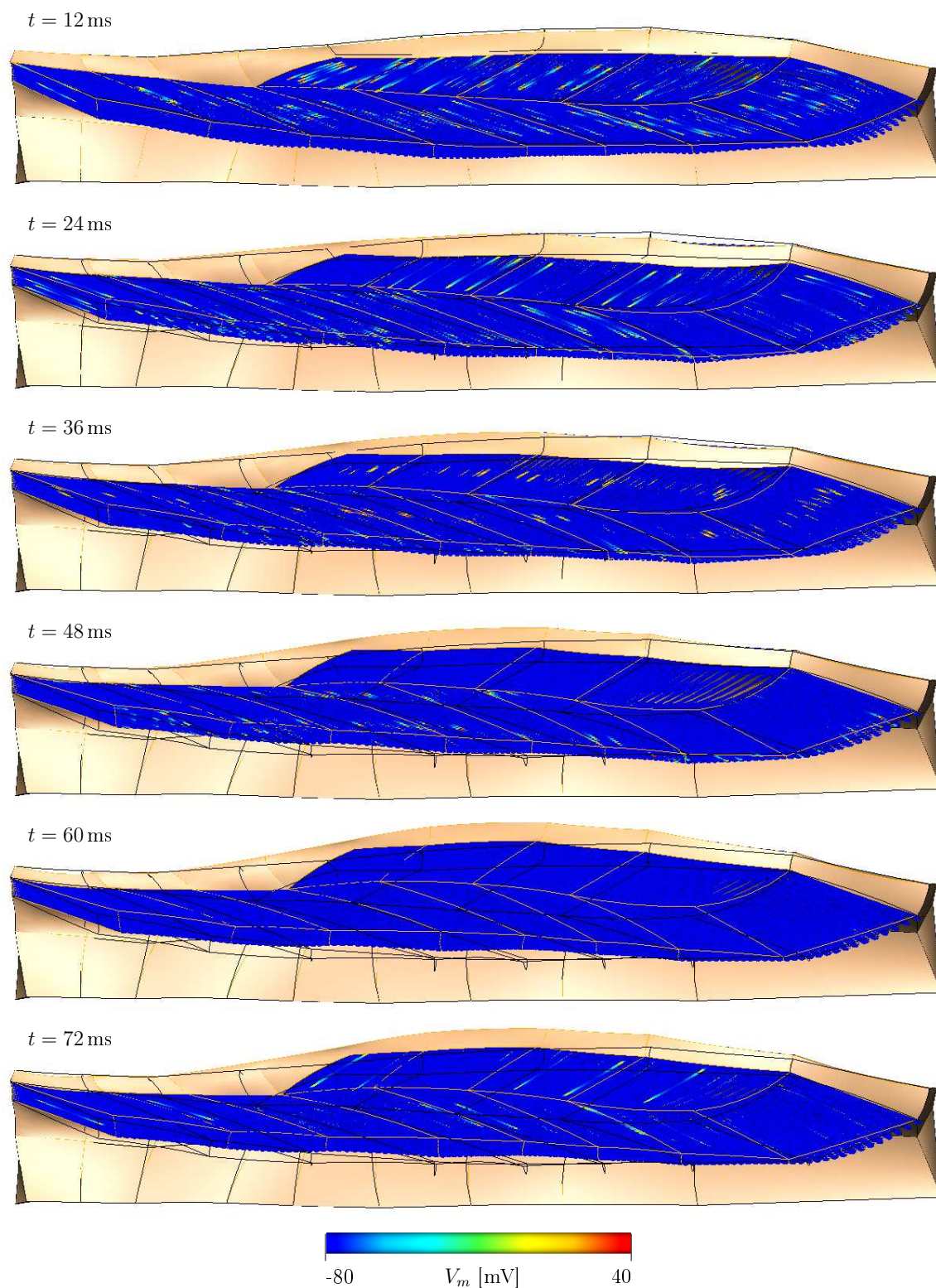


Figure 7.6: Membrane potential distribution along each muscle fibre and contraction-induced deformation of the TA muscle and surrounding fat/skin tissue for six selected times. The black lines refer to the reference (undeformed) configuration.

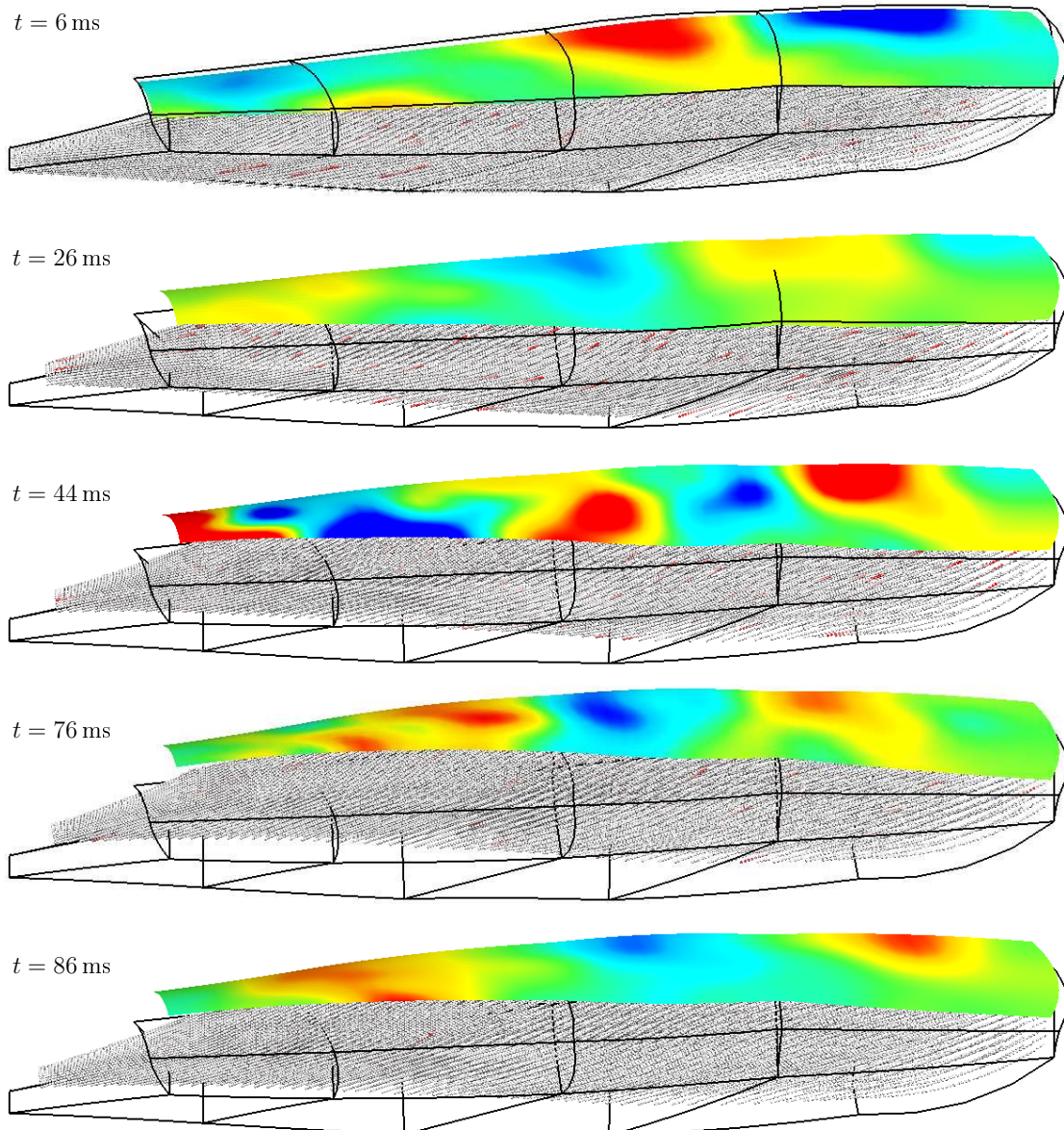


Figure 7.7: The sEMG signal over the superficial TA together with the underlying membrane potential along each muscle fibre for five selected times. The black lines refer to the reference (undeformed) configuration.

Discussion

Due to the complexity of the multiscale model and its associated computational cost, the number of muscle fibres that can currently be included in a simulation on a normal desktop PC using a single processor is limited to a few thousand. The human TA consists of about 250 000 fibres [105], and thus, only about 1% of the fibres can currently be simulated. However, there exists a large potential for parallelisation (cf. Section 6.2.3 and Heidlauf & Röhrle [109]) and model reduction techniques to decrease the computational load and/or allow to include a more realistic number of fibres in the simulations.

Although strategies have been employed to reduce the computational complexity of the model, the computing time is still high for the presented model. On a normal desktop PC (Intel® Core™ i5-3470 CPU, single processor, 3.2 GHz, and 32 GB of memory) the solution of the chemo-electro-mechanical model on the TA (2700 fibre meshes, each of which required the solution of more than 50 biophysical half-sarcomere models, yielding more than $7.5 \cdot 10^6$ degrees of freedom (DOFs) for the bioelectrical problem) required about 3 h to simulate 0.2 ms. The computation of the corresponding EMG was about 15 min. It is, however, noteworthy that about 90% of the EMG computing time is spent on file I/O, and only 10% is required for the actual computation of the EMG signal. This is due to the fact that the membrane potential and the extracellular potential distributions are currently stored in ASCII files, which have to be written out and read in for each time step. A more sophisticated implementation that eliminates the cumbersome I/O of the membrane potential and the nodal positions is feasible, since the entire model is solved within a single framework (OpenCMISS). This, however, has not been realised yet. Since the application of the model is currently limited by the computation time, this issue has to be addressed in the future.

With regard to simulating muscle behaviour under realistic conditions, one also has to raise the question if it is actually necessary to simulate every single fibre of a muscle. Due to the fact that in reality the diameter of a muscle fibre is limited by the time the AP takes to propagate along the T-tubules, it might be possible to accurately simulate muscle contractions and the EMG using fewer “meta-fibres” representing parts of muscle units, cf. Fuglevand et al. [77].

While it might be possible to simulate realistic muscle contractions using “meta-fibres”, the number of MUs included in a contraction significantly affects the force output. For example, Röhrle et al. [221] demonstrated that a smoother force response is generated, when including more MUs in the simulation. Due to the computational complexity of the model, only 10 MUs are considered here. This reduced set of MUs can not accurately represent the 450 MUs of the human TA muscle.

Previous models of the EMG are not restricted by their computation times. However, these models cannot take into account arbitrary fibre architectures. Further, existing models are not capable of predicting changes in the EMG signal or the AP shape and propagation velocity that are due to the mechanical deformation of the tissue or due to underlying biophysical processes such as membrane fatigue.

8 Summary, Discussion, and Outlook

8.1 Summary

The aim of this thesis was the biophysical simulation of the chemo-electro-mechanical processes of the neuromuscular system leading to muscle contraction and force generation. To this end, different approaches have been followed. First, a novel, biophysical model of the neuromuscular system arose from coupling a detailed biophysical model of the excitation-contraction coupling in skeletal muscle fibres to a biophysical, Hodgkin-Huxley-type model of the motor neuron pool that predicts motor unit recruitment and rate coding.

Further, to simulate electrical signals propagating through muscle and subcutaneous tissue, the biophysical muscle model was linked to bioelectrical field equations. This formulation intrinsically accounts for changes in the amplitude and propagation velocity of the action potential, which might result, for example, from membrane fatigue. Based on this approach, the intramuscular and surface EMG signals have been predicted.

Furthermore, during isometric and non-isometric skeletal muscle contractions, the EMG has been simulated using a multiscale chemo-electro-mechanical model, taking into account the contraction-induced tissue deformation. The multiscale, chemo-electro-mechanical skeletal muscle model resulted from incorporating a biophysical description of half-sarcomere-based active stresses within a continuum-mechanical constitutive equation. Being based on a finite-deformation theory, the continuum-mechanical description allows prediction of contraction-induced and externally applied tissue deformations as well as the overall muscle force generation. To demonstrate the capabilities of the resulting multiscale and multiphysics framework, the model was used to reveal differences in the contractile behaviour and the force response that result from the muscle fibre arrangements. Moreover, using the biophysical model of the motor neuron pool to drive the multiscale chemo-electro-mechanical muscle model, voluntary skeletal muscle contractions have been simulated. In particular, a model of the human TA muscle demonstrated the geometric flexibility of the finite element-based formulation.

The following list summarises novel aspects provided by this work to the field of modelling the neuromuscular system.

- The detailed biophysical model of the excitation-contraction coupling of Shorten et al. [240] has been extended to a representation of the different muscle units within a skeletal muscle.
- A partial reparametrisation of the model of Shorten et al. [240] has been proposed to simulate human muscles.
- The resulting muscle model has been used to reveal that doublet potentiation is caused by an increase in the myoplasmic calcium concentration, which results from

the superposition of residual calcium from the first stimulus and the calcium released in response to the second stimulus.

- To simulate non-isometric contractions, the muscle model of Shorten et al. [240] has been extended to account for cooperative effects and a distortion dependence.
- A novel model of the neuromuscular system that is biophysical in all main parts has been developed. To this end, the muscle model of Shorten et al. [240] has been coupled to the Hodgkin-Huxley-type model of the motor neuron pool of Negro & Farina [186].
- It has been demonstrated through numerical examples that the monodomain model is a valid approximation to the more complex bidomain model in the context of modelling the AP propagation in skeletal muscle tissue.
- Following this, a biophysical description of the AP propagation along skeletal muscle fibres based on the monodomain model has been proposed. The model has been used to investigate the effect and origin of membrane fatigue on the amplitude and propagation velocity of APs along muscle fibres.
- A novel, biophysical model of the EMG has been proposed. This model is based on a Hodgkin-Huxley-type description of the membrane electrophysiology and the bidomain/monodomain model. A major advantage of the biophysical description is that it intrinsically accounts for physiological properties, such as changes in the amplitude and AP propagation velocity, rather than prescribing these effects as part of the model constitution.
- A continuum-mechanical constitutive equation for skeletal muscle modelling has been developed. It has been demonstrated that the proposed formulation is flexible enough to accurately represent the passive behaviour of different skeletal muscles. The description of the active part of the constitutive model is based on the biophysical model of Shorten et al. [240] and includes the force-length and force-velocity relations at the microscopic half-sarcomere level. Parameters of the proposed constitutive model for the passive and nerve-activated response of skeletal muscle have been identified using experimental data of the literature.
- The resulting multiscale and multiphysics model has been implemented in the open-source software library `OpenCMISS` taking advantage of a distributed-memory parallelisation, the `CellML` API, and staggered solution schemes. The fully coupled, bidirectional implementation accounts for both electro-mechanic and mechano-electric feedbacks.
- The multiscale muscle model has been used to reveal differences in the contractile behaviour and force generation that result from the arrangement of the muscle fibres within the muscle.
- To simulate voluntary contractions, the multiscale skeletal muscle model has been coupled to the model of the motor neuron pool of Negro & Farina [186]. This yielded a novel multiscale, geometrical model of the neuromuscular system. Using the resulting model, muscle contractions and the EMG have been simulated under isometric and non-isometric conditions. In contrast to previous works, this model can take into account the contraction-induced deformation of the tissue.

8.2 Discussion and Outlook

Many aspects of the presented work have already been discussed (cf. Sections 4.5, 5.5, and 6.3), and this section only highlights a few points. The presented modelling framework unifies several component models to an integrated description of the coordinated action of the neuromuscular system. The resulting integrated model is biophysical in all main parts. The biophysical representation provides many advantages over phenomenological descriptions, as it is based on the underlying anatomy and physiology of the modelled system. The major advantage of the detailed biophysical description is that it allows to investigate internal quantities (e.g. intermediate quantities of a signaling pathway). Many of these internal quantities (e.g. the concentration of certain organic molecules) can now be experimentally determined using, for example, NMR (nuclear magnetic resonance) spectroscopy. This allows to further parametrise and validate biophysical models. Properly parametrised and validated biophysical models can be used, for example, to investigate pathological conditions. This is not possible using phenomenological models, as these models commonly do not include internal quantities.

Moreover, combining for the first time, a biophysical description of the motor neuron pool and a multiscale continuum-mechanical skeletal muscle model, the framework can be used to investigate problems that cannot be studied with existing models. For example, novel neurophysiological control mechanisms can be tested, which, in addition to the size principle, take into account the biomechanical efficiency.

Due to the fact that the multiscale chemo-electro-mechanical model is based on an integrated, fully coupled formulation, the model accounts for bidirectional couplings, such as the ones occurring from the combination of electro-mechanic and mechano-electric feedbacks. Thus, in addition to the contraction-induced deformation of the muscle tissue, the model takes into account changes in the bioelectrical properties of the volume conductor and the force-generating capabilities of the muscle that result from tissue deformation. This is in contrast to previous multiscale skeletal muscle models [219–221]. These models are based on a look-up table containing precomputed solutions to the bioelectrical field equations that are utilised when solving the mechanical model. The bidirectional coupling also allows to include proprioceptors within the framework at a later time.

Within the presented multiscale framework, the description of the active contractile behaviour is completely determined at the microscopic half-sarcomere level. This approach is in contrast to previous continuum-mechanical skeletal muscle models [16, 220] that include the active force-length and the active force-velocity relations at the macroscale. The purely macroscopic approach implies the assumption of an averaged sarcomere length and an averaged sarcomere velocity, and hence, these models cannot represent local changes in the sarcomere length and shortening velocity. Moreover, due to the fact that both the force-length and the force-velocity relations can be attributed to properties at the sarcomere level, they should be modelled at the microscale. In detail, the length dependence of the active force is due to changes in the overlap of thick and thin filaments within the sarcomeres [89], while the velocity dependence is attributed to a lower tension of the cross bridges that reattach in a shortened state and an increased cross-bridge detachment rate [205, 258]. In the presented multiscale model, the length and velocity of individual half-sarcomeres are only restricted by the overall length and velocity of the entire muscle, which depend on the mechanical boundary conditions. This is an advantage of the

multiscale model compared to the half-sarcomere model and also motivates the multiscale model. Following this, the model can be used, for example, to study the effect of sarcomere inhomogeneities on the muscle force generation.

Further, being based on the bioelectrical field equations, the multiscale model can predict intramuscular and surface-EMG signals. While previous models of the EMG were limited to isometric conditions, the present multiscale model can simulate the intramuscular and sEMG during any kind of contraction. By taking into account the contraction-induced deformation of the tissue, the model can investigate the influence of the relative movement of muscle fibres with respect to the electrode at the skin surface on the EMG signal under fixed-length and non-isometric conditions. This might lead to more accurate signal interpretations. Moreover, being based on a biophysical description, the model can predict changes in the EMG signal that result, for example, from biophysical processes such as membrane fatigue, rather than prescribing these effects as part of the model constitution, as in previous, phenomenological models of the EMG.

Validation of the presented multiscale chemo-electro-mechanical muscle model is, of course, a challenging task. Individual parts of the model, such as the biophysical descriptions of the motor neuron pool and the half-sarcomeres, have been adopted from literature. These models have previously been validated, at least, under certain idealised conditions. Furthermore, the bioelectrical field equations are commonly used in the field of biosignal processing, for example, for modelling the electrical activity of the heart. Although the entire active behaviour of the multiscale muscle model is determined at the microscopic half-sarcomere level, the multiscale and multiphysics model can predict macroscopic force-length and force-velocity relations. Furthermore, the presented multiscale chemo-electro-mechanical muscle model predicts both the generated force and the corresponding EMG signal. This provides a unique opportunity to validate the multiscale model by simultaneously measuring muscle forces and EMG signals in an experimental setup. This, however, is beyond the scope of this work.

For a further validation and application of the model, the computing time has to be significantly reduced. Although staggered solution schemes and parallelisation techniques are used within the multiscale framework, the application of the model is currently strongly limited by its enormous computational cost. Within the multiscale modelling framework, the solution of the biophysical half-sarcomere models takes by far most of the computing time. Thus, one has to carefully consider how much biophysical detail is required for a specific problem. If biophysical details are unimportant, one might be able to use a phenomenological cell model instead of a biophysical one, which might dramatically decrease the solution time. If biophysical details are important, model reduction techniques might be applied to decrease the computational cost, while preserving biophysical detail. While this is beyond the scope of the present work, this issue should be addressed in the future.

Another limitation of the chemo-electro-mechanical muscle model results from its multiscale character. Being based on continuum theory, the multiscale approach relies on the assumption of scale separation. This means that the macroscopic structure (the muscle) is several orders of magnitude larger than the microstructural elements of which the macroscopic structure is composed. If this property is satisfied, the macroscopic behaviour can be described statistically by the properties of the microstructural elements. In human muscles, the length of the muscle fibres, however, is often of the same order of magnitude than the length of the whole muscle. This is not unique for skeletal muscle, but applies to

many biological tissues. Nevertheless, continuum theory is commonly used in the field of biomechanics, and little research focusses on this issue. In the context of bone, limitations of the application of continuum theory have been discussed by Harrigan et al. [100].

Due to the modular structure of the presented multiscale and multiphysics framework, extending the model and/or replacing individual parts, when necessary, is straightforward. A few possible extensions of the model are discussed in the following. The model of the excitation-contraction coupling in the muscle fibres does not include a representation of the cell metabolism. Biophysical models of the metabolism in skeletal muscle fibres, however, exist, and these models can potentially be integrated into the biophysical half-sarcomere model and can be coupled to the existing description of metabolic fatigue. Furthermore, within the multiscale skeletal muscle model, the microscopic formulation of the cell metabolism could potentially be coupled to the macroscopic continuum-mechanical balance of energy.

Further, depending on the type of contraction, afferent signals were estimated to account for up to 50 % of the input to spinal cord motor neurons. The presented chemo-electro-mechanical model of the neuromuscular system does not currently include a description of proprioceptors. Since models of muscle spindles and Golgi tendon organs exist in the literature [173, 174], these models can be integrated into the multiscale and multiphysics computational framework to explicitly account for afferent inputs to the motor neurons. This might contribute to a more realistic representation of the synaptic input to the motor neuron pool.

A Additional Continuum-Mechanical Details

A.1 Natural Basis Representation

A.1.1 Covariant and Contravariant Basis

At any position \mathbf{x} in the 3D physical space, two basis systems can be derived from a set of general curvilinear coordinates θ^k with $k = 1, 2, 3$. The covariant (natural) basis, \mathbf{a}_k , and the contravariant (dual) basis, \mathbf{a}^k , are given by

$$\mathbf{a}_k := \frac{\partial \mathbf{x}(\theta^k)}{\partial \theta^k}, \quad \text{and} \quad \mathbf{a}^k := \frac{\partial \theta^k(\mathbf{x})}{\partial \mathbf{x}}. \quad (\text{A.1})$$

While neither the vectors of the covariant basis nor the vectors of the contravariant basis are necessarily orthogonal to each other, the vectors of the different bases satisfy the conditions $\mathbf{a}^k \parallel \mathbf{a}_l \times \mathbf{a}_m$ with cyclic rotations of $k, l, m = 1, 2, 3$ [162]. Following this, one can conclude that, in the special case of orthonormal basis vectors, the covariant and contravariant basis vectors coincide with each other and result in a common Cartesian coordinate system, i. e., $\mathbf{a}_k = \mathbf{a}^k =: \mathbf{e}_k$.

Equation (A.1) defines the natural basis vectors in the actual configuration. Similarly, covariant and contravariant basis vectors can be defined in the reference configuration according to

$$\mathbf{h}_k := \frac{\partial \mathbf{X}(\theta^k)}{\partial \theta^k}, \quad \text{and} \quad \mathbf{h}^k := \frac{\partial \theta^k(\mathbf{X})}{\partial \mathbf{X}}. \quad (\text{A.2})$$

Using the basis vectors of the reference and actual configurations, the deformation gradient tensor can be expressed in terms of the natural bases, yielding the relations

$$\mathbf{F} = \mathbf{a}_k \otimes \mathbf{h}^k, \quad \mathbf{F}^T = \mathbf{h}^k \otimes \mathbf{a}_k, \quad \mathbf{F}^{-1} = \mathbf{h}_k \otimes \mathbf{a}^k, \quad \mathbf{F}^{T-1} = \mathbf{a}^k \otimes \mathbf{h}_k. \quad (\text{A.3})$$

Of course, all quantities that can be derived from the deformation gradient tensor, such as, for example, the deformation and strain measures of Section 3.4.1, can similarly be expressed using the natural bases, see Markert [162] for details.

A.1.2 Covariant and Contravariant Transport Operations

Transport operations are required to relate quantities of the reference configurations to their counterparts in the actual configuration, and vice versa. Although in orthonormal basis systems, the covariant and contravariant basis vectors coincide, it is essential to distinguish between covariant and contravariant quantities at this point, since they obey different transport operations.

Following the transport of line elements (3.28)₁, the deformation gradient has the property to map covariant vectors of the reference configuration to covariant vectors of the actual configuration. Based on this, the inverse of the deformation gradient must obey the property of mapping covariant vectors of the actual configuration back to covariant vectors of the reference configuration. On the basis of these properties, the operations

$$\mathbf{n}_\ell = \mathbf{F} \mathbf{m}_\ell, \quad \text{and} \quad \mathbf{m}_\ell = \mathbf{F}^{-1} \mathbf{n}_\ell, \quad (\text{A.4})$$

are known as covariant push-forward and pull-back operations, where \mathbf{m}_ℓ and \mathbf{n}_ℓ denote covariant vectors of the reference and actual configurations, respectively. Furthermore, the contravariant push-forward and pull-back operations are introduced via

$$\mathbf{n}^\ell = \mathbf{F}^{T-1} \mathbf{m}^\ell, \quad \text{and} \quad \mathbf{m}^\ell = \mathbf{F}^T \mathbf{n}^\ell, \quad (\text{A.5})$$

where \mathbf{m}^ℓ and \mathbf{n}^ℓ denote contravariant vectors of the reference and the actual configurations, respectively. Similar to the transport operations for vectors in (A.4) and (A.5), transport operations can also be introduced for higher-order tensors. The covariant push-forward and pull-back operations for second-order tensors are given by

$$\mathbf{N}_\ell = \mathbf{F} \mathbf{M}_\ell \mathbf{F}^T, \quad \text{and} \quad \mathbf{M}_\ell = \mathbf{F}^{-1} \mathbf{N}_\ell \mathbf{F}^{T-1}, \quad (\text{A.6})$$

where \mathbf{N}_ℓ and \mathbf{M}_ℓ are covariant tensors of the reference and the actual configurations, respectively. Analogously, the contravariant push-forward and pull-back operations read

$$\mathbf{N}^\ell = \mathbf{F}^{T-1} \mathbf{M}^\ell \mathbf{F}^{-1}, \quad \text{and} \quad \mathbf{M}^\ell = \mathbf{F}^T \mathbf{N}^\ell \mathbf{F}. \quad (\text{A.7})$$

Therein, \mathbf{M}^ℓ and \mathbf{N}^ℓ denote contravariant tensors of the reference and the actual configurations, respectively. The transport operations for fourth-order tensors are omitted here, but can be found, for example, in the appendix of Markert [162].

A.2 Thermodynamic Considerations

The formulation of a constitutive equation has to satisfy certain requirements to be thermodynamically consistent. These basic thermodynamic principles are given by the requirements of determinism, equipresence, and local action, as well as material frame indifference, universal dissipation, and material symmetry. These concepts are only briefly discussed here for the sake of completeness, since the material models for the passive mechanical behaviour of muscle and subcutaneous tissue used within this work are known to satisfy the basic thermodynamic principles. For more details, the reader is referred to Wang & Truesdell [273] and references therein.

A.2.1 Determinism, Equipresence, and Local Action

The principles of determinism and equipresence state that the set of uniquely defined, undetermined response functions, $\mathcal{R} = \{\psi, \mathbf{T}\}$, where ψ denotes the Helmholtz free energy, can depend on the entire set of process variables, \mathcal{V} , i.e., $\mathcal{R} = \mathcal{R}(\mathcal{V})$. Further, the principle of local action requires that the set of process variables only consists of

local values. Assuming isothermal conditions, the set of process variables is given by $\mathcal{V} = \{\mathbf{F}, \text{Grad } \mathbf{F}, \mathcal{M}_a, \mathbf{X}\}$, cf. [140]. This choice of process variables allows to consider local inhomogeneities in the material behaviour based on their position in the reference configuration. This is important to distinguish, for example, muscle tissue from subcutaneous tissue. Within this work, the same energy function is used to describe passive muscle and subcutaneous tissue. A difference in the mechanical behaviour of these materials is obtained by the assignment of different material parameters. Therefore, the referential position vector, \mathbf{X} , can directly be omitted from the set of process variables. Furthermore, a structural tensor \mathcal{M}_a is included in the set of process variables to characterise non-isometric material behaviour. Due to the fact that an evaluation of the entropy inequality always yields the independence of the response functions of the second deformation gradient, $\text{Grad } \mathbf{F}$, the process variables of the Helmholtz free energy, ψ , are a priori constitutively assumed to be

$$\psi = \psi(\mathbf{F}, \mathcal{M}_a). \quad (\text{A.8})$$

A.2.2 Material Frame Indifference

The principle of material frame indifference is also known as the principle of objectivity as it states that the constitutive equations have to be independent of the position of the observer. Following this, the constitutive equations have to be invariant under rigid-body rotations of the actual configuration.

Scalar quantities are always invariant with respect to rotations. Further, the structural tensor, \mathcal{M}_a , is defined by quantities of the reference configuration. Hence, it is not affected by rotations of the actual configuration. The deformation gradient, however, is not invariant to rigid-body rotations, and hence, it is not a suitable quantity for the formulation of constitutive equations that satisfy the requirement of material frame indifference. Using the polar decomposition of the deformation gradient (3.29), a more suitable formulation of the constitutive equations can be based on the right stretch tensor, which is a quantity of the reference configuration. Moreover, since the right Cauchy-Green deformation tensor and the Green-Lagrangean strain tensor are also quantities of the reference configuration, the Helmholtz free energy can equally well be defined with respect to these quantities, i. e.,

$$\psi(\mathbf{U}, \mathcal{M}_a) = \psi(\mathbf{C}, \mathcal{M}_a) = \psi(\mathbf{E}, \mathcal{M}_a). \quad (\text{A.9})$$

For the sake of simplicity, different Helmholtz free energy functions are denoted by the same symbol ψ in Equation (A.9).

A.2.3 Universal Dissipation

The principle of universal dissipation states that the entropy inequality, which results from the combination of the balance of entropy and the second law of thermodynamics, has to be satisfied by all thermodynamic admissible processes. In this work, (passive) viscous effects are neglected and the passive muscle tissue is assumed to behave hyperelastically. Hyperelastic materials are characterised by fully reversible material behaviour, i. e., no dissipative effects are observed, and the entropy production vanishes. Following this, the evaluation of the entropy inequality for hyperelastic materials yields the well-known

relation between the 2nd Piola-Kirchhoff stress tensor and the Helmholtz free energy

$$\mathbf{S}_E = 2 \rho_0 \frac{\partial \psi}{\partial \mathbf{C}}. \quad (\text{A.10})$$

Next, a strain energy density defined per unit reference volume \mathcal{W} is introduced. The strain energy describes the elastic potential or the stored elastic energy of the material. From this strain energy, the 2nd Piola-Kirchhoff stress tensor can be derived according to

$$\mathcal{W} := \rho_0 \psi \quad \longrightarrow \quad \mathbf{S}_E = 2 \frac{\partial \mathcal{W}}{\partial \mathbf{C}}. \quad (\text{A.11})$$

A.2.4 Material Symmetry

Like other works, this work assumes an isotropic mechanical behaviour of the subcutaneous tissue and a transversely isotropic material behaviour of muscle tissue, cf. e.g. Böhl et al. [19], Morrow et al. [181], Nie et al. [189], Takaza et al. [256], Van Looke et al. [268]. Isotropic and transversely isotropic material behaviours are the simplest cases within the group of material symmetries. Isotropic behaviour means that the mechanical response of the material under consideration is completely independent of the orientation of the material sample. In contrast, a transversely isotropic material has a single preferred direction, such that the response of the material also depends on the orientation of the sample. This implies that the stored energy of the anisotropic material does not only depend on the deformation, but also on the orientation of the material sample.

The fact that the same material behaviour can be observed for certain orientations of the material sample motivates the introduction of symmetry groups. Mathematically, this requires the invariance of the formulation with respect to an orthogonal transformation of the referential coordinates. Due to the fact that isotropic behaviour is insensible to all orthogonal transformations, the structural tensor of this class of materials is given by

$$\mathcal{M}_a = \mathbf{I}, \quad (\text{A.12})$$

and the argument can be neglected in the formulation of the strain energy.

Further, the behaviour of a transversely isotropic material is insensible to inversion, reflection with respect to a plane normal to the fibre direction, to reflections with respect to any plane that is parallel to the fibre direction, to arbitrary rotations about the fibre direction, and 180-degree rotations about any axis that is perpendicular to the fibre direction, as well as any combinations thereof. To mathematically represent the material symmetries of transversely isotropic materials, one introduces a referential unit vector \mathbf{a}_0 that points in the preferred direction. Using this vector, the structural tensor is given by

$$\mathcal{M}_a = \mathbf{a}_0 \otimes \mathbf{a}_0, \quad (\text{A.13})$$

and obeys the properties

$$\mathcal{M}_a = \mathcal{M}_a^T, \quad \mathcal{M}_a = \mathcal{M}_a \mathcal{M}_a, \quad \text{and} \quad \text{tr } \mathcal{M}_a = 1. \quad (\text{A.14})$$

A.2.5 Theory of Invariants

The theory of invariants is derived from the idea that the formulation of the strain energy function should be independent of the choice of the coordinate system. Since the strain energy in (A.9)₂ depends on the second-order tensors \mathbf{C} and \mathcal{M}_a , and since any tensor is defined with respect to a specific coordinate system, the formulation in (A.9)₂ cannot be independent of the coordinate system. Instead, the strain energy function should be formulated in terms of basic scalar invariants, which are independent of the coordinate system.

Since the structural tensor for isotropic materials equals the identity tensor, it can be omitted from the list of arguments. The remaining dependency of the energy on the right Cauchy-Green deformation tensor can be expressed by the deformation tensor's basic invariants

$$J = \text{tr } \mathbf{C}, \quad JJ = \text{tr } \mathbf{C}^2, \quad JJJ = \text{tr } \mathbf{C}^3, \quad (\text{A.15})$$

where \mathbf{C}^2 denotes the tensor product $\mathbf{C}\mathbf{C}$. Instead of the basic invariants (A.15), similarly the eigenvalues or the principal invariants of the right Cauchy-Green deformation tensor (6.8) can be used, as these sets are all related to each other. As commonly done in finite elasticity, the strain energy is defined based on the principal invariants, i. e.,

$$\mathcal{W}(\mathbf{C}) = \mathcal{W}(I, II, III). \quad (\text{A.16})$$

In the case of transversely isotropic material behaviour, the energy function depends on the right Cauchy-Green deformation tensor and on the structural tensor. In addition to the basic invariants of the right Cauchy-Green deformation tensor, the basic invariants of the structural tensor are computed, which are all equal to unity, cf. Equations (A.14) and (A.15). Furthermore, mixed invariants are introduced that depend on both tensors. Due to the properties of the structural tensor (A.14), several of the mixed invariants coincide, and only two distinct mixed invariants remain, which are given by

$$\begin{aligned} IV &= \text{tr}(\mathcal{M}_a \mathbf{C}) = (\mathbf{a}_0 \otimes \mathbf{a}_0)^T \cdot \mathbf{C} = \mathbf{a}_0 \cdot \mathbf{F}^T \mathbf{F} \mathbf{a}_0 = \mathbf{F} \mathbf{a}_0 \cdot \mathbf{F} \mathbf{a}_0 = \mathbf{a} \cdot \mathbf{a}, \\ V &= \text{tr}(\mathcal{M}_a \mathbf{C}^2) = \mathbf{a}_0 \cdot \mathbf{C}^2 \mathbf{a}_0. \end{aligned} \quad (\text{A.17})$$

Herein, $IV = \lambda_f^2$ is the squared fibre stretch in the direction of the mapped fibre orientation $\mathbf{a} = \mathbf{F} \mathbf{a}_0$, where $\lambda_f = |\mathbf{a}|$ denotes the fibre stretch (length). The mixed invariant V has no direct physical meaning. Following this, the strain energy function of a transversely isotropic material can be given by

$$\mathcal{W}(\mathbf{C}, \mathcal{M}_a) = \mathcal{W}(I, II, III, IV, V). \quad (\text{A.18})$$

A.2.6 Further Physical and Mathematical Requirements

Besides the above discussed restrictions on strain energy functions, further mathematical and physical restrictions apply. First, based on the physical observation that an infinite elongation of a material or the compaction of a mechanical body to a single point requires

an infinite amount of energy, one postulates that

$$\mathcal{W} \longrightarrow \infty \quad \text{if} \quad \begin{cases} \det \mathbf{F} \longrightarrow 0, \\ (\|\mathbf{F}\|_2 + \|\text{cof } \mathbf{F}\|_2 + \det \mathbf{F}) \longrightarrow \infty, \end{cases} \quad (\text{A.19})$$

where $\|(\cdot)\|_2$ denotes the 2-norm (or Euclidean norm).

Furthermore, the combination of polyconvexity and coercivity of the strain energy function guarantees that a unique solution to the variational problem exists, see e.g. Balzani [8] and references therein. The condition of coercivity sets a lower limit for the energy corresponding to a given deformation. Without explicitly defining coercivity here, a stored energy function that is composed of positive additive terms will automatically satisfy the coercivity condition provided that at least one additive term is coercive [8]. Following this, the strain energy functions considered in this work are coercive due to the fact that the part of the strain energy describing the passive isotropic behaviour (the Mooney-Rivlin material) is known to be coercive.

Further, a strain energy function is said to be polyconvex if and only if $\mathcal{W}(\mathbf{F}) = \varphi(\mathbf{F}, \text{cof } \mathbf{F}, \det \mathbf{F})$ is convex with respect to each of the principal minors \mathbf{F} , $\text{cof } \mathbf{F}$, and $\det \mathbf{F}$ separately. This condition is satisfied if the second derivatives of the energy function with respect to the principal minors are positive definite, i. e.,

$$\frac{\partial^2 \varphi}{\partial \mathbf{F} \otimes \partial \mathbf{F}} \cdot (\mathbf{G} \otimes \mathbf{G}) \geq 0, \quad \frac{\partial^2 \varphi}{\partial (\text{cof } \mathbf{F}) \otimes \partial (\text{cof } \mathbf{F})} \cdot (\mathbf{G} \otimes \mathbf{G}) \geq 0, \quad \frac{\partial^2 \varphi}{\partial (\det \mathbf{F})^2} \geq 0,$$

where $\mathbf{G} \neq \mathbf{0}$ denotes an arbitrary second-order tensor. According to Balzani [8], the condition of convexity in 1D can be written in terms of the following inequality:

$$\varphi(\varkappa \lambda_{f,1} + (1 - \varkappa) \lambda_{f,2}) \leq \varkappa \varphi(\lambda_{f,1}) + (1 - \varkappa) \varphi(\lambda_{f,2}) \quad \text{with} \quad \varkappa \in (0, 1), \quad \lambda_{f,1} \neq \lambda_{f,2}.$$

This relation can be geometrically interpreted. Plotting the strain energy versus the fibre stretch, a convex energy is characterised by the fact that no point on a straight line that connects two points on the curve, can denote a lower energy than the strain energy corresponding to the same fibre stretch.

Finally, with regard to the reference configuration, a suitable form of the strain energy has to conform two further requirements. First, due to the fact that the reference configuration is assumed to be stress-free in continuum mechanics, the extra stresses in (6.3) have to vanish for $\mathbf{F} = \mathbf{I}$. Note that the penalty term in (6.3), which results from the incompressibility constraint, is not affected by this condition, since identical normal stresses do not cause a deformation of an incompressible material. Furthermore, the normalisation condition requires that the stress-free reference configuration is also energy free, i. e., $\mathcal{W}(\mathbf{F} = \mathbf{I}) \equiv 0$.

B The Motor Neuron Model

The motor neuron model of Negro & Farina [186] is described by the following ODEs [39]:

$$C_m^d \frac{\partial V_m^d}{\partial t} = -g_L^d (V_m^d - E_L) - g_C (V_m^d - V_m^s), \quad (\text{B.1})$$

$$C_m^s \frac{\partial V_m^s}{\partial t} = -g_L^s (V_m^s - E_L) - g_C (V_m^s - V_m^d) - I_{ion}, \quad (\text{B.2})$$

$$I_{ion} = \bar{g}_{Na} m^3 h (V_m^s - E_{Na}) + \bar{g}_{Kf} n^4 (V_m^s - E_K) + \bar{g}_{Ks} q^2 (V_m^s - E_K), \quad (\text{B.3})$$

$$\frac{\partial m}{\partial t} = 0.32 \frac{13 - V_m^s}{\exp\{(13 - V_m^s)/5\} - 1} (1 - m) - 0.28 \frac{(V_m^s - 40)}{\exp\{(V_m^s - 40)/5\} - 1} m, \quad (\text{B.4})$$

$$\frac{\partial n}{\partial t} = 0.128 (\exp\{(17 - V_m^s)/18\}) (1 - n) - 4 (\exp\{(40 - V_m^s)/5\} + 1)^{-1} n, \quad (\text{B.5})$$

$$\frac{\partial h}{\partial t} = 0.032 \frac{15 - V_m^s}{\exp\{(15 - V_m^s)/5\} - 1} (1 - h) - 0.5 (\exp\{(10 - V_m^s)/40\}) h, \quad (\text{B.6})$$

$$\frac{\partial q}{\partial t} = 3.5 (\exp\{(55 - V_m^s)/4\} + 1)^{-1} (1 - q) - 0.025 q. \quad (\text{B.7})$$

Furthermore, for the conductances and the capacitances, the following relations apply:

$$g_C = 2 \left(\frac{R_i l_d}{\pi r_d^2} + \frac{R_i l_s}{\pi r_s^2} \right)^{-1}, \quad g_L^d = \frac{2 \pi r_d l_d}{R_m^d}, \quad g_L^s = \frac{2 \pi r_s l_s}{R_m^s}, \quad (\text{B.8})$$

$$\bar{g}_{Na} = 30 \cdot 2 \pi r_s l_s, \quad \bar{g}_{Kf} = 4 \cdot 2 \pi r_s l_s, \quad \bar{g}_{Ks} = 16 \cdot 2 \pi r_s l_s, \quad (\text{B.9})$$

$$C_m^d = 2 \pi r_d l_d C_m, \quad C_m^s = 2 \pi r_s l_s C_m. \quad (\text{B.10})$$

The material parameters of the model are provided in Table B.1 for the dendritic and somatic compartments (indicated by subscripts d and s).

Symbol	Description	Value (small–large)
C_m	membrane specific capacitance	$1 \mu\text{F}/\text{cm}^2$
R_i	cytoplasmic resistivity	$70 \Omega \text{ cm}$
R_m^d	specific resistance of dendritic membrane	$14.4\text{--}6.05 \text{ k}\Omega \text{ cm}^2$
R_m^s	specific resistance of somatic membrane	$1.15\text{--}0.65 \text{ k}\Omega \text{ cm}^2$
l_d	dendritic compartment length	$0.55\text{--}1.06 \text{ cm}$
l_d	somatic compartment length	$77.5\text{--}113 \mu\text{m}$
r_d	dendritic compartment radius	$20.75\text{--}46.25 \mu\text{m}$
r_s	somatic compartment radius	$38.75\text{--}56.5 \mu\text{m}$
E_{Na}	sodium equilibrium potential	120 mV
E_K	potassium equilibrium potential	-10 mV
E_L	leakage Nernst voltage	0 mV

Table B.1: *Material parameters of the motor neuron model.*

C Comparing the Monodomain Model and the Bidomain Model

To numerically demonstrate that the monodomain model and the bidomain model lead to similar results for intracellular and extracellular conductivity tensors with equal anisotropy ratios, different test cases are employed. The first test case considers isotropic conductivity tensors (both conductivity tensors have an anisotropy ratio of 1). The conductivities (in mS/cm) for this test case are given by

$$\boldsymbol{\sigma}_i = 8.93 \begin{bmatrix} 1 & 0 \\ 0 & 1 \end{bmatrix} \mathbf{e}_k \otimes \mathbf{e}_l, \quad \boldsymbol{\sigma}_e = 6.7 \begin{bmatrix} 1 & 0 \\ 0 & 1 \end{bmatrix} \mathbf{e}_k \otimes \mathbf{e}_l. \quad (\text{C.1})$$

Therein, \mathbf{e}_j denotes a basis vector of an orthonormal basis. The model setup is the same as the one used in Section 5.3.1.

Based on the isotropic conductivity tensors in (C.1), Figure C.1a shows the distribution of the membrane potential in the 2D domain 0.37 ms after stimulation has been applied at node $(x_1, x_2) = (9, 9)$. The depicted distribution has been computed using the bidomain model. For the same time step, Figure C.1b shows the difference between the bidomain model and the monodomain model.

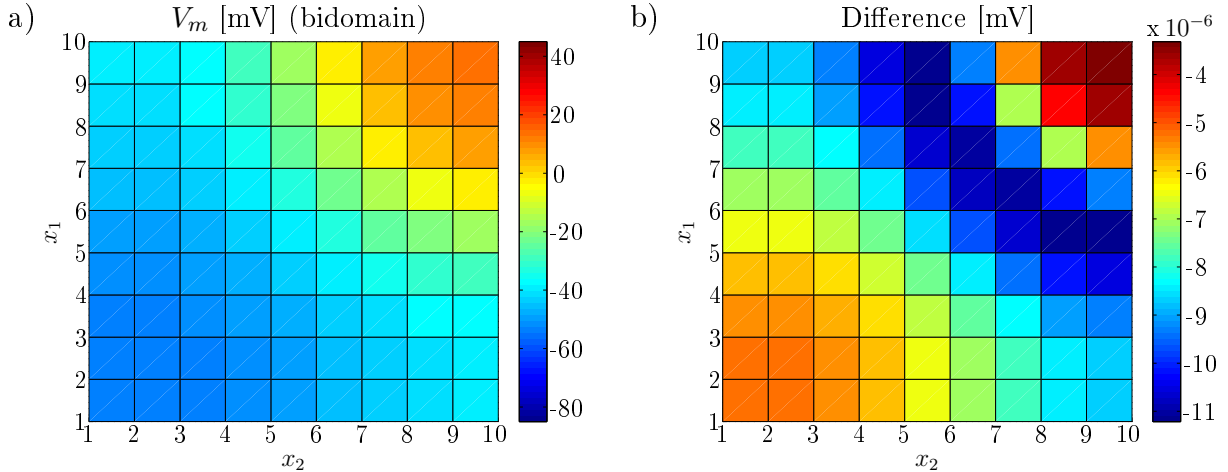


Figure C.1: Distribution of (a) the bidomain-based membrane potential (in mV), and (b) the difference between the bidomain model and the monodomain model (in mV) for isotropic conductivities. Here, the results are shown 0.37 ms after node $(x_1, x_2) = (9, 9)$ has been stimulated.

The choice of isotropic conductivities is reflected in the isotropic propagation of the membrane potential. Similar to the membrane potential, the error plot shows a symmetric distribution. The maximum difference at one node within the entire simulation time is $9.21 \cdot 10^{-5}$ mV and occurs at the beginning of the simulation at a node close to the

stimulation point. Based on the symmetric distributions and the similarity of the results of the monodomain and the bidomain models, one can conclude that the monodomain model is a valid approximation to the bidomain model for isotropic conductivities.

The second test case considers anisotropic conductivity tensors satisfying the condition of equal anisotropy ratios (both conductivity tensors have an anisotropy ratio of 10). The conductivities (in mS/cm) for this test case are given by

$$\sigma_i = 8.93 \begin{bmatrix} 1 & 0 \\ 0 & 0.1 \end{bmatrix} \mathbf{e}_k \otimes \mathbf{e}_l, \quad \sigma_e = 6.7 \begin{bmatrix} 1 & 0 \\ 0 & 0.1 \end{bmatrix} \mathbf{e}_k \otimes \mathbf{e}_l. \quad (\text{C.2})$$

Based on the anisotropic conductivity tensors in (C.2), Figure C.2a shows the distribution of the membrane potential in the 2D domain of the bidomain model 0.28 ms after stimulation has been applied at node $(x_1, x_2) = (9, 9)$. For the same time step, Figure C.2b depicts the difference between the bidomain model and the monodomain model.

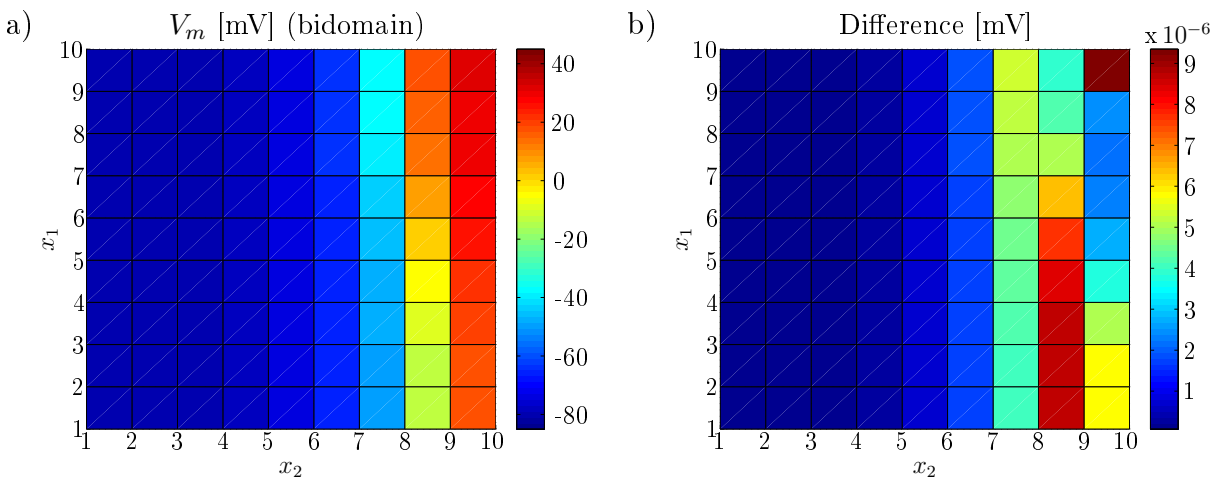


Figure C.2: Distribution of (a) the bidomain-based membrane potential (in mV), and (b) the difference between the bidomain model and the monodomain model (in mV) for anisotropic conductivity tensors with equal anisotropy ratios of 10. Here, the results are shown 0.28 ms after node $(x_1, x_2) = (9, 9)$ has been stimulated.

For the anisotropic conductivities, there is no symmetry in the membrane potential distribution. Due to the higher conductivity in x_1 -direction, the action potential propagates faster in this direction. Similar to the case of isotropic conductivities and as expected for conductivity tensors with equal anisotropy ratios, the difference between the monodomain and bidomain models is very small. The maximum difference at one node within the entire simulation time is $1.55 \cdot 10^{-4}$ mV and occurs at the beginning of the simulation at a node close to the stimulation point. The numerical results confirm the theoretical finding that the monodomain model is a valid approximation to the bidomain model for anisotropic conductivities with equal anisotropy ratios. If the condition of equal anisotropy ratios of the intracellular and extracellular conductivity tensors is not satisfied, one has to investigate the quality of the approximation, cf. Section 5.3.1. If, in addition to the membrane potential, the extracellular potential is of interest, one has to solve either the bidomain equation or successively the monodomain equation and the extracellular bidomain equation (cf. e. g. Section 5.4).

D Weak Forms

D.1 Weak Form of the Monodomain Equation

For the numerical treatment of the monodomain equation (5.19), first the Godunov operator splitting (5.23) is applied to separate the nonlinear reaction term from the diffusion term. Due to the fact that Equation (5.23)₁ only consists of coupled ODEs, no spatial discretisation is required for this part. To discretise the diffusion term using finite elements, the weak form of Equation (5.23)₂ is derived by following the procedure described in Section 3.1. To this end, Equation (5.23)₂ is first multiplied by a test function δV and integrated over the domain. Using the Gaußian integral theorem, the weak form of the transient diffusion equation (5.23)₂ yields

$$\int_{\Omega^M} \frac{V_m^{k+1} - V_m^*}{h} \delta V \, dv = - \int_{\Omega^M} \frac{\boldsymbol{\sigma}_{eff}}{A_m C_m} \text{grad } V_m \cdot \text{grad } \delta V \, dv + \int_{\partial\Omega^M} q \delta V \, da. \quad (\text{D.1})$$

Therein, $q = (A_m C_m)^{-1} \boldsymbol{\sigma}_{eff} \text{grad } V_m \cdot \mathbf{n}$ denotes the Neumann boundary conditions. Since the weak form (D.1) contains no derivatives of the membrane potential of higher order than one, it is sufficient to use linear Lagrange finite elements, cf. Zienkiewicz et al. [286].

For the time-discrete representation, the implicit (backward) Euler method is employed. To this end, the membrane potential on the right-hand side of (D.1) is chosen to be at the new time level, i. e., $V_m = V_m^{k+1}$.

D.2 Weak Form of the Extracellular Bidomain Equation

Following the procedure described in Section 3.1, the weak form of the extracellular bidomain equation is obtained in the form

$$\begin{aligned} - \int_{\Omega^M} (\boldsymbol{\sigma}_i + \boldsymbol{\sigma}_e) \text{grad } \phi_e \cdot \text{grad } \delta\phi \, dv + \int_{\partial\Omega^M} q_\phi \delta\phi \, da = \\ \int_{\Omega^M} \boldsymbol{\sigma}_i \text{grad } V_m \cdot \text{grad } \delta\phi \, dv - \int_{\partial\Omega^M} q_V \delta\phi \, da. \end{aligned} \quad (\text{D.2})$$

Therein, $\delta\phi$ denotes the test function, and $q_\phi = (\boldsymbol{\sigma}_i + \boldsymbol{\sigma}_e) \text{grad } \phi_e \cdot \mathbf{n}$ and $q_V = \boldsymbol{\sigma}_i \text{grad } V_m \cdot \mathbf{n}$ are the Neumann boundary conditions for the extracellular potential and the membrane potential, respectively. Linear Lagrange finite elements are used for the spatial discretisation of the weak form of the monodomain equation.

Further, the generalised Laplace equation (5.11) in the electrically inactive fat and skin tissue reads in its weak form

$$-\int_{\Omega^B} \boldsymbol{\sigma}_o \operatorname{grad} \phi_o \cdot \operatorname{grad} \delta\phi \, dv + \int_{\partial\Omega^B} q_o \delta\phi \, da = 0, \quad (\text{D.3})$$

where $q_o = \boldsymbol{\sigma}_o \operatorname{grad} \phi_o \cdot \mathbf{n}$ denotes the Neumann boundary condition for the potential in the subcutaneous tissue.

Since time derivatives do not occur in the extracellular bidomain equation (5.9) or the generalised Laplace equation (5.11), no temporal discretisation is required. The extracellular bidomain equation is solved for the extracellular potential for each membrane potential distribution that results from the solution of the time-discrete monodomain equation.

D.3 Weak Form of the Continuum-Mechanical Model

For the sake of convenience, this section reviews the governing equations of the continuum-mechanical model. Assuming quasi-static conditions and negligible body forces, the balance of momentum reduces to

$$\operatorname{div} \mathbf{T} = \mathbf{0}. \quad (\text{D.4})$$

Therein, $\mathbf{T} = J^{-1} \mathbf{F} \mathbf{S} \mathbf{F}^T$, and the 2nd Piola-Kirchhoff stress tensor is given by $\mathbf{S} = -p J \mathbf{C}^{-1} + \mathbf{S}_E$, see Section 6.1 for details. The hydrostatic pressure, p , has been introduced into the system as an undetermined Lagrange multiplier to incorporate the incompressibility constraint, cf. Section 6.1. To compute the value of this additional unknown, a further equation is required, since the vector-valued balance of momentum is needed to determine the three components of the current position vector (or, in a displacement formulation, the displacement vector). The additional equation is derived from the balance of mass for incompressible materials in the reference configuration and is given by

$$J - 1 = 0. \quad (\text{D.5})$$

Introducing the vector-valued and scalar-valued test functions $\delta\mathbf{u}$ and δp , respectively, the weak forms of the balance of momentum and the incompressibility condition are obtained as

$$\begin{aligned} -\int_{\Omega} \mathbf{T} \cdot \operatorname{grad} \delta\mathbf{u} \, dv + \int_{\partial\Omega} \mathbf{t} \cdot \delta\mathbf{u} \, da &= 0, \\ \int_{\Omega} (J - 1) \delta p \, dv &= 0, \end{aligned} \quad (\text{D.6})$$

with the Neumann boundary conditions $\mathbf{t} = \mathbf{T} \mathbf{n}$, and $\Omega = \Omega^M \cup \Omega^B$. The system of equations resulting from the finite element discretisation of the linearised version of (D.6) reads

$$\begin{bmatrix} \mathbf{K}_{11} & \mathbf{K}_{12} \\ \mathbf{K}_{21} & \mathbf{0} \end{bmatrix} \begin{bmatrix} \mathbf{x} \\ \mathbf{p} \end{bmatrix} = \begin{bmatrix} \mathbf{f} \\ \mathbf{0} \end{bmatrix}. \quad (\text{D.7})$$

Therein, \mathbf{x} and \mathbf{p} are the nodal values of the position vector in the actual configuration and the nodal values of the hydrostatic pressure, and \mathbf{f} contains the discrete Neumann

boundary conditions. The system of equations (D.7) is solved monolithically.

To avoid instabilities resulting from the fact that the hydrostatic pressure does not explicitly appear in the incompressibility constraint, finite element formulations have to be used that satisfy the LBB condition (Ladyzhenskaya-Babuška-Brezzi or inf-sup condition), cf. e.g. Fortin & Brezzi [75]. In this work, so-called Taylor-Hood elements are employed that use quadratic Lagrange shape functions for the position unknowns and linear Lagrange shape functions for the pressure unknowns, cf. Figure D.1.

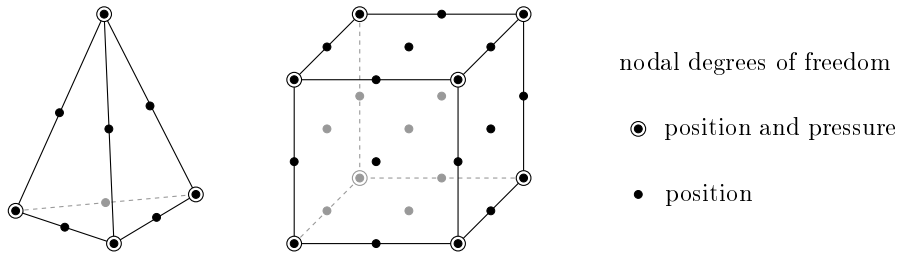


Figure D.1: *10-noded tetrahedral and 27-noded hexahedral Taylor-Hood elements.*

Bibliography

- [1] Abbott, L. F.: Lapicque's introduction of the integrate-and-fire model neuron (1907). *Brain Research Bulletin* **50** (1999), 303–304.
- [2] Adrian, R. H. & Peachey, L. D.: Reconstruction of the action potential of frog sartorius muscle. *The Journal of Physiology* **235** (1973), 103–131.
- [3] Ariano, M.; Edgerton, V. & Armstrong, R.: Hindlimb muscle fiber populations of five mammals. *Journal of Histochemistry & Cytochemistry* **21** (1973), 51–55.
- [4] Ascher, U. M. & Petzold, L. R.: *Computer methods for ordinary differential equations and differential-algebraic equations*, vol. 61. Siam 1998.
- [5] Augusto, V.; Padovani, C. R. & Campos, G. E. R.: Skeletal muscle fiber types in C57BL6J mice. *Brazilian Journal of Morphological Sciences* **21** (2004), 89–94.
- [6] Austin, T. M.; Trew, M. L. & Pullan, A. J.: Solving the Cardiac Bidomain Equations for Discontinuous Conductivities. *IEEE Transactions on Biomedical Engineering* **53** (2006), 1265–1272.
- [7] Baillargeon, B.; Rebelo, N.; Fox, D. D.; Taylor, R. L. & Kuhl, E.: The living heart project: A robust and integrative simulator for human heart function. *European Journal of Mechanics-A/Solids* (2014).
- [8] Balzani, D.: *Polyconvex anisotropic energies and modeling of damage applied to arterial walls*. Dissertation, Universität Duisburg-Essen (2006).
- [9] Barbero, M.; Merletti, R. & Rainoldi, A.: *Atlas of Muscle Innervation Zones*. Springer 2012.
- [10] Barry, B. K.; Pascoe, M. A.; Jesunathadas, M. & Enoka, R. M.: Rate coding is compressed but variability is unaltered for motor units in a hand muscle of old adults. *Journal of Neurophysiology* **97** (2007), 3206–3218.
- [11] Baudry, S. & Duchateau, J.: Postactivation potentiation in a human muscle: effect on the rate of torque development of tetanic and voluntary isometric contractions. *Journal of Applied Physiology* **102** (2007), 1394–1401.
- [12] Baylor, S. M. & Hollingworth, S.: Model of Sarcomeric Ca^{2+} Movements, Including ATP Ca^{2+} Binding and Diffusion, during Activation of Frog Skeletal Muscle. *The Journal of General Physiology* **112** (1998), 297–316.
- [13] Bellemare, F.; Woods, J.; Johansson, R. & Bigland-Ritchie, B.: Motor-unit discharge rates in maximal voluntary contractions of three human muscles. *Journal of Neurophysiology* **50** (1983), 1380–1392.

- [14] Bergh, U. & Ekblom, B.: Influence of muscle temperature on maximal muscle strength and power output in human skeletal muscles. *Acta Physiologica Scandinavica* **107** (1979), 33–37.
- [15] Blemker, S. S. & Delp, S. L.: Three-dimensional representation of complex muscle architectures and geometries. *Annals of Biomedical Engineering* **33** (2005), 661–673.
- [16] Blemker, S. S.; Pinsky, P. M. & Delp, S. L.: A 3D model of muscle reveals the causes of nonuniform strains in the biceps brachii. *Journal of Biomechanics* **38** (2005), 657–665.
- [17] Bobinac, D.; Malnar-Dragojevic, D.; Bajek, S.; Soic-Vranic, T. & Jerkovic, R.: Muscle fiber type composition and morphometric properties of denervated rat extensor digitorum longus muscle. *Croatian Medical Journal* **41** (2000), 294–297.
- [18] Böl, M.: Micromechanical modelling of skeletal muscles: from the single fibre to the whole muscle. *Archive of Applied Mechanics* **80** (2010), 557–567.
- [19] Böl, M.; Ehret, A. E.; Leichsenring, K.; Weichert, C. & Kruse, R.: On the anisotropy of skeletal muscle tissue under compression. *Acta Biomaterialia* **10** (2014), 3225–3234.
- [20] Böl, M.; Kruse, R.; Ehret, A. E.; Leichsenring, K. & Siebert, T.: Compressive properties of passive skeletal muscle – The impact of precise sample geometry on parameter identification in inverse finite element analysis. *Journal of Biomechanics* **45** (2012), 2673–2679.
- [21] Böl, M. & Reese, S.: Micromechanical modelling of skeletal muscles based on the finite element method. *Computer Methods in Biomechanics and Biomedical Engineering* **11** (2008), 489–504.
- [22] Böl, M.; Weikert, R. & Weichert, C.: A coupled electromechanical model for the excitation-dependent contraction of skeletal muscle. *J. Mech. Behav. Biomed. Mater.* **4** (2011), 1299–1310.
- [23] Bonet, J. & Wood, R. D.: *Nonlinear Continuum Mechanics for Finite Element Analysis*. Cambridge University Press, Cambridge, UK, 2 edition 2008.
- [24] Bosboom, E.; Hesselink, M.; Oomens, C.; Bouten, C.; Drost, M. & Baaijens, F.: Passive transverse mechanical properties of skeletal muscle under in vivo compression. *Journal of Biomechanics* **34** (2001), 1365–1368.
- [25] Botterman, B. R.; Hamm, T. M.; Reinking, R. M. & Stuart, D. G.: Distribution of monosynaptic Ia excitatory post-synaptic potentials in the motor nucleus of the cat semitendinosus muscle. *The Journal of Physiology* **338** (1983), 379–393.
- [26] Bradley, C. P.; Bowery, A.; Britten, R.; Budelmann, V.; Camara, O.; Christie, R.; Cookson, A.; Frangi, A. F.; Gamage, T.; Heidlauf, T.; Krittian, S.; Ladd, D.; Little, C.; Mithraratne, K.; Nash, M.; Nickerson, D.; Nielsen, P.; Nordbø, O.; Omholt, S.; Pashaei, A.; Paterson, D.; Rajagopal, V.; Reeve, A.; Röhrle, O.;

- Safaei, S.; Sebastián, R.; Steghöfer, M.; Wu, T.; Yu, T.; Zhang, H. & Hunter, P. J.: OpenCMISS: A multi-physics & multi-scale computational infrastructure for the VPH/Physiome project. *Progress in Biophysics and Molecular Biology* **107** (2011), 32–47.
- [27] Brayton, R. K.; Gustavson, F. G. & Hachtel, G. D.: A new efficient algorithm for solving differential-algebraic systems using implicit backward differentiation formulas. *Proceedings of the IEEE* **60** (1972), 98–108.
- [28] Bryant, S. H.: Cable properties of external intercostal muscle fibres from myotonic and nonmyotonic goats. *The Journal of Physiology* **204** (1969), 539–550.
- [29] Burke, R.: Motor Units: Anatomy, Physiology, and Functional Organization. *Comprehensive Physiology* (1981).
- [30] Burke, R.; Levine, D.; Tsairis, P. & Zajac, F. E.: Physiological types and histochemical profiles in motor units of the cat gastrocnemius. *The Journal of Physiology* **234** (1973), 723–748.
- [31] Burke, R. E.; Levine, D.; Salcman, M. & Tsairis, P.: Motor units in cat soleus muscle: physiological, histochemical and morphological characteristics. *The Journal of Physiology* **238** (1974), 503–514.
- [32] Burkholder, T. J. & Lieber, R. L.: Sarcomere length operating range of vertebrate muscles during movement. *The Journal of Experimental Biology* **204** (2001), 1529–1536.
- [33] Burnett, R. A.; Laidlaw, D. H. & Enoka, R. M.: Coactivation of the antagonist muscle does not covary with steadiness in old adults. *Journal of Applied Physiology* **89** (2000), 61–71.
- [34] Butler, J. E. & Gandevia, S. C.: The output from human inspiratory motoneurone pools. *The Journal of Physiology* **586** (2008), 1257–1264.
- [35] Calvin, W. H. & Stevens, C. F.: Synaptic noise and other sources of randomness in motoneuron interspike intervals. *Journal of Neurophysiology* **31** (1968), 574–587.
- [36] Campbell, K. B.; Razumova, M. V.; Kirkpatrick, R. D. & Slinker, B. K.: Myofilament kinetics in isometric twitch dynamics. *Annals of Biomedical Engineering* **29** (2001), 384–405.
- [37] Campbell, K. B.; Razumova, M. V.; Kirkpatrick, R. D. & Slinker, B. K.: Nonlinear myofilament regulatory processes affect frequency-dependent muscle fiber stiffness. *Biophysical Journal* **81** (2001), 2278–2296.
- [38] Christie, G. R.; Nielsen, P. M.; Blackett, S. A.; Bradley, C. P. & Hunter, P. J.: FieldML: concepts and implementation. *Philosophical Transactions of the Royal Society A: Mathematical, Physical and Engineering Sciences* **367** (2009), 1869–1884.

- [39] Cisi, R. R. & Kohn, A. F.: Simulation system of spinal cord motor nuclei and associated nerves and muscles, in a web-based architecture. *Journal of Computational Neuroscience* **25** (2008), 520–542.
- [40] Clamann, H. P. & Schelhorn, T. B.: Nonlinear force addition of newly recruited motor units in the cat hindlimb. *Muscle & Nerve* **11** (1988), 1079–1089.
- [41] Cushing, S.; Bui, T. & Rose, P.: Effect of nonlinear summation of synaptic currents on the input–output properties of spinal motoneurons. *Journal of Neurophysiology* **94** (2005), 3465–3478.
- [42] Dahlquist, G. G.: A special stability problem for linear multistep methods. *BIT Numerical Mathematics* **3** (1963), 27–43.
- [43] Dal, H.; Göktepe, S.; Kaliske, M. & Kuhl, E.: A fully implicit finite element method for bidomain models of cardiac electromechanics. *Computer Methods in Applied Mechanics and Engineering* **253** (2013), 323–336.
- [44] Darin, N. & Tulinius, M.: Neuromuscular disorders in childhood: a descriptive epidemiological study from western Sweden. *Neuromuscular Disorders* **10** (2000), 1–9.
- [45] Davidson, J. B.: *Biophysical Modelling of Skeletal Muscle*. Dissertation, Auckland Bioengineering Institute - The University of Auckland, New Zealand (2009).
- [46] De Luca, C. J. & Hostage, E. C.: Relationship between firing rate and recruitment threshold of motoneurons in voluntary isometric contractions. *Journal of Neurophysiology* **104** (2010), 1034–1046.
- [47] De Luca, C. J.; LeFever, R. S.; McCue, M. P. & Xenakis, A. P.: Behaviour of human motor units in different muscles during linearly varying contractions. *The Journal of Physiology* **329** (1982), 113–128.
- [48] DeFreitas, J. M.; Costa, P. B.; Ryan, E. D.; Herda, T. J.; Cramer, J. T. & Beck, T. W.: An examination of innervation zone movement with increases in isometric torque production. *Clinical Neurophysiology* **119** (2008), 2795–2799.
- [49] Desmedt, J. & Godaux, E.: Ballistic contractions in man: characteristic recruitment pattern of single motor units of the tibialis anterior muscle. *The Journal of Physiology* **264** (1977), 673–693.
- [50] Dideriksen, J.; Negro, F.; Enoka, R. & Farina, D.: Neuromuscular adjustments that constrain submaximal EMG amplitude at task failure of sustained isometric contractions. *Journal of Applied Physiology* **111** (2011), 485–494.
- [51] Dideriksen, J.; Negro, F.; Enoka, R. & Farina, D.: Motor unit recruitment strategies and muscle properties determine the influence of synaptic noise on force steadiness. *Journal of Neurophysiology* **107** (2012), 3357–3369.

- [52] Dideriksen, J. L.; Farina, D.; Bækgaard, M. & Enoka, R. M.: An integrative model of motor unit activity during sustained submaximal contractions. *Journal of Applied Physiology* **108** (2010), 1550–1562.
- [53] DiFrancesco, D. & Noble, D.: A model of cardiac electrical activity incorporating ionic pumps and concentration changes. *Philosophical Transactions of the Royal Society of London. B, Biological Sciences* **307** (1985), 353–398.
- [54] Dimitrov, G. V.; Disselhorst-Klug, C.; Dimitrova, N. A.; Trachterna, A. & Rau, G.: The presence of unknown layer of skin and fat is an obstacle to a correct estimation of the motor unit size from surface detected potentials. *Electromyography and Clinical Neurophysiology* **42** (2002), 231–241.
- [55] Dorfmann, A. & Ogden, R.: Nonlinear electroelasticity. *Acta Mechanica* **174** (2005), 167–183.
- [56] Duchateau, J. & Baudry, S.: Maximal discharge rate of motor units determines the maximal rate of force development during ballistic contractions in human. *Frontiers in Human Neuroscience* **8** (2014).
- [57] Duchateau, J. & Enoka, R. M.: Human motor unit recordings: origins and insight into the integrated motor system. *Brain Research* **1409** (2011), 42–61.
- [58] Duchateau, J. & Hainaut, K.: Nonlinear summation of contractions in striated muscle. I. Twitch potentiation in human muscle. *Journal of Muscle Research and Cell Motility* **7** (1986), 11–17.
- [59] Duchateau, J. & Hainaut, K.: Nonlinear summation of contractions in striated muscle. II. Potentiation of intracellular Ca^{2+} movements in single barnacle muscle fibres. *Journal of Muscle Research and Cell Motility* **7** (1986), 18–24.
- [60] Duchateau, J. & Hainaut, K.: Effects of immobilization on contractile properties, recruitment and firing rates of human motor units. *The Journal of Physiology* **422** (1990), 55–65.
- [61] Edman, K.: The velocity of unloaded shortening and its relation to sarcomere length and isometric force on vertebrate muscle fibres. *The Journal of Physiology* **291** (1979), 143–159.
- [62] Emery, A. E.: Population frequencies of inherited neuromuscular diseases – a world survey. *Neuromuscular Disorders* **1** (1991), 19–29.
- [63] Emery, A. E.: The muscular dystrophies. *The Lancet* **359** (2002), 687–695.
- [64] Enoka, R. M.: Eccentric contractions require unique activation strategies by the nervous system. *Journal of Applied Physiology* **81** (1996), 2339–2346.
- [65] Enoka, R. M.: *Neuromechanics of human movement*. Human Kinetics 2008.
- [66] Epstein, B. R. & Foster, K. R.: Anisotropy in the dielectric properties of skeletal muscle. *Medical and Biological Engineering and Computing* **21** (1983), 51–55.

- [67] Epstein, M.: *The Elements of Continuum Biomechanics*. John Wiley & Sons Ltd 2012.
- [68] Farina, D.; Crosetti, A. & Merletti, R.: A Model for the Generation of Synthetic Intramuscular EMG Signals to Test Decomposition Algorithms. *IEEE Transactions on Biomedical Engineering* **48** (2001), 66–77.
- [69] Farina, D. & Falla, D.: Discharge rate of sternohyoid motor units activated with surface EMG feedback. *Journal of Neurophysiology* **101** (2009), 624–632.
- [70] Farina, D.; Holobar, A.; Merletti, R. & Enoka, R. M.: Decoding the neural drive to muscles from the surface electromyogram. *Clinical Neurophysiology* **121** (2010), 1616–1623.
- [71] Farina, D. & Merletti, R.: A Novel Approach for Precise Simulation of the EMG Signal Detected by Surface Electrodes. *IEEE Transactions on Biomedical Engineering* **48** (2001), 637–646.
- [72] Farina, D.; Mesin, L.; Martina, S. & Merletti, R.: A Surface EMG Generation Model With Multilayer Cylindrical Description of the Volume Conductor. *IEEE Transactions on Biomedical Engineering* **51** (2004), 415–426.
- [73] Farina, D.; Negro, F. & Dideriksen, J. L.: The effective neural drive to muscles is the common synaptic input to motor neurons. *The Journal of Physiology* **592** (2014), 3427–3441.
- [74] Fernandez, J. W.; Buist, M. L.; Nickerson, D. P. & Hunter, P. J.: Modelling the passive and nerve activated response of the rectus femoris muscle to a flexion loading: A finite element framework. *Medical Engineering & Physics* **27** (2005), 862–870.
- [75] Fortin, M. & Brezzi, F.: *Mixed and hybrid finite element methods*. New York: Springer-Verlag 1991.
- [76] Fuglevand, A. J.; Winter, D. A. & Patla, A. E.: Models of recruitment and rate coding organization in motor unit pools. *Journal of Neurophysiology* **70** (1993), 2470–2488.
- [77] Fuglevand, A. J.; Winter, D. A.; Patla, A. E. & Stashuk, D.: Detection of motor unit action potentials with surface electrodes: influence of electrode size and spacing. *Biological Cybernetics* **67** (1992), 143–153.
- [78] Gabriel, S.; Lau, R. W. & Gabriel, C.: The dielectric properties of biological tissue: II. Measurements in the frequency range 10 Hz to 20 GHz. *Physics in Medicine and Biology* **41** (1996), 2251–2269.
- [79] Galganski, M. E.; Fuglevand, A. J. & Enoka, R. M.: Reduced control of motor output in a human hand muscle of elderly subjects during submaximal contractions. *Journal of Neurophysiology* **69** (1993), 2108–2108.

- [80] Gardiner, P. F. & Kernell, D.: The “fastness” of rat motoneurons: time-course of afterhyperpolarization in relation to axonal conduction velocity and muscle unit contractile speed. *Pflügers Archiv* **415** (1990), 762–766.
- [81] Gareis, H.; Moshe, S.; Baratta, R.; Best, R. & D’Ambrosia, R.: The isometric length-force models of nine different skeletal muscles. *Journal of Biomechanics* **25** (1992), 903–916.
- [82] Garny, A.; Nickerson, D.; Cooper, J.; dos Santos, R.; Miller, A.; McKeever, S.; Nielsen, P. & Hunter, P.: CellML and associated tools and techniques. *Philosophical Transactions of the Royal Society of London A* **366** (2008), 3017–3043.
- [83] Gielen, A. W. J.; Oomens, C. W. J.; Bovendeerd, P. H. M.; Arts, T. & Janssen, J. D.: A finite element approach for skeletal muscle using a distributed moment model of contraction. *Computer Methods in Biomechanics and Biomedical Engineering* **3** (2000), 231–244.
- [84] Gielen, F. L. H.; Wallinga-de Jonge, W. & Boon, K. L.: Electrical conductivity of skeletal muscle tissue: Experimental results from different muscles in vivo. *Medical and Biological Engineering and Computing* **22** (1984), 569–577.
- [85] Gindre, J.; Takaza, M.; Moerman, K. M. & Simms, C. K.: A structural model of passive skeletal muscle shows two reinforcement processes in resisting deformation. *Journal of the Mechanical Behavior of Biomedical Materials* **22** (2013), 84–94.
- [86] Gizzi, A.; Cherubini, C.; Filippi, S. & Pandolfi, A.: Theoretical and Numerical Modeling of Nonlinear Electromechanics with applications to Biological Active Media. *Communications in Computational Physics* **17** (2015), 93–126.
- [87] Göktepe, S. & Kuhl, E.: Electromechanics of the heart: a unified approach to the strongly coupled excitation–contraction problem. *Computational Mechanics* **45** (2010), 227–243.
- [88] Göktepe, S.; Menzel, A. & Kuhl, E.: The generalized Hill model: A kinematic approach towards active muscle contraction. *Journal of the Mechanics and Physics of Solids* **72** (2014), 20–39.
- [89] Gordon, A. M.; Huxley, A. F. & Julian, F. J.: The variation in isometric tension with sarcomere length in vertebrate muscle fibres. *The Journal of Physiology* **184** (1966), 170–192.
- [90] Green, H. J.: Membrane excitability, weakness, and fatigue. *Canadian Journal of Applied Physiology* **29** (2004), 291–307.
- [91] Guharay, F. & Sachs, F.: Stretch-activated single ion channel currents in tissue-cultured embryonic chick skeletal muscle. *The Journal of Physiology* **352** (1984), 685–701.
- [92] Günther, M.; Röhrle, O.; Häufle, D. F. B. & Schmitt, S.: Spreading out muscle mass within a Hill-type model: a computer simulation study. *Computational and Mathematical Methods in Medicine* **2012** (2012), 1–13.

- [93] Günther, M. & Schmitt, S.: A macroscopic ansatz to deduce the Hill relation. *Journal of Theoretical Biology* **263** (2010), 407–418.
- [94] Günther, M.; Schmitt, S. & Wank, V.: High-frequency oscillations as a consequence of neglected serial damping in Hill-type muscle models. *Biological Cybernetics* **97** (2007), 63–79.
- [95] Gupta, G. K.; Sacks-Davis, R. & Tescher, P. E.: A review of recent developments in solving ODEs. *ACM Computing Surveys (CSUR)* **17** (1985), 5–47.
- [96] Gurtin, M. E.: *An Introduction to Continuum Mechanics*. Academic Press, Inc., New York 1981.
- [97] Hairer, E.; Nørsett, S. P. & Wanner, G.: *Solving ordinary differential equations I: nonstiff problems*. Springer Series In Computational Mathematics 2009.
- [98] Hairer, E. & Wanner, G.: *Solving ordinary differential equations II. stiff and differential-algebraic problems*. Springer series in computational mathematics 1996, 2nd edn.
- [99] Hanson, J. & Huxley, H. E.: Structural basis of the cross-striations in muscle. *Nature* **172** (1953), 530–532.
- [100] Harrigan, T. P.; Jasty, M.; Mann, R. W. & Harris, W. H.: Limitations of the continuum assumption in cancellous bone. *Journal of Biomechanics* **21** (1988), 269–275.
- [101] Harris, A. J.; Duxson, M. J.; Butler, J. E.; Hodges, P. W.; Taylor, J. L. & Gandevia, S. C.: Muscle fiber and motor unit behavior in the longest human skeletal muscle. *The Journal of Neuroscience* **25** (2005), 8528–8533.
- [102] Hawkins, D. & Bey, M.: A comprehensive approach for studying muscle-tendon mechanics. *Journal of Biomechanical Engineering* **116** (1994), 51–55.
- [103] Hawkins, D. & Bey, M.: Muscle and tendon force-length properties and their interactions *in vivo*. *Journal of Biomechanics* **30** (1997), 63–70.
- [104] Heckman, C. J. & Binder, M. D.: Computer simulation of the steady-state input-output function of the cat medial gastrocnemius motoneuron pool. *Journal of Neurophysiology* **65** (1991), 952–967.
- [105] Heckman, C. J. & Enoka, R. M.: Physiology of the motor neuron and the motor unit. *Handbook of Clinical Neurophysiology* **4** (2004), 119–147.
- [106] Heckman, C. J. & Enoka, R. M.: Motor Unit. *Comprehensive Physiology* **2** (2012), 2629–2682.
- [107] Hedley, W. J.; Nelson, M. R.; Bellivant, D. P. & Nielsen, P. F.: A short introduction to CellML. *Philosophical Transactions of the Royal Society of London A* **359** (2001), 1073–1089.

- [108] Heidlauf, T.; Negro, F.; Farina, D. & Röhrle, O.: An integrated model of the neuromuscular system. In *Neural Engineering (NER), 2013 6th International IEEE/EMBS Conference on*, IEEE 2013, pp. 227–230.
- [109] Heidlauf, T. & Röhrle, O.: Modeling the Chemoelectromechanical Behavior of Skeletal Muscle Using the Parallel Open-Source Software Library OpenCMISS. *Computational and Mathematical Methods in Medicine* **2013** (2013), 1–14.
- [110] Heidlauf, T. & Röhrle, O.: On the treatment of active behaviour in continuum muscle mechanics. 2013, vol. 13, pp. 71–72.
- [111] Heidlauf, T. & Röhrle, O.: A multiscale chemo-electro-mechanical skeletal muscle model to analyze muscle contraction and force generation for different muscle fiber arrangements. *Frontiers in Physiology* **5** (2014), 1–14.
- [112] Henneman, E.; Somjen, G. & Carpenter, D. O.: Excitability and inhibibility of motoneurons of different sizes. *Journal of Neurophysiology* **28** (1965), 599–620.
- [113] Henneman, E.; Somjen, G. & Carpenter, D. O.: Functional significance of cell size in spinal motoneurons. *Journal of Neurophysiology* **28** (1965), 560–580.
- [114] Hernández-Gascón, B.; Grasa, J.; Calvo, B. & Rodríguez, J. F.: A 3D electro-mechanical continuum model for simulating skeletal muscle contraction. *Journal of Theoretical Biology* **335** (2013), 108–118.
- [115] Heron, M. I. & Richmond, F. J. R.: In-series fiber architecture in long human muscles. *Journal of Morphology* **216** (1993), 35–45.
- [116] Herzog, W.: *Skeletal muscle mechanics: from mechanisms to function*. John Wiley & Sons 2000.
- [117] Hill, A. V.: The heat of shortening and the dynamic constants of muscle. *Proceedings of the Royal Society of London B* **126** (1938), 136–195.
- [118] Hill, A. V.: *First and last experiments in muscle mechanics*. University Press Cambridge 1970.
- [119] Hodges, P.; Pengel, L.; Herbert, R. & Gandevia, S.: Measurements of Muscle Contraction with Ultrasound Imaging. *Muscle & Nerve* **27** (2003), 682–692.
- [120] Hodgkin, A. L. & Huxley, A. F.: A quantitative description of membrane current and its application to conduction and excitation in nerve. *The Journal of Physiology* **117** (1952), 500–544.
- [121] Holzapfel, G. A.: *Nonlinear solid mechanics*. John Wiley & Sons LTD, Chichester, West Sussex, England 2000.
- [122] Hoyt, K. H.; Kneezel, T.; Castaneda, B. & Parker, K. J.: Quantitative sonoelastography for the in vivo assessment of skeletal muscle viscoelasticity. *Physics in Medicine and Biology* **53** (2008), 4063–4080.

- [123] Hughes, T. J.: *The finite element method: linear static and dynamic finite element analysis*. Courier Corporation 2012.
- [124] Huijing, P. A.: Muscle as a collagen fiber reinforced composite: a review of force transmission in muscle and whole limb. *Journal of Biomechanics* **32** (1999), 329–345.
- [125] Huijing, P. A.: Muscular force transmission necessitates a multilevel integrative approach to the analysis of function of skeletal muscle. *Exercise and Sport Sciences Reviews* **31** (2003), 167–175.
- [126] Hunter, P.; McNaughton, P. & Noble, D.: Analytical models of propagation in excitable cells. *Progress in Biophysics & Molecular Biology* **30** (1976), 99–144.
- [127] Hursh, J. B.: Conduction velocity and diameter of nerve fibers. *American Journal of Physiology* **127** (1939), 131–139.
- [128] Huxley, A. F.: Muscle structure and theories of contraction. *Progress in Biophysics and Biophysical Chemistry* **7** (1957), 255–318.
- [129] Huxley, A. F.: Muscular contraction. *The Journal of Physiology* **243** (1974), 1–43.
- [130] Huxley, A. F. & Niedergerke, R.: Structural Changes in Muscle During Contraction: Interference Microscopy of Living Muscle Fibres. *Nature* **173** (1954), 971–973.
- [131] Huxley, A. F. & Stämpeli, R.: Evidence for saltatory conduction in peripheral myelinated nerve fibres. *The Journal of Physiology* **108** (1949), 315–339.
- [132] Huxley, H. E. & Hanson, J.: Changes in the cross-striations of muscle during contraction and stretch and their structural interpretation. *Nature* (1954), 973–976.
- [133] van Ingen Schenau, G. J.; Bobbert, M. F.; Etema, G. J.; de Graaf, J. B. & Huijing, P. A.: A simulation of rat EDL force output based on intrinsic muscle properties. *Journal of Biomechanics* **21** (1988), 815–824.
- [134] Ishizuka, N.; Mannen, H.; Hongo, T. & Sasaki, S.: Trajectory of group Ia afferent fibers stained with horseradish peroxidase in the lumbosacral spinal cord of the cat: three dimensional reconstructions from serial sections. *Journal of Comparative Neurology* **186** (1979), 189–211.
- [135] Johansson, T.; Meier, P. & Blickhan, R.: A finite-element model for the mechanical analysis of skeletal muscles. *Journal of Theoretical Biology* **206** (2000), 131–49.
- [136] Juel, C.: Muscle action potential propagation velocity changes during activity. *Muscle & Nerve* **11** (1988), 714–719.
- [137] Kamavuako, E. N. & Farina, D.: Time-dependent effects of pre-conditioning activation on muscle fiber conduction velocity and twitch torque. *Muscle & Nerve* **42** (2010), 547–555.

- [138] Kamavuako, E. N.; Farina, D.; Yoshida, K. & Jensen, W.: Relationship between grasping force and features of single-channel intramuscular EMG signals. *Journal of Neuroscience Methods* **185** (2009), 143–150.
- [139] Kandel, E. R.; Schwartz, J. H.; Jessell, T. M. et al.: *Principles of neural science*, vol. 4. McGraw-Hill New York 2000.
- [140] Karajan, N.: Multiphasic intervertebral disc mechanics: theory and application. *Archives of Computational Methods in Engineering* **19** (2012), 261–339.
- [141] Katz, B.: The relation between force and speed in muscular contraction. *The Journal of Physiology* **96** (1939), 45–64.
- [142] Keenan, K. G.; Farina, D.; Merletti, R. & Enoka, R. M.: Influence of motor unit properties on the size of the simulated evoked surface EMG potential. *Experimental Brain Research* **169** (2006), 37–49.
- [143] Keenan, K. G. & Valero-Cuevas, F. J.: Experimentally valid predictions of muscle force and EMG in models of motor-unit function are most sensitive to neural properties. *Journal of Neurophysiology* **98** (2007), 1581–1590.
- [144] Keener, J. & Sneyd, J.: *Mathematical Physiology I: Cellular Physiology*, vol. 1. Springer 2009, second edn.
- [145] Keener, J. & Sneyd, J.: *Mathematical Physiology II: Systems Physiology*, vol. 2. Springer 2009, second edn.
- [146] Kleinedler, S. R.: *The American Heritage Medical Dictionary* (2008).
- [147] Kojic, M.; Mijailovic, S. & Zdravkovic, N.: Modelling of muscle behaviour by the finite element method using Hill's three-element model. *International Journal for Numerical Methods in Engineering* **43** (1998), 941–953.
- [148] Kuypers, H. & Brinkman, J.: Precentral projections to different parts of the spinal intermediate zone in the rhesus monkey. *Brain Research* **24** (1970), 29–48.
- [149] Laidlaw, D. H.; Bilodeau, M. & Enoka, R. M.: Steadiness is reduced and motor unit discharge is more variable in old adults. *Muscle & Nerve* **23** (2000), 600–612.
- [150] Laidlaw, D. H.; Kornatz, K. W.; Keen, D. A.; Suzuki, S. & Enoka, R. M.: Strength training improves the steadiness of slow lengthening contractions performed by old adults. *Journal of Applied Physiology* **87** (1999), 1786–1795.
- [151] Lansdown, D. A.; Ding, Z.; Wadington, M.; Hornberger, J. L. & Damon, B. M.: Quantitative diffusion tensor MRI-based fiber tracking of human skeletal muscle. *Journal of Applied Physiology* **103** (2007), 673–681.
- [152] Lateva, Z. C.; McGill, K. C. & Johanson, M. E.: Electrophysiological evidence of adult human skeletal muscle fibres with multiple endplates and polyneuronal innervation. *The Journal of Physiology* **544** (2002), 549–565.

- [153] Lawrence, D. G.; Porter, R. & Redman, S. J.: Corticomotoneuronal synapses in the monkey: light microscopic localization upon motoneurons of intrinsic muscles of the hand. *Journal of Comparative Neurology* **232** (1985), 499–510.
- [154] Lee, E. H.: Elastic-plastic deformation at finite strains. *Journal of Applied Mechanics* **36** (1969), 1.
- [155] LeVeque, R. J.: Finite difference methods for differential equations (2005), Lecture Notes for AMath 585–586, September 2005.
- [156] Levin, A. & Wyman, J.: The viscous elastic properties of muscle. *Proceedings of the Royal Society of London B* **101** (1927), 218–243.
- [157] Lieber, R. & Fridén, J.: Functional and clinical significance of skeletal muscle architecture. *Muscle & Nerve* **23** (2000), 1647–1666.
- [158] Lloyd, C. M.; Halstead, M. D. & Nielsen, P. F.: CellML: its future, present and past. *Progress in Biophysics & Molecular Biology* **85** (2004), 433–450.
- [159] Loeb, G.; Pratt, C.; Chanaud, C. & Richmond, F.: Distribution and innervation of short, interdigitated muscle fibers in parallel-fibered muscles of the cat hindlimb. *Journal of Morphology* **191** (1987), 1–15.
- [160] Lowery, M. M.; Stoykov, N. S.; Tafflove, A. & Kuiken, T. A.: A Multiple-Layer Finite-Element Model of the Surface EMG Signal. *IEEE Transactions on Biomedical Engineering* **49** (2002), 446–454.
- [161] MacIntosh, B. R.; Gardiner, P. F. & McComas, A. J.: *Skeletal Muscle: Form and Function*. Human Kinetics 2006, second edn.
- [162] Markert, B.: A biphasic continuum approach for viscoelastic high-porosity foams: comprehensive theory, numerics, and application. *Archives of Computational Methods in Engineering* **15** (2008), 371–446.
- [163] Markert, B.; Ehlers, W. & Karajan, N.: A general polyconvex strain-energy function for fiber-reinforced materials. *Proc. Appl. Math. Mech.* **5** (2005), 245–246.
- [164] McGill, K. C. & Lateva, Z. C.: History dependence of human muscle-fiber conduction velocity during voluntary isometric contractions. *Journal of Applied Physiology* **111** (2011), 630–641.
- [165] McMahon, T. A.: *Muscles, Reflexes, and Locomotion*. Princeton University Press, Princeton, USA 1984.
- [166] Meehan, C. F.; Sukiasyan, N.; Zhang, M.; Nielsen, J. B. & Hultborn, H.: Intrinsic properties of mouse lumbar motoneurons revealed by intracellular recording in vivo. *Journal of Neurophysiology* **103** (2010), 2599–2610.
- [167] Meier, P. & Blickhan, R.: FEM-Simulation of Skeletal Muscle: The Influence of Inertia During Activation and Deactivation. In Herzog, W. (ed.): *Skeletal Muscle Mechanics: From Mechanisms to Function*. John Wiley & Sons 2000, chap. 12, pp. 207–233.

- [168] Merletti, R. & Parker, P.: *Electromyography - Physiology, Engineering, and Noninvasive Applications*. John Wiley & Sons 2004.
- [169] Mesin, L.: Volume conductor models in surface electromyography: Computational techniques. *Computers in Biology and Medicine* **43** (2013), 942–952.
- [170] Mesin, L.: Real time estimation of generation, extinction and flow of muscle fibre action potentials in high density surface EMG. *Computers in Biology and Medicine* **57** (2015), 8–19.
- [171] Mesin, L.; Joubert, M.; Hanekom, T.; Merletti, R. & Farina, D.: A Finite Element Model for Describing the Effect of Muscle Shortening on Surface EMG. *IEEE Transactions on Biomedical Engineering* **53** (2006), 693–600.
- [172] Meunier, C. & Segev, I.: Playing the Devil’s advocate: is the Hodgkin-Huxley model useful? *Trends in Neurosciences* **25** (2002), 558–563.
- [173] Mileusnic, M. P.; Brown, I. E.; Lan, N. & Loeb, G. E.: Mathematical models of proprioceptors. I. Control and transduction in the muscle spindle. *Journal of Neurophysiology* **96** (2006), 1772–1788.
- [174] Mileusnic, M. P. & Loeb, G. E.: Mathematical models of proprioceptors. II. Structure and function of the Golgi tendon organ. *Journal of Neurophysiology* **96** (2006), 1789–1802.
- [175] Milner-Brown, H. & Miller, R. G.: Muscle membrane excitation and impulse propagation velocity are reduced during muscle fatigue. *Muscle & Nerve* **9** (1986), 367–374.
- [176] Miyamoto, N.; Fukunaga, T. & Kawakami, Y.: Evidence for intermuscle difference in postactivation potentiation in the human triceps surae: a mechanomyographic study. *Muscle & Nerve* **39** (2009), 703–706.
- [177] Monti, R. J.; Roy, R. R.; Hodgson, J. A. & Edgerton, V. R.: Transmission of forces within mammalian skeletal muscles. *Journal of Biomechanics* **32** (1999), 371–380.
- [178] Mordhorst, M.; Heidlauf, T. & Röhrle, O.: Predicting electromyographic signals under realistic conditions using a multiscale chemo-electro-mechanical finite element model. *Interface Focus* **5** (2015).
- [179] Morgan, D.: New insights into the behavior of muscle during active lengthening. *Biophysical Journal* **57** (1990), 209–221.
- [180] Moritz, C. T.; Barry, B. K.; Pascoe, M. A. & Enoka, R. M.: Discharge rate variability influences the variation in force fluctuations across the working range of a hand muscle. *Journal of Neurophysiology* **93** (2005), 2449–2459.
- [181] Morrow, D. A.; Haut Donahue, T. L.; Odegard, G. M. & Kaufman, K. R.: Transversely isotropic tensile material properties of skeletal muscle tissue. *Journal of the Mechanical Behavior of Biomedical Materials* **3** (2010), 124–129.

- [182] Murtada, S.-I.; Kroon, M. & Holzapfel, G. A.: A calcium-driven mechanochemical model for prediction of force generation in smooth muscle. *Biomechanics and Modeling in Mechanobiology* **9** (2010), 749–762.
- [183] Mutungi, G. & Ranatunga, K.: Sarcomere length changes during end-held (isometric) contractions in intact mammalian (rat) fast and slow muscle fibres. *Journal of Muscle Research and Cell Motility* **21** (2000), 565–575.
- [184] Nash, M. P. & Hunter, P. J.: Computational Mechanics of the Heart. From Tissue Structure to Ventricular Function. *Journal of Elasticity* **61** (2000), 113–141.
- [185] Nash, M. P. & Panfilov, A. V.: Electromechanical model of excitable tissue to study reentrant cardiac arrhythmias. *Progress in Biophysics & Molecular Biology* **85** (2004), 501–522.
- [186] Negro, F. & Farina, D.: Decorrelation of cortical inputs and motoneuron output. *Journal of Neurophysiology* **106** (2011), 2688–2697.
- [187] Nelson, M. E.: *Databasing the Brain: From Data to Knowledge (Neuroinformatics)*, John Wiley & Sons, New York 2005, chap. Electrophysiological Models. pp. 285–301.
- [188] Nickerson, D. P.; Ladd, D.; Hussan, J. R.; Safaei, S.; Suresh, V.; Hunter, P. J. & Bradley, C. P.: Using CellML with OpenCMISS to simulate multi-scale physiology. *Frontiers in Bioengineering and Biotechnology* **2** (2014).
- [189] Nie, X.; Cheng, J.-I.; Chen, W. W. & Weerasooriya, T.: Dynamic tensile response of porcine muscle. *Journal of Applied Mechanics* **78** (2011), 021009.
- [190] Niederer, S. A. & Smith, N. P.: An improved numerical method for strong coupling of excitation and contraction models in the heart. *Progress in Biophysics & Molecular Biology* **96** (2008), 90–111.
- [191] Nielsen, B. F.; Ruud, T. S.; Lines, G. T. & Tveito, A.: Optimal monodomain approximations of the bidomain equations. *Applied Mathematics and Computation* **184** (2007), 276–290.
- [192] Nishihara, K.; Kawai, H.; Chiba, Y.; Kanemura, N. & Gomi, T.: Investigation of innervation zone shift with continuous dynamic muscle contraction. *Computational and Mathematical Methods in Medicine* **2013** (2013).
- [193] Nishikawa, K.; Monroy, J. & Pace, C.: A role for titin in force enhancement, doublet potentiation and oscillatory work. In *Abstracts of the 7th World Congress of Biomechanics, Boston, MA, 2014*.
- [194] Noble, D.: Applications of Hodgkin-Huxley equations to excitable tissues. *Physiological Reviews* **46** (1966), 1–50.
- [195] Nordstrom, M. A.; Fuglevand, A. & Enoka, R.: Estimating the strength of common input to human motoneurons from the cross-correlogram. *The Journal of Physiology* **453** (1992), 547–574.

- [196] Odegard, G. M.; Donahue, T. L. H.; Morrow, D. A. & Kaufman, K. R.: Constitutive modeling of skeletal muscle tissue with an explicit strain-energy function. *Journal of Biomechanical Engineering* **130** (2008), 1–9.
- [197] Ogden, R. W.: *Non-linear elastic deformations*. Courier Dover Publications 1997.
- [198] Pandy, M. G.: Computer modeling and simulation of human movement. *Annual Review of Biomedical Engineering* **3** (2001), 245–73.
- [199] Panfilov, A. V.; Keldermann, R. H. & Nash, M. P.: Self-organized pacemakers in a coupled reaction-diffusion-mechanics system. *Physical Review Letters* **95** (2005), 258104.
- [200] Parmiggiani, F. & Stein, R. B.: Nonlinear summation of contractions in cat muscles. II. Later facilitation and stiffness changes. *The Journal of General Physiology* **78** (1981), 295–311.
- [201] Pathmanathan, P.; Bernabeu, M. O.; Bordas, R.; Cooper, J.; Garny, A.; Pitt-Francis, J. M.; Whiteley, J. P. & Gavaghan, D. J.: A numerical guide to the solution of the bidomain equations of cardiac electrophysiology. *Progress in Biophysics & Molecular Biology* **102** (2010), 136–155.
- [202] Paul, A. C.: Muscle length affects the architecture and pattern of innervation differently in leg muscles of mouse, guinea pig, and rabbit compared to those of human and monkey muscles. *The Anatomical Record* **262** (2001), 301–309.
- [203] Pelteret, J.-P. V. & Reddy, B. D.: Development of a computational biomechanical model of the human upper-airway soft-tissues toward simulating obstructive sleep apnea. *Clinical Anatomy* **27** (2014), 182–200.
- [204] Perreault, E. J.; Heckman, C. J. & Sandercock, T. G.: Hill muscle model errors during movement are greatest within the physiologically relevant range of motor unit firing rates. *Journal of Biomechanics* **36** (2003), 211–218.
- [205] Piazzesi, G.; Reconditi, M.; Linari, M.; Lucii, L.; Bianco, P.; Brunello, E.; Decostre, V.; Stewart, A.; Gore, D. B.; Irving, T. C.; Irving, M. & Lombardi, V.: Force transmission in skeletal muscle: from actomyosin to external tendons. *Cell* **131** (2007), 784–795.
- [206] Piitulainen, H.; Rantalainen, T.; Linnamo, V.; Komi, P. & Avela, J.: Innervation zone shift at different levels of isometric contraction in the biceps brachii muscle. *Journal of Electromyography and Kinesiology* **19** (2009), 667–675.
- [207] Powers, R. K. & Binder, M. D.: Distribution of oligosynaptic group I input to the cat medial gastrocnemius motoneuron pool. *Journal of Neurophysiology* **53** (1985), 497–517.
- [208] Powers, R. K.; ElBasiouny, S. M.; Rymer, W. Z. & Heckman, C. J.: Contribution of intrinsic properties and synaptic inputs to motoneuron discharge patterns: a simulation study. *Journal of Neurophysiology* **107** (2012), 808–823.

- [209] Prado, L. G.; Makarenko, I.; Andresen, C.; Krüger, M.; Opitz, C. A. & Linke, W. A.: Isoform diversity of giant proteins in relation to passive and active contractile properties of rabbit skeletal muscles. *The Journal of General Physiology* **126** (2005), 461–480.
- [210] Press, W. H.: *Numerical recipes 3rd edition: The art of scientific computing*. Cambridge university press 2007.
- [211] Pullan, A. J.; Buist, M. L. & Cheng, L. K.: *Mathematically Modelling the Electrical Activity of the Heart: From Cell to Body Surface and Back Again*. World Scientific Publishing Company, Singapore 2005.
- [212] Qu, Z. & Garfinkel, A.: An Advanced Algorithm for Solving Partial Differential Equation in Cardiac Conduction. *IEEE Transactions on Biomedical Engineering* **46** (1999), 1166–1168.
- [213] Ranatunga, K. W.: The force-velocity relation of rat fast- and slow-twitch muscles examined at different temperatures. *The Journal of Physiology* **351** (1984), 517–529.
- [214] Razumova, M. V.; Bukatina, A. E. & Campbell, K. B.: Stiffness-distortion sarcomere model for muscle simulation. *Journal of Applied Physiology* **87** (1999), 1861–1876.
- [215] Razumova, M. V.; Bukatina, A. E. & Campbell, K. B.: Different myofilament nearest neighbor interactions have distinctive effects on contractile behavior. *Biophysical Journal* **78** (2000), 3120–3137.
- [216] Richmond, F. J.; MacGillis, D. R. & Scott, D. A.: Muscle-fiber compartmentalization in cat splenius muscles. *Journal of Neurophysiology* **53** (1985), 868–885.
- [217] Ríos, E.; Karhanek, M.; Ma, J. & González, A.: An allosteric model of the molecular interactions of excitation-contraction coupling in skeletal muscle. *The Journal of General Physiology* **102** (1993), 449–481.
- [218] Rocha, B. M.; Campos, F. O.; Amorim, R. M.; Plank, G.; dos Santos, R. W.; Liebmann, M. & Haase, G.: Accelerating cardiac excitation spread simulations using graphics processing units. *Concurrency and Computation: Practice and Experience* **23** (2011), 708–720.
- [219] Röhrle, O.: Simulating the electro-mechanical behavior of skeletal muscles. *IEEE Computing in Science and Engineering* **12** (2010), 48–58.
- [220] Röhrle, O.; Davidson, J. B. & Pullan, A. J.: Bridging scales: a three-dimensional electromechanical finite element model of skeletal muscle. *SIAM Journal on Scientific Computing* **30** (2008), 2882–2904.
- [221] Röhrle, O.; Davidson, J. B. & Pullan, A. J.: A physiologically based, multi-scale model of skeletal muscle structure and function. *Frontiers in Physiology* **3** (2012), 1–14.

- [222] Röhrle, O. & Pullan, A. J.: Three-dimensional finite element modelling of muscle forces during mastication. *Journal of Biomechanics* **40** (2007), 3363–3372.
- [223] Röhrle, O.; Sprenger, M.; Ramasamy, E. & Heidlauf, T.: Multiscale skeletal muscle modeling: From cellular level to a multi-segment skeletal muscle model of the upper limb. In Holzapfel, G. A. & Kuhl, E. (eds.): *Computer Models in Biomechanics*. Springer Netherlands 2013, pp. 103–116.
- [224] Rossi, S.; Lassila, T.; Ruiz-Baier, R.; Sequeira, A. & Quarteroni, A.: Thermodynamically consistent orthotropic activation model capturing ventricular systolic wall thickening in cardiac electromechanics. *European Journal of Mechanics – A/Solids* **48** (2014), 129–142.
- [225] Rossi, S.; Ruiz-Baier, R.; Pavarino, L. F. & Quarteroni, A.: Orthotropic active strain models for the numerical simulation of cardiac biomechanics. *International Journal for Numerical Methods in Biomedical Engineering* **28** (2012), 761–788.
- [226] Ruiz-Muñoz, M. & Cuesta-Vargas, A. I.: Electromyography and sonomyography analysis of the tibialis anterior: a cross sectional study. *Journal of Foot and Ankle Research* **7** (2014).
- [227] Rupp, T.; Ehlers, W.; Karajan, N.; Günther, M. & Schmitt, S.: A forward dynamics simulation of human lumbar spine flexion predicting the load sharing of intervertebral discs, ligaments, and muscles. *Biomechanics and Modeling in Mechanobiology* (2015), 1–25.
- [228] Rush, S.; Abildskov, A. & McFee, R.: Resistivity of body tissue at low frequencies. *Circulation Research* **12** (1963), 40–50.
- [229] Sánchez, C. A.; Lloyd, J. E.; Fels, S. & Abolmaesumi, P.: Embedding digitized fibre fields in finite element models of muscles. *Computer Methods in Biomechanics and Biomedical Engineering: Imaging & Visualization* **2** (2014), 223–236.
- [230] Sandercock, T. G. & Heckman, C.: Force from cat soleus muscle during imposed locomotor-like movements: experimental data versus Hill-type model predictions. *Journal of Neurophysiology* **77** (1997), 1538–1552.
- [231] Schwarz, H. R.: *Numerical analysis: a comprehensive introduction*, vol. 10. Wiley New York 1989.
- [232] Segev, I.; Fleshman, J. W. & Burke, R. E.: *Methods in neuronal modeling*. MIT Press, Cambridge, MA, USA 1989, chap. Compartmental Models of Complex Neurons, pp. 63–96.
- [233] Sejersted, O. M. & Sjøgaard, G.: Dynamics and consequences of potassium shifts in skeletal muscle and heart during exercise. *Physiological Reviews* **80** (2000), 1411–1481.
- [234] Shampine, L. & Reichelt, M.: The MATLAB ODE Suite. *SIAM Journal on Scientific Computing* **18** (1997), 1–22.

- [235] Shampine, L. F. & Gordon, M. K.: *Computer Solution of Ordinary Differential Equations: The Initial Value Problem*. W. H. Freeman 1975.
- [236] Shampine, L. F.; Reichelt, M. W. & Kierzenka, J. A.: Solving index-1 DAEs in MATLAB and Simulink. *SIAM review* **41** (1999), 538–552.
- [237] Sharafi, B. & Blemker, S. S.: A micromechanical model of skeletal muscle to explore the effects of fiber and fascicle geometry. *Journal of Biomechanics* **43** (2010), 3207–3213.
- [238] Sharafi, B. & Blemker, S. S.: A mathematical model of force transmission from intrafascicularly terminating muscle fibers. *Journal of Biomechanics* **44** (2011), 2031–2039.
- [239] Sharifimajd, B. & Stålhand, J.: A continuum model for skeletal muscle contraction at homogeneous finite deformations. *Biomechanics and Modeling in Mechanobiology* **12** (2013), 965–973.
- [240] Shorten, P. R.; O’Callaghan, P.; Davidson, J. B. & Soboleva, T. K.: A mathematical model of fatigue in skeletal muscle force contraction. *Journal of Muscle Research and Cell Motility* **28** (2007), 293–313.
- [241] Siebert, T.; Günther, M. & Blickhan, R.: A 3D-geometric model for the deformation of a transversally loaded muscle. *Journal of Theoretical Biology* **298** (2012), 116–121.
- [242] Siebert, T.; Rode, C.; Herzog, W.; Till, O. & Blickhan, R.: Nonlinearities make a difference: comparison of two common Hill-type models with real muscle. *Biological Cybernetics* **98** (2008), 133–143.
- [243] Siebert, T.; Wagner, H. & Blickhan, R.: Not all oscillations are rubbish: forward simulation of quick-release experiments. *Journal of Mechanics in Medicine and Biology* **3** (2003), 107–122.
- [244] Soukup, T.; Zachařová, G. & Smerdu, V.: Fibre type composition of soleus and extensor digitorum longus muscles in normal female inbred Lewis rats. *Acta Histochemica* **104** (2002), 399–405.
- [245] Spitzer, V. M. & Whitlock, D. G.: The visible human dataset: The anatomical platform for human simulation. *The Anatomical record* **253** (1998), 49–57.
- [246] Stålhand, J.; Klarbring, A. & Holzapfel, G. A.: Smooth muscle contraction: mechanochemical formulation for homogeneous finite strains. *Progress in Biophysics & Molecular Biology* **96** (2008), 465–481.
- [247] Stålhand, J.; Klarbring, A. & Holzapfel, G. A.: A mechanochemical 3D continuum model for smooth muscle contraction under finite strains. *Journal of Theoretical Biology* **268** (2011), 120–130.

- [248] Staron, R. S.; Kraemer, W. J.; Hikida, R. S.; Fry, A. C.; Murray, J. D. & Campos, G. E.: Fiber type composition of four hindlimb muscles of adult Fisher 344 rats. *Histochemistry and Cell Biology* **111** (1999), 117–123.
- [249] Stein, R. & Parmiggiani, F.: Nonlinear summation of contractions in cat muscles. I. Early depression. *The Journal of General Physiology* **78** (1981), 277–293.
- [250] Stephens, J. A. & Stuart, D. G.: The motor units of cat medial gastrocnemius. *Pflügers Archiv* **356** (1975), 359–372.
- [251] Strang, G.: On the construction and comparison of difference schemes. *SIAM Journal on Numerical Analysis* **5** (1968), 506–517.
- [252] Street, S. F.: Lateral transmission of tension in frog myofibers: A myofibrillar network and transverse cytoskeletal connections are possible transmitters. *Journal of Cellular Physiology* **114** (1983), 346–364.
- [253] Street, S. F. & Ramsey, R. W.: Sarcolemma: Transmitter of active tension in frog skeletal muscle. *Science* **149** (1965), 1379–1380.
- [254] Sundnes, J.; Lines, G. T. & Tveito, A.: An operator splitting method for solving the bidomain equations coupled to a volume conductor model for the torso. *Mathematical Biosciences* **194** (2005), 233–248.
- [255] Sundnes, J.; Nielsen, B. F.; Mardal, K.; Cai, X.; Lines, G. T. & Tveito, A.: On the Computational Complexity of the Bidomain and the Monodomain Models of Electrophysiology. *Annals of Biomedical Engineering* **34** (2006), 1088–1097.
- [256] Takaza, M.; Moerman, K. M.; Gindre, J.; Lyons, G. & Simms, C. K.: The anisotropic mechanical behaviour of passive skeletal muscle tissue subjected to large tensile strain. *Journal of the Mechanical Behavior of Biomedical Materials* **17** (2013), 209–220.
- [257] Tanji, J. & Kato, M.: Firing rate of individual motor units in voluntary contraction of abductor digiti minimi muscle in man. *Experimental Neurology* **40** (1973), 771–783.
- [258] Telley, I. A. & Denoth, J.: Sarcomere dynamics during muscular contraction and their implications to muscle function. *Journal of Muscle Research and Cell Motility* **28** (2007), 89–104.
- [259] Thomas, C. K.; Ross, B. H. & Stein, R. B.: Motor-unit recruitment in human first dorsal interosseous muscle for static contractions in three different directions. *Journal of Neurophysiology* **55** (1986), 1017–1029.
- [260] Tian, M.; Hoang, P. D.; Gandevia, S. C.; Herbert, R. D. & Bilston, L. E.: Viscous elements have little impact on measured passive length-tension properties of human gastrocnemius muscle-tendon units in vivo. *Journal of Biomechanics* **44** (2011), 1334 – 1339.

- [261] Till, O.; Siebert, T.; Rode, C. & Blickhan, R.: Characterization of isovelocity extension of activated muscle: A Hill-type model for eccentric contractions and a method for parameter determination. *Journal of Theoretical Biology* **255** (2008), 176–187.
- [262] Traub, R. D. & Miles, R.: *Neuronal networks of the hippocampus*. Cambridge University Press 1991.
- [263] Truesdell, C. & Noll, W.: *The non-linear field theories of mechanics*. Springer, Berlin 1965.
- [264] Tuckwell, H. C.: *Introduction to theoretical neurobiology: Volume 2, nonlinear and stochastic theories*, vol. 8. Cambridge University Press 2005.
- [265] Usyk, T.; Mazhari, R. & McCulloch, A.: Effect of laminar orthotropic myofiber architecture on regional stress and strain in the canine left ventricle. *Journal of elasticity and the physical science of solids* **61** (2000), 143–164.
- [266] Van Cutsem, M.; Feiereisen, P.; Duchateau, J. & Hainaut, K.: Mechanical properties and behaviour of motor units in the tibialis anterior during voluntary contractions. *Canadian Journal of Applied Physiology* **22** (1997), 585–597.
- [267] Van Looke, M.; Lyons, C. & Simms, C.: Viscoelastic properties of passive skeletal muscle in compression: stress-relaxation behaviour and constitutive modelling. *Journal of Biomechanics* **41** (2008), 1555–1566.
- [268] Van Looke, M.; Lyons, C. G. & Simms, C. K.: A validated model of passive muscle in compression. *Journal of Biomechanics* **39** (2006), 2999–3009.
- [269] Van Looke, M.; Simms, C. & Lyons, C.: Viscoelastic properties of passive skeletal muscle in compression – Cyclic behaviour. *Journal of Biomechanics* **42** (2009), 1038–1048.
- [270] Vigmond, E. J.; Aguel, F. & Trayanova, N. A.: Computational techniques for solving the bidomain equations in three dimensions. *IEEE Transactions on Biomedical Engineering* **49** (2002), 1260–1269.
- [271] Virgilio, K. M.; Martin, K. S.; Peirce, S. M. & Blemker, S. S.: Multiscale models of skeletal muscle reveal the complex effects of muscular dystrophy on tissue mechanics and damage susceptibility. *Interface Focus* **5** (2015), 1–10.
- [272] Wallinga, W.; Meijer, S. L.; Alberink, M. J.; Vliek, M.; Wienk, E. D. & Ypey, D. L.: Modelling action potentials and membrane currents of mammalian skeletal muscle fibres in coherence with potassium concentration changes in the T-tubular system. *European Biophysics Journal* **28** (1999), 317–329.
- [273] Wang, C.-C. & Truesdell, C.: *Introduction to rational elasticity*, vol. 1. Springer 1973.

- [274] Wang, Y. K.; Nash, M. P.; Pullan, A. J.; Kieser, J. A. & Röhrle, O.: Model-based identification of motion sensor placement for tracking retraction and elongation of the tongue. *Biomechanics and Modeling in Mechanobiology* **12** (2013), 383–399.
- [275] Whiteley, J. P.: An efficient numerical technique for the solution of the monodomain and bidomain equations. *IEEE Transactions on Biomedical Engineering* **53** (2006), 2139–2147.
- [276] Woodley, S. & Mercer, S.: Hamstring muscles: architecture and innervation. *Cells tissues organs* **179** (2005), 125–141.
- [277] Young, M.; Paul, A.; Rodda, J.; Duxson, M. & Sheard, P.: Examination of intrafascicular muscle fiber terminations: implications for tension delivery in series-fibered muscles. *Journal of Morphology* **245** (2000), 130–145.
- [278] Yucesoy, C. A.; Koopman, B. H.; Baan, G. C.; Grootenboer, H. J. & Huijing, P. A.: Effects of inter- and extramuscular myofascial force transmission on adjacent synergistic muscles: assessment by experiments and finite-element modeling. *Journal of Biomechanics* **36** (2003), 1797–1811.
- [279] Yucesoy, C. A.; Koopman, B. H.; Huijing, P. A. & Grootenboer, H. J.: Three-dimensional finite element modeling of skeletal muscle using a two-domain approach: linked fiber-matrix mesh model. *Journal of Biomechanics* **35** (2002), 1253–1262.
- [280] Zahalak, G. I.: A distribution-moment approximation for kinetic theories of muscular contraction. *Mathematical Biosciences* **55** (1981), 89–114.
- [281] Zahalak, G. I. & Ma, S.-P.: Muscle activation and contraction: constitutive relations based directly on cross-bridge kinetics. *Journal of Biomechanical Engineering* **112** (1990), 52–62.
- [282] Zajac, F. E.: Muscle and tendon: properties, models, scaling, and application to biomechanics and motor control. *Critical Reviews in Biomedical Engineering* **17** (1989), 359–411.
- [283] Zehr, E. P. & Sale, D. G.: Ballistic movement: muscle activation and neuromuscular adaptation. *Canadian Journal of Applied Physiology* **19** (1994), 363–378.
- [284] Zheng, Y.; A., M. & Lue, B.: Objective assessment of limb tissue elasticity: Development of a manual indentation procedure. *Journal of Rehabilitation Research and Development* **36** (1999), 71–85.
- [285] Zienkiewicz, O. C. & Taylor, R. L.: *The finite element method for solid and structural mechanics*, vol. 2. Butterworth-Heinemann 2005.
- [286] Zienkiewicz, O. C.; Taylor, R. L. & Zhu, J. Z.: *The finite element method: its basis and fundamentals*, vol. 1. Butterworth-Heinemann 2005.
- [287] Zuurbier, C.; J.W., H.; Lee-de Groot, M. & der Laarse, V.: Mean sarcomere length-force relationship of rat muscle fibre bundles. *Journal of Biomechanics* **28** (1995), 83–87.

- [288] Zuurbier, C. J. & Huijing, P. A.: Influence of muscle geometry on shortening speed of fibre, aponeurosis and muscle. *Journal of Biomechanics* **25** (1992), 1017–1026.

Curriculum Vitae

Personal Data:

Name: Thomas Heidlauf
Date of birth: January 6, 1983
Place of birth: Saulgau (now Bad Saulgau), Germany
Nationality: German
Parents: Kurt Heidlauf and Christa Heidlauf
Siblings: Patrick Stevenson

Education:

10/2003 – 04/2009 studies in environmental engineering at the University of Stuttgart
04/2009 degree: “Diplom-Ingenieur (Dipl.-Ing.) Umweltschutztechnik”
09/2006 – 04/2007 study abroad at the University of Waterloo, Ontario, Canada
09/1993 – 06/2002 secondary/high school Störck Gymnasium, Bad Saulgau, Germany
06/2002 degree: “Allgemeine Hochschulreife” (high school diploma)
09/1989 – 07/1993 elementary school Berta Hummel-Schule, Bad Saulgau, Germany

Work Experience:

07/2009 – 09/2015 research assistant at the Institute of Applied Mechanics
(Civil Engineering) at the University of Stuttgart, Germany
01/2011 – 04/2011 visitor at the Auckland Bioengineering Institute,
University of Auckland, New Zealand
10/2008 – 06/2009 student assistant at the Institute of Applied Mechanics (CE),
University of Stuttgart, Germany
04/2008 – 07/2008 internship with Dr. Faerber & Schwarz Acoustics Pvt. Ltd.,
Panhala, Maharashtra, India
10/2007 – 04/2008 student assistant at the Institute of Mechanical Process
Engineering, University of Stuttgart, Germany
05/2007 – 08/2007 internship with Waterloo Hydrogeologic Inc., A Schlumberger
Company, Waterloo, Ontario, Canada
05/2007 – 08/2007 visiting scholar at the Department of Civil and Environmental
Engineering, University of Waterloo, Ontario, Canada
11/2004 – 08/2006 student assistant at the Institute of Applied Mechanics (CE),
University of Stuttgart, Germany
07/2002 – 04/2003 civilian service, Krankenhaus St. Elisabeth, Ravensburg, Germany

Released Report Series

CBM-01 Thomas Heidlauf: *Chemo-Electro-Mechanical Modelling of the Neuromuscular System*, September 2015

